March 2020

Surface Driven Flows : Liquid Bridges, Drops and Marangoni Propulsion

Samrat Sur
University of Massachusetts Amherst

SURFACE DRIVEN FLOWS: LIQUID BRIDGES, DROPS AND MARANGONI PROPULSION

A Dissertation Presented

by

SAMRAT SUR

Submitted to the Graduate School of the
University of Massachusetts Amherst in partial fulfillment
of the requirements for the degree of

DOCTOR OF PHILOSOPHY

February 2020

MECHANICAL ENGINEERING

SURFACE DRIVEN FLOWS: LIQUID BRIDGES, DROPS AND MARANGONI PROPULSION

A Dissertation Presented

by

SAMRAT SUR

Approved as to style and content by:

_____
Jonathan Rothstein, Chair

_____
Horst Henning Winter, Member

_____
Matthew Lackner, Member

_____
Sundar Krishnamurthy, Department Head
Mechanical Engineering

DEDICATION

I dedicate my dissertation work to my family. A special feeling of gratitude to my loving parents. My father, Mr. Prithwiraj Sur and my mother, Mrs. Sucheta Sur whose words of encouragement and push for tenacity ring in my ears. Without them this journey would not have been possible. Their hard work, love and sacrifices have made me the person I am today. Along with your continuous love and encouragement you have always taught me to be a good human being which I have always tried to follow.

"Thank you for telling me what I am capable of.

For giving me the support

that I needed to build a dream

to chase after.

And for believing that

I have the talent to reach my goals."

ACKNOWLEDGMENTS

I want to thank my academic advisor and dissertation chair Professor Jonathan P Rothstein for his unfaltering support and guidance throughout my doctoral studies. I will be forever grateful to him for accepting me as his doctoral student and providing me with opportunities for professional and personal growth. I have been immensely inspired by his passion for research, dedication to his profession, and commitment to excellence. His attention to details and undying enthusiasm have always motivated me to work hard in the pursuit of knowledge. He inspired me to not only develop a deep understanding of research methodologies, but, also to apply them in exciting and innovative ways. It has been a truly rewarding experience for me to have Professor Rothstein as my adviser and mentor.

Besides my adviser I would like to thank the rest of my thesis committee: Professor Winter Henning Horst and Professor Matthew Lackner for their encouragement, insightful comments.

I would also like to thank research scientist from SABIC, Mr. Manojkumar Chellamuthu for his help throughout our collaboration and giving me the opportunity for an internship at SABIC. I would also like to thank Professor Hassan Massoud and his students for their support and discussion also as a part of our collaboration. I would also like to thank my lab colleagues- Anita, David, Sunilkumar and Zara for their help and support throughout my journey. I have enjoyed working and growing with them together. I am really grateful to my friends in Amherst- Ishita, Arnab, Pritha and Atin and also in different parts of US and in India who have been pillars of support throughout my doctoral journey.

I want to end by thanking my parents. My parents have always been invested in my academic progress and have been proud of even my smallest achievements. My parents have been nothing but supportive of my dreams and aspirations. Their unwavering faith in me has given me strength and helped me reach this stage in my life. Along with my parents I would like to thank my elder brother, Joyraj, my sister in law, Anamika, and my niece, Aadita, who have been my constant source of inspiration and helped me throughout this whole journey.

ABSTRACT

SURFACE DRIVEN FLOWS: LIQUID BRIDGES, DROPS AND MARANGONI PROPULSION

FEBRUARY 2020

B.E., MANIPAL INSTITUTE OF TECHNOLOGY, KARNTAKA, INDIA

MS., UNIVERSITY OF MASSAHCUSETTS, AMHERST, MA, USA

Ph.D., UNIVERSITY OF MASSACHUSETTS AMHERST, MA, USA

Directed by: Professor Jonathan P Rothstein

Molecules sitting at a free liquid surface against vacuum or gas have weaker binding than molecules in the bulk. The missing (negative) binding energy can therefore be viewed as a positive energy added to the surface itself. Since a larger area of the surface contains larger surface energy, external forces must perform positive work against internal surface forces to increase the total area of the surface. Mathematically, the internal surface forces are represented by surface tension, defined as the normal force per unit of length. One common manifestation of surface tension is the difference in pressure it causes across a curved surface. This is the main principle behind capillary breakup extensional rheometry (CaBER). The other manifestation is the Marangoni flow which drives the interface towards the direction of the increasing surface tension gradient. The surface tension gradient can be caused by concentration gradient or by a temperature gradient (surface tension is a function of temperature). Both of these phenomenon will be investigated through various experimental techniques.

Predicting and controlling the rheology of polymeric fluids as a function of molecular chemistry has been of great interest in both academia and industry. While extensional rheology measurements of polymer melts have been performed in the past, those experiments were performed under nitrogen and at temperatures chosen to avoid polymer degradation and reaction. In this work we will explore the effect that oxygen at high temperatures can have on both the shear and extensional rheology of a series of polymer melts. We will demonstrate the high temperature evolution of extensional viscosity of three selected commercially available polycarbonates – one linear, one branched and one hyper-branched. The measurements were performed using a custom built high temperature capillary extensional break up rheometer (CABER). The experiments were performed in the temperature range of T=250^{o}C and 370^{o}C both in air and nitrogen. We will present a stark difference in the extensional behavior of the three grades of polycarbonate and demonstrate an obvious differentiation between random chain scission which is the first phase of polymer degradation and repolymerization or crosslinking which takes place at higher temperatures.

In a number of recent studies, the large extensional viscosity of dilute polymer solutions has been shown to dramatically delay the breakup of jets into drops. For the low shear viscosity solutions, the jet breakup is initially governed by a balance of inertial and capillary stresses before transitioning to a balance of viscoelastic and capillary stresses at later times. This transition occurs at a critical time when the radius decay dynamics shift from a 2/3 power law to an exponential decay as the increasing deformation rate imposed on the fluid filament results in large molecular deformations and rapid crossover into the elastocapillary regime. By experimental fits of the elasto-capillary thinning diameter data,

relaxation time as low as 40 microseconds have been successfully measured. In this work, we will show that with better understand of the transition from the inertia-capillary to the elasto-capillary breakup regimes that relaxation times close to a single microsecond can be measured with the relaxation time resolution limited only by the frame rate and spatial resolution of the high speed camera. In this work, the dynamics of drop formation and pinch-off will be presented using Dripping onto Substrate Extensional Rheometry (DoS) for a series of dilute solutions Polyethylene Oxide in water and in a water and glycerin mixture. Four different molecular weights between 100k and 1M g/mol will be shown with varying solvent viscosities between 1mPa-s and 22mPa-s and at concentrations between 0.004 and 0.5c*. We will show the dependence of the relaxation time and extensional viscosity on these varying parameters while searching for the lower limit in solution elasticity that can be detected. We will also show that this approach is a powerful technique for characterizing a notoriously difficult material, namely low-viscosity printing inks.

In this last project we have investigated the flow dynamics around a cylindrical disk propelled by Marangoni propulsion. Self-propulsion was achieved by coating one quarter of the disk with either soap or isopropyl alcohol in order to generate and then maintain a surface tension gradient across the surfer. As the propulsion strength and the resulting disk velocity were increased, a transition from a straight-line translational motion to a rotational motion was observed. Although spinning has been observed before for asymmetric objects, these are the first observations of spinning of a symmetric Marangoni surfer. Particle tracking and Particle Image Velocimetry (PIV) measurements were used to interrogate the resulting flow field and understand the origin of the rotational motion of the disk. These measurements showed that as the Reynolds number was increased, interfacial vortices

attached to sides of the disk were formed and intensified. Beyond a critical Reynolds number of $Re > 120$, a single vortex was observed to shed resulting in an unbalanced torque on the disk that caused it to rotate. The interaction between the disk and the confining wall of the Petri dish was also studied. Upon approaching the bounding wall, a transition from straight-line motion to rotational motion was observed at significantly lower Reynolds numbers than on an unconfined interface. Interfacial curvature was found to either enhance or eliminate rotation motion depending on whether the curvature was repulsive (concave) or attractive (convex). Along with investigations done for the case of a disk shaped Marangoni surfer, we have also look at the effect of shape and orientation of motion on the on the stability of these surfers. We have looked at spherical shaped Marangoni surfers and also at elliptical disks. The stability of the elliptical disks were found to be strongly linked to their aspect ratio and their orientation. While looking at shape effects on Marangoni propulsion we have also investigated the effect of reverse flow underneath the surfer and its effect on the motion. We were experimentally able to observe the phenomenon of reverse Marangoni propulsion of surfers which was found to be a function of water depth underneath the surfer. We performed a parametric study on the effect of depth of water on the mode of motion of a cylindrical disk shaped and a spherical shaped surfer. Along with critical depth, it was found that the Reynolds number also played a critical role in flow reversal. At higher Reynolds number, no reverse phenomenon was observed as inertia dominated the motion of the disk whereas at low Reynolds numbers and at the critical Depth, flow reversal was observed.

TABLE OF CONTENTS

Page

LIST OF TABLES

Table Page

LIST OF FIGURES

Figure Page

CHAPTER 1

HIGH TEMPERATURE EXTENSIONAL RHEOLOGY OF LINEAR, BRANCHED AND HYPER-BRANCHED POLYCARBONATE

1.1 Introduction

Polycarbonate (PC) is a widely used engineering polymer and with excellent mechanical properties, dimensional stability, heat resistance, and transparency. Since its introduction in the late 1950s, the use of bisphenol-A polycarbonate has grown steadily. Over the years a variety of new uses for PC have been created by tailoring the base polycarbonate polymer with modification that enhances its end-use properties. One main approach is to modify the backbone of the polycarbonate. As with most polymers, polycarbonate can be formulated with linear, branched and hyper-branched backbone architecture. Each of these polymers architectures shows different rheological behavior and solid state properties. As an example, branched polymers are often used for the applications characterized by strong extensional flow fields in the molten state such as extrusion coating, blow molding, foam extrusion, and melt phase thermoforming because addition of branching is known to enhance the extensional viscosity of polymer melts.

In many applications, polymer materials can be exposed to high temperatures either intentionally or unintentionally. Unfortunately, polymers are highly flammable, with combustion most often accompanied by the production of corrosive or toxic gases and smoke. Consequently, improving the fire retardant behavior of polymers has become a major challenge for extending their use to a wide array of commercial applications. The scientific and technical literature contains a very diverse array of strategies for improving polymer fire resistance. These strategies depend primarily on the nature and chemical

structure of the polymer concerned, its decomposition mode, the required level of fire safety, and the global performances of the resulting materials [1]. The development of flame retardant materials and the understanding of the phenomena that take place during combustion often require close collaboration between several fields of scientific expertise including macromolecular and physical chemistry, physics of mass and heat transfer and rheology, etc.

Solid polymeric materials undergo both physical and chemical changes when heat is applied, accompanied by undesirable changes to the properties of the material [2]. Thermal degradation is a process whereby the action of heat or elevated temperature on a material product or assembly cause loss of physical properties and extensive chemical reactions. The various physical processes that occur during the thermal decomposition depends on the nature of the material. For example, thermoplastic polymers are softened at elevated temperatures through reversible changes which provide a major advantage for thermoplastic materials in the ease of molding or thermoforming. However beyond a materials decomposition temperature, irreversible changes can occur [2]. Many materials produce carbonaceous chars on thermal decomposition [3]. The physical structures of these chars will strongly affect the continued thermal decomposition process. The minimum decomposition temperatures are typically lower in the presence of an oxidant such as air which is why polymer processing is often performed in an inert environment like nitrogen [2]. The most common chemical changes that can take place during thermal decomposition of polymers includes, random chain scission, in which the polymer chain is cleaved at random locations along its backbone; end chain scission, in which individual monomer units are successively removed at the chain end; chain stripping, in which side groups or

atoms are cleaved; and crosslinking, in which bonds are created between polymer chains [2]. All these changes can be detected through rheological measurements. The first three changes involve chain scission which will reduce the viscosity of the polymer melt, while crosslinking will increase both the shear and the extensional viscosity of the melt.

The flammability of polymers can be characterized by their ignitability, flame-spread rate and heat release. Depending on the targeted application of the polymeric material, one or more of these flammability criteria need to be measured by appropriate flammability tests. There are numerous small-, intermediate- or full-scale flammability tests used in industrial or academic laboratories for either screening materials during product development or testing manufactured products [4]. Here we focus on the vertical flame test UL 94V [5]. The set of UL94 tests has been approved by the "Underwriters' Laboratories" as tests of the flammability of plastic materials for parts in devices and appliances. It includes a range of flammability tests (small and large flame vertical tests, horizontal tests for bulk and foamed materials, radiant panel flame spread test). In terms of practice and usage, the most commonly used test is UL94 V for measuring the ignitability and flame spread of vertical bulk materials exposed to a small flame. This test is the subject of an international standard (IEC 60695-11-10) for small flames (50 W). It is a simple test of vertical combustion that classifies materials as V-0, V-1 or V-2 where V-2 is an unacceptable material and V-0 meets all the standards for a flame resistant material. In this experiment, a burner is controlled to produce a blue flame with a 20 mm-high central cone and a power of 50 W. The flame is applied to the bottom of the specimen with the top of the burner has to be located at 10 mm from the bottom edge of the specimen. The flame is applied for 10 seconds and removed. The after flame time t_1, (the time required for the

flame to extinguish) is noted. After extinction, the flame is applied for another 10 seconds. The after flame time t_2 is noted, together with the afterglow time t_3 (the time required for the fire glow to disappear). During the application of the flame, the distance between burner and specimen must remain constant. If drops fall, the burner must be tilted through a maximum angle of 45^{o} or slightly isolated from the specimen flame. Depending on the application of the flame and the dripping behavior of the polymer ratings are given to the materials.

In order to better understand the process of drop formation that can feed a flame and negatively affect a material's flame resistance, one must consider the dynamics of dripping and the formation of droplets. More than a century ago, Lord Rayleigh showed that as the length of a jet exceeds its circumference, it will become unstable and eventually break up into droplets [6, 7]. How that jet or a similar dripping liquid breaks up into droplets depends entirely on the properties of the liquid [8, 9]. In the small Ohnesorge number regime, $Oh = \eta / \sqrt{\rho\sigma R} << 1$, the drip breakup is resisted by inertia and the characteristic time for breakup scales with the inertio-capillary or Rayleigh timescale, $\tau_R = \sqrt{\rho R_0 / \sigma}$. Here σ is the surface tension, R_0 is the initial jet or drip radius, ρ is the density of the fluid, and η is the shear viscosity of the fluid. If, however, the Ohnesorge number is greater than one, $Oh >> 1$, the drip breakup is resisted by viscous forces and the characteristic time for breakup scales with the viscous timescale, $\tau_v = \eta R / \sigma$. This visco-capillary flow regime is often experienced by high viscosity fluids, like the polymer melts studied here. It is important to note, however, that during breakup, the drainage of fluid from the drip into the primary drops is a purely extensional flow. This is critically important for

viscoelastic fluids because the extensional viscosity, η_E, can increase by several orders of magnitude as the extension rate and the accumulated strain are increased, $\eta_E >> \eta$ [10-12]. The resulting Ohnesorge number evaluated using the extensional viscosity can be quite large even if the shear viscosity of the fluid is small. As a result, for viscoelastic liquids, the capillary breakup of the drip into individual drops is typically resisted by the extensional viscosity of the fluid. In this regime, the characteristic timescale for breakup becomes the visco-elastic-capillary timescale $\tau_v = \eta_E R/\sigma$ [13-15]. As the time between drips increases for these viscoelastic fluids, the time exposed to a high temperature heat source increase along with the time available to undergo thermal decomposition.

A number of recent studies have shown that it is possible to measure the extensional viscosity of polymer melts in the filament stretching rheometer (FSR) and using counter rotating cylinders like the Sentmanat extensional rheometer (SER). ([16];[17];[18];[19]; [20]; [21]. Bach et al. [22] studied the strain hardening characteristics of two polymer melts- LDPE and LLDPE. Experiments were performed at strain rates from $\dot{\varepsilon}$ =0.09 to 1 s^{-1} using a high temperature filament stretching rheometer (FiSER) and it was shown that Trouton ratio of the branched LDPE $Tr = \eta^{+}_{E}/\eta_0$, close to $Tr \approx 20$ as while the linear LLDPE only reached $Tr \approx 5$. In their filament stretching experiments Bach et al. [22] had difficulty obtaining a steady state elongation viscosity for the more strain hardening LDPE melt due to a rapid necking of the filament at large strains. This observation is indicative of the highly elastic nature of the branched LDPE. No necking was observed for the less elastic linear LLDPE. Their results showed good agreement with other extensional rheology measurement devices. Using the SER, Sentmenat et al. [23] similar extensional measurement for similar LDPE and LLDPE melts were made. These measurements also

showed an enhanced strain hardening for LDPE as compared to LLDPE because of its branched architecture.

Through our experiments, we will demonstrate how uniaxial extensional rheology measurement can be used as a method for characterizing the performance of polycarbonates (PC) of different molecular structure (linear, branched and hyper branched) at high temperatures where degradation is expected similar to those experienced by the PC when exposed to a flame. The extensional rheology measurements were performed using the capillary breakup extensional rheometry (CaBER). The hypothesis is that, because dripping is a purely extensional flow, by using a controlled extensional rheology measurement such as CaBER, the effect of elevated temperatures on the extensional viscosity could be used to better understand and even predict the flame resistant properties of any given polymer. In this paper, experiments were performed both in air and inert nitrogen environment for comparison of the extensional rheology response with and without oxygen exposure. In addition, our experiments were performed to systematically explore the time evolution of extensional viscosity for PC at these high temperature. Previous work on extensional rheology of linear and branched polycarbonate blends have been performed using a Meissner type extensional rheometer in the temperature range of $T = 220^{o}\mathrm{C}$ to $260^{o}\mathrm{C}$ where polymer degradation is not expected in these measurements. Park et.al. [24] have shown an increase in the extensional viscosity with increasing branching percent. Studies on the rheological response of branched polycarbonate prepared by an ultrasound- assisted intensive mixer using a rotary clamp rheometer have shown an increase in the strain hardening behavior of branched polycarbonates as compared to linear polycarbonates as the strain rates were increased at a temperature of $T = 190^{o}\mathrm{C}$ [25]. They

observed a gradual increase in extensional viscosity of the branched PC with a maximum extensional viscosity that was close to a ten times larger than the linear PC at the same fixed extension rate. These studies have shown the viscoelastic behavior of the polycarbonate melts at low to moderate temperatures ([26]; [24]) however, none of those studies have examined the shear or the extensional properties of PC at high temperatures where polymer degradation, scission and crosslinking is expected. Through our study, we will show how crosslinking leads to divergence in extensional viscosity at high temperatures and how these polycarbonate samples can be classified into flame resistant materials based on their evolution of extensional viscosities at high temperature changes.

1.2 Experimental Setup

1.2.1 Materials

High-temperature extensional rheology measurements were performed on a series of commercially- available polycarbonates. These included a linear PC (Lexan 130, a branched PC (Lexan) and a hyper-branched PC. The material was generously provided by SABIC in the form of pellets. The linear polycarbonate PC had a molecular weight of M_w= 36 kg/mol with a PDI of 2.74. The branched polycarbonate had a molecular weight of M_w=36kg/mol with a PDI of 2.88 and contained the branching agent (1.1.1.tris hydroxy phenyl ethan (THPE)). The hyper-branched had a molecular weight of M_w=28kg/mol with the end group hydroxy benzoyl nitrile (HBN) and PDI of 4. Before being tested in shear and extensional rheometers, the pellets were first molded to fit the plate geometry in the hot press under vacuum at $T = 250^{o}\mathrm{C}$.

1.2.2 Thermal Analysis

Thermal properties of all the samples were measured by thermo-gravimetric analysis using (TA-Q50) under nitrogen and air at a heating rate of $10^{o}\mathrm{C/min}$ from $T = 30^{o}\mathrm{C}$ to $900^{o}\mathrm{C}$. In nitrogen, the mass loss, which is a sign of degradation, began at a temperature of $T = 450^{o}\mathrm{C}$ for the linear PC, $T = 425^{o}\mathrm{C}$ for the branched PC and $T = 400^{o}\mathrm{C}$ for the hyper-branched PC. In comparison to mass loss in nitrogen, mass loss in air consistently started about $20^{o}\mathrm{C}$ earlier for each polymer. The residue was found to remain constant in nitrogen beyond $T = 600^{o}\mathrm{C}$, but the residue continued to decrease in air and eventually went to zero. From DSC measurements (TA-Q100), the glass transition temperatures, T_g, was found to be $T_g = 140^{o}\mathrm{C}$ for the hyper-branched, $T_g = 150^{o}\mathrm{C}$ for the linear and $T_g = 151^{o}\mathrm{C}$ for the branched PC.

1.2.3 Shear Rheology

Small amplitude oscillatory and steady shear measurements were carried out using a controlled-strain rheometer (ARES-G2). A parallel plate geometry with a 25 mm diameter and a 1.5 mm gap was employed at temperatures between $T = 160^{o}\mathrm{C}$ and $300^{o}\mathrm{C}$. Storage modulus, G', and loss modulus, G'', ranging over eight decades of frequency covering the response from the terminal regime to glassy regime has been plotted using Time Temperature Superposition (TTS). Time sweep measurements at a fixed frequency of ω=10rad/s were performed at different temperatures and the variation in the storage modulus $G^{\cdot}$ as a function of time t was measured.

1.2.4 Capillary Breakup Extensional Rheometry

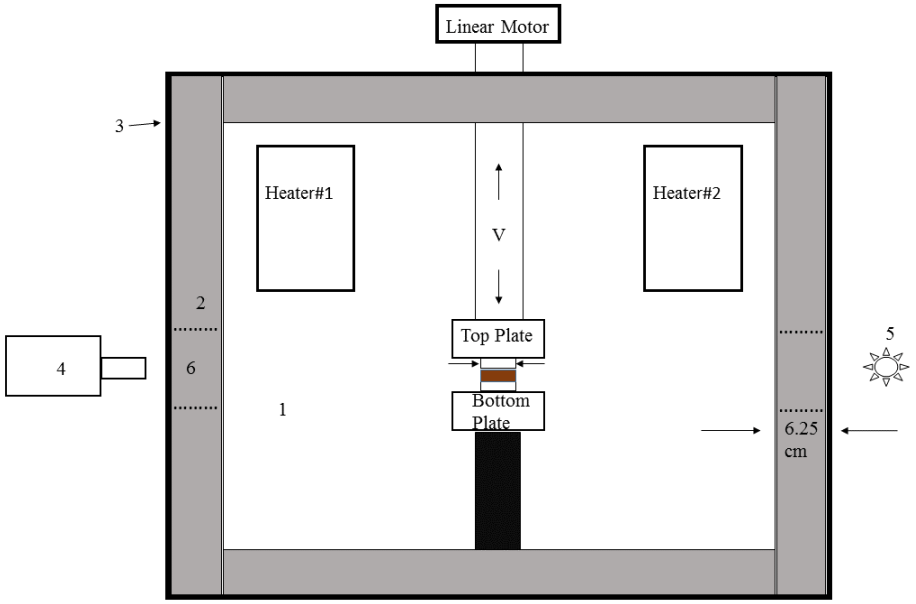

Figure 1. Front view of the high temperature extensional rheometer. The figure includes (1) Inner box with the heaters, top plate and the bottom plate, (2) heat shield (silica based insulation) of thickness 6.25 cm on all sides, (3) outer box with the motor mounted on top, (4) camera for visualizing the stretch, (5) light source, and (6) windows for filament observation.

A schematic diagram of the capillary breakup extensional rheometer (CaBER) with its main components is shown in figure 1. The design of the CaBER was based on previous design found in the literature (Rothstein 2003, Rothstein and Mckinley 2002a, Rothstein and Mckinley 2002b). Here we have customized it for high temperature measurements by building an oven around it that can reach up to $400^{o}C$ using three 250W resistance heaters (Omega-WS series). The oven temperature is controlled using a PID temperature controller (Omega-CN-2110) with a temperature accuracy of $\pm 2^{o}C$. The oven is made of an inner and outer box fabricated from steel plates with insulation between the two boxes to reduce heat transfer out of the oven. The thickness of insulator was designed to maintain an inside

temperature of $T = 400^{o}\mathrm{C}$ without exceeding an outside oven surface temperature of $35^{o}\mathrm{C}$. A thickness of 6.25 cm of a silica-based insulator (Microsil, Zircar) with a thermal conductivity of $k = 0.024\,\mathrm{W/mK}$ was used to maintain the outside temperature below $35^{o}\mathrm{C}$. Rectangular openings were cut into the sides of both the inner and outer box and covered with an inner and outer window made of Pyrex glass to allow optical access for the camera to allow for visualization of the filament diameter so that it could be measured optically as a function of time. The diameter measurements had a resolution of 6.3 μm/pixel based on the maximum magnification of the lens and the pixelation of the camera sensor. Provisions were made for supplying nitrogen and air into the oven so that measurements could be made in an inert or an oxygen rich environment. The top plate was connected to a liner motor (LinMot-C1250) using a glass mica rod to reduce heat flow out of the oven and minimize the risk of heat damages to the motor. The motor was capable of stretching the fluid at speeds up to 200 mm/s. An edge detection software (Edgehog) was used to capture the diameter decay with time with subpixel resolution. In order to calculate the extensional viscosity, the diameter decay was fit with a spline and then differentiated.

Capillary breakup extensional rheometry measurements have become an increasingly common technique for determining the extensional rheology of viscoelastic fluids [27-36]. In the CaBER experiments presented here, a cylindrical sample which had been melt cast using a hot press under vacuum was placed between two cylindrical plates at room. The oven was then turned on and heated to the desired experimental temperature with a ramp of $5^{o}\mathrm{C}/\mathrm{min}$. Once the oven reached the desired temperature, the sample was allowed to reach equilibrium by holding oven at the desired temperature for a minute before beginning the stretch. The sample was then stretched with the top

plate moving at a velocity of 0.01m/s^2 until a gap of $3L_0$ =6.75 mm was reached. Here L_0 =2.25 mm is the initial starting gap between the plates and R_0 =2.25 mm is the initial radius of the sample melt. The stretch was then stopped and the capillary thinning of the liquid bridge that was formed between the two endplates subsequently produced a uniaxial extensional flow from which the extensional viscosity and relaxation time of the test fluid could be measured. A schematic diagram of the stretch is shown in Figure 2.

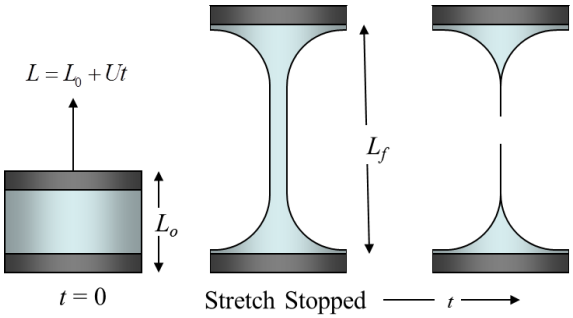

Figure 2. Schematic diagram of Capillary Breakup Extensional Rheometry (CaBER)

The breakup of the fluid filament is driven by capillary stresses and resisted by a combination of inertial, viscous and elastic stresses developed within the flow. The specific balance of forces that dictate the breakup regime of the fluid depend on the properties of the fluid. As the fluids we will investigate here are all quite viscous, inertial effects can in all cases be safely neglected as the Ohnesorge number is in all cases $Oh>>1$. In the viscous-capillary regime, capillary decay is opposed by viscous stresses. In this regime, the extensional viscosity of the fluid can be determined by measuring the change in the filament diameter as a function of time. Papageorgiou [15] showed that for a Newtonian

fluid with a constant shear viscosity, η, the radius of the fluid filament will decay linearly with time such that, $R_{\text{mid}}(t) = 0.07095(t_b - t)/\eta$. Here σ is the surface tension, η is the shear viscosity and t_b is the time at breakup. In the Newtonian limit the extensional viscosity is equal to $\eta_E = 3\eta$. In the elasto-capillary regime, elastic stresses generated within the non-Newtonian fluid filament resist capillary drainage. In this regime a cylindrical filament is formed and Entov and Hinch [31] showed that for an Oldroyd-B fluid with an extensional relaxation time of λ_E, the radius will decay exponentially with time such that, $R_{\text{mid}}(t) \propto \exp(-t/3\lambda_{\text{E}})$. The result is an extension rate that is constant, independent of time and only dependent on the fluids relaxation time,

$$\dot{\varepsilon} = -\frac{2}{R_{\text{mid}}(t)}\frac{\mathrm{d}R_{\text{mid}}(t)}{\mathrm{d}t} = \frac{2}{3\lambda_{\text{E}}}. \tag{0.1}$$

Hence for an Oldroyd-B fluid, the filament decay results in a flow which has a constant Weissenberg number of $Wi = \lambda_{\text{E}}\dot{\varepsilon} = 2/3$. This value is larger than the critical Weissenberg number of $Wi = 1/2$ needed to achieve coil-stretch transition and thus can be used to measure the extensional viscosity of these polymer melts which can be calculated directly from the measurement of diameter decay,

$$\eta_{\text{E}} = \frac{-0.213\sigma}{\mathrm{d}R_{\text{mid}}/\mathrm{d}t}. \tag{0.2}$$

In order to calculate the apparent extensional viscosity, the diameter measurements as a function of time were first fit with a spline to smooth the data and then differentiated.

The value of the surface tension was taken from the literature to be $\sigma = 34.2$ mN/m from surface energy data for handbook (www.surface-tension.de).

1.3 Results and Discussions

1.3.1 Shear Rheology

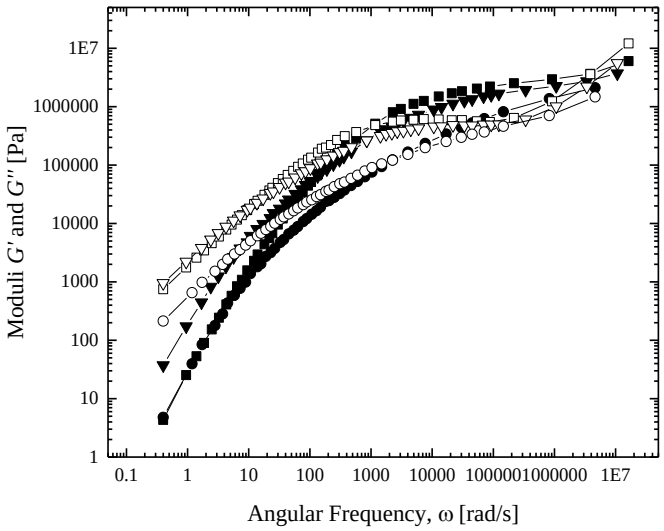

Figure 3. Small amplitude oscillatory shear measurements of the storage and loss moduli (G' and G'') as a function of applied angular frequency for three different polycarbonates: linear PC (□), branched PC (∇) and hyper branched PC (○). Filled symbols correspond to G' while hollow symbols correspond to G''. Data was taken at temperatures between $160^{o} \le T \le 300^{o}$ and shifted to a temperature of $T = 300^{o}\mathrm{C}$.

Small amplitude oscillatory and steady shear measurements were carried out using a controlled-strain rheometer (ARES-G2). A parallel plate geometry with a 25 mm diameter and a 1.5 mm gap was employed at temperatures between $T = 160^{o}\mathrm{C}$ and $300^{o}\mathrm{C}$. A plot of storage modulus, G', and loss modulus, G'', ranging over eight decades of

frequency covering the response from the terminal regime to glassy regime is presented in figure 3 utilizing, time-temperature superposition. For the linear PC, a typical rheological response was observed exhibiting the expected terminal regime behavior with storage modulus varying as $G' \propto \omega^2$ and loss modulus proportional to $G'' \propto \omega$ in the lower the frequency range. The Arrhenius time- temperature superposition activation energy calculated using the shift factors presented in figure 4, was found to be the same $E_a = 108$ kJ/mol for the linear, branched and hyper-branched PC. The shift factors were not valid beyond $T = 300^{\circ}\mathrm{C}$ because degradation of the PC was found to lead to time-dependent rheology. The crossover point, which is the point of intersection of the G' and G'', can be used to estimate the relaxation time of the fluid. Although it is quite clear for the linear PC it becomes less distinct as the degree of branching was increased. This is likely due to long relaxation time associated with the branch points and the polydispersity of the molecular weight of the branches. Reptation is the main relaxation method for linear polymers whereas branched chains relaxes by arm retraction. Research has shown that this leads to a retardation of chain movement along its backbone and consequently a broadening of the relaxation spectrum which can be seen in the in the broad shoulder observed in the G', G'' data [37].

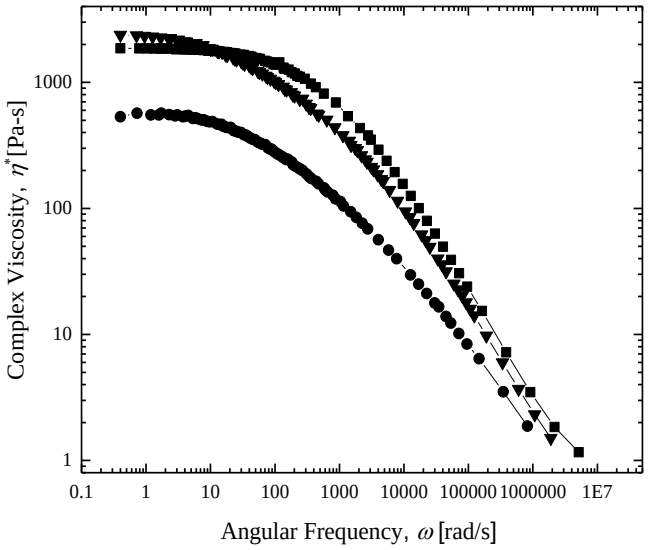

Figure 4. Complex viscosity η^* as a function of angular frequency ω for the linear (■), branched (▼) and hyper-branched PC (●) at a temperature of $T = 300^{\circ}\mathrm{C}$.

In Figure 4, is a plot of complex viscosity, η^*, is shown as a function of angular frequency, ω , at a temperature of T=300°C for linear, branched and hyper branched PC. From the literature [38], we know that the zero-shear-rate viscosity for a linear PC scales with molecular weight as $\eta_0 \propto M_w^{3.4}$. This dependence on molecular weight increases as the level of branching increases which can be observed from the plot where branched PC has a higher complex viscosity as compared to linear PC at lower frequencies even though they are of the same molecular weight. Also from Figure 5, a rapid shear thinning for hyper-branched and branched PC as compared to linear PC can be observed which is due to the presence of long relaxation time related to branched chains. Similar results have been seen in literature [39]. From the above Figure, the relaxation time of the three sample can be approximated in a number of ways. Here, we fit a line through the Newtonian region and

through the power law region and taking the inverse of the frequency ω at which it intersects to be the relaxation time. Using the above fitting method the calculated relaxation time for linear PC is $\lambda = 0.0025\text{s}$, for branched PC $\lambda = 0.005\text{s}$ and for hyper branched PC $\lambda = 0.01\text{s}$ at $T = 300^{\circ}\text{C}$. This relaxation time can be shifted to lower temperature range using the time-temperature superposition shift factors presented in Figure 4.

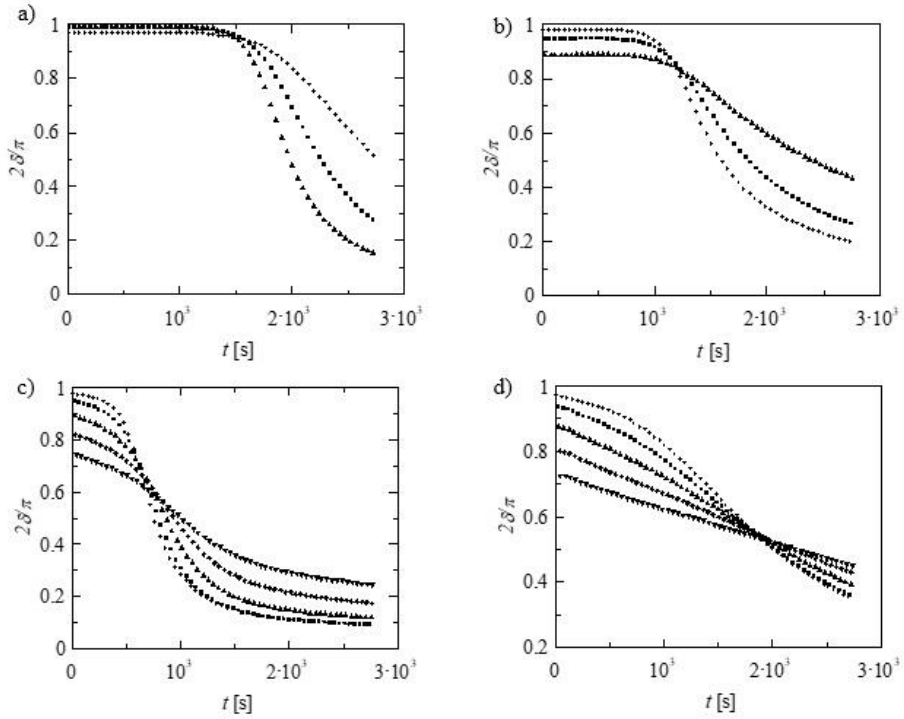

Figure 5. Time Resolved Rheometry of loss tangent for a) linear PC, b) branched PC, c) hyper-branched PC at 340ºC in the presence of air and d) hyper-branched PC in the presence of nitrogen at frequency of (▼) ω=100rad/s, (♦) ω=31.6rad/s, (▲) ω=10rad/s, (■) ω=3rad/s and (●) ω=1rad/s.

A series of time-resolved rheometry measurements were performed on all three samples at T = 340ºC. These measurements were performed at several frequencies between ω = 1rad/s and ω = 100rad/s to look for the critical gel point of these material which indicates the transition from a viscoelastic liquid to a soft solid. The frequencies were chosen to be as large as possible so that the change in polymer properties could be

minimized during each measurement point. The results are shown in Figure 5 as the nomalized loss tangent, $2\delta/\pi$. Similar experimental protocols have been used in the literature to study thermo-oxidative degradation of polyethylene terephthalate [40] and also polyamide 11 [41]. For the linear and branched PC in air, a crossover of the of all the normalized loss tangents tested is observed at t = 1600s and 1200s, while no crossover was observed under nitrogen. This crossover, where the loss tangent becomes independent of frequency, is known as the critical gelation point. Winter and Chambon [42] showed that at the critical gel point, the material transitions from a liquid phase to a solid phase. In Figure 5, the presence of this critical gel point clearly demonstrates that the linear and branched PC are undergoing a crosslinking reaction under air at $T = 340^{o}\mathrm{C}$. For the case of hyper-branched PC, the gel point was observed both in the presence of air and nitrogen at a time of t = 700s and 1600s respectively. The crosslinking reaction clearly occurs much faster in air. However, the fact that the hyperbranched PC crosslinks at all in nitrogen while the linear and branched do not might be due to the presence of an end group which promoted both branching and crosslinking reactions even in the presence of nitrogen.

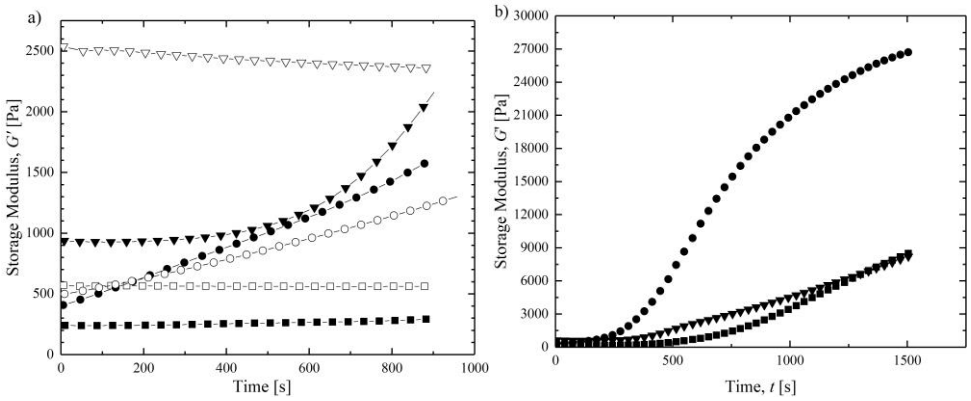

Figure 6. Storage modulus, G', of linear (□) branched (∇) and hyper-branched (o) PC as a function of time t at a frequency of ω=10rad/s in air at temperatures of a) T=320°C (hollow symbols) and T=340°C (filled symbols) and b) at T=360°C.

Although the loss tangent is an effective way to determine the critical gel point, perhaps a more intuitive way to understand the changes that are occurring the polymers at these extreme temperatures is to present the storage modulus as a function of time. In Figure 6, the storage modulus, G', as a function of time for the linear and the branched PC at frequency of ω=10 rad/s and at temperatures of $T = 320^{o}\mathrm{C}$, $T = 340^{o}\mathrm{C}$ and $T = 360^{o}\mathrm{C}$ in the presence of air. At $T = 320^{o}\mathrm{C}$ and $T = 340^{o}\mathrm{C}$, the storage modulus of the linear PC was found to show very little variation with time, whereas, for branched PC and hyper-branched PC at $T = 340^{o}\mathrm{C}$, the storage modulus was found to increase by a factor of two and three over time due to molecular structure buildup which takes place at that temperature respectively. As the temperature was increased to $T = 360^{o}\mathrm{C}$, an increase in the storage modulus was observed for all the three samples as shown in Figure 6b. For the case of linear PC and branched PC an increase in the storage modulus by a factor of 15 was observed whereas for the case of hyper-branched PC an increase by a factor of 45 was observed. This rapid increase in storage modulus is due to the rapid buildup of molecular

structure which has also been observed in the works of [43]. Similar trend in storage modulus, *G*', was observed in the works of Shangguan et al. [44]. By using the term molecular structure buildup, we are hypothesizing that the increase in elastic modulus is a direct result of creation of additional short or long branches along the polymer backbone or the cross-linking of adjacent polymeric chains together to build-up an interconnected elastic network structure over time. Either would result in an increase in the storage modulus and are difficult to distinguish in the DSC, TGA measurements that were performed after the experiments and will be described in detail later in the text. In Shangguan et al. [44], they concluded that the increase in storage modulus is attributed to crosslink reaction and that oxidative degradation and crosslinking are the main reasons for the rheological changes observed in the polymer melt.

The maximum increase in storage modulus over time was seen for hyper-branched PC at $T = 360^{o}\mathrm{C}$. In that case, an increase by a factor of 45 over the same period was observed which was likely due to the presence of the additional end groups available for crosslinking or perhaps residual catalyst in the resin. Similar measurements were performed in the presence of nitrogen. Unlike in the case of air, for the linear and branched PC no increase in storage modulus was observed over the period of experiment. Thus the polymer was found to be thermally stable in the presence of nitrogen at T=320^{o}C and T=360^{o}C. Although, at T=360^{o}C the storage modulus during the experiment was found to be lower as compared to that at T=320^{o}C. This was due to the effect of time temperature superposition. Whereas, for the case of hyper-branched case an increase in the storage modulus was observed in the presence of nitrogen at T=320^{o}C and at T=360^{o}C over the period of experiment. Thus hyper-branched PC was found to be thermally less stable due

to the presence of an end group as discussed earlier. Along with the time sweeps, temperature ramp measurements were also performed to further investigate the degradation behavior of the linear, branched and hyper-branched PC in the presence of air and nitrogen. In those experiments, similar rapid increase in the storage modulus, *G*', was observed beyond a temperature of *T*=380^{o}C in the presence of air for the case of linear and branched PC. Whereas, in the presence of nitrogen no upturn in the storage modulus was observed until a temperature of *T*=420^{o}C. This difference clearly shows the higher rate of degradation that the polymer experience in the presence of oxygen, which leads to earlier degradation as compared to that in the presence of nitrogen. While for the case of hyper-branched, deviation of the storage modulus was observed 30^{o}C and 70^{o}C prior to that of the linear and the branched PC in the presence of air and nitrogen respectively.

1.3.2 Extensional Rheology

1.3.2.1 Linear Polycarbonate

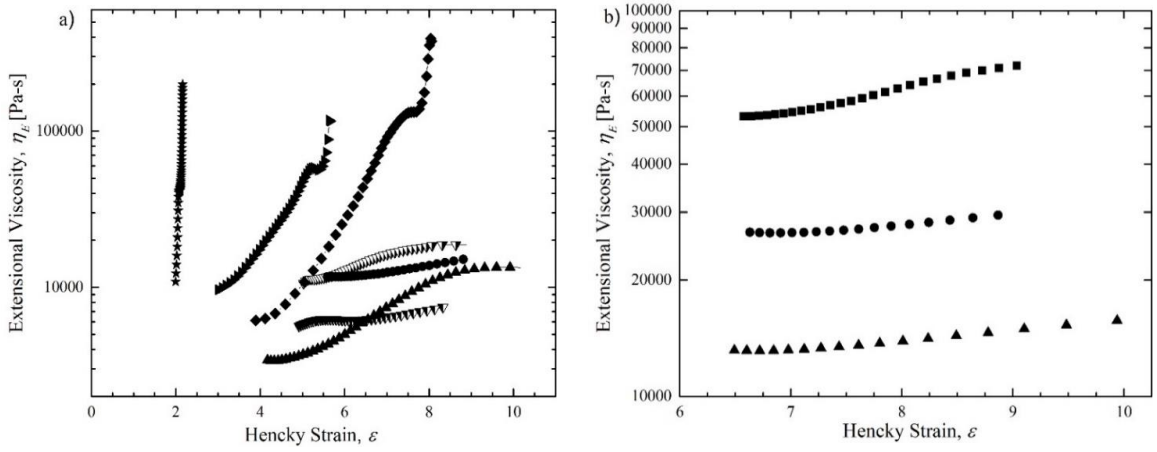

Figure 7. (a) Capillary breakup extensional rheology measurement of extensional viscosity, η_E, as a function of Hencky strain, ε, for a) the linear polycarbonate in air and b) in nitrogen at temperatures $T = 260^{\circ}\mathrm{C}$ (■), $T = 280^{\circ}\mathrm{C}$ (▽), $T = 300^{\circ}\mathrm{C}$ (●), $T = 320^{\circ}\mathrm{C}$ (▼), $T = 340^{\circ}\mathrm{C}$ (▲), $T = 350^{\circ}\mathrm{C}$ (♦), $T = 360^{\circ}\mathrm{C}$ (▶) and $T = 370^{\circ}\mathrm{C}$ (★)

In Figure 7, the extensional viscosity, η_E, is plotted as a function of the Hencky strain, ε, for the linear PC for temperatures ranging from $T = 260^{\circ}\mathrm{C}$ to $T = 370^{\circ}\mathrm{C}$ in air (Figure 7a) and in nitrogen (Figure 7b). All experiments were performed in the presence of either air or nitrogen for the entirety of the heating cycle and the stretch. The heating resulted in a temperature rise of $4^{\circ}\mathrm{C}$/min. In the experiments presented in Figure 7, the stretch was performed as soon as the temperature reached the design temperature with no additional time delay. For temperature below $T = 300^{\circ}\mathrm{C}$ in air, the shear rheology measurements suggest that no significant scission or cross-linking of the PC should be observed. As anticipated, at these temperatures, the extensional viscosity was found to decrease with

temperature while maintaining a nearly constant Trouton ratios, $Tr = \eta_E(T)/\eta_0(T)$, right around the Newtonian limit of Tr = 3. As described in the introduction, extensional viscosity plays a large role in the dynamics of dripping and the breakup of filaments into drops. As the extensional viscosity decreases with temperature, the result is a decrease in the time needed for the filament to breakup. Under air, the break-up time reduced from 780s to 310s as the temperature increased from $T = 260^{o}\mathrm{C}$ to $300^{o}\mathrm{C}$.

As seen in Figure 7a, a decrease in extensional viscosity of 50% was observed with a temperature increase in air from $T = 300^{o}\mathrm{C}$ to $330^{o}\mathrm{C}$. Although the decrease is significant, some decrease is expected as time-temperature superposition (TTS) predicts a reduction in the extensional viscosity of 66-70% across that same temperature range. This suggests that, from $T = 300^{o}\mathrm{C}$ to $330^{o}\mathrm{C}$, a modest amount of molecular structure buildup is occurring. This buildup in molecular structure becomes more and more significant as the temperature was increased. At $T = 340^{o}\mathrm{C}$ in air, the extensional viscosity of the linear PC in Figure 7a was found to diverge with increasing time at temperature. As seen by the data taken under nitrogen, the molecular structure build-up is slowed or inhibited by the presence of oxygen in the air perhaps due to oxygen-induced chain scission occurring simultaneously to polymer crosslinking.

In order to compare the data for air and nitrogen experiments more clearly, the Trouton ratio for experiments performed at temperatures between $T = 260^{o}\mathrm{C}$ to $340^{o}\mathrm{C}$ under both inert and oxygen-rich environment are presented in Figure 8. By normalizing the extensional viscosity as the Trouton ratio, one can account for reversible temperature-dependent changes to the shear and extensional viscosity associated with the principle of time-temperature superposition. At $T = 260^{o}\mathrm{C}$, the Trouton ratio of both the linear PC

stretched in air and nitrogen are similar. However, with increasing strain and time at temperature, the linear PC samples under nitrogen were found to crosslink more rapidly resulting in an extensional viscosity and Trouton ratio roughly 50% larger than the sample under air. At $T = 300^{o}\mathrm{C}$, the initial low-strain Trouton ratio under nitrogen was found to be $Tr = 7$ while in air the Trouton ratio was found to be Tr = 5. This indicates that temperature-induced molecular structure changes had begun during the heating process as the polymer was brought to $300^{o}\mathrm{C}$. By increasing the temperature further to $T = 340^{o}\mathrm{C}$, the low-strain Trouton ratio in nitrogen was found to grow to roughly $Tr = 13$, while remaining close to $Tr = 3$ under air. In this case, the differences between the response of the linear PC under air and nitrogen is nearly a factor of five at small strains. As was observed at $300^{o}\mathrm{C}$, under air there is a gradual buildup of Trouton ratio over time and strain. However, the growth rate is much faster for the $340^{o}\mathrm{C}$ case in air as the Trouton ratio at large strains approaches, but does not quite reach that of the linear PC under nitrogen.

The temperature at which the buildup in the extensional viscosity is observed will be referred to as the transition temperature. This build-up in the extensional viscosity is likely due to temperature-induced crosslinking or branching of the linear PC chains. In fact, if one inspects the extensional viscosity data in Figure 7a for temperatures beyond $340^{o}\mathrm{C}$ one observes a dramatic increase in extensional viscosity with increasing temperature under air. Initially, at $T = 350^{o}\mathrm{C}$, the extensional viscosity starts at $\eta_E = 3000\mathrm{Pa.s}$ and Trouton ratio of $Tr = 4$. However, as the temperature was increased, the extensional viscosity was found to diverge as the filament stopped draining and solidified. This divergence occurred at a smaller imposed strain as the test temperature was increased. The

net result was a dramatically increased time for filament break-up which in these extreme cases was found to diverge to infinity. This massive build-up of molecular structure and the resulting growth in extensional viscosity would clearly improve the performance of the linear PC exposed to a flame as it would eliminate dripping that could feed the flame.

From the literature, it has been shown, that the thermal degradation of polycarbonate in nitrogen appears to occur through one initial fast major degradation step and then two minor slow degradations steps. While, under air, an additional minor subsequent slow degradation step has been observed [45]. The decomposition of PC is initiated by chain scission of the polymer at the weak $O\text{-}CO_2$ group. This chain scission results in the reduced molecular weight of the PC and in the extensional viscosity. No degradation is generally seen until a temperature of $T = 300^{o}\mathrm{C}$. Crosslinking, has been shown to take place at higher temperatures and it is a process that generally occurs after some stripping of the substituents and involves the creation of bonds between two adjacent polymer chains [2]. This process is very important in the formation of chars, since it generates a structure with a higher molecular weight that is less easily volatilized. As seen by our experiments, cross-linking also dramatically increases the extensional viscosity of the polymer melts thus resisting dripping.

In our experiments the basic structural difference among PCs used is the type of branching which has been influenced by the type of branching agents used to synthesize them. This significantly changes the viscoelastic behavior due to the intrinsic intermolecular entanglements in polymers. Unfortunately, degree of branching is not evident from Fourier transform infrared spectroscopy (FTIR) analysis. That being said, FTIR analysis is still a strong tool to investigate the changes in the chemical structure of

PCs upon thermal degradation in oxygen and nitrogen flow environment [46-50]. Here we discuss data from a series of FTIR measurements performed on both neat and heat-treated linear, branched and hyperbranched PC to gain more insight into the extensional viscosity change in the PC samples. From these FTIR measurements, a characteristic peak at 1770 cm^{-1} was observed in all neat samples which can be attributed to the infrared absorption from the stretching vibration of C=O of the ester group in polycarbonates. In addition, peaks at 1603 and 1504 cm^{-1} corresponding to the stretching vibrations of C-C bond in the phenylene group in benzene ring were observed. Important to note that change in peak position for C=O or C-O and appearance of new peaks would be evident if there is any significant influence of heat treatment in oxygen or nitrogen on PCs. Following heat treatment at $T = 360^{o}\mathrm{C}$ under air, the FTIR spectra of the linear PC, was found to contain new peaks at 1656, 1705 and 1728 cm^{-1} which correspond to the C=O vibrations of hydrogen bonded ester groups [48, 51]. In addition, the appearance of a broad peak at 3330 cm^{-1} gives evidence of an –OH group which is likely hydrogen bonded to C=O group. This broad peak is an indication of crosslinking of linear chains in PC. This explains the reason for substantial increase in extensional viscosity at $T = 360^{o}\mathrm{C}$ in the presence of O_2 while such change cannot be observed for samples treated under N_2 environment. Similar structural changes could be observed for branched and hyperbranched PC after heat treatment at $T = 320^{o}\mathrm{C}$ in the presence of air.

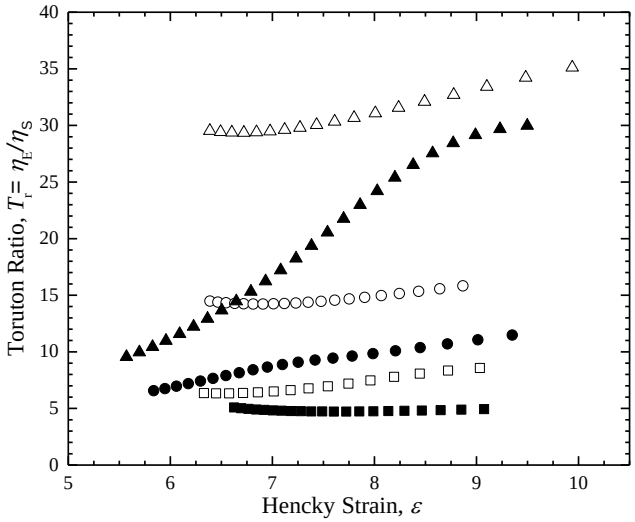

Figure 8. Comparison of Trouton ratio, *Tr*, of linear polycarbonate in air and nitrogen at temperatures T=260°C (□), T=300°C (○) and T=340°C (Δ). Filled symbols refers to experiments done under air and hollow symbols under nitrogen.

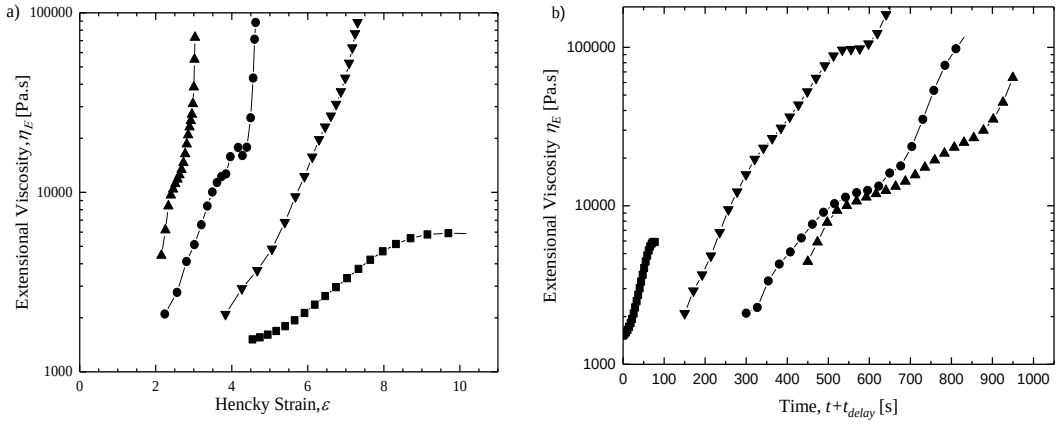

Figure 9. Plot of (a) Extensional viscosity of linear polycarbonate at temperature *T*=340°C as a function of Hencky strain and (b) time at the experimental temperature which includes a delay time imposed before the onset of stretch. This data include experiments with a delay time after the experimental temperature was reached with a delay time of t_{delay}=0s (■),150s (▼), 300s (●) and 450s (▲). All experiments were performed in air.

In Figure 9, the extensional viscosity of linear PC at $T = 340^{o}\mathrm{C}$ in air is plotted as a function of the time delay, t_{delay}, imposed after the oven reached the desired experimental temperature and before commencing the stretch. This figure shows the evolution of extensional viscosity as a function of time and reinforces the importance of experimental protocol as time at temperature can have a dramatic effect on the extensional viscosity. During stretch following a delay time of t = 0s, an increase in extensional viscosity can be seen with strain in Figure 9a, or equivalently, with time in Figure 9b. This increase is due to the buildup of molecular structure over the period time needed for the capillary bridge to breakup. In this experiment, the break-up takes 75s. The fact that the extensional viscosity reaches a steady-state value and does not diverge suggests that, although drainage is inhibited, there has not been enough time to fully cross-link or char the sample significantly enough to stop drainage completely. After a delay of $t_{\mathrm{delay}} = 150\mathrm{s}$, the extensional viscosity was found to diverge rather than reaching a steady state due to the considerable crosslinking that has taken place while being held at $340^{o}\mathrm{C}$. This can also be seen with the increase in the extensional viscosity at low strains. As the delay time for stretch was increased further, the extensional viscosity was found to diverge at smaller and smaller strains. It would be convenient to find a way to collapse all these data onto a single master curve by plotting the extensional viscosity against time at temperature for instance rather than strain. In these experiments, strain is equivalent to $\varepsilon = \dot{\varepsilon} t$ so the time of the stretch can be found from $t_{\mathrm{flow}} = \varepsilon / \dot{\varepsilon}$. Unfortunately as seen in Figure 9b, this does not result in the anticipated master curve as the kinematics of the extensional flow appear to also play a role in the rate of cross-linking. As a result, the delay time is not precisely

equivalent to the flow time with respect to reaction kinetics. This could be because the imposed flow changes the filament geometry, increasing the surface area and exposing more material to the environment or it could be because the stretching flow deforms the chains in the polymer melt allowing for more cross-linking opportunities.

1.3.2.2. Branched Polycarbonate

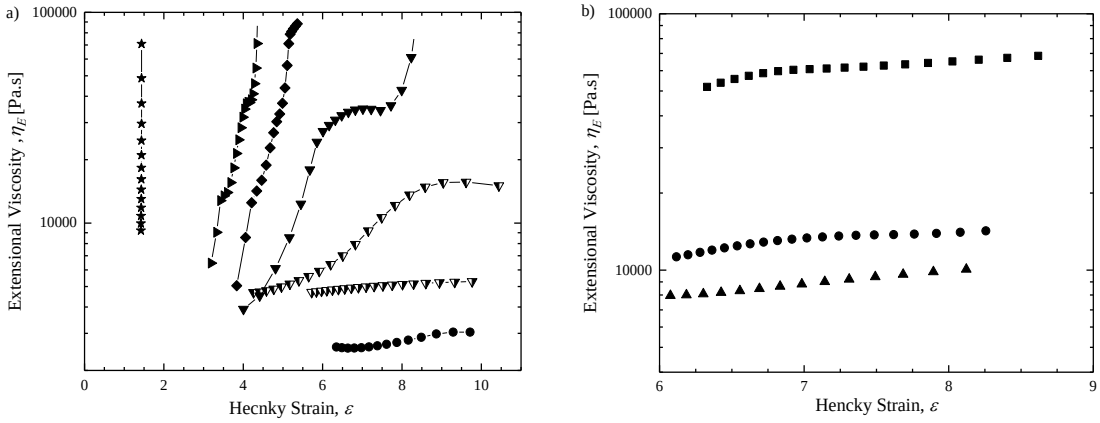

Figure 10. (a) Capillary breakup extensional rheology measurement of extensional viscosity, η_E, as a function of Hencky strain, ε, for a) the Branched polycarbonate in air and b) in nitrogen at temperatures T=260ºC (■), T=280ºC (▽), T=300ºC (●), T=320ºC (▼), T=330ºC (▼), T=340ºC (▲), T=350ºC (♦), T=360ºC (►), T=370ºC (★).

In Figure 10, the extensional viscosity of the branched Polycarbonate is plotted as a function of Hencky strain for temperature ranging from $T = 280^{\circ}\mathrm{C}$ to $T = 370^{\circ}\mathrm{C}$ in air (Figure 10a) and in nitrogen (Figure 10b). The same experimental protocol used for the linear PC measurement was followed here. For temperature below $T < 300^{\circ}\mathrm{C}$, no obvious sign of polymer degradation was observed. For those temperatures, the extensional viscosity was found to decay with temperature following TTS and under air a constant

Trouton ratio of $Tr = 3$ was found. As the temperature was increased from $T = 300^{o}\mathrm{C}$ to $T = 320^{o}\mathrm{C}$, an increase in the extensional viscosity with strain and time similar to that observed for the linear PC case was observed due to buildup of molecular structure either through cross-linking or branching. The Trouton ratios are compared for the branched PC experiments performed in Figure 11. A closer inspection of the data in Figure 11, shows that at $T = 300^{o}\mathrm{C}$, the calculated Trouton ratio under nitrogen was found to be $Tr = 4$ while under air the Trouton ratio was $Tr = 1$. The larger Trouton ratio under nitrogen suggests that the branched PC in air had experienced some thermal degradation under air likely the result of chain scission or perhaps the loss of branches along the backbone. The branched PC appears to be more sensitive to polymer degradation than the linear PC. This three-fold reduction in the extensional viscosity and Trouton ratio in air is 60% larger than the reduction observed at these temperatures for the case of the linear PC. As for the experiments performed at $T = 320^{o}\mathrm{C}$, at lower strains the extensional viscosity under air starts at a value one third that under nitrogen but then recovers a significant amount of the extensional viscosity with increasing strains and time at temperature. Compared to the linear PC, significant crosslinking appears to happen at much lower temperatures for the branched PC samples. For instance, the divergence in the extensional viscosity observed in Figure 10a was found to occur at a transition temperature of $T = 330^{o}\mathrm{C}$ for the branched PC samples in air, but not until $T = 350^{o}\mathrm{C}$ for the linear PC case. This could be due in part to the increase in the number of chain end in the branched case or due to the presence of some unused branching agent remaining in the sample. It is important to note that the divergence in the extensional viscosity is only observed for samples under air for both the linear and branched PC melts. Beyond the temperature $T = 330^{o}\mathrm{C}$ in air, the growth rate of

the extensional viscosity with strain accelerated with increasing temperature. This growth rate is clearly visible from Figures 10 and 11, where if one compares, for instance, the early strain Trouton ratio at temperature $T = 340^{\circ}\mathrm{C}$ under air to that under nitrogen one finds a Trouton ratio of $Tr = 5$ and $Tr = 15$ respectively. As strain was increased, the Trouton ratio under nitrogen was found to be almost constant. However, under air the Trouton ratio was found to quickly grow to $Tr = 25$ at a strain of $\varepsilon = 7$, clearly resulting from significant cross-linking or branching in air. This dramatic increase in the extensional viscosity resulted in an increased time for filament break-up of the branched PC in air compared to the linear PC. It is therefore expected that the branched PC will provide better flame resistance than the linear PC when exposed to a high temperature heat source like a flame.

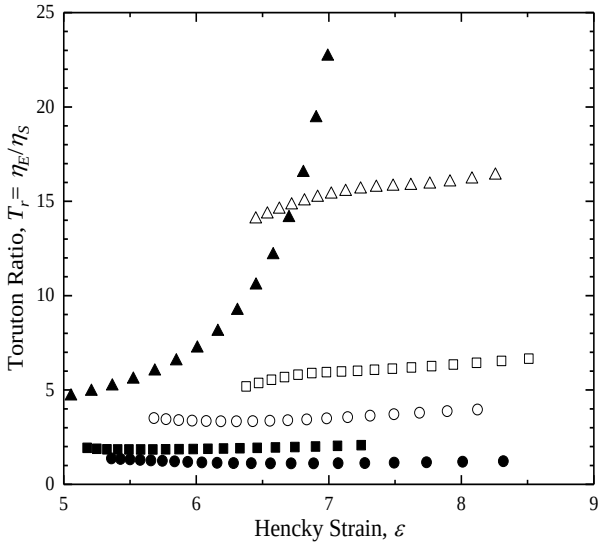

Figure 11. Comparison of Trouton ratio, *Tr*, of branched polycarbonate in air and nitrogen at temperatures *T*=260ºC (□), *T*=300ºC (○) and *T*=340ºC (Δ). Filled symbols refers to experiments done under air and hollow symbols under nitrogen.

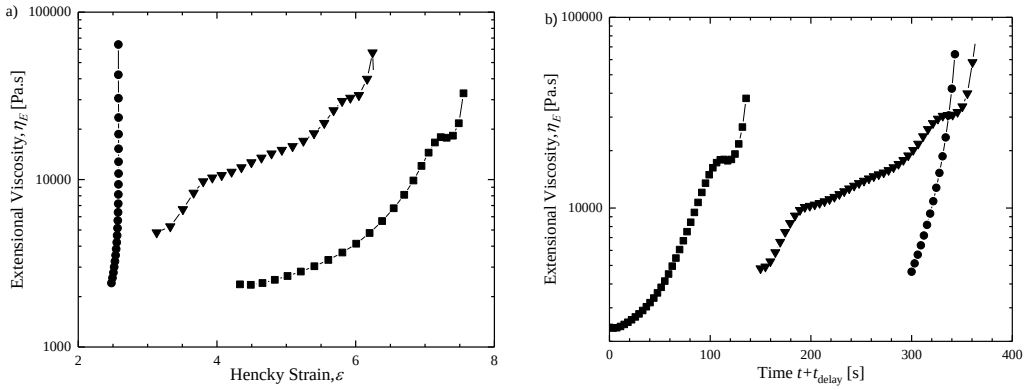

Figure 12. Plot of (a) Extensional viscosity of branched polycarbonate at temperature T=340°C as a function of Hencky strain and (b) time at the experimental temperature which includes a delay time imposed before the onset of stretch. This data include experiments with a delay time after the experimental temperature was reached with a delay time of t_{delay} =0s (■), 150s (▼) and 300s (●). All experiments were performed in air.

In Figure 12, the extensional viscosity of branched PC at $T = 340^{o}\mathrm{C}$ in air is plotted as a function of delay time imposed after the oven reached the desired temperature and before beginning the stretch. During the stretch following a delay time of $t_{delay} = 0\mathrm{s}$, an increase in extensional viscosity can be seen with strain in Figure 12a and with time in Figure 12b. The extensional viscosity was found to reach a plateau at larger strains before diverging at t =120s. With increasing delay time, the divergence of the viscosity was found to occur at earlier and earlier strains. As before, the data was not found to collapse if replotted versus total time at temperature as seen in Figure 12b. However, when compared to the linear PC, the branched PC was found to be even more sensitive to time at temperature as the filament solidified more quickly resulting in the observed divergence in the extensional viscosity.

1.3.2.3 Hyper-branched Polycarbonate

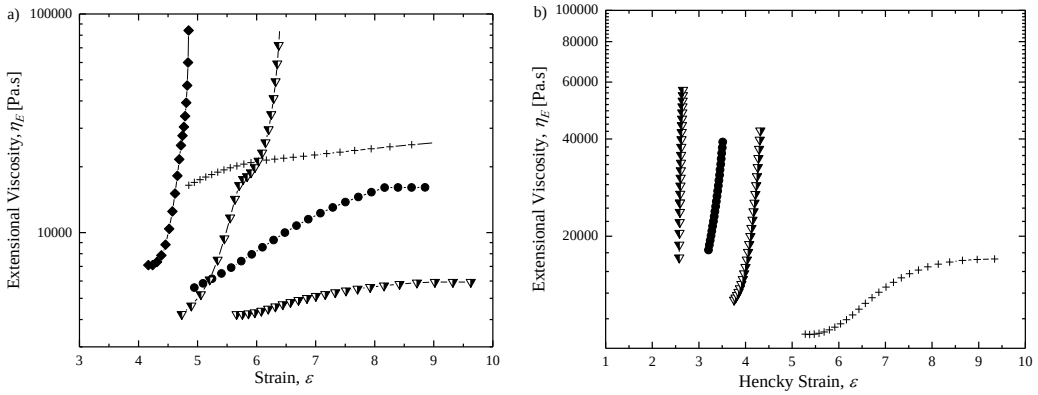

Figure 13. (a) Capillary breakup extensional rheology measurements of extensional viscosity, η_E as a function of Hencky strain, ε, for a) the hyper-branched polycarbonate in air and b) in nitrogen at temperatures T=250°C (+), T=280°C (∇), T=300°C (●), T=320°C (▼), T=350°C (♦).

In Figure 13, the extensional viscosity of the hyper-branched PC is plotted as a function of Hencky strain for temperature ranging from $T = 250^{\circ}\mathrm{C}$ to $T = 350^{\circ}\mathrm{C}$ in air (Figure 13a) and nitrogen (Figure 13b). As the temperature was increased from $T = 250^{\circ}\mathrm{C}$ to $T = 280^{\circ}\mathrm{C}$ in air, no significant molecular changes were observed. The Trouton ratio remained constant at $Tr = 14$ across the entire temperature range. With a further increase in the temperature to $T = 300^{\circ}\mathrm{C}$, an increase in extensional viscosity was observed with increasing strain. Under air, the transition temperature at which the extensional viscosity was found to diverge was even lower than for the branched PC; $T_t =$ 320°C versus 330°C . Additionally, as seen in Figure 13b, it appears that, for the hyper-branched PC, the presence of air actually inhibits build-up of molecular structure. Under nitrogen, the transition temperature drops from $T_t = 320^{\circ}\mathrm{C}$ in air to $T_t = 280^{\circ}\mathrm{C}$. These trends are opposite to those observed for the linear and branched PC where the presence of air was necessary to initiate significant polymer cross-linking at elevated temperatures. In the previous cases, the data did not diverge under nitrogen in any of the tests that were

performed. This observation demonstrates the importance that the number or chemistry of the polymer end group can play in flame resistance. The linear and branched PC samples had end groups composed of the ester group, while the hyper-branched PC had HBN end groups. The activity of these end groups appears to be suppressed by the presence of oxygen. Above a flame, the gas is often devoid of air as it has been depleted by the flame and replaced with various products of combustion. Having a material that can heavily crosslink in the absence of air may be critical to the flame resistant performance when exposed to a flame. For the hyper-branched PC the divergence of η_E at low temperatures may be highly desirable.

1.3.2.4 Filament Breakup Time and Steady State Extensional Viscosity

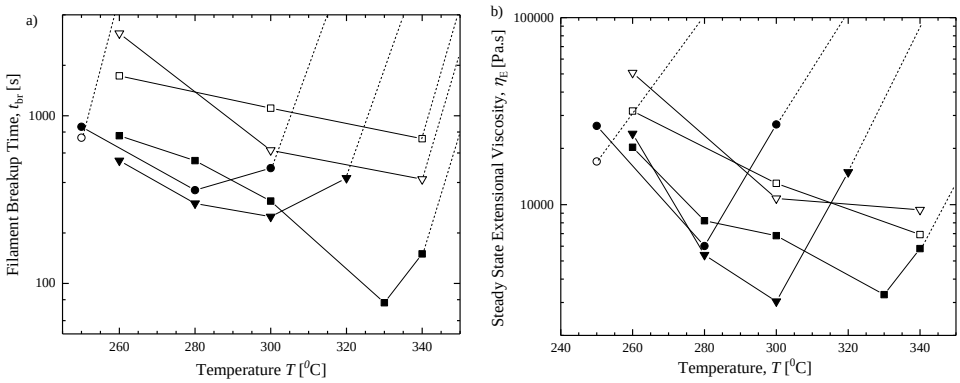

Figure 14. (a) Plot of breakup time, t_{br}, and (b) steady state extensional viscosity, η_E, as a function of temperature, T, for linear (■), branched (▼) and hyper-branched (●) polycarbonate. Filled symbols correspond to experiment in air while hollow symbols correspond to nitrogen. The dashed lines show the point of divergence when the filament solidifies.

In Figure 14(a), plot of the filament break-up time, t_{br}, is plotted against temperature for the linear, branched and hyper-branched PC under air and nitrogen. Take for example the case of the linear PC in air. The break-up time was initially found to be $t_{br} = 780\text{s}$

seconds at $T = 260^{o}\mathrm{C}$, with increasing temperature, the break-up time was found to decrease until it reached a minimum of $t_{br} = 80\mathrm{s}$ at $T = 330^{o}\mathrm{C}$. This initial decrease is due primarily to the reduction in viscosity expected from time-temperature superposition, but may also include effects of some modest degradation of the polymer chains at these moderate temperature. This can also be seen from the data in Figure 14b, where the steady state extensional viscosity decreased from $\eta_E = 22,000\mathrm{Pa.s}$ at $T = 260^{o}\mathrm{C}$ to $\eta_E = 3500\mathrm{Pa.s}$ at $T = 330^{o}\mathrm{C}$. As the temperature increased further, the break-up time increased to $t_{br} = 160\mathrm{s}$ at $T = 340^{o}\mathrm{C}$ before diverging at higher temperature because of significant crosslinking resulting in a divergence of the extensional viscosity as seen in Figure 14b. At that point, the filament diameter was found to stop decaying and the break-up time went to infinity as the filament solidified with time. The minimum break-up time under air was found to increase from $t_{br} = 80\mathrm{s}$ to 250s and finally to 360s as the degree of polymer branching was increased. Under nitrogen, the minimum break-up time for the hyper-branched case was nearly 1000s. Conversely, the break-up time under nitrogen at moderate temperatures was only a factor of two or three higher for both linear and branched PC as compared to the break-up time in air. However, the divergence of the extensional viscosity under air suggests that in these cases, the presence of oxygen would make these polymers more flame resistant at higher temperatures.

1.4 Conclusion

The variation in the extensional viscosity of three selected commercially-available linear, branched and hyper branched polycarbonates was studied using a newly designed

high–temperature capillary breakup extensional rheometer (CaBER). Extensional rheology measurements were performed at temperatures varying from $T = 250^{o}\mathrm{C}$ to $370^{o}\mathrm{C}$ in both an inert and an oxygen-rich environment for all three polycarbonates. The design of the CaBER oven allowed us to make measurements under condition where polymer degradation was either expected or not. The goal of these experiments was to use extensional rheology to better understand the behavior of polymers like polycarbonate when they are exposed to a high temperature heat source like a flame. Under these extreme conditions, the determination of whether a polymer is flame resistant or not depends largely on whether or not the molten polymer drips and feeds the fire. As the formation and release of a drip is a process dominated by an extensional flow, it was our hypothesis that characterization of the evolution of a polymer's extensional viscosity with time and temperature under extreme conditions can be a sensitive probe of changes to a polymer's chemical architecture and a powerful new tool for predicting the polymer's behavior when exposed to a flame.

At the low end of the temperature range studied, no degradation of the linear and branched PC was observed in the shear rheology measurements. However, the extensional rheology measurements showed evidence of a modest amount of chain scission under air which was found to reduce the Trouton ratio of the polycarbonate by 10 or 15%. The branched PC was found to be more sensitive to chain scission than the linear PC. At higher temperatures, beyond $T > 300^{o}\mathrm{C}$, significant increases in the extensional viscosity of the three different PC's were observed resulting from changes to the molecular structure of the PC. These changes to the molecular structure are likely the result of polymer cross linking or increased branching of the polymer chain at high temperatures. In all cases, the rate of

growth in the extensional viscosity was found to increase with both temperature and time at temperature. In the case of the linear and branched PC, the largest changes to the extensional viscosity were observed in the presence of air. For the hyper-branched case, however, changes to the molecular structure of the PC were found to occur more quickly under nitrogen resulting in large extensional viscosity growth. Under air, at extremely high temperatures, the extensional viscosity of all three polycarbonates was found to diverge to infinity ultimately resulted in the cessation of the filament drainage as the polymer melt became so heavily cross-linked that it essentially solidified. In some cases, the polymer would blacken and form a char. For the hyper-branched PC, the presence of air had an inhibiting effect on polymer crosslinking. However, due to the presence of the polymer end group used to enhance branching, the buildup of molecular structure was found to be even more rapid in the presence of nitrogen than either the linear or the branched PC in air. In fact, for both the linear and the branched PC, the extensional viscosity was not found to diverge under nitrogen even at 370°C. For comparison, the extensional viscosity of the hyperbranched PC was found to diverge under nitrogen at just 280°C.

This temperature-induced crosslinking and increase in the extensional viscosity of the PC can improve the flame resistant properties of the polycarbonate by slowing and even restricting dripping from polymeric components near high heat surges. In many cases, the regions of high heat near an open flame are also devoid of oxygen. As a result, the divergence of the hyperbranched PC under nitrogen might be a distinct advantage and a feature that could be incorporated when designing and testing other flame resistant polymers. Finally it should be noted that with these experiments, we have demonstrated measurement of the extensional viscosity were found to be several orders of magnitude

more sensitive to temperature-induced changes to the molecular structure than measurements of shear rheology.

1.5 Acknowledgement

The authors would like to thank SABIC for funding this research. Additionally, the authors would like to thank Christian Clasen of KU Leuven for use of his Edgehog software and Md Arifur Rahman (University of Massachusetts, Amherst) for the FTIR analysis.

1.6 Publication

The work described in this chapter has been published in the Rheologica Acta Journal. The complete reference is S Sur, M Chellamuthu and J P Rothstein "High Temperature Extensional Rheology of Linear, Branched and Hyper-Branched Polycarbonates", Rheologica Acta, 1-16, (2019)"

CHAPTER 2

HIGH TEMPERATURE EXTENSIONAL RHEOLOGY OF COMMERCIALLY AVAILABLE POLYCARBONATES MIXED WITH FLAME RETARDANT SALTS

2.1 Introduction

Polymer combustion is driven by the thermally induced decomposition into smaller fragments, which then volatilize, mix with oxygen, and combust. This combustion releases more heat, which reradiates unto unburned polymer, thus continuing to drive pyrolysis and combustion until a lack of heat/fuel/oxygen causes the fire to extinguish. Thermoplastics polymers have a tendency to drip and flow under fire conditions, which can then lead to additional mechanism of flame spread or propagation. Thus, improving the fire-retardant behavior of polymers is a major challenge for extending the use of polymers to an ever increasing number of applications. The flame resistance of a polymer is often characterized by whether or not it drips when exposed to a high heat source. The melting and dripping drops can either remove the polymer fuel from the burning region, and hence stop further burning, or they can become a secondary source of ignition. If the melting and dripping drops further ignites the polymer or other materials in the vicinity, they can subsequently increase the intensity of the flame. As a result, the presence of polymer can become a serious fire hazard. Flame resistance can be improved through the addition of flame-retardant additives to the polymer [53-57]. The addition of flame retardants can cause a disruption to the burning process so that the dripping of the molten polymer is terminated within an acceptable period of time, preferably before ignition of the polymer occurs [58-60]. In this way, flame retardants additives can help in the prevention of fires. In the event

of a fire, the presences of flame retardant additives in the polymers act to give more escape time to the people caught in the blaze. They do this by slowing the burning process, lowering the amount of heat released, and lowering the amount of smoke that is emitted during combustion [61]. Not all flame retardant additives are alike. Flame retardant additives can be separated into two different classes: halogenated, and non-halogenated. Halogenated flame retardants include additives most commonly in the form of organic halogen compounds, such as brominated aromatic compounds, chorine and fluorine. The second kind, non-halogenated, contain one of many different additives including phosphorous, sulfur and silicon-based chemicals [62]. A lot of effort is being made towards the use non-halogenated additives since they are more environmental friendly and less toxic. Halogenated additives are known to release toxic gases on combustion which can have disastrous consequences, especially in the case of an aircraft or an housing complex [63].

As the temperature of a polymer melt is increased, its viscosity decreases both through an increase in the mobility of the polymer molecules and through the thermal degradation of the polymer which can result in scission of the polymer backbone and the reduction of the polymer molecular weight [61]. The addition of flame retardant additives can influence the shear and extensional viscosity of the pyrolysing melt, and hence, modify its dripping behavior [61, 64, 65]. Our recent work has shown that measurements of the extensional viscosity of neat polycarbonate (PC) as a function of temperature can be an excellent tool for understanding and predicting the dripping dynamics of polymers exposed to high temperature flames [52]. In the Capillary Breakup Extensional Rheometry measurements presented in Sur et al [52], a plug of PC was first heated to temperature and

then stretched between two end plates to form a fluid filament. The decay of the filament diameter with time was monitored and used to make measurements of the fluids extensional viscosity and relaxation time as a function of time over a range of temperatures (T=260^{o}C to 360^{o}C) in both an oxygen- rich and inert environment. Using the high- temperature extensional rheometer the evolution of extensional viscosity over time at temperature (T=260^{o}C to 360^{o}C) was investigated for the linear, branched and hyper-branched PC in the presence of nitrogen and oxygen. For the linear and branched PC, increasing temperature initially led to a drop in the extensional viscosity due to time- temperature superposition effects. With increasing temperature, evidence of changes to the molecular structure or chain scission was observed. As the temperature was increased still further, a transition temperature was found beyond which a divergence in extensional viscosity was observed with time due to the onset of significant crosslinking. This divergence in the extensional viscosity was accompanied by a solidification of the fluid filament and a complete suppressing of dripping. The transition temperature for the hyper-branched, branched and linear PC was found to be $T_t = 320^o\text{C}$, $T_t = 330^o\text{C}$ and $T_t = 350^o\text{C}$ respectively. Whereas, in the presence of nitrogen no divergence in extensional viscosity was observed for the linear and branched PC. The hyper-branched PC showed more dramatic effects under nitrogen as the oxygen was found to quench the crosslinking resulting from the polymers hydroxyl benzoyl nitrile (HBN) end terminated group. Thus, based on the evolution of extensional viscosity along with results from shear rheology experiments it was concluded that hyper-branched PC had the best anti-dripping properties followed by the branched and linear PC. This previous study also suggests that alternative

additives that can promote crosslinking like the HBN could be highly affective flame retardant additives.

In the past, various techniques have been used to characterize the flammability of polymers. These techniques include- limiting oxygen index (LOI), cone calorimetry, flame spread test and UL94 test [61]. The vertical flame test UL 94V [5] is a small-scale laboratory test used to classify the flammability of polymers under controlled conditions for polymers where melt dripping is observed. It is a simple test of vertical combustion that classifies materials as V-0, V-1 or V-2. Achieving a V0 classification is the important goal for a polymer to be labeled as the flame retardant. It is known that dripping during a fire test is a complex interaction of physical and chemical processes which can include softening due to increasing sample temperature and viscosity changes (positive or negative) due to chemical decomposition [66]. In order to better understand the process of drop formation that can feed a flame and affect a material's flame resistance rating one must fully consider the extensional flow dominated dynamics of dripping and the formation of drops

In this paper, we will investigate the melt dripping characteristics of polycarbonates mixed with a number of different flame retardant additives. In most cases, the addition of flame retardant known to cause thermally induced molecular changes to the polymers chains. These changes, typically lead to an increase in the viscosity of the polymer melt, because the flame resistant additives are often designed to function as plasticizers or as reinforcing fillers [60]. The efficiency of these flame retardant additives has been shown to depend on the viscosity of the modified polymers [60, 64] and, as we will show here, more precisely on the extensional viscosity of the modified polymer melt . There are many

questions that needs to be considered while preparing a flame resistant polymer including: what flame retardant additive or combinations of flame retardant additives to choose, how much needs to be added, and what are the material properties like extensional viscosity that indicate when a polymer is flame resistant enough. Through a detailed set of extensional viscosity measurements at multiple temperature and across many different material compositions we will begin to answer these questions.

2.2 Experimental Setup

2.2.1 Capillary Breakup Extensional Rheometer

A schematic diagram of the capillary breakup extensional rheometer (CaBER) with its main components is shown in figure 1 in chapter 1. The design of the CaBER was based on previous design found in the literature [67]. Here we have customized it for high temperature measurements by building an oven around it that can reach up to 400^{o}C using three 250W resistance heaters (Omega-WS series). The oven temperature is controlled using a PID temperature controller (Omega-CN-2110) with a temperature accuracy of $\pm 2^{o}C$. The oven is made of an inner and outer box fabricated from steel plates with insulation between the two boxes to reduce heat transfer out of the oven. The thickness of insulator was designed to maintain an inside temperature of T=400^{o}C and without exceeding an outside oven surface temperature of 35^{o}C. A thickness of 6.25 cm of a silica-based insulator (Microsil, Zircar) with a thermal conductivity of k =0.024 W/mK was used to maintain the outside temperature below $35^{o}C$. Rectangular openings were cut into the sides of both the inner and outer box and covered with a Pyrex glass to allow optical access for the camera to allow for visualization of the filament diameter so that it could be

measured optically as a function of time. The diameter measurements had a resolution of 6.3 μm/pixel based on the maximum magnification of the lens and the pixalation of the camera sensor. Provisions were made for supplying nitrogen and air into the oven so that measurements could be made in an inert or an oxygen rich environment. The top plate was connected to a liner motor (LinMot-C1250) using a glass mica rod to reduce heat flow out of the oven and minimize the risk of heat damages to the motor. The motor was capable of stretching the fluid at speeds up to 200 mm/s. An edge detection software (Edgehog) was used to capture the diameter decay with time with subpixel resolution. In order to calculate the extensional viscosity, the diameter decay was fit with a spline and then differentiated.

Capillary breakup extensional rheometry measurements have become an increasingly common technique for determining the extensional rheology of viscoelastic fluids [27-36]. In the CaBER experiments presented here, a cylindrical sample melt cast using a hot press under vacuum was placed between two cylindrical plates at room. The oven was then turned on and heated to the desired experimental temperature with a ramp of $5^{o}\mathrm{C}/\min$. Once the oven reached the desired temperature the sample was then stretched with the top plate moving at a velocity of $0.01\mathrm{m/s}^{2}$ until a gap of $3L_0 = 6.75\mathrm{mm}$ was reached. Here $L_0 = 2.25\mathrm{mm}$ is the initial starting gap between the plates and $R_0 = 2.25\mathrm{mm}$ is the initial radius of the sample melt. The stretch was then stopped and the capillary thinning of the liquid bridge that was formed between the two endplates subsequently produced a uniaxial extensional flow from which the extensional viscosity and relaxation time of the test fluid could be measured.

The breakup of the fluid filament is driven by capillary stresses and resisted by a combination of inertial, viscous and elastic stresses developed within the flow. The specific

balance of forces that dictate the breakup regime of the fluid depend on the properties of the fluid. As the fluids we will investigate here are all quite viscous, inertial effects can in all cases be safely neglected as the Ohnesorge number is in all cases *Oh*>>1. In the viscous-capillary regime, capillary decay is opposed by viscous stresses. In this regime, the extensional viscosity of the fluid can be determined by measuring the change in the filament diameter as a function of time, $R_{\mathrm{mid}}(t) = 0.07095(t_b - t)/\eta$. Here σ is the surface tension, η is the shear viscosity and t_b is the time at breakup. In the Newtonian limit the extensional viscosity is equal to $\eta_E = 3\eta$ and can be calculated from the decay of the radius with time. In order to calculate the apparent extensional viscosity of a fluid undergoing a visco-capillary decay, like those observed here, the diameter measurements as a function of time were first fit with a spline to smooth the data and then differentiated before substituting into equation 2 [52, 68, 69]. The value of the surface tension was taken from the literature to be σ=34.2mN/m. The extensional viscosity was calculate using equation 1.1 as presented in chapter 1.

2.2.2 Materials

Linear polycarbonate (LEXAN-130) of molecular weight, M_w= 36 kg/mol with a polydispersity index of PDI=1.74 mixed with various flame retardant (FR) were investigated. The various flame retardant additives studied included potassium perfluorobutane sulfonate (Rimar), potassium diphenyl sulfone-3-Sulfonate (KSS), polytetrafluoroethylene encapsulated with styrene acrylonitrile resin (TSAN) and 1.1.tris hydroxy phenyl ethane (THPE) were supplied by SABIC innovative plastics. Before being

tested in the shear and the extensional rheometers, the polymer pellets were first molded to fit the various plate geometry needed in a hot press under vacuum at T=250^{o}C. The various composition of the flame retardant additives mixed with the linear PC are listed in table 1 alongside their UL-94 rating.

2.2.3 Thermal Analysis

Thermal properties of the PC/FR additives samples were measured using a differential scanning calorimetry (DSC) and thermogravimetric analysis (TGA). Differential scanning calorimetry were performed using a Q100 (TA Instruments) at a heating rate of $10^{o}\,\mathrm{C/min}$ in the presence of nitrogen. The glass transition temperature, T_g, was found to be $T_g = 146^{o}\mathrm{C}$ for the linear PC. As seen in Table 1, a variation in T_g by 5-10^{o}C was observed because of the variation in the molecular weight of the different blends. Thermogravimetric measurements were performed using a Q-5000 (TA Instruments) under nitrogen at a heating rate of $T = 20^{o}\,\mathrm{C/min}$. All the samples decomposed in a single decomposition step. The onset of decomposition temperature,$T_{5\%}$, set to be when the mass loss equaled 5wt%, was found to be $T_{5\%} = 502^{o}\mathrm{C}$ for the linear PC. Along with the temperature for onset of degradation the temperature of maximum rate of degradation, T_{max}, is also presented in the table 1 below. On its own, addition of Rimar showed the earliest onset of decomposition while TSAN appeared to have a retardation effect on the onset of decomposition. The onset decomposition temperature and the maximum weight loss temperature varied by as much as $\pm 20^{o}\mathrm{C}$ with the different flame retardant additives. All the TGA data is presented in Table 1. The maximum weight change was observed for the linear PC and PC/KSS which

was found to be 80 and 81wt% respectively. The residue for all the samples at the end of the experiment varied between 20 to 25wt%.

Table 1. Thermal Properties of the combination of flame retardant additives polycarbonate along with its UL-94 vertical burn test rating for a flame bar thickness of 1.2mm

Sample	Percent Flame Retardant Additive (wt%)	UL-94 Rating	T_g (°C)	$T_{5\%}$ (°C)	T_{max} (°C)	Residue After TGA (*wt*%)
Linear PC	-	V2	146	502	512	22%
Rimar salt and linear PC (PC/Rimar)	0.08wt% Rimar	V0	151	488	518	19%
KSS and linear PC (PC/KSS)	0.3wt% KSS	V2	151	506	515	20%
TSAN and linear PC (PC/TSAN)	0.5wt% TSAN	V0	155	514	537	22%
KSS, TSAN and linear (PC) (PC/KSS/TSAN)	0.3%wt KSS and 0.3wt % TSAN	V0	154	483	517	20%
Rimar, TSAN, THPE and linear PC(PC/Rimar/TSAN/THPE)	0.08wt% Rimar,0.1wt% TSANand 0.2mol% THPE	V0	150	510	512	20%

2.3 Results and Discussions

2.3.1 Shear Rheology

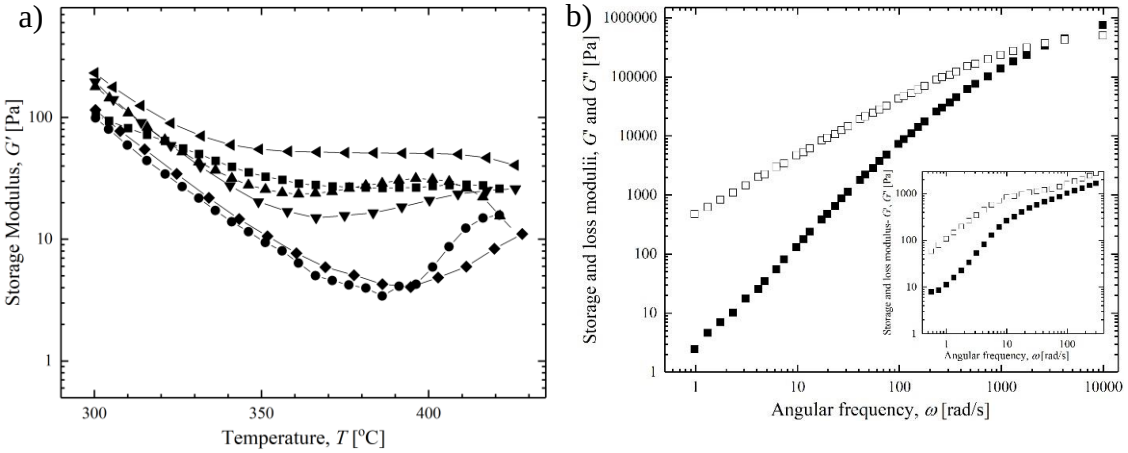

Figure 15. Plot of the a) Storage modulus, G', as a function of temperature, *T*, at an angular frequency of ω=10rad/s for the PC/0.08% Rimar salt (▼), PC/0.08wt% Rimar/0.1wt% T-SAN/0.2mol% THPE (■), PC/0.3wt% KSS (●), PC/0.5wt% T-SAN (◄), PC/0.3wt% KSS/0.3wt% T-SAN (▲) and linear PC (♦) in the presence of nitrogen b) Storage, G'(■), and loss modulus, G'' (□), of the linear PC as a function of angular frequency, ω, shifted to a reference temperature of T_{ref} =300°C. The inset in Figure 10b shows the plot of G'(■) and G''(□) as a function of angular frequency at *T*=380°C for the linear PC.

The shear rheology of the linear PC with different flame retardant additives was studied as a function of temperature using an ARES-G2 rheometer (TA instrument) with temperatures varying from *T*=300°C to 430°C at a frequency of $\omega = 10\text{rad/s}$ in the presence of nitrogen. Before starting the analysis of the temperature sweep it is important to note that the frequency was selected such that the material response was in the terminal regime. This was important in order to interpret the deviations in the expected storage modulus variation due to temperature changes close to changes resulting from crosslinking as the temperature was increased. In the terminal regime if the angular frequency is held fixed, the storage modulus should decrease with increasing temperature due to the principles of time temperature superposition because the effective frequency decreases with increasing

temperature. As a result in the terminal regime the elastic modulus is expected to scale like $G' \sim a_t^2 \omega^2$ where a_t is the shift factor. Thus any deviation in the storage modulus away from this decay with increasing temperature would indicate a change in the material resulting from temperature induced changes to polymer like crosslinking or scission. To ensure that the selected frequency of ω=10rad/s was in the terminal regime, a series of frequency sweeps were performed for the linear PC at non-degrading temperatures from T=220°C to 280°C and all the data were shifted using TTS to a reference temperature of T=300°C. As observed from the Figure 15b, it is clear that that the response of the linear PC was in the terminal regime and thus the data in Figure 15b can be treated quantitatively to determine the onset temperature of polymer degradation. The storage modulus of linear PC and PC/KSS in Figure 2a were found to decrease with expected slope as the temperature was increased from T=300°C to 380°C. Beyond T=380°C, the storage modulus was found to increase. This deviation from the time temperature superposition response was likely due to the buildup of molecular structure due to either crosslinking or charring. The deviation from TTS was found to occur at a lower temperature of T=340°C for the PC/TSAN. Similar trends were observed for PC/0.08wt% Rimar, PC/0.08wt% Rimar/0.1wt% TSAN/0.2mol% THPE and PC/0.3wt% KSS/0.3wt% TSAN where the deviation from TTS was observed at temperatures T=360°C, T=340°C and T=350°C respectively. It is important to note here that, though the storage modulus was found to be sensitive to the onset of crosslinking in the material, no direct information about the effect of these changes on the dripping of the polymer could be garnered from this data.

Past studies have shown that presence of oxygen degrades the PC and leads to changes in the molecular backbone structure [70-72] leading to crosslinking and charring.

Thus, it is difficult to differentiate the effect of the flame retardant additives degradation mechanism from the neat PC in an oxygen-rich environment. The environment of the decomposing sample will therefore affect the degradation pathway so it is important to make it as close to combustion conditions as possible. It has been shown that in the case of combustion, the effect of oxygen during combustion may be quite minimal because oxygen has been shown not to be present in the degrading polymer [70]. This is likely the result of the oxygen in the environment being depleted by the burning flames. As a result most temperature sweep measurements are performed in the presence of nitrogen as we have presented here in the case of shear rheology. However, for completeness we will study the extensional rheology of these PC in both air and nitrogen to observe the competing or additive effects of oxidation during stretching and dripping of these polymers with and without flame additives.

2.3.2 Extensional Rheology

2.3.2.1 Linear Polycarbonate

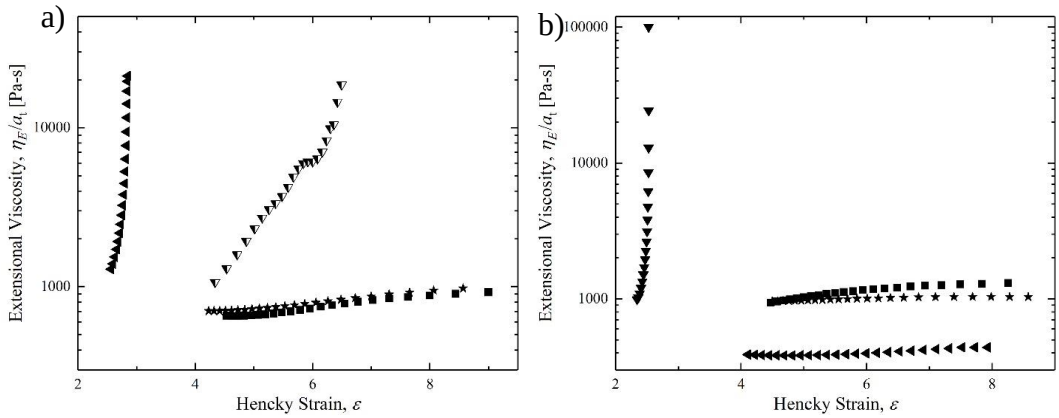

Figure 16. Capillary breakup extensional rheology measurement of extensional viscosity, η_E, as a function of Hencky strain, ε, for the linear polycarbonate in a) air and in b) nitrogen at temperatures of $T = 320^{o}\mathrm{C}$ (■), $T = 340^{o}\mathrm{C}$ (★), $T = 350^{o}\mathrm{C}$ (▼), $T = 360^{o}\mathrm{C}$ (◀) and $T = 380^{o}\mathrm{C}$ (▼). All extensional viscosities have been shifted to a reference temperature of $T = 320^{o}\mathrm{C}$.

In Figure 16, the extensional viscosity, η_E, is plotted as a function of the Hencky strain, ε, for the linear PC at temperatures ranging from T=320°C to T=360°C in air and in nitrogen. All experiments were performed three times in the presence of either air or nitrogen for the entirety of the heating cycle and the stretch. For those temperature at which a steady state extensional viscosity values were achieved a maximum variation of 20% was observed between each data set of experiments, while for those temperatures where a divergence in the extensional viscosity was observed, a variation in the Hencky strain is mentioned which was within a range of ε_{err}=±0.5. Thus the average values have been presented for all the cases. New samples were used for each measurements at each temperatures. From the shear rheology in Figure 15, it is clear that all the samples appear to be chemically stable at temperatures below T=340°C. Thus, an initial temperature of T=320°C was chosen as a baseline against which the higher temperature measurements

were compared to understand the physical and chemical changes occurring to the polymer melts as were exposed to the heat. Using the shift factors from Time Temperature Superposition (TTS), all the extensional viscosities in Figure 16 through Figure 8 have been shifted to a reference temperature of T=320°C using the relation $\eta_E(T) = a_T \eta_E(T_{ref})$, where a_T is the shift factor, T_{ref} is the reference temperature and T is the temperature from which the extensional viscosities are shifted.

Plotted in this way, any deviation of the extensional viscosity curve from the reference curve signifies a change in molecular structure due to crosslinking or chain scission. As can be observed from Figure 16a, for an initial temperature increase from T=320°C to 340°C, the extensional viscosities were found to match the prediction of the TTS and thus collapse into a single curve. As the temperature was further increased to T=350°C, the extensional viscosity of the neat linear PC was found to increase significantly and diverge due to significant crosslinking. Whereas, in the presence of nitrogen, the extensional viscosities were found to match the prediction of the TTS up to T=340°C. Beyond T=360°C, a reduction in the extensional viscosity from the reference extensional viscosity by a factor of three was observed. This observation suggests chain scission occurring under nitrogen at these high temperatures. Note that these observation of loss of extensional viscosity at $T = 360^{\circ}\mathrm{C}$ for the linear PC under nitrogen is not consistent with the shear rheology measurements which showed a deviations from TTS which always showed a growth in the viscosity and elasticity of the sample suggesting cross-linking under nitrogen and not chain scission. The origin of these differences is not clear, but if it is a direct result of the flow type, shear or extension, then it is imperative that the flow type more closely resulted to dynamics of dripping should be used to study the response of the

fluid at temperature. The extensional viscosity was eventually found to diverge at T=380^{o}C in the presence of nitrogen as it did under oxygen due to crosslinking. At that moment, the filament stopped draining and fully solidified resulting in a measured extensional viscosity that became infinite. From the literature, it has been shown, that the thermal degradation of polycarbonate in nitrogen occurs through one fast major degradation step followed by two minor slow degradations steps. While, under air, an additional minor slow degradation step has been observed [45]. The decomposition of PC is initiated by chain scission of the polymer at the weak $O\text{-}CO_2$ group. This chain scission results in the reduced molecular weight of the PC and a reduction in the extensional viscosity. No degradation is generally seen until a temperature of T=340^{o}C. Crosslinking has been shown to take place at higher temperatures and it is a process that generally occurs after some stripping of the substituents and involves the creation of bonds between two adjacent polymer chains [2]. This process is very important in the formation of chars, since it generates a structure with a higher molecular weight that is less easily volatilized. As seen in our experiments, cross-linking also dramatically increases the extensional viscosity of the polymer melts thus resisting dripping. The net result is a decreased likelihood in dripping when exposed to flames [52]. From the UL-94 tests performed in the SABIC labs, the linear PC had a poor V-2 rating over 1.2mm thickness which means that further improvements are needed to achieve the desired V-0 rating and achieve the necessary flame resistance.

2.3.2.2 Polycarbonate with 0.8wt% Rimar Salt

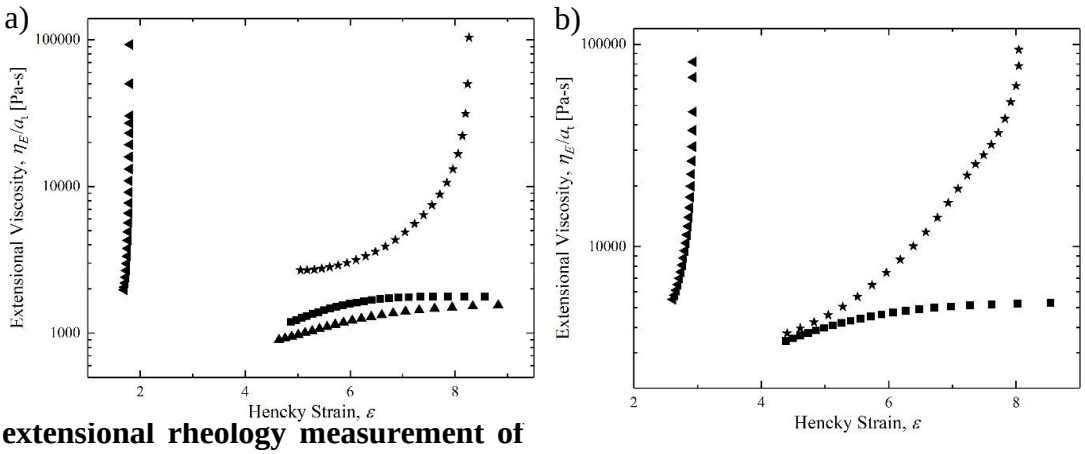

extensional rheology measurement of extensional viscosity, η_E, as a function of Hencky strain, ε, for the linear polycarbonate with 0.08wt% Rimar salt (PC/Rimar) in a) air and in b) nitrogen at temperatures of $T = 320^{o}\mathrm{C}$ (■), $T = 330^{o}\mathrm{C}$ (▲), $T = 340^{o}\mathrm{C}$ (★) and $T = 360^{o}\mathrm{C}$ (◀). All extensional viscosities have been shifted to a reference temperature of $T = 320^{o}\mathrm{C}$.

In Figure 17, the extensional viscosity is plotted as a function of the Hencky strain for the PC with 0.08wt% Rimar salt for temperatures ranging from T=320°C to T=360°C in air and in nitrogen. All data has been shifted to a reference temperature of T=320°C using TTS. Rimar salt have been shown to be an effective flame retardant additive as it reduces the dripping likelihood of a polycarbonate even when added in the small amount tested here [73, 74]. In the presence of air, during the initial temperature rise from T=320°C to T=330°C, PC/Rimar was found to be stable. The extensional viscosity was found to diverge at a temperature of T=340°C and beyond. When compared to the linear PC in the presence of nitrogen, a steady state extensional of $\eta_E = 5000\text{Pa.s}$ was observed for the PC/Rimar which was higher by a factor of three. This is consistent with the higher storage and loss modulus observed for the PC/Rimar system presented in Figure 15a. Thus, the addition of Rimar salt made the PC melt both more elastic and more viscous in addition resulting in a 5°C increase in the glass transition temperature. Interestingly with the

addition of Rimar salt the extensional viscosity was found to diverge at temperature T=340^{o}C both in the presence of air and nitrogen. Compare to the neat linear PC, which did not diverge until T=360^{o}C. In fact, the extensional viscosity initially decreased with increasing temperature for the neat linear PC. The decrease in the divergence temperature under nitrogen is a desirable characteristic of a flame retardant additive because of the earlier onset temperature of crosslinking as was observed in the shear rheology data in Figure 15a. However, the magnitude in the observed change in the elastic modulus was only a few percent at T=340^{o}C and could easily be overlooked. The divergence in the extensional viscosity data cannot be easily overlooked and it clearly signals a transition from dripping to not dripping of the polymer melt when exposed to heat. This information about the dripping nature of the polymer cannot be easily inferred form the shear rheology data making extensional viscosity measurements an even more powerful tool for understanding flame retardation. The high rate of crosslinking of the PC/Rimar salt has been shown by Huang et al. [73]. In their study, the PC/Rimar was found to have crosslinking rate twice as fast as the neat linear PC. Rimar salt has been shown to be a very efficient flame retardant additive and is particularly effective when added to PC where it has been found to achieve a V0 rating with as low as 0.05-0.1wt% Rimar addition [74]. Here we stretched a sample with 0.08wt% Rimar salt. It has been speculated that aromatic sulfonates promote isomerization of polycarbonate which leads to higher concentrations of CO_2 and dilution of combustion products as well as faster crosslinking and char formation. Additionally, the aromatic sulfonates has been shown to accelerate Fries-type rearrangement which also results in faster decomposition and crosslinking [74] . From the UL-94 tests performed in the SABIC labs, the PC/Rimar had a V-0 rating.

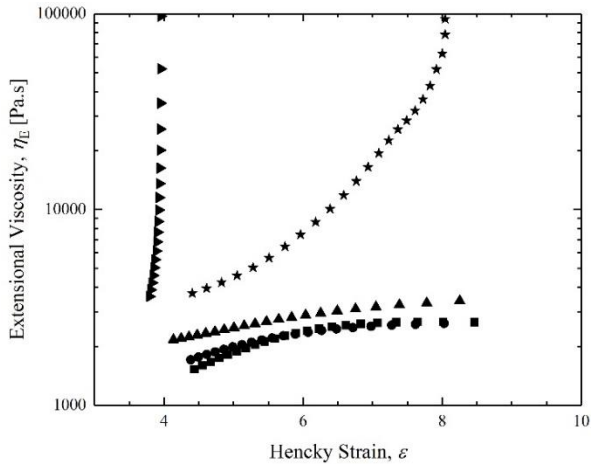

Figure 18. Capillary breakup extensional rheology measurement of extensional viscosity, η_E, as a function of Hencky strain, ε, for the linear polycarbonate with different wt% of Rimar salt (■) 0.02 wt%, (●) 0.04 wt%, (▲) 0.06 wt%, (★) 0.08 wt% and (►) 0.1wt% at temperature of $T = 340^{\circ}\mathrm{C}$ in nitrogen.

In Figure 18, the extensional viscosity is plotted as a function of the Hencky strain for the different wt% of Rimar salt at a temperature of T=340°C in the presence of nitrogen. A systematic study of the effect of variation in the concentration of the salt on the evolution of extensional viscosity was performed. The tests were performed at a fixed temperature of T=340°C to find the divergence in the extensional viscosity as a function of concentration of the salt. As observed in Figure 18, at concentrations of 0.02wt% and 0.04wt% the extensional viscosity was found to be similar to each other with a steady state extensional viscosity value of close to $\eta_E = 2500\mathrm{Pa.s}$. As the concentration was increased to 0.06wt%, there was a slight increase in the steady state extensional viscosity but nothing significant and the filament was found to breakup. On further increasing the concentration to 0.08wt% and 0.1wt% a clear divergence in the extensional viscosity was observed. Through this study it can also be observed that the high temperature capillary breakup extensional measurements were highly sensitive to variation in concentration of the salts and thus could be used to optimize the concentration of flame retardant additives.

2.3.2.3 Polycarbonate with 0.3wt% KSS Salt

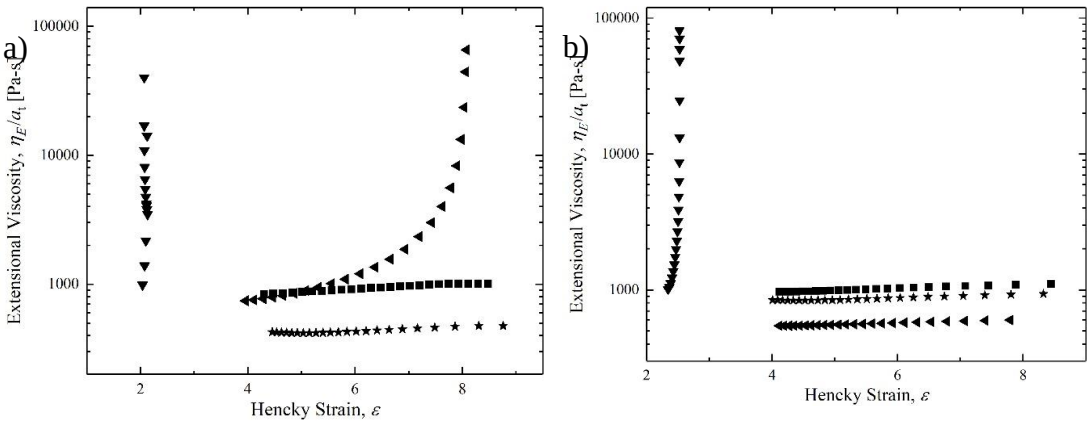

Figure 19. Capillary breakup extensional rheology measurement of extensional viscosity, η_E, as a function of Hencky strain, ε, for the linear polycarbonate with 0.3wt% KSS salt in a) air and in b) nitrogen at temperatures of $T = 320^{\circ}\mathrm{C}$ (■), $T = 340^{\circ}\mathrm{C}$ (★), $T = 360^{\circ}\mathrm{C}$ (◀) and $T = 380^{\circ}\mathrm{C}$ (▼). All extensional viscosities have been shifted to a reference temperature of $T = 320^{\circ}\mathrm{C}$.

In Figure 19, the extensional viscosity is plotted as a function of the Hencky strain for the PC with 0.3wt% KSS salt for temperatures ranging from T=320°C to T=380°C in air and in nitrogen shifted to a reference temperature of T=320°C using TTS. For an initial temperature rise from T=320°C to 340°C in air the effects of thermal degradation are observed as the shifted extensional viscosity was found to decrease by a factor of three from the reference extensional viscosity value at T=320°C. No degradation was observed for the linear PC in air over a similar temperature range. As the temperature was further increased the extensional viscosity was found to diverge at a temperature of T=360°C and beyond in the presence of air. In the presence of nitrogen, the extensional viscosity was found to collapse onto the reference extensional viscosity value until T=340°C. With further increasing to the temperature at T=360°C, a deviation from the reference extensional viscosity was observed as the extensional viscosity was found to decrease by a factor of two due to the direct effect of the thermal degradation. As the temperature was

increased to T=380^{o}C, a clear divergence in the extensional viscosity was observed similar to what was seen for the linear PC at that temperature. Due to the lack of extensional viscosity enhancement, this sample was not expected to perform well in the UL-94 tests and it did not. From the UL-94 tests performed in the SABIC labs, the PC/KSS had a V-2 rating. In fact, the extensional viscosity in air suggest that the system will perform even worse than the neat PC. Liu et al. [75] have studied the effect of addition of KSS salt to PC through TGA, FTIR and UL94 testing. They showed that a small amount (0.01-0.3wt%) of KSS strongly influences the thermal degradation of PC. With an increase in loading of KSS upto 3wt% they saw a decrease in the $T_{5\%}$ but they observed that beyond a loading of 0.1wt% of KSS there was a decrease in the maximum mass loss rate of PC and lower LOI values which led to poor flame retardancy. So why use KSS at all? It is a flame poison and the off gases will extinguish nearby flames. On its own, it may not prevent dripping, but in combination with another additive that does increase the extensional viscosity of the polymer, the addition of the flame poisoning effects may be quite desirable. Thus mixtures of flame retardant additives with PC have been tested whose results will be presented later in the paper.

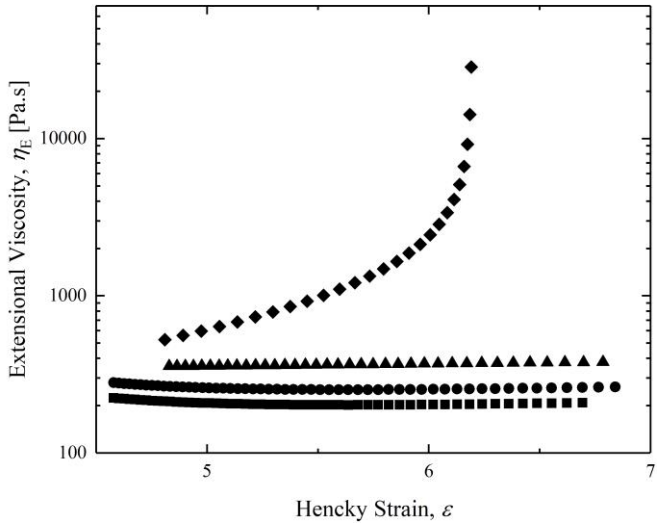

Figure 20. Capillary breakup extensional rheology measurement of extensional viscosity, η_E, as a function of Hencky strain, ε, for the linear polycarbonate with different wt% of KSS salt (■) 0.03 wt% (●) 0.08 wt% (▲) 0.3 wt% and (♦) 0.5 wt% at temperature of $T = 360^{\circ}\mathrm{C}$ in nitrogen.

In Figure 20, the extensional viscosity is plotted as a function of the Hencky strain for the different wt% of KSS salt at a temperature of T=360°C in nitrogen. A systematic study of the effect of variation in the concentration of the salt on the evolution of extensional viscosity was also performed. The tests were performed at a fixed temperature of T=360°C to find the divergence in the extensional viscosity as a function of concentration of the salt. As observed in Figure 20, at concentrations of 0.03wt% and 0.08wt% the extensional viscosity was found to be similar to each other and lower by a factor of two as compared to the extensional viscosity at 0.3wt% KSS salt. As the concentration was increased to 0.5wt% a clear divergence in the extensional viscosity was observed which shows that a higher loading of KSS salt was required in order to improve the anti-dripping properties of the PC.

2.3.2.4 Polycarbonate with 0.5wt% TSAN

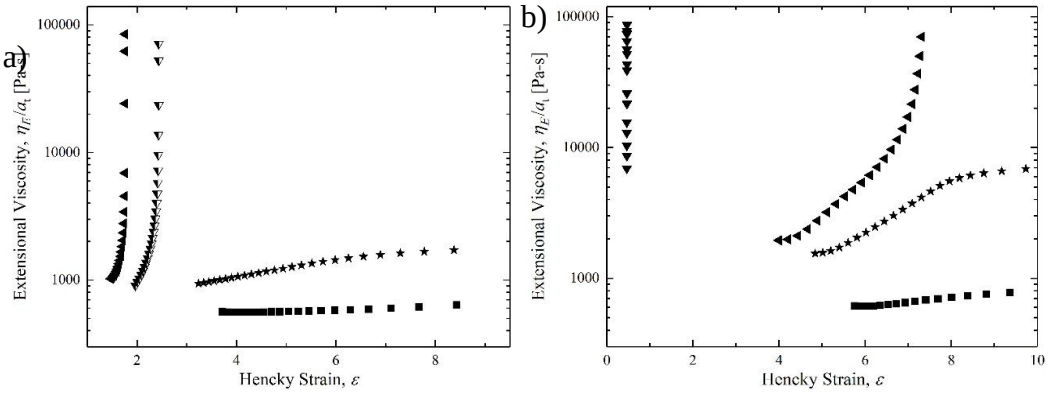

Figure 21. Capillary breakup extensional rheology measurement of extensional viscosity, η_E, as a function of Hencky strain, ε, for the linear polycarbonate with 0.5wt% TSAN in a) air and in b) nitrogen at temperatures of $T = 320^{\circ}\mathrm{C}$ (■), $T = 340^{\circ}\mathrm{C}$ (★), $T = 350^{\circ}\mathrm{C}$ (▽), $T = 360^{\circ}\mathrm{C}$ (◀) and $T = 380^{\circ}\mathrm{C}$ (▼). All extensional viscosities have been shifted to a reference temperature of $T = 320^{\circ}\mathrm{C}$.

In Figure 21, the extensional viscosity is plotted as a function of the Hencky strain for the linear PC with 0.5wt% TSAN for temperatures ranging from T=320°C to T=380°C in air and in nitrogen. All the extensional viscosities in Figure 21 have been shifted to a reference temperature of T=320°C using TTS. The evolution of the extensional viscosity of the PC/TSAN presents qualitatively similar trends in the presence of air and nitrogen. In each case, a slow increase in the extensional viscosity was observed beyond T=320°C followed by a divergence of the extensional viscosity at temperatures beyond $T \geq 350^{\circ}\mathrm{C}$. This sample was found to be nearly insensitive to the presence of oxygen. In that way it is similar to PC/Rimar although the divergence temperature for PC/TSAN system was about $10^{\circ}\mathrm{C}$ higher than that of the PC/Rimar. TSAN is comprised of PTFE dispersed in styrene acrylonitrile (SAN) matrix. PTFE is a completely inert polymer which is not affected by the chemical agents and also thermally stable until T=250°C [76, 77]. Odochian et al. [76] have showed through TGA-FTIR analysis that the thermal degradation of PTFE proceeds in two steps. First step involves the elimination of the gases evolved from the

decarboxylation of the –COOH group followed by a zipper depolymerization with the formation of the monomer C_2F_4. PTFE has proven to be a very effective additive in improving the flame retardant behavior of aryl phosphates in PC/ABS blend [78]. From the UL-94 tests performed in the SABIC labs, the PC/0.5% TSAN had a V-0 rating as expected from the extensional viscosity data.

2.3.2.5 Polycarbonate with 0.3wt% KSS and 0.3wt% TSAN

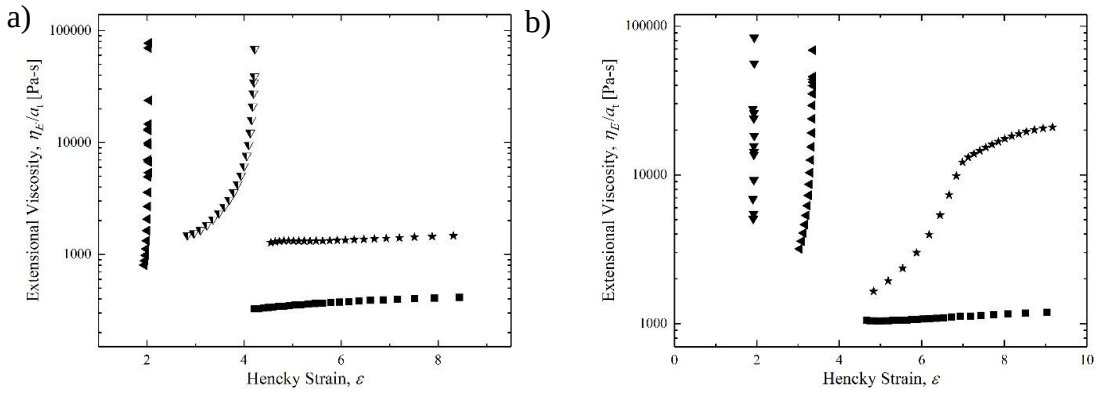

Figure 22. Capillary breakup extensional rheology measurement of extensional viscosity, η_E, as a function of Hencky strain, ε, for the polycarbonate with 0.3wt% KSS and 0.3wt% TSAN salt in a) air and in b) nitrogen at temperatures $T = 320^{\circ}\mathrm{C}$ (■), $T = 340^{\circ}\mathrm{C}$ (★), $T = 350^{\circ}\mathrm{C}$ (▽), $T = 360^{\circ}\mathrm{C}$ (◀) and $T = 380^{\circ}\mathrm{C}$ (▼). All extensional viscosities have been shifted to a reference temperature of $T = 320^{\circ}\mathrm{C}$.

In this section and the following we will present results for a mixture of various flame retardant additives used in the previous sections. The main idea behind the mixtures was to optimize the concentration of various additives and make the polymer more cost effective. Also since the implementation of environmental directives banning or limiting the use of halogenated compounds, the development of flame retardants has focused on more environmentally friendly alternatives or halogen free additives. In Figure 22, the extensional viscosity is plotted as a function of the Hencky strain for the linear PC mixed

with 0.3wt% KSS and 0.3wt% TSAN salt at temperatures T=320^{o}C to T=380^{o}C in air and in nitrogen. This is an interesting mixture because KSS alone acts as a flame poison and was found to have poor dripping properties whereas TSAN is a non-halogen crosslinker which was found to have an earlier onset temperature of crosslinking. Thus this mixture was blended in order to investigate whether the mixture of T-SAN and KSS would help in improving the dripping properties and thus achieving a better UL-94 rating. As observed in the all the previous cases, a divergence in viscosity is observed above a critical temperature. Here, under air and nitrogen the extensional viscosity was found to diverge at T=350^{o}C which was similar to the PC/TSAN sample even though the concentration of TSAN was reduced from 0.5wt% to 0.3wt%. The addition of TSAN to the KSS salt has clearly allowed the sample achieve a much better anti-dripping properties while maintaining the flame poison properties of the KSS. Like the PC/TSAN case the PC/KSS/TSAN sample was found to insensitive to the presence of oxygen or nitrogen as the increase in the extensional viscosity was observed as throughout the temperature range. The presence of KSS appeared to have little effect on the extensional viscosity. This mixture was found to be a good flame retardant additive which resulted in a UL94-V0 rating.

2.3.2.6 Polycarbonate with 0.08wt% Rimar salt, 0.1wt% TSAN an 0.2mol% THPE

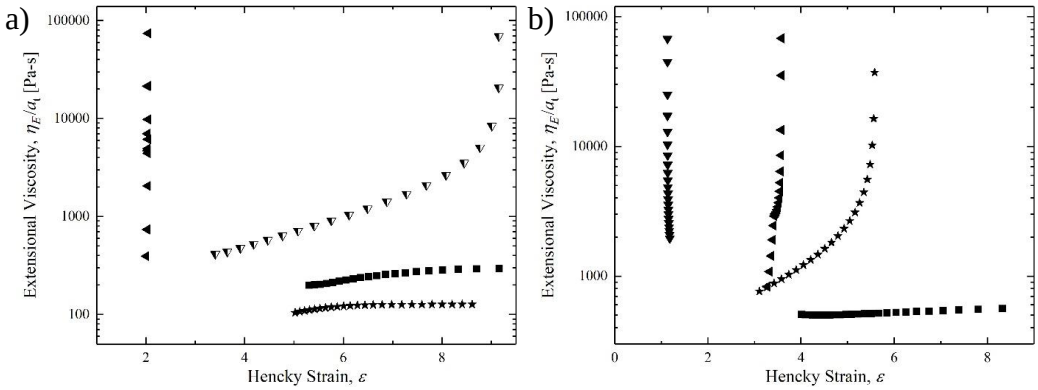

Figure 23. Capillary breakup extensional rheology measurement of extensional viscosity, η_E, as a function of Hencky, ε, strain for the polycarbonate with 0.08wt% Rimar, 0.1wt% T-SAN and 0.2mol% THPE in a) air and in b) nitrogen at temperatures of $T = 320^{o}\mathrm{C}$ (■), $T = 340^{o}\mathrm{C}$ (★), $T = 350^{o}\mathrm{C}$ (▼), $T = 360^{o}\mathrm{C}$ (◀) and $T = 380^{o}\mathrm{C}$ (▼). All extensional viscosities have been shifted to a reference temperature of $T = 320^{o}\mathrm{C}$.

In Figure 23, the extensional viscosity is plotted as a function of the Hencky strain for the PC with 0.08wt% Rimar, 0.1% TSAN and 0.2mol% THPE at temperatures ranging from T=320°C to T=360°C in air and in nitrogen shifted to a reference temperature of T=320°C using TTS. In this sample both Rimar salt and TSAN was mixed with linear PC along with 0.2mol% of a branching agent (THPE). Individually, Rimar salt and TSAN additives achieved a rating of UL94-V0 as they were found to induce an onset of crosslinking at a lower temperature and were also found to be insensitive to the presence of oxygen. Thus the idea behind this mixture was to further improve the anti-dripping performance of the PC by mixing two crosslinkers along with a branching agent. The data in Figure 23 clearly shows that the mixture of Rimar salt and TSAN or perhaps the addition of branching agent negatively affects the performance under air while the extensional viscosity under nitrogen appears to follow the best case scenario result of PC/Rimar alone. The three fold reduction in the extensional viscosity in air has not been observed for any

of the other additives or the neat linear PC. Similar reductions have, however, been observed for the branched PC in the presence of air as shown in the studies done by Sur et al. [52]. This strongly suggests that the initial drop in the extensional viscosity under air is the result of the branching agent addition to this mixture. The goal of creating this mixture was to enhance crosslinking at lower temperatures. However, instead of promoting crosslinking THPE appears to have promoted chain scission or possibly reduced the effectiveness of the Rimar and TSAN in air. On further increasing the temperature beyond T=340^{o}C the extensional viscosity was found to diverge both in the presence of nitrogen and in air. The rate of crosslinking was found to be faster in the presence of nitrogen as compared to that in air. The extensional viscosity was found to diverge at T=340^{o}C which was 40^{o}C earlier as compared to the linear PC in the presence of nitrogen. The evolution of the extensional viscosity of this mixture under nitrogen was found to be similar to the PC/Rimar. This implies that the path of degradation is being dominated by the Rimar. As a result the UL-94 tests performed in the SABIC labs, the PC/0.08wt% Rimar/0.1wt% TSAN/0.2mol% THPE had a V-0 rating as expected from the extensional viscosity data.

2.4 Conclusion

The variation in the extensional viscosity of polycarbonates mixed with flame retardant additives was studied using a newly designed high–temperature capillary breakup extensional rheometer (CaBER). Extensional rheology measurements were performed at temperatures varying from T=320^{o}C to 380^{o}C in both an inert and an oxygen-rich environment for all the polycarbonates. The design of the CaBER oven allowed us to make measurements under conditions where polymer degradation was either expected or not. As

showed in our previous paper Sur et al. that extensional rheology could be used to better understand the dripping behavior of polymers like polycarbonate when they are exposed to a high temperature heat source like a flame. Thus in our current article using high temperature CaBER experiments we looked at the effectiveness of the various combinations of flame retardant additives mixed with PC based on the evolution of extensional viscosity as a function of temperature.

The extensional viscosities at various temperatures were shifted to a reference temperature of $T_t = 320^{o}\mathrm{C}$ where the effect of thermal degradation on the samples were negligible. Thus any deviations from the extensional viscosity curve at the reference temperature implied the onset of chain scission in some cases or crosslinking in some cases. The divergence temperature for the linear PC was found to be T=380^{o}C in the presence of nitrogen. As compared to linear PC, the divergence temperatures in the presence of nitrogen for the PC/Rimar, PC/KSS, PC/TSAN, PC/Rimar/TSAN/THPE and PC/KSS/TSAN were found to be T=340^{o}C, T=380^{o}C, T=360^{o}C, T=340^{o}C, T=360^{o}C respectively. While the presence of Rimar and TSAN considerably improved the flame dripping properties of the PC through significant crosslinking, KSS salt alone had a negative impact on the dripping behavior of the PC as a large drop in extensional viscosity was observed on increasing the temperature from T=320^{o}C to 360^{o}C and no crosslinking was observed until temperature T=380^{o}C. An interesting observation was that when KSS was mixed with TSAN, it showed an improvement in the flame retardant properties of the PC, thus demonstrating the sensitivity of our experimental techniques. Rimar salt was found to be an effective anti-drip additives in very small concentration of 0.08wt%. Similar trends in the deviation of the storage modulus from the temperature sweep measurements

were observed although the magnitude of the deviations were not as significant as was observed in the high temperature CaBER measurement. On comparing the UL-94 ratings of the above polymers one can observe that all the samples except linear PC and PC/KSS had a V0 rating. Linear PC and PC/KSS polymers had a V2 rating. Closely looking at the evolution of extensional viscosity between the temperature range of T=320^{o}C to T=360^{o}C in the presence of nitrogen, either the system was found to be stable or a drop in the extensional viscosity was observed for linear PC and PC/KSS system respectively as the temperature was increased whereas an increase in the extensional viscosity or divergence in the extensional viscosity was observed for the V0 rated samples. Thus a clear correlation was observed between the ratings of the polymer systems and the evolution of the extensional viscosity.

Through our concentration variation study of KSS and Rimar salts we have also shown how high temperature Capillary breakup extensional rheology can be used to optimize the concentration of flame retardant salts which in turn can help in improving the dripping properties. For example, PC with 0.3wt% KSS salt had a V2 ratings whereas as the concentration of KSS salt was increased to 0.5wt% as observed from Figure &, a clear divergence in extensional viscosity was observed and a transition from a V2 to a V0 rating was achieved. Thus, through these measurements we can create a better design criteria map as addition of more salts increases the cost and also can alters the properties of the polymer. Similarly, for the case of PC with Rimar salt, it was observed that at concentration of 0.08wt% and above a V0 rating was achieved whereas below that concentration, a V2 rating was achieved.

Our experiments suggests that through simple visualization of the time diameter decay at different temperatures one can give a quick assessment of the onset temperature of crosslinking which is important in understanding the FR properties of the polymer. We also showed the sensitivity of our experiments to different combinations of FR salts on the dripping properties of the polycarbonate which would enable us to make better formulations which is crucial in improving the dripping properties of the polymers.

2.5 Acknowledgement

The authors would like to thank Sabic for funding this research. Additionally, the authors would like to thank Christian Clasen of KU Leuven for use of his Edgehog software.

2.6 Publication

The work described in this chapter was submitted for publication to the Korean-Australian Rheology Journal (Under Review). The complete reference is S Sur, M Chellamuthu and J P Rothstein “High Temperature Extensional Rheology Of Commercially Available Polycarbonate mixed with Flame Retardant Salts (2019)”.

CHAPTER 3

DROP BREAKUP DYNAMICS OF DILUTE POLYMER SOLUTIONS: EFFECT OF MOLECULAR WEIGHT, CONCENTRATION AND VISCOSITY

3.1 Introduction

The addition of a small amount of moderate to high molecular weight polymer to a Newtonian solvent can yield rather dramatic changes to the rheological behavior of the fluids. This is especially true in extensional flows where presence of polymers can significantly increase the resistance to stretching flows [79]. The resistance to extensional flows is characterized by the extensional viscosity of the fluid. For dilute solutions of high molecular weight polymers, the extensional viscosity can be several orders of magnitude larger than the shear viscosity. The effects of large extensional viscosity can be readily observed through the ability of these solutions to form persistent filaments and to delay the breakup into droplets when stretched [80-85]. This polymer-induced viscoelasticity has many industrial applications, including in inkjet printing. In inkjet printing, the addition of a small amount of polymer to the ink can help minimize satellite and daughter droplet formation which is essential for printing quality. However, the addition of too much polymer to the ink can make printing impossible by delaying breakup of ink jets into drops [86, 87].

The influence of polymers in inkjet printing fluids or other low-viscosity dilute polymer solutions is often difficult to see in standard shear rheology measurements. The shear viscosity often appears to be Newtonian in steady shear measurements and, in small amplitude oscillatory tests, the relaxation time is often so small (in the range of micro to

milliseconds) that it is difficult to measure using standard rheometric techniques. However, for these micro-structured fluids, the extensional viscosity, which is a function of both the rate of deformation and the total strain accumulated, is often clearly evident even if it is not readily measurable. Some of the most common manifestations of extensional viscosity effects in complex fluids can be observed in the dramatic increase in the lifetime of a fluid thread undergoing capillary break-up driven by interfacial tension. Depending on the composition of the fluid, viscous, elastic and inertial stresses may all be important in resisting the filament breakup resulting from capillary forces. The breakup dynamics can thus be used to obtain a number of fluid properties including the surface tension, σ, the shear viscosity, η, the extensional viscosity, η_E, and the relaxation time of the fluid, λ. Here, we will be using dripping onto substrate capillary breakup extensional rheometry (CaBER-DoS) developed by Dinic et al. [88, 89] to visualize and characterize the extensional rheology of dilute, low-viscosity polymer solutions.

In the past several decades, a number of measuring techniques have been used to characterize the extensional flow rheology of complex fluid. Of those techniques, filament stretching extensional rheometry (FiSER) and capillary breakup extensional rheometry (CaBER) techniques are the most common ones [82, 90-93]. In both these techniques, a small amount of liquid is placed between two cylindrical discs or plates. In a filament stretching device, at least one of the cylindrical discs is driven in a controlled manner so that a constant extension rate can be imposed on the fluid filament while the stress response of the fluid to the stretching deformation is measured through a combination of a force transducer and a laser micrometer to measure the filament diameter [83, 94]. This technique is limited by the maximum strain that can be achieved ($\varepsilon_{\max} \approx 6$) and the maximum

imposed deformation rates ($\dot{\varepsilon}_{\max} \approx 10 \text{s}^{-1}$) that can be imposed. As a result, the use of FiSER is limited to mostly polymer melts or higher viscosity polymer solutions where the zero shear rate viscosity is greater than approximately $\eta_0 > 1$ Pa.s [95].

In CaBER, a step strain is rapidly imposed on the fluid between the two plates by rapidly displacing the top plate by a linear motor over a short distance [96]. This extension produces a liquid filament between the two plates. The minimum diameter of the thinning filament is then measured as a function of time until break-up in order to calculate the apparent extensional viscosity and the relaxation time of the fluid. This is a common technique for determining the extensional rheology of viscoelastic fluids with viscosities as low as $\eta_0 = 70$ mPa.s and relaxation times as small as $\lambda = 1$ ms [97]. Along with the viscosity limit of the CaBER technique, another limitation of this method is the inertial effects resulting from the dynamics of the rapid step stretch imposed by the motor motion. At the high velocities required to measure the breakup dynamics of low viscosity fluids, the rapid step strain can lead to oscillations in the filament that make measurement of extensional rheology difficult. Recently Campo-Deano et al. [98] used a slow retraction method (SRM) to investigate filament thinning mechanisms of fluids with shear viscosities similar to water and very short relaxation times. This experimental technique involves slowly separating the pistons just beyond the critical separation distance for which a statically stable liquid bridge can exist. At this point, the filament becomes unstable and the thinning and breaking process is initiated. This SRM technique avoids inertial effects allowing the authors to extract relaxation times as short as $\lambda = 200$ μs for dilute aqueous solutions of polyethylene oxide (PEO) with a molecular weight of $M_w = 1 \times 10^6$ g/mol and

shear viscosities between $1 < \eta_0 < 3$ mPa.s [98]. Vadillo et al. [97] have further pushed the limit by measuring relaxation times as short as $\lambda = 80$ μs by using a Cambridge Trimaster rheometer (CTM) [99] along with a high speed camera with adjustable fps with reduction of frame size for a series of solution of monodisperse polystyrene dissolved in diethyl phthalate (DEP) with concentration of polystyrene ranging from dilute to concentrated with solution viscosity of $\eta_0 = 12$ mPa.s. More recently Greiciunas et al. [100] have used the Rayleigh Ohnesorge jetting extensional rheometer (ROJER) technique [101] to measure relaxation times of dilute solutions of PEO, with molecular weight $M_w = 3 \times 10^5$ g/mol mixed in 25%/75% (by weight) glycerol/water solution. The ROJER is one of the more technically challenging of all the extensional rheology methods for characterizing low viscosity fluids to implement. However, it does have the benefit of eliminating the need for high speed imaging which can reduce costs substantially. In their work, they were able to measure relaxation time as low as $\lambda = 102$ μs for a solution viscosity with zero shear viscosity of $\eta_0 = 2.9$ mPa.s. In this technique, fluid is jetted through a small diameter nozzle where a small perturbation is applied to drive a capillary instability along the liquid jet. The instability eventually grows large enough to cause the jet to break up into droplets downstream. A camera is used to capture the thinning dynamics from which the extensional rheology of the fluids can be calculated in much the same way as in CaBER.

Amazingly, there are industrial applications like inkjet printing which require devices that can experimentally characterize the extensional rheology of dilute solutions with relaxation times even lower than those described above. Recently, Dinic et al. [88] have developed a dripping onto substrate CaBER technique called CaBER-DoS which can

measure relaxation times much less than $\lambda \approx 1\ \text{ms}$ for low viscosity fluids ($\eta_0 \approx 1\ \text{mPa.s}$). In their experimental setup, a fluid dispensing system is used to deliver a drop of fluid at a relatively low flow rate onto a glass substrate placed at a fixed distance below the exit of the nozzle. As the droplet slowly drips from the nozzle, a filament is formed. By capturing the droplet on the substrate and not allowing it to fall further, the filament is allowed to breakup under capillary action in much the same way that CaBER works. The advantage is that the inertia associated with the moving of the top plate is removed as are the acceleration and the velocity limit of the actuator. Additionally, compared to the slow retraction method, CaBER-DoS is much better suited for highly volatile fluid where evaporation can play a large role because the experiments are performed much more quickly. For visualization, a high-speed imaging system was used, with a frame rates varying from 8000 to 25,000 fps. Dinic et al. [88] performed a series of studies on aqueous solutions of PEO having a of molecular weight of $M_w = 1\times10^6\ \text{g/mol}$. In all their experiments, the concentration of PEO was kept within the dilute region. They demonstrated a dependence of relaxation time on concentration, *c*, for dilute, aqueous PEO solution as $\lambda_E \propto c^{0.65}$ rather than the expected $\lambda_E \propto c$ from dilute theory [102]. This deviation was attributed to the much lower concentration required in extensional flows for a fluid to truly be within the dilute regime [88]. In fact, Clasen et al. [80] showed that in extensional flows an ultra-dilute concentration below $c/c^*<0.01$ is needed to recover the expected relaxation times and scaling's for dilute systems. Here, c/c^* is the reduced concentration with c^* defined as the coil overlap concentration. Dinic et al. [88] were successfully able to measure relaxation times as low as $\lambda_E \approx 0.3\ \text{ms}$. In follow up papers, the authors further extended their technique by performing extensional rheometry

measurements on various other complex fluids [103] such as glycerol-water mixtures, ketchup, mayonnaise, photovoltaic ink and semi-dilute solutions of poly-acrylamide. They were able to capture and differentiate between the inertio-capillary thinning, visco-capillary thinning and elasto-capillary thinning dynamics using the CaBER-DoS. Through this technique, Dinic et al. [89] captured the differences in the necking region for different fluids during pinch-off. For pure water, it was observed that the necking region forms a cone close to pinch-off point as predicted by theory. For a polymer solution, a long cylindrical filament was formed and the pinch-off was found to occur in a location near the mid-plane of the filament. For a multicomponent complex fluid, such as shampoo, a non-slender liquid bridge was formed resulting in the formation of two axisymmetric cones after break-up. Through these initial studies, Dinic et al. [89] have established a quick, reliable method to perform extension rheometry on low-viscosity fluids while establishing the microstructured effects on the pinch-off dynamics.

In this paper, we extend the work into thinning dynamics of low viscosity, elastic fluids using the CaBER-DoS technique by systematically probing the effects of polymer molecular weight, solution viscosity and concentration down to the point at which measurements of extensional viscosity and relaxation time become limited by camera resolution. In this study, we focus on the transition between the early time inertia-capillary regime and late stage elasto-capillary regime. The sharpness of this transition allows us to measure the extensional rheology of these PEO solutions with very few data points. In fact, from the parametric studies performed here, we have developed a simple relation to determine the relaxation time of low concentration, low molecular weight and low viscosity polymer fluids by capturing a single image of fluid filament before breakup. Using this

technique, we have demonstrated that relaxation time measurements as low as $\lambda_E = 20$ μs can be measured using the CaBER-DoS technique.

3.2 Experimental Setup

3.2.1 Methodology

The dripping onto substrate capillary breakup extensional rheometry (CaBER-DoS) setup is shown in Figure 24. CaBER-DoS requires a high speed camera (Phantom- Vision optics, V-4.2) to capture the filament break-up process, a liquid dispensing system (KD Scientific) to control the volume flow rate, a cylindrical syringe tip, a glass substrate and a high intensity light source. In CaBER-DoS, a liquid bridge is formed between the substrate and the nozzle by allowing a drop of liquid to drip from the nozzle onto the glass substrate. The height of the nozzle, H_0, from the substrate is selected such that an unstable liquid bridge is formed as soon as the drip makes contact and spreads on the substrate. In the experiments presented here, an aspect ratio of $H_0 / D_{nozzle} = 3$ was used. The high speed camera used for visualization can record at frame rates well over 100,000fps, but at those rates the number of pixels per image was quite small. For most of the measurements presented here a frame rate of 25,000 fps was used with a resolution of 192x64pixel^2. The magnification attained using Edmund optics long range microscope lens (EO-4.5x zoom) is 5μm/pixel. However, to minimize the effect of the resolution error (± 5μm) on the diameter values reported, we do not report data below a filament diameter length of $D_{filament} < 10$ μm even though the edge detection algorithm we used to capture the diameter decay (Edgehog, KU Leuven) has sub-pixel resolution. In order to calculate the extensional viscosity, the diameter decay was fit with a spline and then differentiated as described

below. The diameter of the nozzle was $D_{nozzle} = 800$ μm and the volume flow rate of $Q = 0.02$ ml/min was maintain

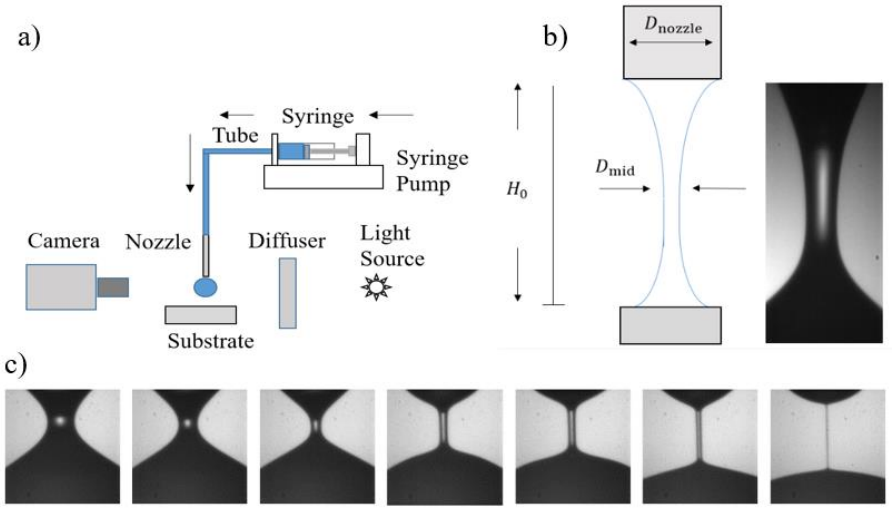

Figure 24. a) Schematic diagram of the drip onto substrate capillary breakup extensional rheometry (CaBER-DoS) setup with all the major components labeled and b) a magnified image of the filament formation between the exit of the nozzle and the substrate along with appropriate dimensions c) sequence of images showing the development of the filament and subsequent thinning.

The dynamics of the filament thinning of low viscosity fluids in the CaBER-DoS experiments presented here can be characterized by some of the well-defined physical models used to characterize the dynamics of drop formation for dilute polymer solutions from dripping nozzles [85] and continuous jets [104]. In this section, we will define some of the dimensionless numbers used to characterize the filament thinning dynamics along with the models used to categorize the thinning dynamics into three different regimes – inertio-capillary, visco-capillary and elasto-capillary. The three different regimes will be discussed below and highlighted in the results for different PEO solutions.

The driving force of the filament thinning in CaBER-DoS originates from the capillary pressure and depends, therefore, on the surface tension, σ, and the local curvature of the filament, $\kappa = 1/R_1 + 1/R_2$, where R_1 and R_2 are the principle radii of curvature on the filament. The capillary thinning is resisted by a combination of fluid viscosity, inertia, and elasticity depending on the fluid physical and rheological properties and the size of the filament. The important dimensionless groups characterizing this necking process are the Ohnesorge number, $Oh = \eta_0 / (\rho\sigma R)^{1/2}$, which represents a balance of the inertial and viscous forces for a slender filament; the intrinsic Deborah number, $De = \dfrac{\lambda}{\sqrt{\rho R_0^{\,3} / \sigma}}$, which represents the ratio of the characteristic relaxation time of the fluid to the timescale of the flow; and the elasto-capillary number, $Ec = \lambda_E \sigma / \eta_0 R_0$, which represents a ratio of the characteristic relaxation time of the fluid and the viscous timescale of the flow. In this case, the intrinsic Deborah number, $De = \lambda_E / t_R$, is a ratio of the extensional relaxation time of the fluid to the Rayleigh time, $t_R = (\rho R_0^{\,3} / \sigma)^{1/2}$. In these dimensionless groups, η_0 is the shear viscosity of the fluid, R_0 is the radius of the filament, σ is the surface tension, ρ is the density and λ_E is the relaxation time in extension. Clasen et al. [105] have shown that for Ohnesorge numbers less than $Oh < 0.2$, the thinning of the fluid filament will be dominated by a balance of inertial and capillary forces (inertia-capillary regime), while for $Oh > 0.2$, the thinning of the fluid filament will be dominated by a balance of viscous and capillary forces (visco-capillary regime). For a low Ohnesorge number flow, for $De > 1$, the thinning process will be dominated by a balance of elastic and capillary forces (elasto-capillary regime), while, for $De < 1$, elastic forces will play no role in the breakup dynamics

[85]. Finally, for a large Ohnesorge number flow and an elasto-capillary number less than $Ec < 4.7$ the filament thinning will remain visco-capillary while for $Ec > 4.7$ the flow will again transition to elasto-capillary thinning [105].

In the inertia-capillary regime, the radius decays with time following a 2/3 power law dependence [83],

$$\frac{R(t)}{R_0} = 0.64\left(\frac{\sigma}{\rho R_0^3}\right)^{1/3}(t_c - t)^{2/3} = 0.64\left(\frac{t_c - t}{t_R}\right)^{2/3}. \tag{0.3}$$

Here, t_c is the time at which the filament breaks up, R_0 is the initial radius and t_R is the Rayleigh time which is a characteristic timescale for the breakup of fluids in this inertia-capillary regime [88]. The prefactor in equation 1 has been reported to be between 0.64 and 0.8 with some experimental measurements finding values as large as 1.0 [83, 88, 98, 105]

For the visco-capillary regime, the radius decays linearly with time as shown by Papageorgiou [106],

$$\frac{R(t)}{R_0} = 0.0709\left(\frac{\sigma}{\eta_0 R_0}\right)(t_c - t) = 0.0709\left(\frac{t_c - t}{t_v}\right). \tag{0.4}$$

Here, $t_v = \eta_0 R_0 / \sigma$, is the characteristic viscous timescale for breakup.

For the elasto-capillary regime, the Entov [31] showed that, for an Oldroyd-B fluid, the radius will decay exponentially with time,

$$\frac{R(t)}{R_0} = \left(\frac{GR_0}{2\sigma}\right)^{1/3}\exp\left(-\frac{t}{3\lambda_E}\right). \tag{0.5}$$

Here, G is the elastic modulus of the fluid. Unlike the inertio-capillary regime where a conical filament is formed with two principle radii or curvature, in the elasto-capillary regime a cylindrical filament with a single radii of curvature is formed. In CaBER measurements, the extensional rheology of the fluid can be extracted from measurements of the diameter decay with time. The extension rate of the filament is given by

$$\dot{\varepsilon} = -\frac{2}{R_{\text{mid}}(t)}\frac{\mathrm{d}R_{\text{mid}}(t)}{\mathrm{d}t}. \tag{0.6}$$

Hence, for an Oldroyd-B fluid, the extension rate is constant, independent of time and only dependent on the fluids relaxation time, $\dot{\varepsilon} = 2/3\lambda_{\text{E}}$. The resulting filament decay has a constant Weissenberg number of $Wi = \lambda_{\text{E}}\dot{\varepsilon} = 2/3$. The Weissenberg number represents the relative importance of elastic to viscous stresses in a flow. This value is larger than the critical Weissenberg number of Wi = 1/2 needed to achieve coil-stretch transition and thus can be used to measure the extensional rheology of these polymer solutions. As seen in Equation 3, the relaxation time can be calculated from the slope of the log of the radius or diameter decay with time. In addition, the extensional viscosity can also be calculated from the measurement of diameter or radius decay with time,

$$\eta_{\text{E}} = \frac{\sigma / R_{\text{mid}}(t)}{\dot{\varepsilon}(t)} = -\frac{2\sigma}{\mathrm{d}R_{\text{mid}}/\mathrm{d}t}. \tag{0.7}$$

3.2.2 Materials

The low-viscosity elastic fluids tested in this work are dilute solutions of polyethylene oxide (PEO) (supplied by Aldrich Chemical Co.) with molecular weights ranging from $M_{\text{w}} = 1\times10^{5}$ to 1×10^{6} g/mol in glycerol and water mixtures. In general, commercial PEO samples are known to be polydisperse. Tirtaamadja et al. [85] measured the polydispersity

index of the M_w=1×10^6 g/mol PEO sample used in their study to be PDI=1.8. Since our samples were purchased from the same supplier, we expected them to have similar polydispersity as those used in the works of Tirtaamadja et al. [85]. The polydispersity of the polymer can have an impact on measurements and comparisons to Zimm theory which assumes a perfectly monodisperse polymer sample. In this work, the polymer concentrations were varied, while keeping it below the coil overlap concentration, c^*, which was calculated using the definition provided by Graessley [107] such that $c^*=0.77/[\eta]$. Here $[\eta]$ is the intrinsic viscosity of the polymer solution which depends on the molar mass of the chain according to the Mark-Houwink-Sakurda equation $[\eta]=KM^a$, where K=0.072 cm^3/g and $a=0.65$ for PEO in water and glycerol [85]. To arrive at the value of these Mark-Houwink constants, Tirtaamadja et al. [85] used a linear regression analysis to obtain a line of best fit to all the previously published data for PEO in water and PEO in water/glycerol over a range of molecular weight spanning from 8x10^3<M_w<5x10^6 of PEO. They observed that all the data agreed well with each other and were within the experimental error for variation in the solvent composition. The concentration of PEO was varied from 0.004c^* to 0.5c^*. The glycerol and water mixtures were chosen such that the shear viscosity of the solution varied between $6\ \text{mPa.s} \le \eta_0 \le 22\ \text{mPa.s}$. The shear viscosity was measured using a cone and plate rheometer (DHR-3, TA instruments) and showed a constant shear viscosity over the shear rate range that could be probed by the rheometer (1 s^{-1}< $\dot{\gamma}$ <100 s^{-1}). The surface tension for each glycerol and water mixture was selected based on values available in the literature [108]. In preparing the solutions, water was first mixed with the required concentration of the PEO and mixed in a magnetic stirrer

(CIMAREC) for 2 hours and then the required amount of glycerol was added, and again mixed for another 24 hours at 500 rpm at room temperature.

3.3 Results and Discussions

3.3.1 CaBER-DoS of PEO solutions with constant *c/c** and varying M_w and η_0

Throughout the results and discussion section, we will present CaBER-DoS results for a series of PEO solutions with varying solution viscosity, polymer molecular weight and concentration so that trends for each of these parameters can be identified and compared to theory. For most of the experiments presented here, the overarching goal was to extend the experimental characterization capabilities of CaBER-DoS to less and less elastic fluids. As we will demonstrate, this can be done either by extending the CaBER-DoS experimental capabilities or by finding trends with solvent viscosity, molecular weight or concentration that can be used to extrapolate from more elastic and measurable solutions to lower elasticity solutions that cannot be characterized even in CaBER-DoS. In all cases, the concentration levels of the PEO were maintained in the dilute region, $c/c^* < 1$, where the results can be compared against theory.

In this subsection, we will focus on solutions with a fixed values of reduced concentration, c/c^*=constant for each polymer molecular weight. Although a wide spectrum of reduced concentrations were tested using CaBER-DoS, only a small subset of these concentrations will be systematically presented here. CaBER-DoS results are presented in Figures 2 and 3 for solutions of PEO with molecular weights of $M_w = 1\text{x}10^6$, $6\text{x}10^5$, $2\text{x}10^5$, and $1\text{x}10^5$ g/mol and solution viscosity of η_0 =6 mPa.s, 10 mPa.s and 22 mPas.

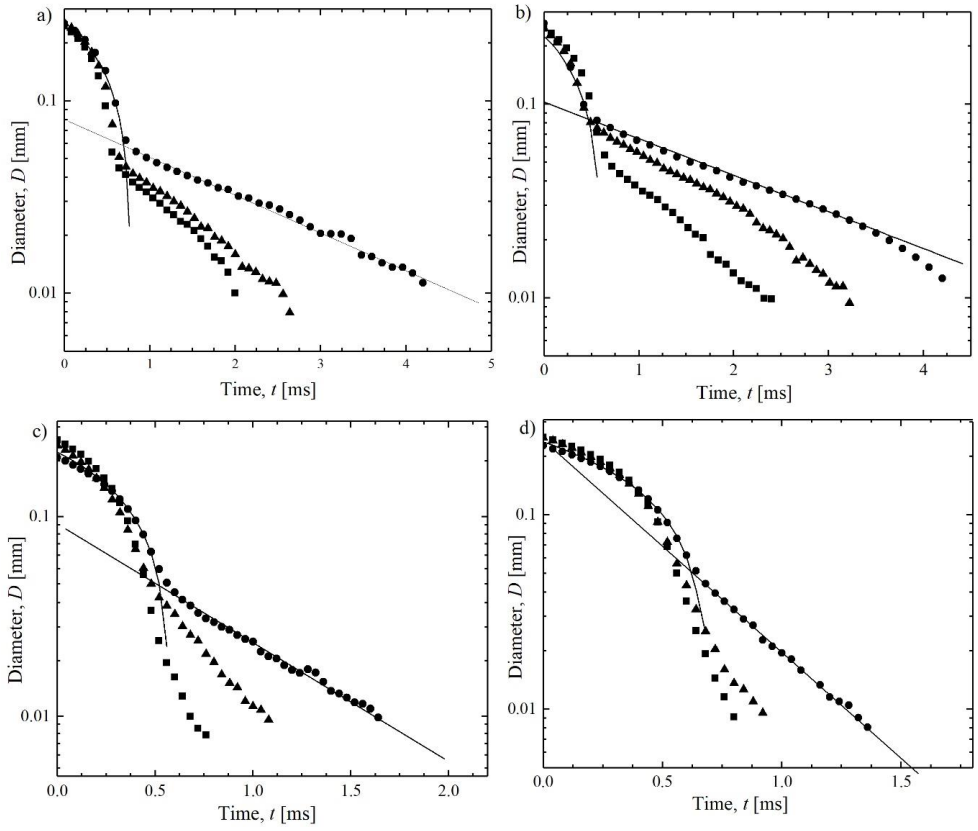

Figure 25. Plot of diameter, D, as a function of time, *t*, for a series of PEO solutions in glycerin and water with a) molecular weight of M_w =1x10^6 g/mol and a reduced concentration of *c/c=0.02, b) M_w =600k g/mol and *c/c**=0.03, c) M_w =200k g/mol and *c/c**=0.05, and d) M_w =100k g/mol and *c/c**=0.08. In each plot the solution viscosity is varied from η_0=6 mPa.s(■), to η_0=10 mPa.s (▲) and finally to η_0=22 mPa.s (●).Solid lines represent the inertia-capillary and elasto-capillary fits to the experimental data from theoretical predictions.**

The diameter decay as a function of time is plotted in Figure 25 for each of the four different molecular weight PEO solutions tested. In each subfigure, the diameter decay is shown as a function of solution viscosity at a fixed reduced concentration. Note that the value of the reduced concentration presented increases with decreasing polymer molecular weight to insure that a transition to an elasto-capillary thinning could be observed even at

the lowest solvent viscosity, $\eta_0 = 6$ mPa.s, for each molecular weight PEO. In all cases, the diameter evolution in time was found to exhibit two distinct regimes: an inertial capillary regime characterized by a decay of the diameter with a 2/3 power law with time followed by an elasto-capillary regime characterized by an exponential decay of the diameter with time. Late time deviation from the exponential decay in some data sets shows the effects of the finite extensibility of the polymer solution. A solid line was superimposed over one data set in each figure to demonstrate the quality of the fit to theoretical predictions of each of these regimes. Note that in these figures, the diameter decay begins at roughly D = 250 μm and not at the diameter of the initial filament which was close to the diameter of the nozzle, D = 800 μm. This was a result of the high optical magnification needed to capture the late time dynamics of the extremely fine filament and to characterize the extensional rheology of the fluid.

As can be observed from Figure 25, the transition from the initial power law decay to the late stage exponential decay was extremely sharp in all cases with no more than one or two data points spanning less than one millisecond within this transition regime. In the section that follows, the sharpness of this transition will be utilized to significantly enhance the resolution and sensitivity of relaxation time measurements from CaBER-DoS. The transition from an inertia-capillary to an elasto-capillary response is due to the growth of elastic stresses within the fluid filament as it was stretched over time. Within the inertia-capillary regime, the extension rate of the fluid filament increases with time such that $\dot{\varepsilon} = 4/\left(3\left(t_c - t\right)\right)$. At early times during the stretch, the extension rate is too small to deform the polymer within the solution because the Weissenberg number is less than one half, Wi < 1/2. As a result, in this regime, the elasticity of the fluid plays no role in the breakup

dynamics. However, as the time approaches the cutoff time, t_c, the extension rate can grow large enough such that the Weissenberg number becomes larger than $Wi > 1/2$ and the polymer chain can begin to deform and build up elastic stress which will resist the extensional flow and dominate the breakup dynamics. In CaBER-DoS, theoretical predictions suggest that the elasto-capillary breakup should occur with a constant Weissenberg number of $Wi < 2/3$. Using this Weissenberg number, one can set an extension rate of $\dot{\varepsilon} = 2/3\lambda$ as the theoretical criteria for the transition from the inertia-capillary to the elasto-capillary regime. Doing this, a critical radius for the transition to the elasto-capillary regime was found. This is a reasonable first approximation, but, as will be discussed in detail in later sections, this critical radius over predicts the actual transition radius by a factor of approximately five times because it assumes that buildup of extensional deformation and stress in the polymer is instantaneous when in reality a finite amount of strain is required to build up sufficient elastic stress to surpass the inertial forces and become the dominant resistance to the capillary forces [109]. That being said, once the flow becomes elasto-capillary, given enough data points, the diameter decay can be used to characterize both the extensional viscosity and relaxation time of the PEO solutions as described in the previous section. An important observation that one can make from Figure 25 is that increasing either the molecular weight of the polymer or the solution viscosity leads to an increase in breakup time of the filament due to an increase in the relaxation time of the polymer solution. Note also that the inertia-capillary dynamics, which manifest before the transition point, appears to be nearly independent of concentration. This variation in the relaxation time is plotted as a function of solutions viscosity and molecular weight in Figure 26.

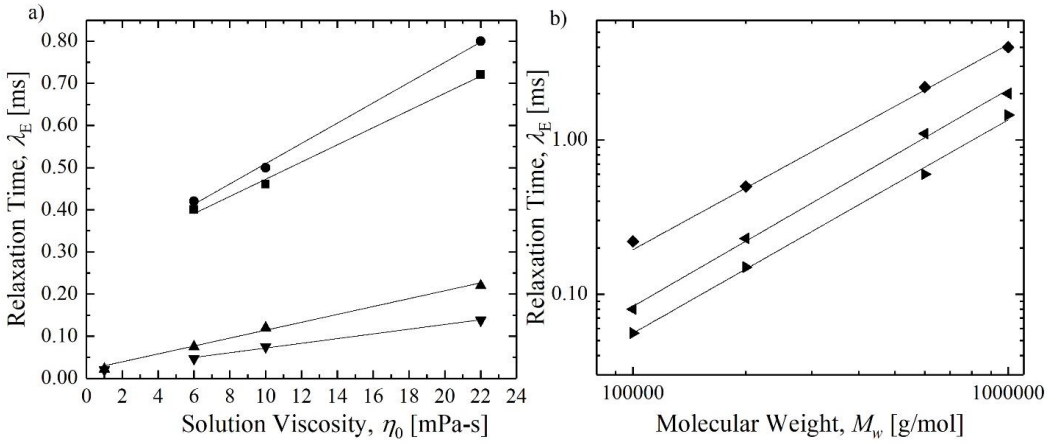

Figure 26. Plot of extensional relaxation time, λ_E, as a function of solution shear viscosity, η_0, and molecular weight, M_w, for a series of PEO solutions in glycerin and water with a) molecular weight of M_w =1x10^6 g/mol and a reduced concentration of c/c^*=0.02 (■), M_w =600k g/mol and c/c^*=0.03 (●), M_w =200k g/mol and c/c^*=0.05 (▲)and M_w =100k g/mol and c/c^*=0.08 (▼) and b) solution viscosity of η_0=6 mPa.s and c/c^*=0.5 (♦),η_0=6 mPa.s and c/c^*=0.1 (◄) and η_0=1 mPa.s and c/c^*=0.5 (►). Solid lines represent the fits to the experimental data.

For the case of PEO with a molecular weight of $M_w = 1\times10^6$ g/mol, the relaxation time for a solution viscosity with shear viscosity of $\eta_0 = 6$ mPa.s was found to be $\lambda_E = 0.4$ ms. The relaxation time increased to $\lambda_E = 0.72$ ms as the shear viscosity of the solution was increased to $\eta_0 = 22$ mPa.s. Similarly, for PEO with molecular weight of $M_w = 600$k g/mol, the relaxation time for a solution with a shear viscosity of $\eta_0 = 6$ mPa.s was found to be $\lambda_E = 0.42$ ms and $\lambda_E = 0.8$ ms for a solution with a shear viscosity of $\eta_0 = 22$ mPa.s. A reduction of close to a factor of four was observed for the relaxation times measured for the lower molecular weights polymer solutions as compared to the higher molecular weights polymer solutions. Similar trends were observed for the lower molecular weights polymer solutions where for the case of PEO with molecular weight of

$M_w = 100$k g/mol, the relaxation time for a solution with shear viscosity of $\eta_0 = 6$ mPa.s was found to be $\lambda_E = 0.045$ ms. The relaxation time increased to $\lambda_E = 0.13$ ms as the shear viscosity of the solution was increased to $\eta_0 = 22$ mPa.s. From theory it has been shown that the relaxation time of a dilute polymer solution should increase linearly with the viscosity as shown in equation 1.8, a linear increase with solvent viscosity was observed for all of our experimental measurements. According to kinetic theory, the longest relaxation time of an isolated polymer coil in dilute solution is proportional to the solvent viscosity as [80, 110]

$$\lambda_z = \frac{1}{U_{\eta\tau}} \frac{[\eta]\eta_s M_w}{RT}. \tag{0.8}$$

Where $U_{\eta\tau} = \lambda_\eta / \lambda_o$ is the universal ratio of the characteristic relaxation time of a dilute polymer solution system λ_η and the longest relaxation time λ_0. In addition, M_w is the molecular weight, η_s, is the solvent viscosity, $[\eta]$ is the intrinsic viscosity, R is the universal gas constant and T is the absolute temperature. The numerical value of the universal ratio depends on the relaxation spectrum of the specific constitutive model [80]. Given the molecular weight dependence of the intrinsic viscosity for PEO in water and glycerol as shown earlier, the Zimm model can be used to compare the dependence of the relaxation time on the molecular weight of the PEO. For a constant solvent viscosity, the relaxation time for the PEO should scale with molecular weight as $\lambda_z \propto M_w^{1.65}$. In our experiments, a power law dependence of $\lambda_E \propto M_w^{1.4}$ was observed. This value is close, but does not precisely match the predictions of the Zimm theory as seen in Figure 17b. It is important to note that a similar discrepancies between the Zimm theory and experimental measurements have

been observed in the past by Tirtaamadja et al. [85] and others. In their experiments, the relaxation time of a series of different molecular weights of PEO in glycerol/water mixtures was measured by monitoring a droplet formation from a nozzle due to gravity. Although they do not quantify it, a scaling of $\lambda_{Eff} \propto M_w^{1.2}$ can be fit to their data. As with the measurements here, the measured value of the power-law coefficient was less than the value predicted by the Zimm model. As we will discuss in detail later, this discrepancy is likely due to the fact that even though these solutions all have polymer concentrations less than coil overlap concentration, c^*, they are not truly dilute in extensional flows until the reduced concentration is below $c/c^* < 10^{-4}$ [80]. Thus the Zimm scaling in Equation 1.8 may not hold in extensional flows until the concentration becomes extremely small, $c/c^* < 10^{-4}$.

The effect of solution viscosity on the evolution of the apparent extensional viscosity, η_E, as a function of strain, ε, can be found in Figure 18. An important point to note here is that the strain reported in figure 18, which is defined as $\varepsilon = 2\ln(R_0 / R(t))$, depends heavily on the value of the initial radius, R_0, used to define it. The strain therefore requires a consistent and repeatable choice for R_0. One possibility is to choose the radius of the syringe tip which can be made a priori without knowledge of the fluid rheology. Here, however, we chose to use the radius at which the dynamics of the filament decay begins to transition from an inertia-capillary to an elasto-capillary flow. This transition point is defined as the radius at which the Weissenberg number becomes greater than $Wi = ½$. This is a more physically correct choice for R_0 because, at larger radii, the Weissenberg number is less than $Wi < ½$ and no appreciable strain is accumulated in the polymer chains. However, for radii smaller than $R < R_0$, strain is continuously accumulated in the polymer

chains up until the point of filament failure. Using equations 1.3, 1.5 and 1.6, a value for R_0 becomes $R_0 = 1.23\left(\lambda_E{}^2\sigma/\rho\right)^{1/3}$ [97, 98, 110]. The only downside to this choice is that extensional relaxation time of the fluid must be measured from the data before the strain can be determined, however, because all the data presented here had a measurable relaxation time, this was not an issue.

In Figure 27, an increase in the extensional viscosity was observed with increasing strain for all solutions tested. At large strains, the extensional viscosity in each case approached a steady-state value signifying that the polymer chains had reached their finite extensibility limit. At this point, the resistance to filament thinning is not viscoelastic but rather returns to a viscous response albeit with a viscosity several orders of magnitude larger than the zero shear viscosity [97]. For the case of PEO with molecular weight of $M_w = 1\times10^6$ g/mol, a steady state extensional viscosity of $\eta_E = 8$ Pa.s and $\eta_E = 3$ Pa.s were observed for a solution with shear viscosities of $\eta_0 = 22$ mPa.s and $\eta_0 = 6$ mPa.s respectively. The resulting Trouton ratio, $Tr = \eta_E/\eta_0$, was between $Tr \approx 400$ and $Tr \approx 500$ for all the high molecular weight PEO solutions tested. This value is much larger than the Newtonian limit of Tr =3 showing the degree of strain hardening by these high M_w PEO solutions. Additionally, a roughly linear increase in the value of the steady state extensional viscosity with increasing solution viscosity was observed for each of the different molecular weight PEOs tested. The result was a collapse of the data when the Trouton ratio was plotted as a function of Hencky strain for a given molecular weight obtained at fixed concentration but variable shear viscosity. These trends with solvent

viscosity conform to the predictions of the FENE-P model as long as the value of the steady state Trouton ratios are significantly larger than Tr =3.

Note that in Figure 27, both the reduced concentration and the molecular weight were varied between subfigures. Here, the reduced concentration of the lowest molecular weight samples was purposefully increased in order to obtain coherent filaments from which clean extensional viscosity measurements could be extracted. In fact, unlike the $M_w = 1\times10^6$ g/mol PEO solutions at c/c^*=0.02, measurements of extensional rheology for the $M_w = 100$k g/mol at c/c^*=0.02 did not result in the formation of a viscoelastic filament, but broke up without transitioning from an inertia-capillary decay. Thus a natural lower limit in the measurable extensional viscosity of about $\eta_E = 0.1$ Pa.s was obtained, although we will show in the sections that follow that this is not truly a lower limit on extensional viscosity, but a lower limit on extensional relaxation time as the transition radius described above gets smaller and smaller with decreasing extensional relaxation time and eventually becomes so small that it cannot be resolved optically.

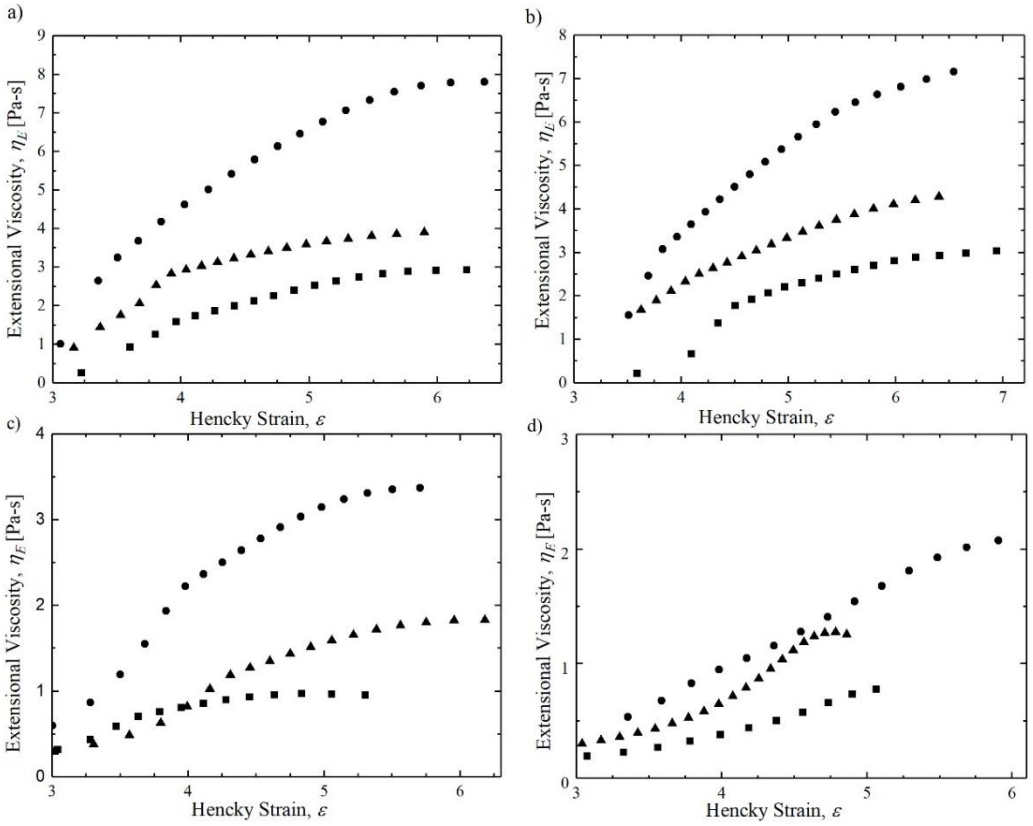

Figure 27. Plot of extensional viscosity, η_E, as a function of strain, ε, for a series of PEO solutions in glycerin and water with a) molecular weight of M_w =1x10^6 g/mol and a reduced concentration of c/c^*=0.02, b) M_w =600k g/mol and c/c^*=0.03, c) M_w =200k g/mol and c/c^*=0.05 and d) M_w =100k g/mol and c/c^*=0.08 at solution viscosity of η_0=6 mPa.s (■),η_0=10 mPa.s (▲) and η_0=22 mPa.s (●).

3.3.2 CaBER-DoS of PEO solutions with a fixed solution viscosity $\eta_0 = 6\text{mPa.s}$ and varying *c/c** and M_w

Similar to the discussions in the last section, CaBER-DoS results for a series of PEO solutions with varying polymer concentration and molecular weight are presented in this section so that trends for each of these parameters can be identified and compared to theory. Once a relation has been established, the relationship can be used to extrapolate the data to lower concentration or lower M_w solution which are not measurable using CaBER-DoS technique. In all cases, the concentration levels of the PEO were maintained in the dilute region, $c/c^* < 1$, so that the results could be compared against dilute theory. In this subsection, results are presented for values of reduced concentration varying from, c/c^*=0.004 to 0.5, but with the shear viscosity fixed at $\eta_0 = 6$ mPa.s . A small subset of the CaBER-DoS results are presented in Figures 19 and 20 for solutions of PEO with each sub figure corresponding to a fixed molecular weights of $M_w = 1\text{x}10^6$, $6\text{x}10^5$, $2\text{x}10^5$, and $1\text{x}10^5$ g/mol.

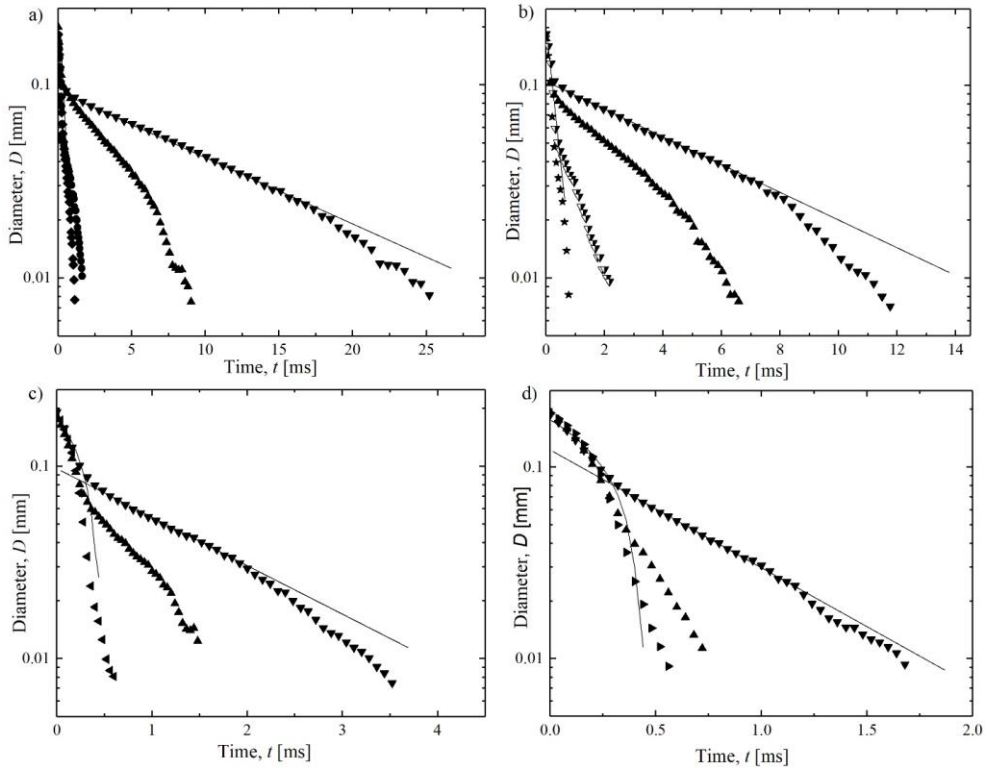

Figure 28. Plot of diameter, D, as a function of time, *t*, for a series of PEO solutions in glycerin and water at a fixed solution viscosity of η_0=6 mPa.s and molecular weight varying from a) M_w =1x10^6 g/mol, b) M_w =600k g/mol, c) M_w =200k g/mol and d) M_w =100k g/mol. In each subfigure, reduced concentration is varied from *c/c=0.004 (♦), *c/c**=0.005(★), *c/c**=0.02 (●), *c/c**=0.03 (▽), *c/c**=0.05 (◄), *c/c**=0.08 (►), *c/c**=0.1 (▲) and *c/c**=0.5(▼). Solid lines represent the inertia-capillary and elasto-capillary fits to the experimental data from theoretical predictions.**

The diameter decay as a function of time is plotted in Figure 28 for each of the four different molecular weight PEO solutions tested. In each subfigure, the diameter decay is shown as a function of reduced concentration at a fixed solution viscosity. For a given molecular weight, an increase in the reduced concentration was found to result in an increase in both the relaxation time and, subsequently, the time required for the filament to breakup. The increased relaxation time can be seen qualitatively as a decrease in the slope of the linear region of the data in this semi-log plot. The breakup times of the filaments

were greatly affected by both the concentration and molecular weight. For the highest molecular weight PEO tested, the breakup times were an order of magnitude larger than the lowest molecular weights PEO tested at the same reduced concentration. The sensitivity of the break up time to change in concentration was not as strong as to molecular weight. For instance, a tenfold increase in the breakup time could be induced by increasing the molecular weight by a factor of roughly six at a given reduced concentration. However, to achieve the same tenfold increase in the break up time at a fixed molecular weight required an increase in the reduced concentration by a factor of one hundred.

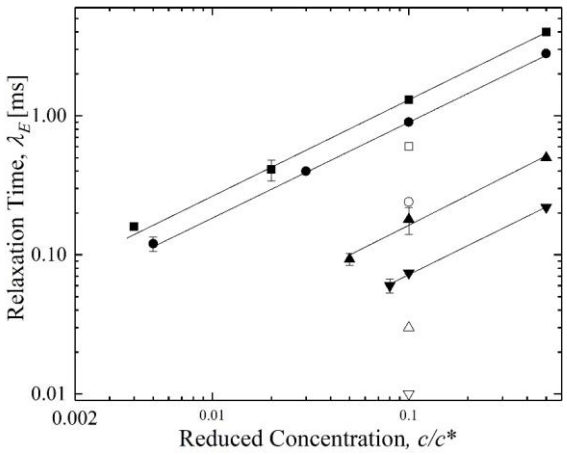

Figure 29. Plot of extensional relaxation time, λ_E, as a function of reduced concentration, *c/c, for a series of PEO solutions in glycerin and water at fixed shear viscosity of η_0=6 mPa.s with a molecular weight of M_w =1x10^6 g/mol (■), M_w =600k g/mol (●), M_w =200k g/mol (▲) and d) M_w =100k g/mol (▼). Solid lines represent a power law fit to the data having the form $\lambda_E \sim (c/c^*)^{0.7}$. The hollow symbols shows the Zimm time at η_0=6 mPa.s for the molecular weight of (□) M_w =1x10^6 g/mol, (○) M_w =600k g/mol, (△) M_w =200k g/mol and (▽) M_w =100k g/mol.**

In Figure 29, the relaxation time, λ_E, is presented as a function of reduced polymer concentration, *c/c**, for a series of PEO solutions in glycerin and water at a fixed shear viscosity of η_0=6 mPa.s. One can observe that, with an increase in the reduced

concentration, an increase in the relaxation time was observed. For the case of PEO with molecular weight of $M_w = 1\times10^6$ g/mol, the relaxation time increased from λ_E =0.16 ms to 0.4 ms as the reduced concentration was increased from $c/c^* = 0.004$ to 0.5. These relaxation times are similar to those measured by Dinic et al. [88, 89] using the CaBER-DoS technique for a similar $M_w = 1\times10^6$ g/mol aqueous PEO solution. Note that below a concentration of *c/c**=0.004, a viscoelastic filament could not be observed given the limitations in the temporal and spatial resolution of our high speed camera. Similar trends observed for each of the different molecular weight PEO solutions tested. With increasing molecular weight, the relaxation time measured for a given concentration was found to decrease. Additionally, the minimum concentration that could be characterized using CaBER-DoS was found to increase quite significantly with decreasing molecular weight as the cut-off appears to be limited by a minimum relaxation time of just below $\lambda_{\min} \approx 100\mu s$ that can be confidently characterized using CaBER-DoS.

For the case of PEO with molecular weight of M_w =100k g/mol, the relaxation time was found to increase from λ_E =0.06 ms to 0.22 ms as the reduced concentration was increased from $c/c^* = 0.08$ to 0.5. For this molecular weight, the minimum concentration that could be characterized in CaBER-DoS was twenty times larger than that of the highest molecular weight sample. The increase in the relaxation time for all the different molecular weights PEO solutions tested was found to have power law dependence on the reduced concentration such that $\lambda_E \propto (c/c^*)^{0.7}$. Similar observation were made by Dinic et al. [88] where they observed a power law dependence of relaxation time on reduced

concentration as $\lambda_E \propto (c/c^*)^{0.65}$ for their set of measurements on a series of aqueous PEO solution of a single molecular weight of, $M_w = 1\times10^6$ g/mol [88]. Tirtaamadja et al. [85] also observed a power law dependence of the relaxation time on reduced concentration as $\lambda_E \propto (c/c^*)^{0.65}$ for their set of measurements on a series of PEO in water/glycerol solution. This observation is counter-intuitive because according to equations 1.8, the relaxation time of isolated coils within dilute solution should be independent of the concentration. Clasen et al. [80] also noted a dependence of the longest relaxation time in extension on the reduced concentration, c/c^*. They rationalized this by noting that the polymer viscosity can have a concentration dependence depending on the model used. For instance, using the Martin equation, Clasen et al. [80] were able to fit the relaxation time data to an exponential dependence on the reduced concentration predicted by the Martin equation. This model also showed that the concentration dependence should disappear as one moves farther and farther from the critical overlap concentration into the ultra-dilute regime where the relaxation time measurement was found to approach the Zimm relaxation time. Compared to the results of Clasen et al. [80], the range of concentrations for our working fluids in Figure 29 may be too narrow to observe a true dilute response as the data in Figure 29 do not appear to reach an asymptotic limit. From Clasen et al. [80], it is clear that only for reduced concentrations less than $c/c^* < 10^{-4}$ can a truly dilute value of the extensional relaxation be recovered. Thus, even though under quiescent conditions all of the PEO solutions studied in the present work were well within the dilute regime, $c/c^*<1$, when deformed by an extensional flow the fluids all appear to exhibit semi-dilute solution behavior. This semi-dilute behavior arises from chain-chain interactions resulting from the increase in pervaded volume of the stretched chain. Thus, even though $c/c^*<1$, excluded

volume interaction between neighboring chains can become important. Using semi-dilute theory [111], Dinic et al. [88] showed through an alternate theoretical approach to Clasen et al. [80] that a power law dependence similar to that observed experimentally here, $\lambda_E \propto (c/c^*)^{0.7}$, could be rationalized.

An important final observation from Figure 29 should be made. From Figure 29 it is clear that the measured relaxation time do not asymptote to the Zimm relaxation time as the concentration was reduced. For the low molecular weight cases, M_w =100k g/mol and 200k g/mol, all the values of the measured relaxation time were larger than the Zimm relaxation time. However, for both the higher molecular weight PEOs cases, M_w =1x10^6 g/mol and 600k g/mol, the measured relaxation times were found to decrease with decreasing concentration and, at the lowest concentrations tested, were measured to be smaller than the Zimm relaxation time. For the case of M_w =1x10^6 g/mol and 600k g/mol, the Zimm relaxation time is λ_z =0.6 ms and λ_z =0.24 ms respectively for reduced concentrations less than c/c^*<0.01. The value of the Zimm relaxation time for all the fluids tested here are presented in Table 2. Note that there are a number of differences between these CaBER experiments and the conditions under which the Zimm model predictions of relaxation time are made. First, the relaxation time predicted by the Zimm model is the shear relaxation time and these measurements are of the extensional relaxation time. Second, and perhaps more importantly, the Zimm model predictions assume a small deformation of the polymer chains, while the extensional flow studied here can result in a nearly fully extended polymer chain. Thus, it is not unreasonable to expect that differences would be observed between the Zimm relaxation time and the extensional relaxation time measured through CaBER.

It is important to note here that these relaxation time measurements do not appear to be in error. Each experiment were repeated multiple times and the exponential fits to the data used to determine the relaxation times were fit to between 10-20 pts of data over nearly a decade of time and diameter variation. Clasen et al. [80] observed similar trend and argued that for the cases where $\lambda_E < \lambda_z$ that the data was interpreted incorrectly. They fit their data with the assumption that the finite extensibility limit had been reached during the inertia-capillary decay and thus the relaxation time measurement were in error. Unfortunately, this argument does not hold for our data for several reasons. As seen in Figure 30, the filaments in our experiments, even as the relaxation time was found to drop below that predicted by the Zimm model, bore the expected cylindrical shape of an elasto-capillary thinning.

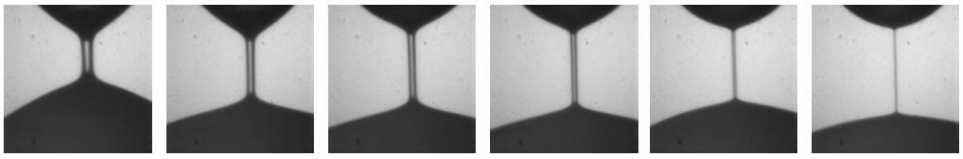

Figure 30. A sequence of images showing the formation of a slender filament and subsequent thinning for a PEO of M_w =1x10^6 g/mol at c/c^*=0.02 and shear viscosity of η_0=6 mPa.s.

In addition, following the experimental decay in the diameter as in Figures 25 and 28, a deviation was observed at late time which is clearly the onset of the finite extensibility limit well after the relaxation time has been fit to the data. Finally, it should be noted that all of the concentrations used in our experiments were an order of magnitude higher than the theoretical minimum concentration, c_{low}, above which theory predicts that a true

elasto-capillary balance should be observable [97]. We are thus confident in the measurements of relaxation time and note that similar values of relaxation times in extensional flows have been observed in the past both in Clasen et al. [80] and Bazilevskii et al. [112]. The reason for these observations is still not fully understood, but requires further theoretical development along with and further experimental testing and development of this and other techniques to probe smaller and smaller concentrations and extensional relaxation times.

Table 2. Zimm relaxation times for the PEO solutions.

Molecular Weight M_w =1x10^6 g/mol		Molecular Weight M_w =600k g/mol		Molecular Weight M_w =200k g/mol		Molecular Weight M_w =100k g/mol	
Solution Viscosity [mPa.s] η_0	Zimm time, λ_z [113]	Solution Viscosity [mPa-s] η_0	Zimm time, λ_z [113]	Solution Viscosity [mPa-s] η_0	Zimm, time, λ_z [113]	Solution Viscosity [mPa-s] η_0	Zimm time, λ_z [113]
				1	0.006	1	0.0016
6	0.6	6	0.27	6	0.03	6	0.01
10	1.1	10	0.45	10	0.06	10	0.018
22	2.4	22	0.95	22	0.14	22	0.04

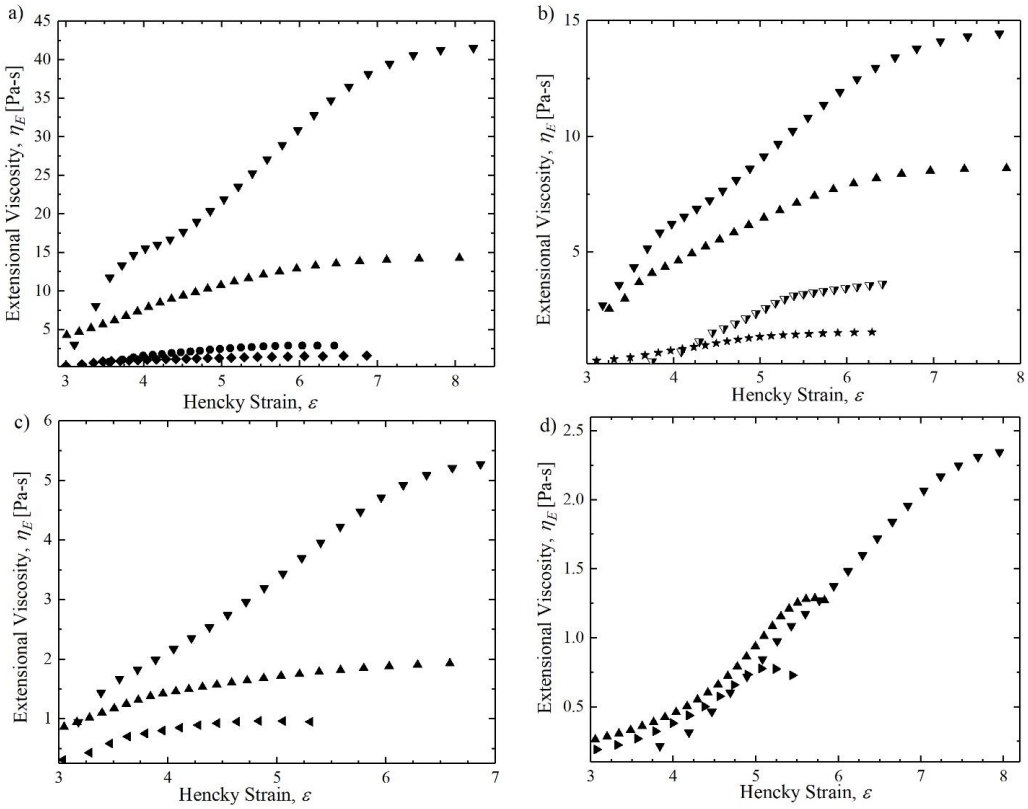

Figure 31. Plot of extensional viscosity, η_E, as a function of Hencky strain, ε, for a series of PEO solutions in glycerin and water at fixed shear viscosity of η_0=6 mPa.s with a molecular weight of a) M_w =1x10^6 g/mol, b) M_w =600k g/mol, c) M_w =200k g/mol and d) M_w =100k g/mol. The reduced concentration is varied from *c/c=0.004 (♦), *c/c**=0.005 (★), *c/c**=0.02 (●), *c/c**=0.03 (▽), *c/c**=0.05 (◄), *c/c* *=0.08 (►), *c/c**=0.1 (▲) and finally to *c/c**=0.5 (▼).**

In Figure 31, the extensional viscosity, η_E, is plotted as a function of Hencky strain, ε, for a series of PEO solutions in glycerin and water at fixed shear viscosity of η_0=6 mPa.s and varying reduced concentration, *c/c** and molecular weights, M_w. In all cases, a steady-state extensional viscosity was reached at large values of Hencky strain. For the case of PEO with molecular weight of M_w=1x10^6 g/mol, the steady-state extensional viscosity observed varied from η_E=1 Pa.s to 40 Pa.s as the reduced concentration was

varied from *c/c**=0.004 to 0.5. Trouton ratios in the range of $Tr = 10^2 - 10^4$ are observed for the highest molecular weight PEO. Similar variations were observed for all the molecular weight tested. For the case of lowest molecular weight PEO tested, $M_w = 100\text{k g/mol}$, the steady state extensional viscosity observed varied from $\eta_E = 0.7$ Pa.s to 3 Pa.s as the reduced concentration was varied from *c/c**=0.08 to 0.5. This corresponds to Trouton ratios of the order of roughly $Tr \approx 10^2$. As observed from the diameter decay in Figure 25, at later times a deviation from the viscoelastic exponential fit was observed.

3.3.3 A method for extending CaBER-DoS to make micro-seconds relaxation time measurements

In this section, a new approach to extend CaBER-DoS beyond the inherent limitations of the technique in order to make relaxation time measurements on the order of micro-seconds by taking advantage of the sharp transition between the inertia-capillary dominated thinning at early time and the elasto-capillary dominated thinning at later times is presented. As shown in the previous sections, CaBER-DoS can measure relaxation times greater than λ_E =0.1 ms without running into any temporal or spatial resolution limits of the chosen high speed camera. This is true independent of the solutions shear viscosity. However, the relaxation times were driven down even further by decreasing the shear viscosity of the solution or decreasing molecular weight of the polymers. The resulting rheological measurements were limited by the temporal resolution which limited the number of data points that could be captured in the elasto-capillary region and the spatial resolution which limited the minimum size filament that could be accurately resolved. To directly measure the relaxation time, an exponential decay must be fit to the diameter decay

data in the elasto-capillary thinning regime. In order for this fit to be accurate, a minimum of 5-10 data points is required. Here we show that a full exponential fit is not necessary to measure the relaxation time. In fact, in order to make relaxation time measurements for extremely low viscosity-low elasticity solutions only a single data point in the elasto-capillary region needs to be captured, thus increasing the resolution of CaBER-DoS by a full order of magnitude. This extension of CaBER-DoS takes advantage of the sharp transition between the inertia-capillary and the elasto-capillary thinning to define an experimentally observed transition radius, R^*. By calibrating the experimentally observed transition radius against the transition radius predicted from theory, R^*_{theory}, we demonstrated that an empirical correlation between the experimentally observed transition radius and the relaxation time can be formed. This finding significantly enhanced the resolution and sensitivity of the relaxation time measurements obtainable through CaBER-DoS.

Thinning dynamics of low viscosity dilute polymer solutions with Ohnesorge number, $Oh<0.2$ are known to be dominated by inertial decay [105]. As the diameter decays, the extension rates can eventually become large enough that the polymer chains to under-go a coil-stretch transition. This is known to occur for Weissenberg numbers greater than $Wi>1/2$. At these Weissenberg numbers, elastic stresses will grow with increasing accumulated strain. As they grow, the elastic stresses will become increasingly important to the flow and will eventually dominate the breakup dynamics of the liquid bridge [105]. In a CaBER experiments of an Oldroyd-B fluid, the thinning dynamics of the liquid bridge are known to occur at a constant Weissenberg number of $Wi = 2/3$. Thus, a reasonable approach taken by a number of previous groups [97, 98, 110] to determine the transition

point is to assume that the transition from inertio-capillary to elasto-capillary flow occurs when the extension rate induced by the intertio-capillary flow grows to $\dot{\varepsilon} = 2/3\lambda_E$. Using this value of the extension rate in combination with Equations 1 and 4, a relation for the theoretical transition radius can be obtained,

$$R^*_{\text{theory}} = 1.01\left(\frac{\lambda_E{}^2\sigma}{\rho}\right)^{1/3}. \tag{0.9}$$

If equation 1.9 is valid, the extension relaxation time can be estimated by measuring the initial radius of the cylindrical filament that is characteristic of the elasto-capillary flow. An example of a radial decay showing the transition between inertia-capillary and elasto-capillary thinning is shown in Figure 32. From the data in Figure 32, one can independently determine the experimental transition radius, R^*, from the intersection of the inertia-capillary and elasto-capillary region of the radial decay and the relaxation time from the late stage exponential decay of the data.

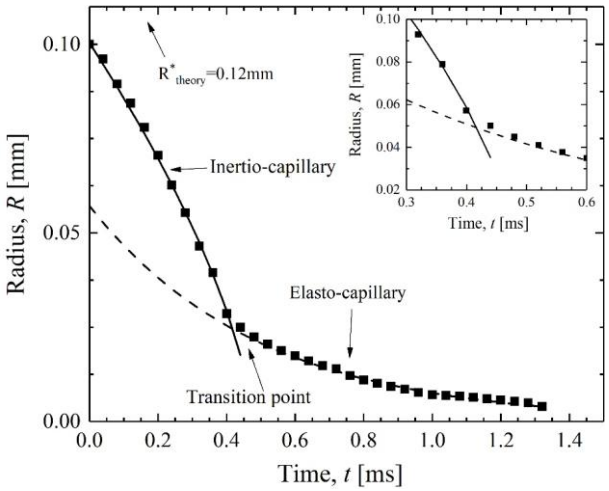

Figure 32. Radial decay, *R*, as a function of time, *t*, for the PEO of molecular weight M_w =1x10^6 g/mol in water at a reduced concentration of *c/c=0.05 and shear viscosity of η_0=1 mPa.s (■) showing the transition from an inertia dominated thinning to an elasticity dominated thinning. Solid lines represents the inertial (—) and exponential fits (- -) to the experimental radius. An inset figure is provided with the magnified image to demonstrate the sharpness of the transition point.**

By comparing the theoretical transition radius obtained from equation 1.9 and the experimentally determined transition radius, it can be seen from Figure 32 that the theoretical transition radius predictions was significantly larger than the experimentally measured value. From the data presented in Figure 32, for a PEO solution with $M_w = 1\times10^6\,\text{g/mol}$, $\eta_0 = 1\,\text{mPa.s}$ and *c/c**=0.05, the transition radii were found to be $R^*_{theory} = 0.12\text{mm}$ and $R^* = 0.022\text{mm}$. The magnitude of the theoretical over prediction in the transition radius was found to be consistent across molecular weight, shear viscosity and reduced concentration. If one takes the ratio of the experimental and theoretical transition radius, a correction factor can be found such that $\beta = R^* / R^*_{theory}$ =0.18. Similar values of the correction factor, β, were observed for all the PEO solutions tested. The average correction factor for all the PEO solution data was found to be $\beta = 0.18 \pm 0.01$. The small size of the uncertainty in the correction factor data is remarkable given the data spans several orders of magnitude in M_w, η_0 and c/c^*. Additionally, it gives us confidence that an experimentally observed transition radius can be used to predict the relaxation time of low viscosity and low concentration PEO solution by capturing just a single data point. Rewriting equation 1.9 in terms of the experimentally observed transition radius, R^* by using the average correction factor $\beta = 0.18$ as

$$\lambda_E = 13.1\left(\frac{R^{*3}\rho}{\sigma}\right)^{1/2} \tag{0.10}$$

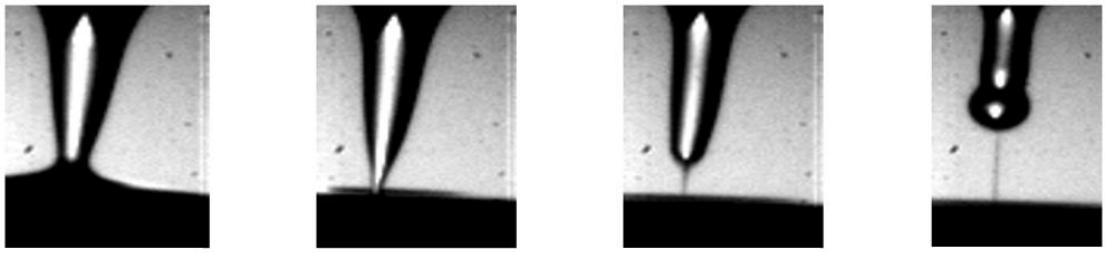

Figure 33. Filament thinning dynamics of an aqueous solution of PEO with a molecular weight of M_w =200k g/mol at a reduced concentration of c/c^*=0.05 and a shear viscosity of η_0=1 mPa.s. Images were captured at 50,000 frames per seconds.

An example showing the power of this technique is shown in Figure 33 for CaBER-DoS breakup of a PEO with molecular weight of M_w =200k g/mol, and reduced concentration of c/c^*=0.05 in water with η_0=1 mPa.s. Note that in the images in Figure 33, the breakup of the fluid is in the inertia-capillary regime up until the last two frames. At time t = 0.18 ms, hints of a cylindrical filament can be seen and at t = 0.22 ms a clear cylindrical filament is produced. From those two images and the last $t = 40\ \mu s$ of the data, the relaxation time of the fluid can be calculated from equation 1.10. For this fluid, the extensional relaxation time was found to be $\lambda_E = 22\ \mu s$. A similarly late stage cylindrical filament was observed for M_w =100k g/mol PEO in water at c/c*=0.08. For that solution, the extensional relaxation time calculated using equation 8 was found to be $\lambda_E = 20\ \mu s$. To demonstrate the viability of our technique for that the relaxation time data for the 100k g/mol PEO solution was superimposed over the relaxation time data in Figure 26a obtained through the standard exponential fit to the time diameter decay data. As can be seen in Figure 26a, the relaxation time obtained with our experimental technique fits quite nicely

in the trend line extrapolated from the higher relaxation time data. Given the maximum magnification of our high speed camera setup, the minimum resolvable radius can be used to calculate a theoretical lower limit of the relaxation time can be determined directly from equation 8. For a solution with water as the solvent and a minimum radius of R_{min} = 5 μm equivalent to a single pixel, a minimum relaxation time of $\lambda_E = 17\ \mu s$ can be measured here. However, further improvements can be made with an increase in the magnification, speed, and resolution of the high speed camera and optics. Perhaps with increased improvements a better understandings of the differences observed between these extensional rheology measurements and the predictions of the Zimm theory can be obtained.

Although, the empirical correction factor β appears to do an adequate job at rectifying the observed differences between the observed transition radius and radius predicted by theory, it is desirable to obtain a better understanding of the origins of these differences and perhaps put them into a theoretical framework that allows us to derive β directly from theory. Here we direct the readers to an excellent paper by Wagner et al. [109]. In this paper, Wagner et al. [109] showed in great detail the transition between breakup regimes in CaBER measurements. Using a FENE-P constitutive model, they were able to calculate the diameter evolution and better understand transition between regimes. They demonstrated, that it is not the Weissenberg number that dictates the transition to elasto-capillary decay, but the level of the elastic extensional stresses. Beyond a Weissenbeg number of $Wi > 1/2$ elastic stresses are built up as strain is accumulated in the polymer chains in solution. Wagner et al. [109] demonstrated that the transition to elasto-capillary flow occurs when the elastic stresses become comparable in magnitude to the viscous and/or inertial contributions from the solvent. Using the FENE-P model, Wagner

et al. [109] were able to derive an analytical solution for the transition radius and the transition time by considering the point at which the visco-capillary or inertia-capillary and elasto-capillary balances hold simultaneously. Their calculations were in excellent agreement to their experimental data. It is important to note, however, that although this analysis is quite powerful when enough data is available in the elasto-capillary regime to fit the exponential decay and independently determine the values of the finite extensibility, *b*, plateau modulus, *G* and relaxation time, λ, for our experiments, where only a single data point is available in the elasto-capillary region, it is not possible to calculate the longest relaxation time using Wagner et al. [109] analysis without already knowing the elastic modulus and finite extensibility through other measurements. That being said, their work clearly explains the need for the correction factor, β, as the overshoot in the extension rates beyond $Wi = \lambda\dot{\varepsilon} > 2/3$ and the reduction in measured transition radius compared to theory was shown to be the direct result of the need to build up adequate elastic stress.

Using the CaBER-DoS technique, this overshoot in the extension rate beyond *Wi* = 2/3 can be studied and is presented in Figure 25a. The extension rate as a function of accumulated strain for three different concentration of PEO with M_w =200k g/mol is shown for a solution with shear viscosity of $\eta_0 = 6$ mPa.s. The first observation is that the extension rate observed for all three solutions was found to overshoot well past *Wi*=2/3. In all cases, *Wi*=2 was achieved before sufficient elastic stress was built up in the filament to slow the extension rate slowed back to the expected CaBER value of *Wi*=2/3. The form of the extension rate variation with time for the three cases presented in Figure 34 and in fact all the cases studied was quite similar. If the data were normalized with relaxation time and replotted as *Wi*, they quite nearly collapse into a single curve as shown in the inset of Figure

34a. The form was also consistent with changes in molecular weight and solvent viscosity. As seen in Figure 34b, the magnitude of extension rate overshoot was found to increase linearly with the inverse of relaxation time of the solutions. The average Weissenberg number observed during the extension rate overshoot for all the PEO solutions tested was found to be $Wi_{averge} = 1.7 \pm 0.1$. From our parametric study it has also been observed that the average Hencky strain accumulated during the extension rate overshoot was $\varepsilon_{average} = 3$. This strain accumulated during the overshoot account for the difference between the theoretical and experimentally measured transition radii.

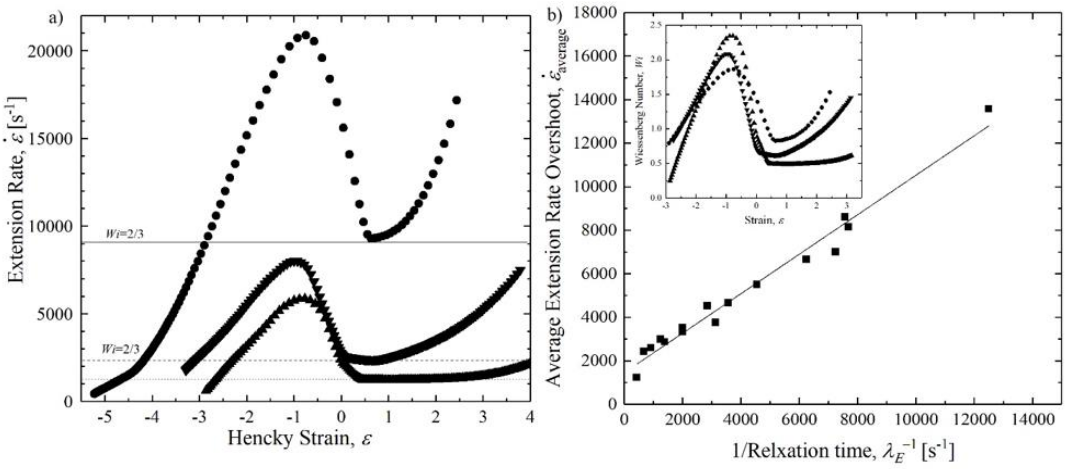

Figure 34. (a) Plot of the extension rate, $\dot{\varepsilon}$ as a function of Hencky strain, ε, for a PEO solution with molecular weight of M_w =200k g/mol at reduced concentrations of c/c^*=0.05 (●), c/c^*=0.1 (▼) and c/c^*=0.5 (▲) and shear viscosity of η_0=6 mPa.s showing the overshoot beyond the expected Wi=2/3 decay at the transition from the inertia-capillary to the elasto-capillary regimes. Horizontal lines represents the Weissenberg number Wi=2/3 for c/c*=0.05 (solid line), c/c^*=0.1 (--) and c/c^*=0.5 (··), (b) Plot of the average extension rate overshoot , $\dot{\varepsilon}_{average}$, as a function of inverse of relaxation time, $1/\lambda_E$, for a series of PEO solution in glycerin and water with varying molecular weight, solution viscosity and reduced concentration. The inset Figure in 11b shows the plot of Weissenberg number Wi as a function of strain, ε.

3.3 Conclusion

The filament breakup process of a series of dilute PEO solutions of varying molecular weight, shear viscosity and reduced concentration using the Dripping onto Substrate Capillary Breakup Extensional Rheometry (CaBER-DoS) was investigated. For the low viscosity fluids, at early times during the stretch viscous and elastic stresses are irrelevant for Wi<1/2 and thus the dynamics are controlled by the inertia-capillary balance. However, as the time approaches the cutoff time t_c, the extension rate can grow large enough such that Wi >1/2 and as a result of this significant polymer chain extension, the elastic stresses grows to match the capillary pressure, preventing the neck from breaking off. In CaBER-DoS, the stretching happens at a constant extension rate of $\dot{\varepsilon} = 2/3\lambda$.

Scaling laws were established for the variation of extensional relaxation time as a function of reduced concentration, molecular weight and solution shear viscosity. The extensional relaxation time, λ_E was calculated through an exponential fit to the diameter decay data in the elasto-capillary thinning regime. In order for this fit to be accurate, a minimum of 5-10 data points is required. Most of the trends were found to be in accordance with the theory and thus these scaling relations can be used for extrapolating data for low viscosity, concentration and molecular weight PEO solutions. However, unlike the predictions of theory the measured extensional relaxation time at extremely low concentration did not agree with the predictions of Zimm theory, but significantly under predicted it.

As discussed in earlier sections, this transition from an initial power law decay to the late stage exponential decay was found to be extremely sharp. By taking advantage of this sharp transition, the resolution and sensitivity of the CaBER-DoS technique were significantly enhanced and extensional relaxation time close to ten microseconds was measured within the limits of the spatial and temporal resolution of our optics and high speed camera. A consistent correction factor $\beta = R^* / R^*_{theory} = 0.18$ was found using the experiments performed on high viscosity and molecular weight PEO solutions. Here, R^* is the experimental transition radius and R^*_{theory} is the theoretical transition radius. Using this correction factor an empirical relation was derived which was used to predict the extensional relaxation time of low viscosity and low concentration PEO solution by capturing just a single image showing a cylindrical filament. The minimum extensional relaxation time that was calculated using the correction factor β for one of our

experiments on a PEO solution was found to be $\lambda_E = 20\ \mu s$. Through our empirical relation the lower limit of the minimum measured extensional relaxation time available in the literature was further pushed but further improvements are still required so that full characterization of ultra-dilute solution with smaller and smaller relaxation times can be characterized.

3.4 Publication

The work described in this chapter has been published in the Journal Of Rheology. The complete reference is S Sur and J P Rothstein, “Drop breakup dynamics of dilute polymer solutions: Effect of molecular weight, concentration, and viscosity, Journal Of Rheology, (2018)”

CHAPTER 4

DRIPPING-ONTO-SUBSTRATE CAPILLARY BREAKUP EXTENSIONAL RHEOMETRY OF LOW-VISCOSITY PRINTING INKS

4.1 Introduction

In many industrial processes, a wide range of printing and patterning technologies are currently being used to deposit well-defined 2D and 3D patterns of polymeric fluids onto both static and moving substrates. Innovations in printing technologies like inkjet printing have opened up a wide range of application spaces beyond their classical use in printing documents, photos and magazines. More recently these printing techniques have been extended to manufacture solar panel, electronics, optical devices and functional biomaterials [114-116]. Inkjet printing technologies can be separated into two classes: drop-on-demand (DOD) and continuous injket (CIJ) [115, 116]. In the first, individual drops are created from pressure or displacement pulses from within the nozzle. In the second, a continuous jet is produced and allowed to break up into drops. In this way, a continous stream of drops is produced with the excess unneeded drops deflected into a gutter through either electrostatics or aerodynamics.

In order to understand the dynamics of either of these inkjet processes, one requires a deep understanding of the capillary breakup phenomena and of the rheology of the inkjet fluids. This is because the composition of inkjet fluids can be quite complicated with the relatively large fractions of low molecular weight polymers, particles and dyes added to the final composition. The addition of a polymer binders to a solution is especially relavent to jetting as it can make the ink weakly elastic resulting in some dramatic changes to the drop impact and filament breakup dynamics. For instance, satellite droplets in drop-on-

demand devices can be eliminated by adding polymer to the solution, but that comes with a significant breakup delay [117]. Consequently, architecture, concentration and molecular weight of a polymer into the solution must be chosen wisely. Unfortunately, the low viscosity, weak elasticity and extremely short relaxation times of most commercial ink jet fluds have made them extremely challenging to characterize rheologically. The influence of polymers concentration on drop formation and filament breakup has been widely studied both experimentally and numerically for more elastic monodisperse polymer solutions in the dilute regime up to the coil overlap concentration, c^* [117, 118]. These studies found that such flows typically involve high extension rates which can result in a strong increase in the transient extensional viscosity of the polymeric fluid. The observable consequence of which has been shown to be the formation of long fluid threads [119, 120] and a significant increase in the time required for the filament to break up into drops [121]. In order to be able to predict the breakup dynamics of inkjet fluids as they are printed, we will use a recently developed extensional rheometry technique known as dripping-onto-substrate capillary breakup extensional rheometry (CaBER-DoS) [122, 123].

Our knowledge of extensional properties of fluids widened significantly with the development of elongational filament stretching methods, reviewed by McKinley and Sridhar [67]. In such devices, a liquid bridge is formed and becomes a filament whose minimum diameter evolution is recorded. In filament stretching methods, a cylindrical liquid bridge is formed between two plates. These plates are then moved appart with an exponential velocity profile, resulting in a constant extensional strain rate and significant strain on the polymeric liquid bridge and eventually its breakup [124]. This method is

convenient for polymer melts and moderate viscosity solutions ($\eta_0 > 1\text{Pa.s}$) and has enabled the measurement of polymer relaxation times of several seconds.

In filaments thinning techniques [32], after having filled the gap between plates with the fluid to be tested, the upper plate is moved and then stopped at a desired separation distance. The liquid bridge that is formed is unstable, and a result, it begins to thin down and breaks up under the action of capillary forces. Bazilevsky's device [32] has been further improved by a number of other researchers including Anna and McKinley [28] and is now sold under the name CaBER (Capillary Breakup Extensional Rheometry) by Thermo scientific. This is a common technique for determining the extensional rheology of viscoelastic fluids with viscosities as low as $\eta_0 = 70\text{mPa.s}$ and relaxation times as small as $\lambda = 1\text{ms}$ [97]. In order to reach even smaller relaxation times for even lower viscosity fluids, an alternate high speed filament stretching method has been developed under the name Cambridge Trimaster (CTM) [99]. It is based on the synchronized separation of the two pistons in order to get a centred filament. Using the CTM, Vadillo et al. [97] measured relaxation times as short as $\lambda = 80\mu\text{s}$ by for a series of solution of monodisperse polystyrene dissolved in diethyl phthalate (DEP) with concentration of polystyrene ranging from dilute to concentrated with solution viscosity of $\eta_0 = 12\text{mPa.s}$. One limitation of high-speed CaBER measurements and the CTM is the inertial effects resulting from the dynamics of the rapid step stretch imposed by the motor motion. At the high velocities required to measure the breakup dynamics of low viscosity fluids, like printer inks, the rapid step strain can lead to oscillations in the filament that make measurement of extensional rheology difficult. In order to avoid inertial effects, Campo-Deano et al. [98] used a slow retraction method (SRM) to investigate filament thinning mechanisms of fluids

with shear viscosities similar to water, $1 < \eta_0 < 3\,\text{mPa.s}$, and very short relaxation times, $\lambda > 80\mu\text{s}$. This experimental technique involves slowly separating the pistons just beyond the critical separation distance for which a statically stable liquid bridge can exist. At this point, the filament becomes unstable and the thinning and breaking process is initiated. This SRM technique avoids inertial effects allowing the authors to extract relaxation times as short as $\lambda = 200\mu\text{s}$ for dilute aqueous solutions of polyethylene oxide (PEO) with a molecular weight of $M_w = 10^6\,\text{g/mol}$ and shear viscosities between $1 < \eta_0 < 3\,\text{mPa.s}$ [98]. More recently, Keshavarz *et al.* [101] took advantage of the Rayleigh capillary instability breakup process [6] to develop a new technique called Rayleigh Ohnesorge Jetting Extensional Rheometry (ROJER). This method involved the application of a perdiocical radius disturbance to a fluid jet in order to trigger a capillary instability and the tracking of the perturbation necks diameter until the jet breakup. Like all the techniques cited above, it allows the measurement of the fluid relaxation time as well as the Hencky strain, the strain rate and the transient extensional viscosity in the filament. Recently, Greiciunas *et al.* [125] were able to measure relaxation times with this technique down to $\lambda = 100\mu\text{s}$ for solutions with shear viscosities as low as $\eta_0 = 3\,\text{mPa.s}$.

Amazingly, in order to characterize common inkjet printing inks, one often requires a device that can experimentally characterize the extensional rheology of polymeric solutions with relaxation times even lower than those described above. The time scales involved in the jetting process are on the order of microseconds, while the shear and extension rates experienced by the fluid can be on the order of a million reciprocal seconds [117]. As a result, viscoelastic polymeric solutions with relaxation times on the order of ten microseconds can have a significant impact on the jet formation and breakup. These

relaxation times of inkjet fluids are often beyond the limit of the state of the art of extensional rheology characterization described above. For that reasons, in this paper, we will utilize the dripping-onto-substrate capillary breakup extensional rheometry method (CaBER-DoS) developed by Dinic et al. [122, 123]. In this measurement technique, a single drop of fluid is dispensed at a relatively low flow rate onto a substrate which is placed at a fixed distance below the exit of the nozzle. Under the appropriate experimental conditions, a filament is formed when the droplet wets the substrate. By capturing the droplet on the substrate and not allowing it to fall, a capillary breakup extensional rheology measurement is initiated without the inertial effects associated with the moving of the top/bottom plate. Additionally, compared to the slow retraction method, CaBER-DoS is better suited for highly volatile fluid, like the methyl ethyl ketone (MEK) used here, because the experiments are performed much more quickly thereby limiting the effect of evaporation. Dinic et al. [123] succesfully measured extensional properties of a large variety of fluids, including a commercially-available printing ink, and were able to characterize fluids with relaxation times as low as $\lambda_E = 0.3\text{ms}$. Sur et al. [126] extended their work to relaxation times an order of magnitude by measuring dilute PEO aqueous solutions with relaxation times as low as 20 μs [126].

In the present work, the extensional rheology of several solutions of polymers commonly used in the printing industry was studied so that the impact of polymers on the dynamics of jet formation and breakup into drops and its implications on the printability of inkjet fluids could be better understood in the context of real ink formulations. One of the differences between this study and other similar works reported in literature [122, 123, 126] is that, as is common in ink jet fluids, all the polymer solutions studied here were in

the semi-dilute regime. This is the case even though the molecular weight of the polymers used here were all low, M_w < 60,000 g/mol, because the polymer concentration was increased well beyond the coil overlap concentration, c^*. The solutions studied here had shear viscosities as low as $\eta_0 \sim 3$ mPa. s and the polymers were all highly polydisperse. This chemical complexity, when added to the intense shearing upstream within the ink jet printer nozzle and the enormous extension rates experienced during the jet thinning and breakup makes predicting the dynamics of jet breakup and the impact of different additives on the viability of different inks extremely challenging. This is especially true when the fluid rheology cannot be fully characterized at the deformation rates at which these inks are processed. In the present work, we used CaBER-DoS to study the influence of the polymer concentration, polymer chemistry and polymer molecular weight on extensional viscosity, relaxation time and jet breakup. Of great interest were the transitions in filament thinning between inertia-dominated, viscous-dominated and elasticity-dominated regimes. These transitions were found to strongly correlate to the reduction in the size of satelite drops formed during jetting and a delay in the breakup of fluid jets into drops which could negatively impact the jetability of a given ink formulation.

4.2 Experimental Setup

4.2.1 Methodology

A schematic diagram of the dripping-onto-substrate capillary breakup extensional rheology (CaBER-DoS) experimental setup is presented on Figure 35. In the CaBER-DoS experiment, a liquid drop was formed at the nozzle tip with a diameter of D_{nozzle} = 800μm using a syringe pump (KD Scientific). The flow rate was maintained low enough to remain

in the dripping regime and so that the motion before wetting was only driven by gravity. The substrate was made of glass and was separated from the tip by a distance, H_0 = 1.6cm. A high-speed camera (Phantom- Vision optics, V-4.2) was used to capture the filament breakup process at a frame rate of 20,000 fps using a window of 128x128 pixels. A 5 μm/pixel magnification was obtained using a long distance microscope lens (Edmund Optics). The diameter decay was digitized over time using an automated software called Edgehog (KU Leuven).

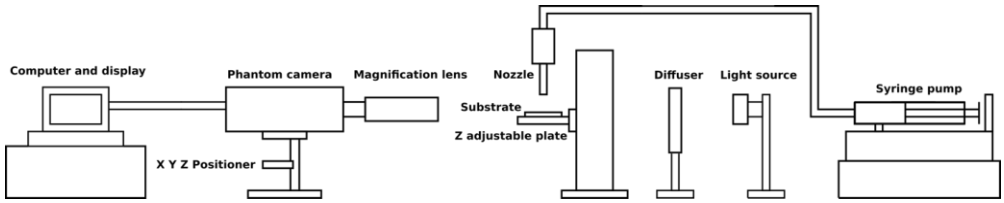

Figure 35. Schematic diagram of the Drip onto substrate capillary breakup rheometry (CaBER-DoS) setup.

The thinning dynamics of a fluid filament in CaBER-DoS is driven by capillary forces which depends on the surface tension, σ, and the local curvature of the filament. The capillary thinning is resisted by a combination of fluid viscosity, inertia, and elasticity depending on the fluid physical and rheological properties and the size of the filament. The shape of the filament and the rate of draining can also be influenced by gravity although in most instances it can be neglected. The Bond number, $Bo = \rho g R^2 / \sigma$, compares the influence of gravity to surface tension. Here, ρ is the density, g is the acceleration of gravity, R is the radius of the filament and σ is the surface tension. In all the experiments presented in this paper, a diameter of $D_0 = 250\mu m$ was chosen to be the initial diameter at t=0s. This choice is a bit arbitrary, but to achieve good results as the filament decayed, a very high magnification was required making it impossible to observe the diameter decay for larger

filaments. All tested fluids had densities between $\rho = 800\,\mathrm{kg/m^3}$ and 900kg/m^3 and a surface tension of $\sigma = 24\,\mathrm{mN/m}$ which results in a maximum Bond number $Bo = 0.02$. At this Bond number, Clasen et al. [127] demonstrated that gravitational effects could be neglected in CaBER experiments for $Bo < 0.2$.

The competition between inertia, viscosity and elasticity in filament thinning processes give rise to three distinct filament breakup regimes known as the inertio-capillary, the visco-capillary and the elasto-capillary regime [8, 9]. A number of important dimensionless groups characterize the necking process. These include: the Ohnesorge number, $Oh = \eta_0 / \left(\rho\sigma R_0\right)^{1/2}$, which represents a balance of the inertial and viscous forces for a slender filament; the intrinsic Deborah number, $De_0 = \dfrac{\lambda_E}{\sqrt{\rho R_0^{\,3} / \sigma}}$, which represents the ratio of the characteristic relaxation time of the fluid to the inertial timescale of the flow; and the elasto-capillary number, $Ec = \lambda_E \sigma / \eta_0 R_0$, which represents a ratio of the characteristic relaxation time of the fluid and the viscous timescale of the flow. In these dimensionless groups, η_0 is the shear viscosity of the fluid, R_0 is the radius of the filament, σ is the surface tension, ρ is the density and λ_E is the relaxation time in extension. For low-viscosity inelastic fluids, $Oh << 1$ and $De_0 << 1$, the thinning dynamics are driven by the competition between inertia and capillary forces and the filament radius follows a power law with an exponent of 2/3 [9],

$$\frac{R(t)}{R_0} = 0.8\left(\frac{\sigma}{\rho R_0^3}\right)^{1/3}(t_c - t)^{2/3} = 0.8\left(\frac{t_c - t}{t_R}\right)^{2/3}. \qquad (0.11)$$

Here t_c is the filament breakup time and $t_R = (\rho R_0^{\,3} / \sigma)^{1/2}$ is the Rayleigh time which is a characteristic timescale for the breakup of fluids in this inertio-capillary regime

[122, 123]. The prefactor in equation 1 has been reported to be between 0.64 and 0.8 with some experimental measurements finding values as large as 1.0 [83, 88, 98, 105].

For more viscous inelastic fluids with, $Oh >> 1$ and $Ec << 1$, the filament is known to decay linearly with time [15],

$$\frac{R(t)}{R_0} = 0.0709\left(\frac{\sigma}{\eta_0 R_0}\right)(t_c - t) = 0.0709\left(\frac{t_c - t}{t_v}\right). \tag{0.12}$$

Here, $t_v = \eta_0 R_0 / \sigma$, is the characteristic viscous timescale for breakup. The transition between inertio-capillary and visco-capillary regimes has been shown by Clasen et al. [9] to occur at an Ohnesorge number of $Oh = 0.2077$.

For viscoelastic liquids such as the polymer solutions studied her, an elasto-capillary thinning regime can also exist. In this regime, the radius is known to decay exponentially with time for fluids well characterized by an Oldroyd-B or FENE-P model [28, 31, 128, 129],

$$\frac{R(t)}{R_0} = \left(\frac{GR_0}{2\sigma}\right)^{1/3} \exp\left(-\frac{t}{3\lambda_E}\right). \tag{0.13}$$

Here G is the elastic modulus and λ_E is the relaxation time of the solution in an extensional flow. A transition from the inertio-capillary to the elasto-capillary regime has been shown for intrinsic Deborah numbers above $De_0 > 0.98$ while the transition from an visco-capillary to an elasto-capillary thinning has been shown to occur above an elasto-capillary number of $Ec > 4.7$ [9].

The use of analytical thinning regimes can be particularly helpful for the fast and accurate prediction of fluid behaviours in industrial processes. Unfortunately, in the literature, few examples deal with actual industrial fluids. This is why, in the present work,

a special attention has been given to the influence of the polymer concentration onto the thinning regime.

4.2.2 Materials

The study focused on four different polymeric binders: Paraloïd™ B-66 (Dow) which is an acrylic polymer mainly used for surface coating compounds and printing inks; CAB-381-2 (Eastman) which is a cellulose acetate butyrate polymer; and Vinnol E15/45M and Vinnol E22/48A (Wacker Chemie), which are vinyl chloride ter-polymer and co-polymers respectively. The molecular weights and coil overlap concentrations of each of these polymers listed in Table 3 were either provided by the suppliers directly or measured by our collaborators at Markem-Imaje. The solvent for each solution was methyl ethyl ketone (MEK), which has a zero-shear viscosity of $\eta_s = 0.43\,\text{mPa.s}$ and an equilibrium surface tension with air of $\sigma = 24\,\text{mN/m}$ at 20^{o}C [130]. The time scales involved in the CaBER-DoS breakup process are on the order of a few milliseconds or even less. Unfortunately, we did not have access to a measurement device capable of measuring the dynamic surface tension of our solutions at such a short surface lifetime. However, it is a reasonable assumption to make that the surface tensions of the fluid filaments formed is equal to that of the solvent. This is because the rate of interface creation during filament breakup far outpaces the rate of diffusion of the dissolved polymer to the interface [131, 132]. The density of each solution was measured and found be the same as the solvent to within measurement uncertainty, $\rho = 865\ \text{kg/m}^3$.

Table 3. List of the polymers used in the experiments along with their chemical natures, molecular weights and coil and overlap concentrations.

Name	Chemical Nature	M_n [g/mol]	M_w [g/mol]	PDI	c^* [wt%]
Paraloïd B66™	Acrylic	27300	51800	1.9	6.8
CAB-381-2	Cellulose	52900	158900	3.0	1.4
Vinnol E15/45M	Vinyl Chloride	28900	67700	2.3	3.7
Vinnol E22/48A	Vinyl Chloride	37800	118300	3.1	3.2

As shown in Table 3, the reduced polymer concentrations of all the solutions tested were just above the overlap concentration, $c/c^* > 1$, in the semi-dilute regime. In the semi-dilute regime, polymer chains entanglements can lead to significant modifications of the fluid rheology. These entanglements enhance confinement and resistance to polymer motion leading to a fast increase in the solution's shear viscosity and the relaxation time with increasing molecular weight and concentration [133]. In extensional flows, like the CaBER experiments studied here, polymer entanglements can lead to a reduction in the extensibility of the polymer chain and a decrease in the strain hardening of the extensional viscosity compared to a dilute, unentangled solutions [134, 135]. The polydispersity index in each case was found to be significantly greater than one, $PDI = M_w/M_n > 1$, meaning that polymers were not monodisperse, but were polydisperse. Polydispersity of the polymer can lead to issues, especially in the extensional flows experienced during ink jet printing, as it is known that even small fractions of a high molecular weight tails in the molecular weight distribution can have a disproportionate effect on the extensional viscosity and extensional relaxation time measured for a given solution [136].

The influence of polymer concentrations on the zero-shear-rate viscosity of the solutions was investigated using a stress controlled rheometer (Malvern) with a Couette

geometry at a constant applied shear rate of $\dot{\gamma} = 30 s^{-1}$. The results are presented for each solution in Table 4. As we will demonstrate in the next section from the CaBER-DoS extensional rheology data, the relaxation time of the solutions tested were all below $\lambda <$ 200μs. As a result, the shear rates required to probe shear thinning of the viscosity ($\dot{\gamma} > 5000 s^{-1}$) and the oscillatory frequencies required to probe the linear viscoelasticity of the samples ($\omega > 5000 \text{rad/s}$) were well beyond the upper limit of our shear rheometer. As a result, no shear thinning data was measured and the shear relaxation time could not be characterized. Trend in the zero-shear-rate viscosity, however, can be observed from Table 4. The shear viscosities of the solutions tested here cover the range of viscosity usually found for industrial inks, $3 \text{mPa.s} < \eta_0 < 25 \text{mPa.s}$. The shear viscosity was found to increase with increasing concentration with a power-law exponent that was between 1.5 and 3.0. The CAB-381-2 was found to require least polymer addition to achieve a given solution viscosity while the Paraloid B66 was found to require the most. These effects of concentration appeared to be roughly normalized out if one compared solutions based on reduced concentration instead. The lone exception there was the Vinnol E22/48A which had a markedly higher molecular weight than either of the other two flexible polymer binders, Paraloid B66 and Vinnol E15/45M. The CAB-381-2 had the highest molecular weight by far, but being a cellulosic polymer, it has a rigid backbone. The impact of polymer rigidity and polymer molecular weight of these binders will be evident in the measurements of extensional rheology.

Table 4. Shear viscosity and reduced concentrations for the solutions tested

Paraloïd B66				
c [wt%]	15 %	20 %	25 %	30 %
η_0 [mPa.s]	5	6.9	13.3	25
c/c^*	2.2	2.9	3.7	4.4
CAB-381-2				
c [wt%]	4 %	5 %	6 %	
η_0 [mPa.s]	6.9	9.4	16.9	
c/c^*	2.9	3.7	4.4	
Vinnol E 15/45 M				
c [wt%]	8 %	12 %	16 %	
η_0 [mPa.s]	3.5	7.9	17.5	
c/c^*	2.1	3.2	4.3	
Vinnol E 22/48 A				
c [wt%]	6 %	8 %	10 %	
η_0 [mPa.s]	6	8.1	13	
c/c^*	1.9	2.5	3.1	

4.3 Results and Discussions

4.3.1 CaBER-DoS Measurements of Paraloid B66 Solutions

Throughout the results and discussion section, we will present CaBER-DoS results for a series of MEK solutions with polymer binders typical of ink jet printing inks. The solutions were developed to explore the effects of solution viscosity, polymer chemistry, polymer backbone rigidity, polymer molecular weight and concentration on extensional rheology and jettability. The trends associated with each of these parameters will be identified and, where possible, better understood through comparison to theory. The results and discussion section will be broken down into two sub-sections. In the first, we will

present the experimental measurements and the summary results for the Paraloid B66 solutions in great detail. In the second, we will present the results for the CAB-382-2 and the two Vinnol polymer solutions with a focus on the trends in the data and less on the details of each experiment with an eye towards facilitating comparisons between different polymers and different ink jet fluid compositions.

As described in section 4.2, in the CaBER-DoS experiments as well as in many filament thinning or stretching methods, the observed thinning regime is dictated by a balance of the capillary force with the dominant force resisting drainage. The characteristic thinning velocities of the inertio-capillary (U_ρ), visco-capillary (U_η) and elasto-capillary (U_λ) regimes can be calculated from the radius decay for each regime found in Equations 1.11, 1.12 and 1.13.

$$U_\rho = 0.48\sqrt{\frac{\sigma}{\rho R}} \tag{0.14}$$

$$U_\eta = 0.0709\frac{\sigma}{\eta} \tag{0.15}$$

$$U_\lambda = \frac{1}{3}\frac{R}{\lambda_E} \tag{0.16}$$

Clasen *et al.* [9] explained that the lowest characteristic velocity will determine the thinning pathway because the force resisting drainage is largest. A few important observations can be made from Equations 1.14, 1.15 and 1.16. Assuming a constant shear viscosity, η, the visco-capillary drainage velocity, U_η, is independent of filament radius. Additionally, inertio-capillary drainage velocity increases as the filament radius decreases while the elasto-capillary drainage velocity decreases. As a result, a series of regime transitions are expected from inertio-capillary to visco-capillary and finally to elasto-capillary if the fluid is viscoelastic. The transition radius from inertio-capillary to visco-

capillary drainage can be predicted from the measurements of shear rheology, density and surface tension presented in Tables 3 and 4. This is shown graphically in Figure 36, where the characteristic velocities for each of the Paraloid B66 solutions is plotted as a function of the filament diameter for diameters below $D < 250\mu m$. Note that the evolution of the inertio-capillary drainage velocity is independent of polymer concentration as none of the parameters in Equation 1.14 are affected by adding binder. Also note that a line for the elasto-capillary drainage of the 30wt% Paraloid B66 solution has been plotted in Figure 36. However, this was added for completeness and cannot be added from the shear rheology data because the relaxation time was too small to measure in shear. The CaBER-DoS measurements that follow are necessary in order to calculate the extensional relaxation time, λ_E, needed to feed into Equation 1.16.

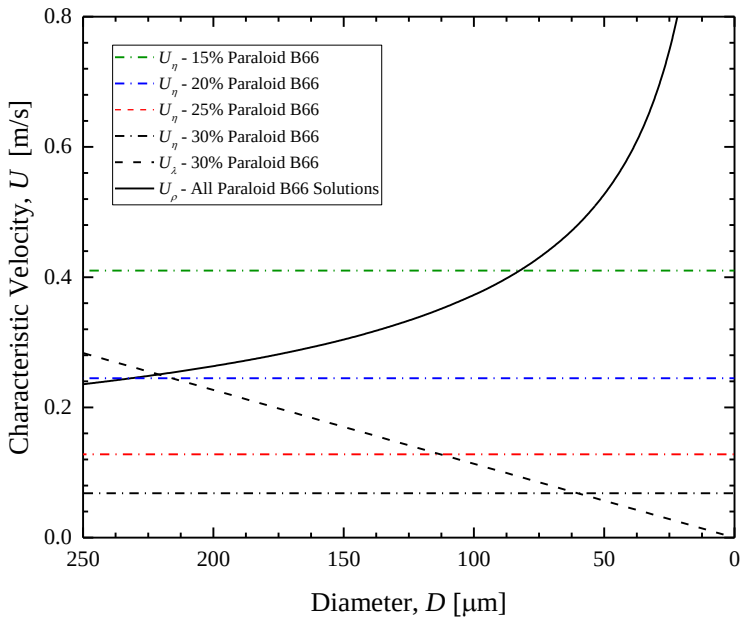

Figure 36. Characteristic velocities calculated for the filament breakup of various concentrations of Paraloid B-66 into MEK. The solid line represents the evolution of the inertio-capillary velocity, U_ρ, which does not depend on the binder concentration. The dash-dot lines represent the evolutions of the visco-capillary velocities, U_η, for each polymer concentration as shown in the legend. The dashed line respresents the elasto-capillary drainage velocity, U_λ, for the 30wt% Paraloid B-66 solution.

Transitions from inertio-capillary to visco-capillary regimes can be predicted from Figure 36 for both the 15wt% and the 20wt% Paraloid B66 solutions from the intersection of the lines for U_ρ and U_η. Based on the characteristic velocity calculations, these transitions should occur at diameters of D = 70 μm for the 15wt% and D = 216 μm for the 20wt% Paraloid B66 solutions. For the highest polymer concentration solutions tested, the transition velocity was expected to be reached at a diameter of D = 430μm and nearly 2mm for the 25wt% and 30wt% solutions. For each of these systems, the transition was outside of our operation window for the CaBER-DoS measurements and for the case of the 30wt% Paraloid B66 solutions, it was larger than the diameter of the syringe tip used in the experiments. As a result, the 30wt% Paraloid B66 solution was expected to transition from visco-capillary to elasto-capillary drainage without ever experiencing inertio-capillary drainage. These velocity predictions and the transitions that result will be used to determine both extensional viscosity and the extensional relaxation time from the diameter decay measured from the CaBER-DoS experiments. These transitions are also very useful in predicting the lifetime of inelastic fluid filament breaking up into drops during ink-jet printing and seeing exactly how detrimental fluid elasticity can be on the breakup time and distance.

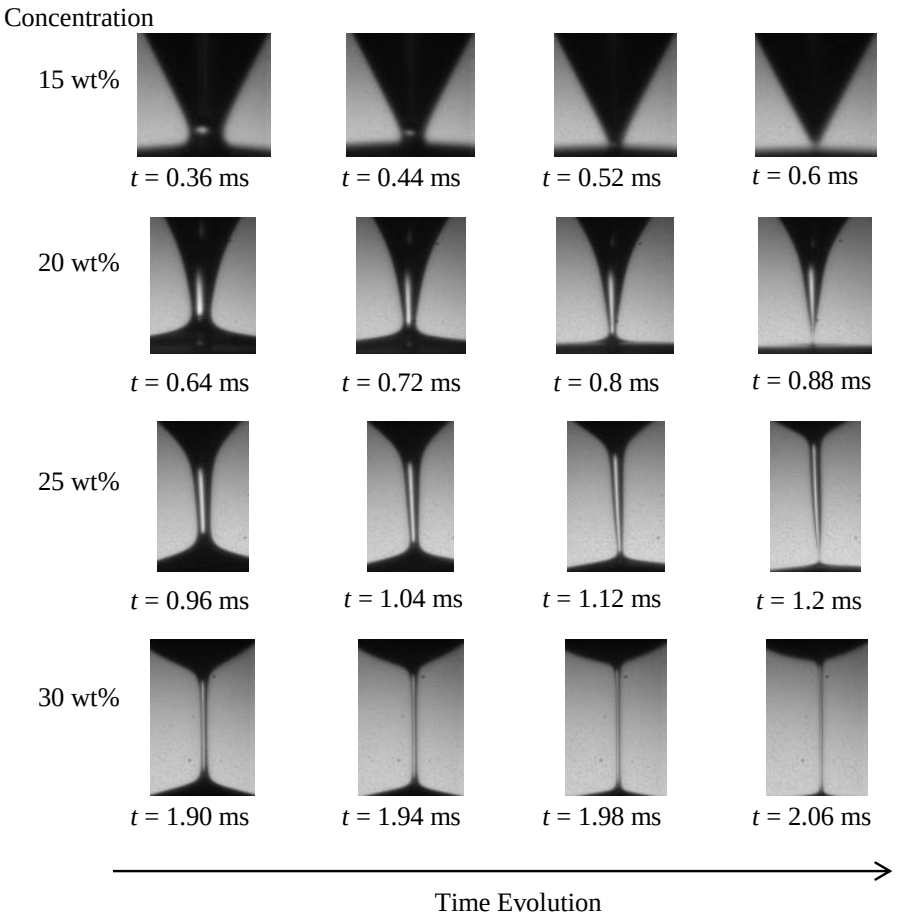

Figure 37. Evolution of the filament formed in the neck during the breakup of various concentrations of Paraloid B-66 dissolved in MEK during a CaBER-DoS experiments.

In Figure 37, a series of images from the time evolution of CaBER-DoS experiments on each of the Paraloid B66 solutions are presented. The images show the necking region between the drop deposited on the substrate and the drop which remains attached to the syringe tip. For a given concentration, these data show the evolution of the neck with time while, for varying concentration, these data show the change in neck shape and breakup regime. All the data is normalized such that time, t = 0ms corresponds to a filament diameter of D_0 = 250μm. The final images are a frame or two (~10^{-4}s) prior to the breakup of the filament. For the lowest concentration shown in Figure 37, 15wt%

Paraloid B66, a triangular conical shape, commonly observed for low viscosity Newtonian fluids is obtained [137]. This focused shape is expected for filaments breaking up in the inertio-capillary regime. This is also the desired breakup shape for continuous ink jet printers because fluids in this regime tend to break up quickly and cleanly with minimal satellite drop generation [138]. As the concentration of the Paraloid B66 was increased, the shape of the necking region was found to change. The cone became progressively less triangular with axial curvature appearing along the neck. This curvature signals the transition to a visco-capillary breakup regime. With higher concentrations, the shear viscosity of the solution was found to increase by a factor of nearly five. This increased viscosity can be observed in the shape of the neck as it becomes extended and narrows. Finally, at a concentration of 30wt% Paraloid B66, the neck can be seen to become highly elongated as it forms a cylindrical filament with little to no axial curvature along the filament. Such long thin filaments are characteristic of elastic fluids and mark the elasto-capillary thinning regime. The first measurable elasto-capillary thinning is observed for the 30wt% Paraloid B66 solution, however, if one looks closely at the final images of the 20wt% and 25wt% Paraloid B66 solutions, the presence of an extremely fine cylindrical filament, hinting at the presence of fluid elasticity, can be observed just prior to breakup. Without a large number of data points to fit to the exponential decay predicted by Equation 1.13, it is not possible to make a direct measurement of the relaxation time or the extensional viscosity of the either the 20wt% or 25wt% solution, however, the recent work of Sur et al. [126] showed that an approximate measure of the relaxation time could be calculated from a single frame of data like that shown in Figure 37. We will return to the

predictions of Sur et al. [126] after fully analysing the extensional rheology of the 30wt% Paraloid B66 solution.

As can be seen from the images in Figure 37, with increasing polymer concentration, both the breakup length and the breakup time were increased. For the case, case of 20wt% and 25wt% Paraloid B66 solutions, elastic stresses can be neglected, at least until the final 80μs, and thus the observed increase is due to an increase in the shear viscosity and the resulting increase in the viscous stresses resisting the breakup. For the 30wt% Paraloid B66 solution, the elastic stresses also play a role in resisting the breakup, resulting in an even more significant increase in breakup time and length. To quantify the change, the breakup time increased by 280μs, 600μs and 1460μs as the concentration was increased from 15wt% to 20wt%, 15wt% to 25wt%, and 15wt% to 30wt% respectively. As expected from Equation 1.12, the breakup time appeared to grow linearly with shear viscosity for the two inelastic samples. The viscoelastic 30wt% solution showed a marked increase in the breakup time, well beyond what would be predicted by the increased viscosity of the solution only.

In Figure 38, the diameter evolution of the three inelastic Paraloid B66 solutions tested here are presented as a function of time. Experimental data are represented in Figure 38 by symbols, while solid lines representing the inertio-capillary breakup predicted by Equation 1.11 and dashed lines representing the visco-capillary breakup predicted by Equation 1.12 are superimposed over the experimental data. As predicted by the characteristic velocity maps in Figure 36, the early stage neck drainage for the 15wt% and the 20wt% Paraloid B66 solutions were found to be inertio-capillary and were well fit by the expected 2/3 power law slope.

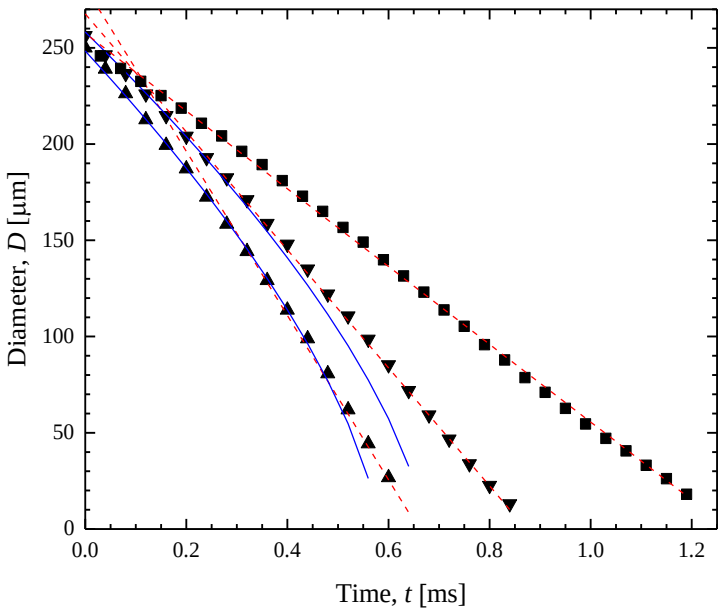

Figure 38. Diameter evolution of CaBER-DoS experiments on a series of Paraloid B66 solutions in MEK solvent The figure includes experimental data for (▲) 15wt% Paraloid B66, (▼) 20 wt% Paraloid B66, (■) 25 wt% Paraloid B66, along with solid lines (—) representing the fit to the inertio-capillary drainage in Equation 1 and dashed lines (--) representing the fit to the visco-capillary drainage in Equation 2.

The transition from the inertio-capillary to the visco-capillary regimes were observed at a diameter of D=60μm for the 15wt% Paraloid B66 solution and at a diameter of D=200μm for the 20wt% Paraloid B66 solution. This measurement is in good agreement with the predictions that can be made *a priori* from the characteristic drainage velocities in Equations 1.14 and 1.15 which are calculated to be D=70μm and D=216μm from measurements of the shear viscosity for the 15wt% and 20wt% Paraloid B66 solutions respectively.

At long times, as the diameter of the neck grew small, a linear diameter decay was observed for both the 15wt% and the 20wt% Paraloid B66 solutions. The 25wt% Paraloid B66 solution showed a linear diameter decay over the entire range of diameters measured

as expected from the drainage velocity predictions in Figure 36. The transition to visco-capillary drainage resulted in a delayed breakup in each case as the filaments would all have failed earlier if the drainage had remained in the inertio-capillary regime. For the 15wt% Paraloid B66 solution, the increase in the breakup time due entirely to viscous effects was only 12μs, for the 20wt% Paraloid B66 solution, the increase was 130μs while, for the 25wt% Paraloid B66 solution, the increase is more than 500μs. By fitting the predictions of Equation 1.12 to the data in Figure 37, the shear viscosity of each solution was calculated. In Table 5, a comparison between the shear viscosity measured in the Couette rheometer and the viscosity obtained from the fit to Equation 1.12 is presented. Reasonable agreement between the two viscosities were found, especially for the higher concentration solutions. The fits were found to over predict the shear viscosity measurements from the Couette rheometer at low concentrations. This difference could be the result of the limited number of data points following the inertia-capillary decay that were used to determine the viscosity. The Papageorgiou [15] solution used to fit the data neglects inertia, however, for the two lower concentration samples, the data points used in the fit are close to the transition point from the inertia-capillary to the visco-capillary decay. Thus in this region, inertia could play an important, although secondary, role in the breakup dynamics resulting in the larger values of viscosity seen in low concentration samples. Eggers [139] showed that for a inertia-visco-capillary decay, the prefactor in equation two is reduced from 0.0709 to 0.0304. This change in the prefactor would reconcile the lowest concentration results with the shear viscosity measurements and is likely the more appropriate one to use when so few data points outside of the inertia-capillary regime are used to fit the viscosity.

Table 5. A comparison of the shear viscosity measured in a Couette rheometer, η_0, to the shear viscosities obtained through a fit of the Equation 2 to the CaBER-DoS data, η_{fitt}, for a series of Paraloid B66 solutions.

	20wt%	25wt%	30wt%
η_{fit} [mPa.s]8	11±0.4	18±0.6	26±0.5
η_0 [mPa.s]	6.9	13.3	25.0

The diameter decay for the 30wt% Paraloid B66 solution is plotted on Figure 30. This solution is plotted separately from the rest and using semi-log axes to emphasize the differences in the diameter decay of the fluid. As with the 25wt% Paraloid B66 solutions, the early diameter decay is linear with time as the drainage is within the visco-capillary regime. However, as the filament approached breakup, a transition to an exponential diameter decay was observed. This observation confirms that the highly elongated, cylindrical filament observed in Figure 36 was the result of fluid elasticity. From the initial linear diameter decay a fluid viscosity of η_{fit}=26mPa.s was calculated from Equation 1.12 matching the measurements from shear. By fitting the exponential decay prior to breakup to the elasto-capillary decay predicted by Equation 1.13, an extensional relaxation time of $\lambda_E = 146 \pm 3\mu s$ was measured. This value of relaxation time is one of the smallest relaxation times published in the literature, thus demonstrating the versatility and value of the CaBER-DoS technique for measuring the rheology of weakly elastic fluids like printer inks.

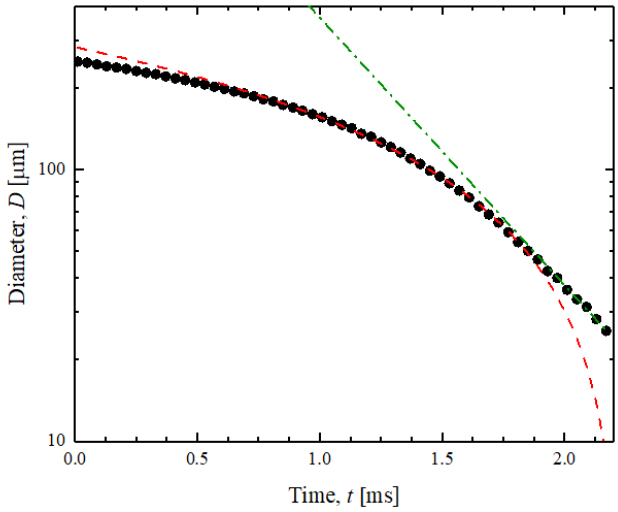

Figure 39. Diameter decay as a function of time measured using CaBER-DoS for the viscoelastic 30wt% Paraloid B-66 solution in MEK. The data include: the experimental data (●),the fit to the visco-capillary thinning regime in Equation 2 (- -), and the fit to the elasto-capillary regime given in Equation 3 (- · -).

Note that, it may be possible to measure the even smaller values of the relaxation time using CaBER-DoS. Sur et al. [126] demonstrated that due to the sharpness in the transition between the inertio-capillary and the elasto-capillary drainage for PEO in a solution of water and glycerol, that relaxation time data could be determined from the diameter measurement of a single image of a viscoelastic filament. In Figure 37, the presence of a viscoelastic filament is hinted at in the final image of the 25wt% Paraloid B66 solution. In order to calculate the extensional relaxation time, we assume that the filament exists at the transition point between the visco-capillary and the elasto-capillary regimes where $U_\lambda = U_\eta$. Substituting from Equations 1.15 and 1.16 we find that

$$\lambda_E = 4.7\frac{R\eta}{\sigma} \tag{0.17}$$

For the viscoelastic filament captured in Figure 37, the filament is only one pixel or 5μm wide. As a result, to form this filament, from Equation 1.17, the 20wt% Paraloid B66 solutions can be approximated to have a relaxation time of $\lambda_E = 13.4\mu s$.

As described by Sur et al. [126] and by the theoretical predictions of Wagner et al. [140] this value of relaxation time calculated from the final image in Figure 37 is an underprediction because it assumes that the elastic stresses in the filament are built up instantaneously. In reality, it requires a non-trivial amount of accumulated strain to induce the deformation and elastic stress growth in the polymer chains needed to achieve the constant Wi = 2/3 drainage predicted for a viscoelastic CaBER diameter decay. It is interesting to note, that in Sur et al. [126], where the filaments undergo a transition from an inertia-capillary drainage regime to a elasto-capillary drainage regime, the discrepancy between the theoretical predictions and the experimental measurements of the radius at which this transition should occur was off by a factor of five. However, in the experiments presented here, where the transition is from visco-capillary to elasto-capillary, the error between the theoretical calculations in Equation 1.17 and the experimental measurements inferred from the 30wt% Paraloid B66 solution data is only approximately 20%. This could be a direct result of the nature of the inertio-capillary and visco-capillary drainage velocities. The visco-capillary drainage velocity is constant, however, as shown by Equation 1.14 and observed in Figure 36, the inertia-capillary drainage velocity increases quickly with decreasing filament radius especially as the radius decreases towards zero. This acceleration of the drainage velocity exacerbates the error between the experimental measurements and the theoretical predictions of the transition radius as it introduces a significant overshoot in the drainage velocity and, as a result, in the extension rate in the

filament well beyond the $\dot{\varepsilon} = 2/3\lambda_E$ predicted for CaBER [126]. This is because a finite time is needed for the elastic stress to grow to its steady state value in the thinning filament once the coil stretch transition has been reached beyond a Weissenberg number of *Wi* > 1/2.

We can investigate this transition a little further by plotting the measured extension rate given by

$$\dot{\varepsilon}(t) = -\frac{2}{D(t)}\frac{dD(t)}{dt}, \tag{0.18}$$

for the 25wt% and the 30wt% Paraloid B66 solutions as a function of time. The results are shown in Figure 40a. The extension rate measured for the 25wt% Paraloid B66 solution was found to increase monotonically until breakup with extension rates of over $\dot{\varepsilon} > 15{,}000\,\mathrm{s}^{-1}$ achieved just prior to breakup. The extension rate of the 30wt% Paraloid B66 solution, on the other hand, was found to increase until reaching an asymptotic value of just over $\dot{\varepsilon} = 4100\,\mathrm{s}^{-1}$ after 1.6ms. Unlike the observations for the transition from inertia-capillary to elasto-capillary drainage [126], no significant overshoot in the extension rate was observed. As a result the, Equation 1.17 should be reasonably good for determining the extensional relaxation time from just a single image during the breakup of a viscoelastic fluid filament.

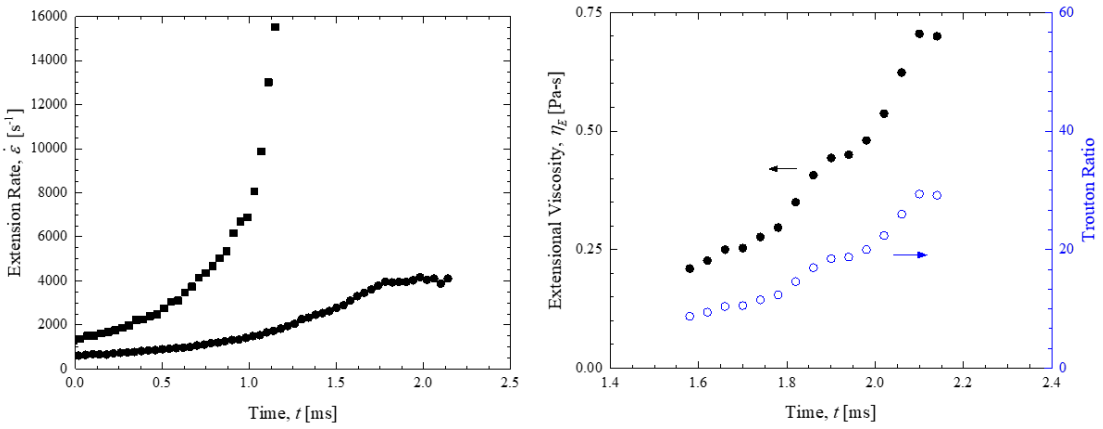

Figure 40. Results for CaBER-DoS measurements of the 25wt% (■) and 30wt% (●) Paraloid B66 solutions in MEK. In a) the extension rate is plotted as a function of time while in b) the extensional viscosity (●) and Trouton ratio (○) are presented as a function of time.

The transient extensional viscosity can also be calculated directly from the diameter decay once the filament has become cylindrical and the flow enters the elasto-capillary regime. The extensional viscosity is given by

$$\eta_E = -\frac{\sigma}{dD(t)/dt}, \tag{0.19}$$

And is presented in Figure 40b alongside the Trouton ratio, $Tr = \eta_E / \eta_0$. Note that in Figure 31b, the data does not begin until a time of 1.6ms. Before that time, the filament is not cylindrical and the force balance used to determine the extensional viscosity in Equation 1.19 is not valid. The extensional viscosity was found to increase monotonically until filament breakup. Over that time, the extensional viscosity rose from η_E = 0.2Pa.s to 0.7Pa.s or, equivalently, from a Trouton ratio of Tr = 8 to Tr = 29. Note that for a Newtonian fluid, the Trouton ratio will be exactly Tr = 3, so a Trouton ratio of Tr = 29 represents a reasonably amount of strain hardening for the 30wt% Paraloid B66 solution. It should be noted that the maximum Trouton ratio varied some from experiment to

experiment as it is highly dependent on the final diameter measured at the end of the CaBER-DoS experiment and those diameters are subject to uncertainty that is plus or minus one pixel or ±5μm. Thus, the extensional viscosity, which requires a derivative of the diameter, tends to amplify the noise in the data, especially as the diameters get towards the resolution limit of the optics. As a result, the data were uniformly cut when the diameters became less than 20μm to minimize the influence of the measurement uncertainty on the extensional viscosity values presented. The increase of the extensional viscosity just prior to breakup explains the significant breakup delay observed for filaments of Paraloid B66 solutions at the highest polymer concentrations tested. It is interesting to point out that an increase of 5% in polymer concentration can have such a dramatic effect on the breakup time. In this case, increasing the concentration from 25wt% to 30wt% increased the breakup time by nearly 100% and dramatically changed the breakup shape as well. Using CaBER-DoS to gain knowledge of the polymer concentrations where transitions between thinning regimes occur can thus be a crucial tool to aid in the development of fluids for industrial devices such as inkjet printers.

4.2.2 Comparisons with Other Industrial Binders.

In this section, we extend the CaBER-DoS measurements from Paraloid B66 to a series of other polymer binders commonly used in the ink jet printing industry. As described in the section 4.1, all the studied fluids were in the semi-dilute regime. The concentrations that were used were chosen in order to cover the same range of shear viscosity for each choice of polymer. A description of each polymer, their molecular weight and the shear viscosity at each of the concentrations tested is presented in Tables 3 and 4. Beside their chemical composition, there are a number of other difference between the four

binders used of which we should take note. For instance, CAB-381-2 and Vinnol E22/48A each have a significantly higher molecular weight than either Paraloid B66 or Vinnol E15/45M. For this reason, to achieve similar shear viscosities and reduced concentrations, the solutions of CAB-381-2 and Vinnol E22/48A tested were at lower concentration than either the Paraloid B66 or the Vinnol E15/45M. Additionally, while the Vinnol and Paraloid polymers are relatively flexible, CAB-381-2 has a rigid backbone that limits its extensibility [141].

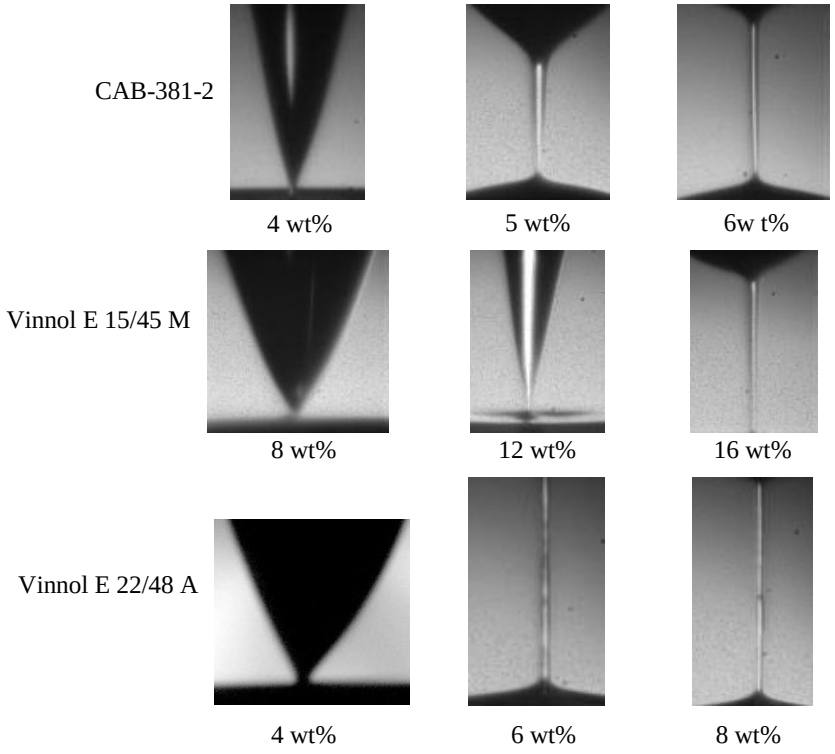

Figure 41. Breakup shapes obtained for several binders at different concentrations

The breakup shapes observed during CaBER-DoS measurements of the solutions of CAB-381-2, Vinnol E22/48A and Vinnol E15/45M in MEK are presented on Figure 41. At the lowest concentrations tested, all solutions showed a drainage similar to the low concentration results for the Paraloid B66 with a transition from inertia-capillary to visco-

capillary breakup. As the concentration of binder was increased, a transitions from visco-capillary to elasto-capillary was observed for all the polymers tested. For the CAB-381-2, this transition occurred between 5wt% and 6wt%. For the, Vinnol E15/45M, this transition occurred between a concentration of 12wt% and 16wt%. While for the higher molecular weight vinyl polymer, Vinnol E22/48A, this transition occurred at a much lower concentration between 4wt% and 6wt%. Finally, recall that, for the Paraloid B66, this transition was observed between 25wt% and 30wt%. The first observation is that the observed transition to elasto-capillary drainage cannot be directly correlated to the shear viscosity of the solutions. As a specific example, the transition occurs for Paraloid B66 at a concentration with a shear viscosity of 25mPa.s while for the Vinnol E22/48A, the shear viscosity is less than 5mPa.s. Molecular weight clearly plays a role in this transition as increasing the molecular weight from the Vinnol E15/45M to the Vinnol E22/48A results in a decrease in the transition concentration from 16wt% to 6wt% and a reduction in the shear viscosity of the solution from 17.5 to 6.5mPa.s. Polymer architecture also clearly plays a role in the jettability of a solution. CAB-381-2 has a similarly high molecular weight compared to the Vinnol E22/48A, requires similar concentration, but a much higher viscosity, 16.9mPa.s versus 6.5mPa.s, to transition to an elasto-capillary drainage. This is because the CAB-381-2 is a cellulosic polymer whose backbone is quite rigid. In flow, it behaves like a rigid rod, which can align, but is difficult to deform and stretch. As a results, for the same molecular weight, the extensibility of a rigid polymer is much lower than a flexible polymer leading to a lower relaxation time and a lower extensional viscosity. This can be seen explicitly in relaxation time data presented in Table 6 and the extensional viscosity data shown in Figure 42.

In Figure 42, the extension rate, extensional viscosity and Trouton ratio are presented as a function of time for the 6wt% CAB-381-2 solution, the 16wt% Vinnol E15/45M solution, and the 6wt% Vinnol E22/48A solution in MEK. These three cases were chosen as representative for the CAB and Vinnnol binders as they were the lowest concentration for which an elasto-capillary response was observed. The data for the CAB-381-2 and the lower molecular weight Vinnol E15/45M solution are quite similar. Each showed an increasing extension rate during the visco-capillary drainage stage before reaching an asymptotic value of just over $\dot{\varepsilon} = 8000 s^{-1}$ the elasto-capillary drainage just prior to breakup. As shown in Table 6, this extension rate corresponds to a relaxation time of approximately λ_E = 80μs. In each case, only the last half dozen or so data points are within the elasto-capillary drainage regime.

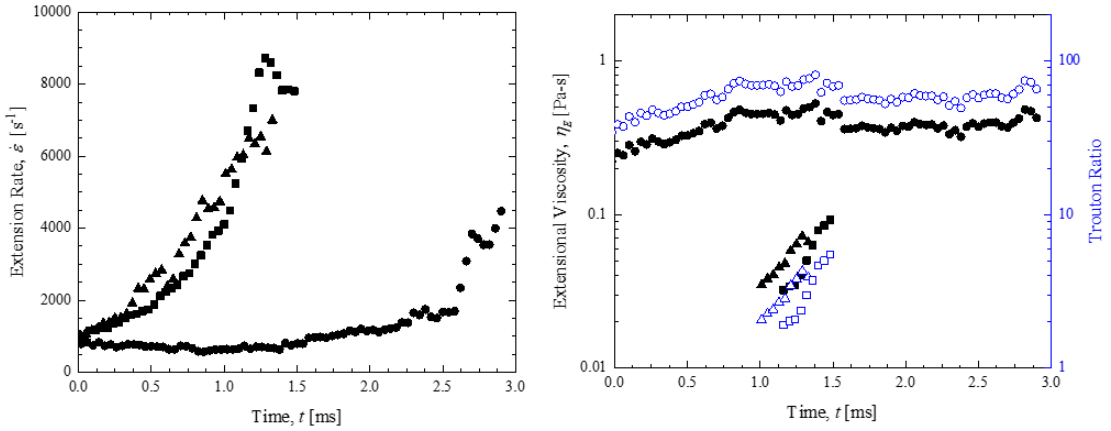

Figure 42. Results for CaBER-DoS measurements of the 6wt% CAB-381-2 (▲), 16wt% Vinnol E15/45M (■), and 6wt% Vinnol E22/48A (●) solutions in MEK. In a) the extension rate is plotted as a function of time while in b) the extensional viscosity and Trouton ratio are presented as solid and hollow symbols respectively as a function of time.

From Equation 1.19, the extensional viscosity can be calculated from the late time data and is presented in Figure 42b alongside the Trouton ratio. For both the the CAB-381-2 and the lower molecular weight Vinnol E15/45M solutions, little strain hardening is observed with Trouton ratios of Tr = 4 or 5 achieved before filament breakup. This is a reflection of the low molecular weight of the Vinnol E15/45M and the rigidity of the CAB-381-2 [141]. By contrast, the high molecular weight Vinnol E22/48A transitions to the elasto-capillary drainage regime at a much lower extension rate, $\dot{\varepsilon} = 850 s^{-1}$, resulting in measured extensional relaxation time of λ_E = 740μs. At long times and diameters below about D < 100μm, the exponential decay in the diameter decay data transitioned back to a linear decay with time resulting in an upturn in the extension rate data beyond t = 1.5s. This occurred because the finite extensibility of the 6% Vinnol E22/48A solution was reached at a steady-state extensional viscosity of η_E = 0.5mPa.s and a Trouton ratio of Tr = 70. In this regime, the polymer solution again behaves like an inelastic fluid with a constant, albeit with a much larger viscosity. Similar results were observed for the 8wt% and 10wt% Vinnol E22/48A solutions tested. As summary of these data can be found in Table 5.

For the case of Vinnol E22/48A, enough experiments were performed at concentrations within the elasto-capillary regime that an approximate scaling could be calculated for the relaxation time with reduced concentration, c/c^*. For Vinnol E22/48A, the relaxation time was found to increase as $\lambda_E \propto \left(c / c^*\right)^{1.6}$. For a dilute solution, c/c^* < 1, the relaxation time has been found experimentally to increase like $\lambda_E \propto \left(c / c^*\right)^{0.65}$ [122, 126]. For semi-dilute polymer solutions like the Vinnol E22/48A studied here, the

extensional relaxation time was found to increase with reduced concentration as, $\lambda_E \propto c/c^*$ when the reduced concentration was just above one, c/c* ~ 1 [142] and with a slightly stronger power-law dependence, $\lambda_E \propto \left(c/c^*\right)^{4/3}$, when the reduced concentrations significantly larger than one, $c/c^* > 1$ [143]. This stronger power-law dependence for systems like the Vinnol E22/48A studied here, was argued to be the result of the presence of entanglements and shear thinning and solvent quality [142].

As seen from Equation 1.17, it is the extensional relaxation time along with the shear viscosity of a given fluid that will dictate whether the elasto-capillary flow regime will be observable in CaBER-DoS or during the breakup of a jet into drops during inkjet print. Rearranging Equation 1.17, we find for the elasto-capillary drainage regime to be visible, $\lambda_E/\eta > 4.7R_{\min}/\sigma$. For the case or the solutions studied here with MEK as the solvent and a 5μm resolution of our optics, the ratio of relaxation time to shear viscosity must be larger than $\lambda_E/\eta > 9.8\text{x}10^{-4}\,\text{Pa}^{-1}$ in order for an viscoelastic filament to be observed. In reality, however, for the elasticity of the fluid to have a significant impact on the drainage and the time to breakup, elastic effects should become important at a radius much larger than the optical resolution of the high-speed video camera. In Figure 43, the time required for each solution to break up from an initial diameter of D = 250μm is plotted as a function of the zero-shear-rate viscosity of each fluid. An approximately linear increase with increasing shear viscosity is observed for all the inelastic solutions. The onset of elasto-capillary drainage breaks down this linear relationship. This is easiest to observe in Figure 43 for the case of the higher molecular weight Vinnol E22/48A because of its large relaxation time and Trouton ratio. Note, that even though they are not easy to observe in Figure 43, small deviations from linearity do exist for the highest concentrations of the

Paraloid-B66, CAB-381-2 and Vinnol E15/45M tested. They are difficult to see because of the extremely short relaxation times of these solutions and because the magnitude of the deviation found for the Vinnol E22/48A required the x-axis to be stretched to accommodate the data.

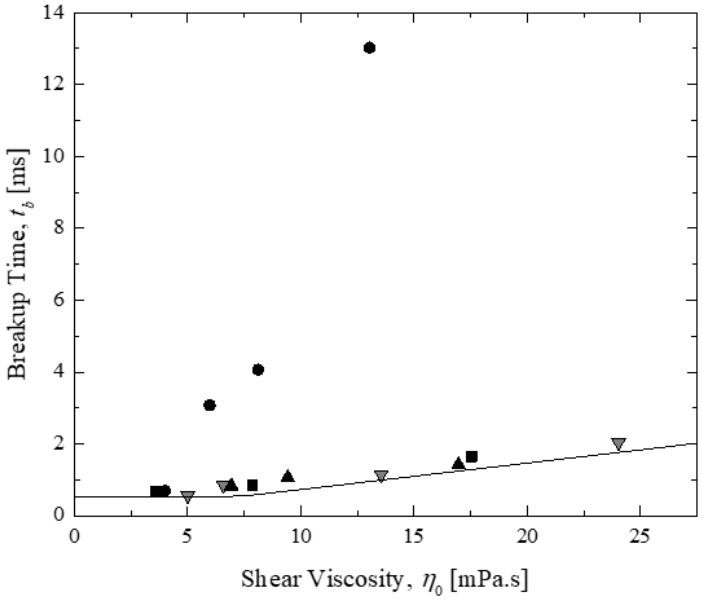

Figure 43. Breakup time from *D* = 250mm for each of the solutions tested in CaBER-DoS as a function of shear viscosity of each solution. The data include: CAB-381-2 (▲), Vinnol E15/45M (■), Vinnol E22/48A (●) and Paraloid B66 (▼) solutions in MEK. A line showing the theoretical prediction of breakup time for a Newtonian fluid given by Equation 10 is superimposed over the data.

The variation of the data with shear viscosity for a Newtonian fluid can be understood by manipulating Equations 1.11, 1.12, 1.14 and 1.15 to find the breakup time for a fluid initially in the inertio-capillary drainage regime and transitioning to the visco-capillary regime when $U_\rho = U_\eta$. The breakup time becomes.

$$t_b = \left(\frac{\rho}{0.26\sigma}\right)^{1/2}\left(R_0^{3/2} - R_{trans}^{3/2}\right) + \frac{R_{trans}}{0.0709}\frac{\eta}{\sigma}, \qquad (0.20)$$

where the R_{trans} is the radius at which the drainage transitions from the inertia-capillary to the visco-capillary regime,

$$R_{trans} = 45.8\frac{\eta^2}{\rho\sigma}. \tag{0.21}$$

The theoretical predictions of Equation 1.20 do a good job of predicting the breakup time and its change with increasing solution viscosity. Note that the breakup time does not quite increase linearly with shear viscosity as the transition radius depends on the viscosity of the solutions. As a result, increasing viscosity increases the transition radius and causes the filament decay to reside within the slower visco-capillary regime for more time. Beyond a viscosity of η_0 > 25mPa.s, the drainage from D = 250μm is entirely within the visco-capillary regime. A similar approach can be attempted for a transition from a visco-capillary to an elasto-capillary drainage, but here one has two fluid properties that are varying; viscosity and relaxation time. As a result, a universal line like the one from Equation 1.20 cannot be superimposed on the data in Figure 43. Nonetheless, the breakup time for the viscoelastic solutions studied here can be calculated from theory once the relaxation time has been fit. This of course is a bit of a recursive argument as it is this same theory that we are using to fit the relaxation time in the first place. Here the visco-capillary breakup time becomes

$$t_{b,vc} = \frac{R_0 - R_{trans,vc}}{0.0709}\frac{\eta}{\sigma} - 3\lambda_E \ln\left(\frac{R_{cut-off}}{R_{trans,vc}^{4/3}}\left(\frac{2\sigma}{G}\right)^{1/3}\right) \tag{0.22}$$

As in Equation 1.17, the transition radius is given by $R_{trans,vc} = \frac{\lambda_E\sigma}{4.7\eta}$ and $R_{cut\text{-}off}$ = 5μm is the cut-off radius where we assume the filament has broken. Here we chose the resolution of our optics for the cut-off radius. This analysis assumes the polymer does not

reach its finite extensibility limit during the necking of the fluid filament. As a result, this approach does not work well for the high molecular weight Vinnol E22/48A solutions, as it over predicting the breakup by quite a significant amount. Unfortunately, to understand the breakup dynamics of these highly elastic systems a full FENE-P solution like that found in Wagner et al. [140] is likely necessary. Of course this is only possible after fully characterizing the rheology of the fluid like we have done in this paper.

Table 6. Rheological data for the solutions of the four different polymer binders studied. Data includes the shear viscosity measured in a Couette rheometer, η_0, the shear viscosities, η_{fitt}, obtained through a fit of the Equation 2 to the CaBER-DoS data, and the extensional relaxation time, λ_E, obtained through a fit to Equation 3 to the CaBER-DoS data

CAB-381-2			
Concentration [wt%]	η_0 [mPa.s]	η_{fitt} [mPa.s]	λ_E [µs]
5	9.4	12 ± 0.4	-
6	16.9	17 ± 0.2	71 ± 1
Vinnol E15/45M			
12	7.9	11 ± 0.5	-
16	17.5	18 ± 0.5	78 ± 2
Vinnol E22/48A			
6	6.0	-	740 ± 43
8	8.1	-	1000 ± 50
10	13.0	-	1700 ± 65
Paraloid B66			
20	6.9	11 ± 0.4	-
25	13.3	18 ± 0.6	-
30	25.0	26 ± 0.5	146 ± 3

4.4 Conclusion

In this paper, the capillary thinning dynamics of a series of solutions containing polymers commonly used in the coating industry as low-viscosity printing inks were studied. Four different polymer binders were studied in the same MEK solvent. These polymers included one acrylic polymer (Paraloid B66), one cellulose polymer (CAB-381-

2) and two vinyl polymers of a low (Vinnol E15/45M) and higher (Vinnol E22/48A) molecular weight. The dripping-onto-substrate capillary breakup extensional rheometry (CaBER-DoS) method was used to characterize the extensional rheology for solutions with viscosities as low as η_0=3.5mPa.s and relaxation times ranging from unmeasurable all the way to λ_E=1700μs. This technique is based on the measurement of the decay of a fluid filament under the influence of surface tension and has been shown to be capable of measuring extremely small relaxation times for weakly elastic liquids. Here we showed that by utilizing a single image in time, relaxation times as low as λ_E = 13.4μs could be measured from the diameter decay of these model inkjet fluids. These relaxation times are the smallest ever reported in the literature.

The influence of the polymer concentration on the dynamics of filament breakup was investigated for each polymer solution and the results were compared to those obtained with different polymer binders. With an increase in polymer concentration, a critical concentration was identified for the transition between the inertio-capillary, the visco-capillary and the elasto-capillary breakup regimes. These values were found to vary quite strongly with the polymer molecular weight as well as with its backbone chemistry and its resulting rigidity. Increasing molecular weight and decreasing backbone rigidity were both found to reduce the concentrations needed to observe elasto-capillary drainage while increasing the relaxation time and extensional viscosity of the resulting solutions. Within the elasto-capillary breakup regime, the transient extensional viscosity resulted in Trouton ratios ranging from just above the Newtonian limit of Tr = 3 to values close to Tr = 100.

With the onset of elasto-capillary breakup at moderate to high polymer concentrations, a delay in the filament breakup was observed due to the rise of viscous and

elastic stresses. The change in breakup time was predicted by a series of simple theoretical models. These viscous and viscoelastic breakup time delays, if significant, could be detrimental to most ink jet printing applications. The CaBER-DoS technique, thus appears to be an extremely useful technique for evaluating potential fluids for their jettability and suitability for use in ink jet applications.

4.5 Acknowledgement

The authors would like to thank Markem Imaje for funding this research and Christian Clasen of KU Leuven for use of the Edgehog software.

4.6 Publication

The work described in this chapter has been published in the Journal Of Non Newtonian Fluid Mechanics. The complete reference is M Rosello, S Sur, B Barbet and J P Rothstein “Dripping-onto-substrate capillary breakup extensional rheometry of low-viscosity printing inks, Journal of Non-Newtonian Fluid Mechanics 266, 160-170, 2019).

CHAPTER 5

TRANSLATIONAL AND ROTATIONAL MOTION OF DISK-SHAPED MARANGONI SURFERS

5.1 Introduction

Marangoni flows are induced by a gradient in interfacial tension resulting from a local variation of composition or temperature [144]. In the past Marangoni flows have been used for propulsion of small objects attached to a fluid-fluid interface. In biological systems, self-induced Marangoni propulsion has been observed in organisms ranging in size from bacteria to water-walking insects. For example, surface-associated bacteria such as *Pseudomonas aeruginosa* have been shown to use signaling molecules exuded from their bodies to reduce the local surface tension. They have been observed to use the Marangoni flow that results to rapidly migrate across the air-water interface towards nutrient-rich regions ripe for colonization [145, 146]. In the case of water-walking insects like Dianous (rove beetle) and Velia (small water strider), these insects have been shown to secrete surface-active materials to boost their water walking speed in emergency situations [147-150].

In the case of man-made objects, perhaps the most ubiquitous example of Marangoni propulsion is the camphor boat [151-153]. Suematsu et al. [152] investigated the motion of a camphor boat by placing a disk of camphor underneath a small boat. They observed a number of different propulsion modes including continuous, intermittent or an oscillatory motion depending on the placement location of the camphor disk on the boat. They explained these different modes as being the result of differences in the diffusion length of the camphor from beneath the boat to the air water interface. Renney et al. [153]

investigated the Marangoni propulsion of a series of different shaped boats using a number of low-surface-tension water-miscible solutions to induce surface tension gradients. Their investigations showed that symmetric boat designs tended to move with a straight-line motion while asymmetries in the design of the boat could be used to induce rotational motion of the boat. Rotation of other asymmetric particles has been commonly observed in the literature. Nakata et al. [154] showed through experimental studies on camphor scrapings that the direction of rotation motion is governed by the shape and asymmetry of the particle. In some cases, the asymmetry was specifically designed to maximize rotation rate to create interfacial Marangoni rotors [155].

Even in the absence of Marangoni propulsion, objects floating on an air-water interface can spontaneously move because of interfacial curvature. For a dense particle, with a large contact angle, floating on the surface of a liquid, the weight of the particle can deform the fluid interface downward. On a flat interface devoid of other particles, interfacial curvature alone will not result in particle motion. However, the presence of a second dense particle or a wall around which a similar interfacial curvature exists will result in an attractive force between the particles that scales like the inverse of their separation and will result in spontaneous particle motion [156]. This is because for two objects that have like (concave or convex) curvature around them, both the gravitation potential energy and the capillary energy will decrease as the objects approach each other [156]. This attractive force can result in the self-assembly of floating objects into particle rafts [157-161] or the accumulation or particles near regions of high interfacial curvature [162, 163].

In this study, we investigated the motion of a self-propelled axisymmetric Marangoni surfers in order to understand the role of propulsion strength, Reynolds number and interface curvature on its motion and the details of the flow around it. In these experiments, a cylindrical disk was propelled either by a solution of isopropyl alcohol (IPA) or a commercially-available soap. The motion of the disk was optically tracked while the details of the fluid dynamics were probed using Particle Image Velocimetry (PIV). At low speeds and low Reynolds numbers, the disks were observed to move in a straight line. However, disks moving at higher speeds, above a critical Reynolds number, were observed to spontaneously rotate. Through PIV measurements, this rotational motion was found to be directly linked to the shedding of an attached vortex. Under the right conditions, the presence of a confining boundary wall with and without interface curvature was also found to result in particle rotation, although at a significantly lower Reynolds number. These studies are the first to show that a transition from linear to rotational motion can exist for a self-propelled Marangoni surfer even if the surfer is axisymmetric.

5.2 Experimental Setup

Experiments were performed in a large and small Petri dish of diameter D=150mm and D=86mm as shown in Figure 44. The depth of water was maintained at h=50mm in the large Petri dish and at h=12mm in the small Petri dish. In both cases, the motion of the Marangoni surfers was found to be insensitive to the depth of the water in the Petri dish. All the experiments were performed in the large petri dish except for the experiments where the effect of the boundary wall on the mode of motion of the Marangoni surfer was probed. Isopropyl alcohol (IPA) and commercially available soap (Dawn) were used to induce the gradient in surface tension needed to produce the desired Marangoni flow. This was done

by dip coating one quarter of the cylindrical disk in a number of different strength solutions of IPA and water or a solution of 50% soap and water as shown in Figure 44. The surface tension of pure IPA was taken from literature to be σ = 22mN/m, while the surfactant in the Dawn soap is known to reduce the interfacial tension of water from σ = 72mN/m to 30mN/m [164]. The cylindrical disk had a diameter of D_{disk}=4mm and a thickness of t_{disk}=1mm. The disks were fabricated from polydimethylsiloxane (PDMS) which has a density of ρ=965Kg/m^3. Due to the near density matching of the disks with the water they displaced, a close optical inspection of the interface around the floating disk showed little to no deformation or curvature.

The disks were placed on to the air-water interface and released using a mechanical stage to ensure a reproducible release protocol. The disks were initially balanced on the top of a post measuring 30mm tall with a diameter of 3mm. The post was connected to a stepper motor through a thin cantilever fully submersed in the water. To deposit the disk, the post was driven down at a velocity of 10mm/s and submersed to a depth of 3mm below the water's interface. As a result, from initial touchdown to release of the disk, the disk was held stationary by the post for 0.1s before it was allowed to move freely. A digital camera was used to track the motion of the swimmer. The videos were captured at 17fps and the images fed into a particle tracking software (Tracker) which was used to analyze the motion of the particles. For the Particle image velocimetry (PIV) measurements, a 300mW argon ion laser was used to create a laser light sheet and illuminate $40\mu m$ PIV particles dispersed in the water and captured using a high speed video camera. PIV measurements were used to analyze the flow field induced by Marangoni flow along the air-water

interface and underneath the disk. The PIV videos were analyzed using a commercial PIV software (LaVision).

In order to study the effect of confinement and the role that interface curvature can play on the motion of the disk, the small petri dish was used. At the edge of the petri dish, a concave, convex, or a flat interface was created by first filling dish with water until the contact line was pinned to the top edge of the petri dish as shown in Figure 45. Once the contact line was pinned, a syringe pump was then used to either add or withdraw 9ml of water to produce the desired curvature of the air-water interface.

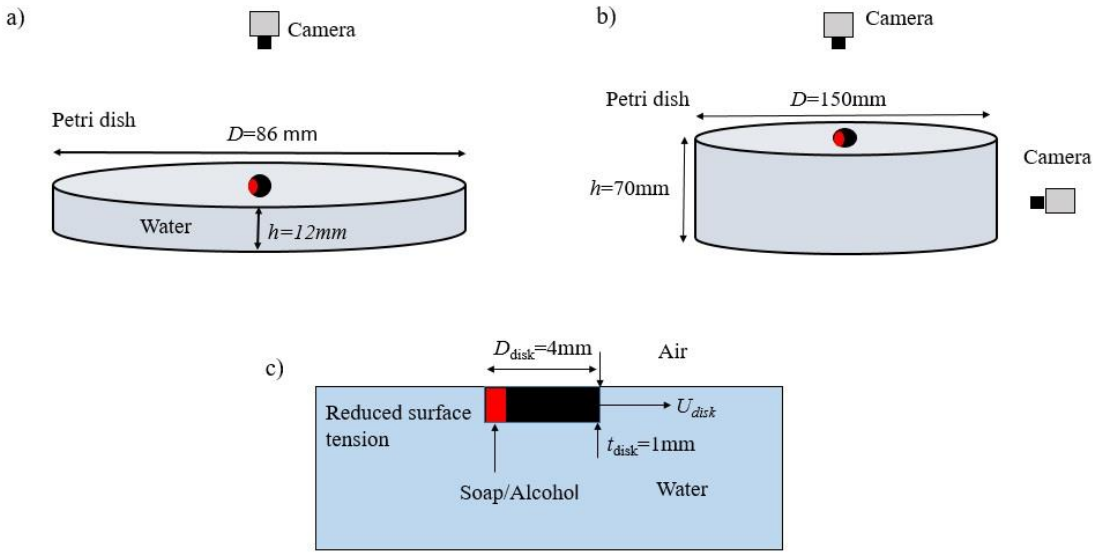

Figure 44. A schematic of the experimental setup of a a) small and a b) large Petri dish. The diameter of the small Petri dish was *D*=86mm and the large Petri dish was *D*=150mm. The depth of water in the small Petri dish was maintained at *h*=12mm and in the large Petri dish it was maintained at *h*=50mm. Two different optical setups were used for recording as shown in a) and b). Side view of the D_{disk}=4mm and t_{disk}=1mm cylindrical disk is shown in (c). The disk is propelled by Marangoni flow induced by soap/alcohol released on the back of the disk in the area denoted in the red region.

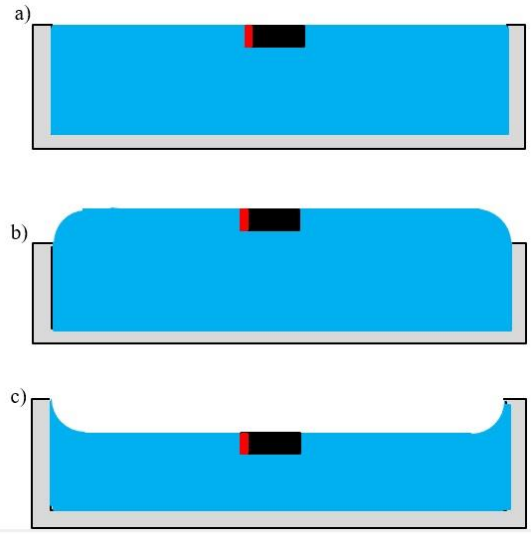

Figure 45. A schematic of interface curvature at the boundary of a *D*=86mm Petri dish showing a) a flat b) a convex and c) a concave interface.

5.3 Results and Discussions

5.3.1 Motion of a Disk-Shaped Interfacial Swimmer Propelled by Soap

In this section, the motion of the disk-shaped Marangoni swimmer that uses soap as the propulsion agent is presented. As described in section 5.2, a solution of 50% soap and water was used to coat over one quarter of the disk, Upon deposition of the disk onto the air-water interface, the surfactants in the soap quickly began to dissolve in the water and to populate the air-water interface reducing its interfacial tension towards $\sigma = 30\text{mN/m}$ which is the interfacial tension value if the water interface is fully saturated with surfactant. The minimum surface tension will arise where the surfactant concentration at the interface is largest. As a result, the minimum surface tension should be found next to the regions of the disk coated by soap. The surface tension gradients that results induces a Marangoni flow along the interface that drives the observed motion of the disk. When soap was used as the propulsion agent, a linear, straight-line translation of the disk was observed. As seen in Figure 46, upon its release, the disk, initially accelerated before reaching a

maximum velocity of roughly U_{disk}=14mm/s after a time of t=0.7s. This translates to a maximum Reynolds number of, $Re = \rho U_{disk} D_{disk} / \mu = 60$ where, ρ is the density of the fluid, U_{disk} is the maximum velocity of the disk, D_{disk}, is the diameter of the disk and μ is the dynamic viscosity. During the initial start-up of motion, the acceleration was found to remain roughly constant at a= 25mm/s^2. Beyond the peak velocity, the disk was found to decelerate slowly before reaching a steady-state velocity of U_{disk}=4mm/s (Re=16) approximately t=5s after the disk was released. This steady state motion was observed for several minutes or until the disk collided with the wall of the Petri dish. These observations suggest that, at long times, a constant release rate of the soap was achieved to the interface. The duration of this steady-state motion is a function of the quantity of soap applied to the boat as well as the rate at which the soap is dissolved into the water.

Finally, it is important to note that, in these experiments, the variations in the surfactant concentration field is dominated by convection of the induced Marangoni flow and not the diffusion of the surfactant molecules across streamlines. This can be demonstrated by calculating the Peclét number, $Pe = D_{disk}U_{disk}/D$, where the appropriate length scale is the diameter of the disk, D_{disk}, U_{disk} is the velocity of the disk and D is the diffusion coefficient of the surfactant in water. Given that the diffusion coefficients for the two surfactants in the soap, sodium laureth sulfate and sodium lauryl sulfate, are approximately $D \sim 10^{-9}$ m^2/s, the resulting Peclét number becomes extremely large, $Pe \sim 10^5$.

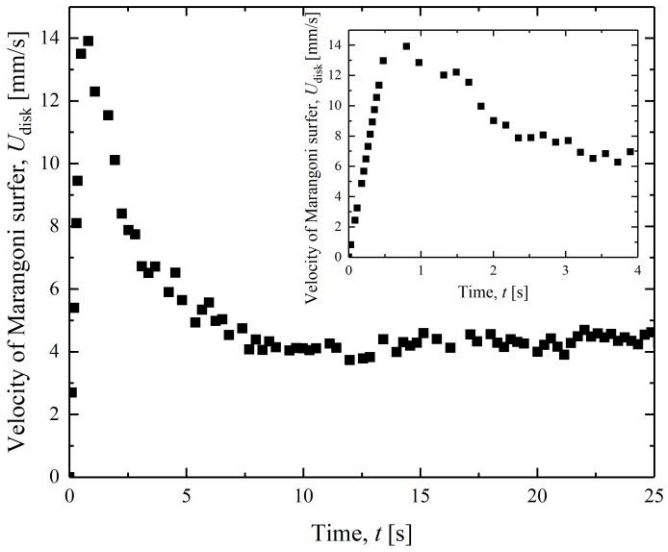

Figure 46. Plot of disk velocity, U_{disk}, as a function of time, t, for the Marangoni swimmer using surfactant as the propulsion agent. Inset shows close up of data at early times.

4.3.2 PIV of the Flow Field around a Disk-Shaped Interfacial Swimmer Propelled by Soap

In this section, Particle Image Velocimetry (PIV) measurements of the flow field in the water around a disk-shaped Marangoni swimmer propelled by soap are presented. Flow fields at various stages during the motion of the disk are presented to highlight the evolution of the fluid dynamics that occur as the disk is released.

In Figure 47, PIV measurements of the interfacial flows around the disk is shown for the disk undergoing a steady-state constant velocity translational motion as shown in the final 20s of data in Figure 46. As the steady-state translation is the simplest case we have chosen to analyze it first. In Figure 47, the disk motion is from left to right. As seen in Figure 47, the interface appears to dilate, spreading radially from a stagnation point roughly one diameter downstream of the trailing edge of the disk. The stagnation point in the PIV data represents the location of the minimum in the interfacial tension. It is from

the trailing edge of the disk that the surfactants is released and where the interfacial tension is minimized. The presence of a stagnation point in the wake of the disk is not surprising, however, its location is perhaps unexpected. Although the bulk concentration of surfactant should be maximized in the fluid adjacent to the coated regions of the disk, a finite adsorption time, t_{ads}, is required for the surfactant to diffuse to and then populate the air-water interface. During the adsorption time, the disk has moved a distance $L=U_{disk}\ t_{ads}$, which, given the velocity of the disk and typically adsorption times for surfactant, can mean the minimum interfacial tension can exist a millimeter or more downstream of the disk. Although this argument can begin to explain the movement of the stagnation point into the wake of the disk, it still under predicts the extent of movement. To fully understand the location of the stagnation point likely would require an understanding of how the three-dimensional (3D) flow around the disk affects the surfactant concentration near the interface. In order to better understand the interfacial flow, a centerline velocity profile of the interfacial flow upstream and downstream of the disk is shown in Figure 47b. Here, the interfacial velocity has been normalized by the disk velocity, U/U_{disk}, and the x-position has been normalized by the diameter of the disk, x/D_{disk}. The presence of the stagnation point can be seen more clearly here at a position of x/D_{disk} =-1.5. Note that x/D_{disk} =0 represents the center of the disk. From the interfacial velocity profile it can also be observed that the interfacial velocity in the wake decays at a much slower rate compared to the velocity upstream of the disk. The far-field interfacial velocity was found to require a distance of $10D_{disk}$ to decay from its maximum to zero in the wake of the cylinder and a distance of $7D_{disk}$ to decay to zero upstream of the disk. For both the upstream and downstream of the disk, the interfacial velocity was found to decay like $1/x$ which is

consistent with the predictions and experiments performed on interfaces dilated by a drop of surfactant in the absence of a Marangoni surfer [165]. The maximum velocity observed in the wake was roughly the same as the velocity of the disk U/U_{disk}=-1, while the maximum velocity upstream of the disk was roughly 10% higher, U/U_{disk}=1.1. This is expected as some relative velocity between the interface and the disk is needed to provide enough propulsive force to overcome the resistive drag force exerted by the water beneath the disk. In this steady-state, constant velocity regime, these forces are well balanced.

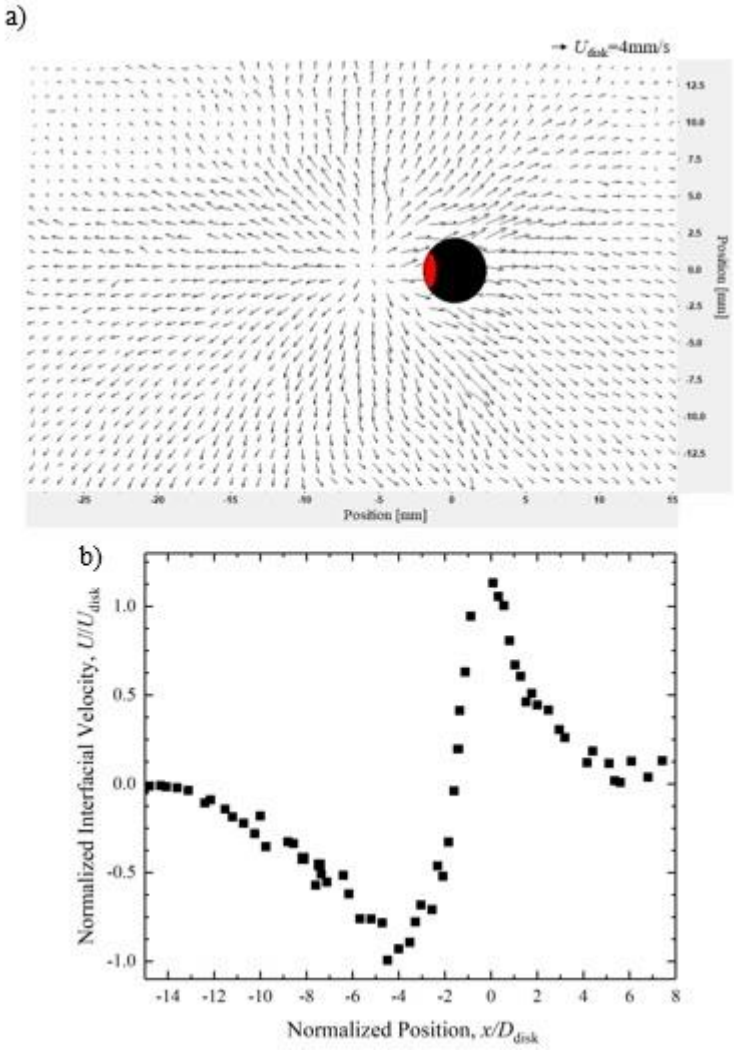

Figure 47. a) Plot of the particle image velocimetry measurements of the steady state flow field around a floating disk propelled by the Marangoni flow induced by soap released from the disk in the area denoted by red region at its rear. b) Plot of the normalized interfacial centerline flow velocity, U/U_{disk}, as a function of normalized position, x/D_{disk}. The center of the disk is placed at x=0. A velocity vector scale bar is presented in a).

The transient motion of the cylinder during the start up flow can be broken down into two distinct regimes. The first occurs during deposition of the disk onto the air-water interface. In this regime, the disk is held stationary during this process even as the surfactant is released into the water. The disk is released once the the full thickness of the disk has been submerged. This process takes 0.1s. The second regime involves the

acceleration of the disk upon release. In Figure 48, PIV measurements of the interfacial flows around a stationary disk are shown for a disk held within a Maranogni flow field induced by the relase of soap. As before, the interface is observed to dilate from a stagnation point at the water interface downstream of the disk. Interestingly, even without disk motion, the stagnation point is not attached to the trailing edge of the disk, but at a point roughly $x_{stagnation}/D_{disk}$ =-0.8 downstream of the disk. Although this is significantly closer than the steady-state flow case presented previously, it clealry shows the importance of the 3D flow field in the wake of the disk and in particular the upwelling of the liquid in the wake needed to replace the fluid spreading radially outwards along the interface from the stagnation point. The magnitude of the velocity (to the left) in the wake of the disk was found to be a factor of four time larger then the velocity along the interface upstream (to the right) of the disk. This difference can more easily be observed from the centerline interfacial velocity in Figure 48b. The maximum velocity at the interface in the wake of the disk was found to be U=8mm/s, whereas, the the maximum velocity upstream of the disk was found to be U=2 mm/s. In addition, a clear velocity deficit can be observed along the interface to the right of the disk. The velocity deficit affects a section of fluid roughly one diameter wide all the way to the edge of the field of view. If the flow field were 2D and not 3D, an integration of the velocity deficit could be used to calculate the drag force exerted on the disk. In this region, the x velocity decay seen previously for the steady-state case is not recovered.

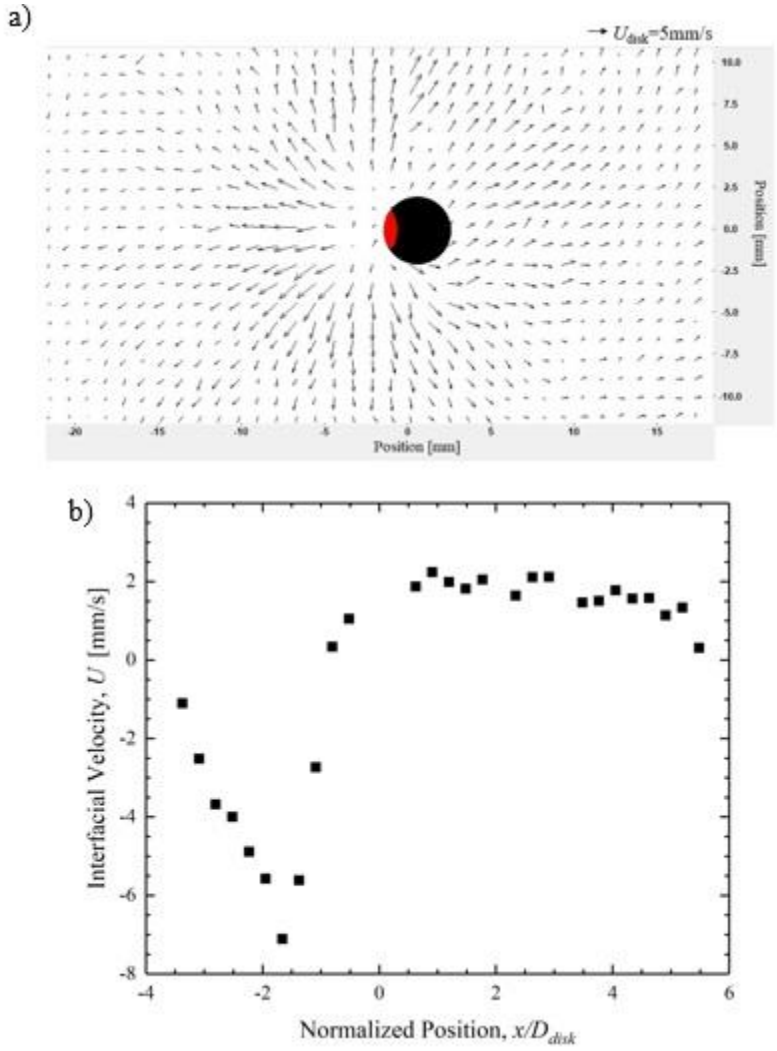

Figure 48. a) Plot of the particle image velocimetry measurements of the transient flow field around a stationary disk (U_{disk}=0) floating on an air-water interface with a Marangoni flow induced by soap released on the left side of the disk in the region denoted by red. b) Centerline velocity profile of the interfacial flow upstream and downstream of the disk. The center of the disk was placed at x/D_{disk}=0.

In Figure 49, a snapshot of the interfacial PIV vector field is shown t=0.2s after the stationary disk in Figure 48 was released. As seen through a comparison to the PIV in Figure 48, the start-up of motion of the disk drastically changes the interfacial velocity field. In Figure 49, the instantaneous velocity of the disk was found to be U_{disk}=6mm/s and it is accelerating. In the wake of the cylinder, the maximum interfacial velocity was found

to be unchanged from the stationary case in Figure 48 at U=7mm/s. Upstream of the disk the interfacial velocity increased from 2mm/s in the stationary case to U=9mm/s. Additionally, the velocity defect observed in Figure 48, is not evident in Figure 49 suggesting a large reduction in the drag force exerted by the disk on the surrounding fluid. The maximum flow velocity was roughly 50% larger than the disk velocity, U/U_{disk}=1.5. In Figure 49b, the stagnation point can be observed at a distance of x/D_{disk}=0.7 downstream of the trailing edge of the disk. This is similar to the separation distance of the stationary disk and closer than its eventual location at steady state. The slow evolution of the stagnation point further downstream could be a result of the decreasing rate of surfactant release with time. As the disk convects away from the regions of the highest bulk concentration the location on the interface with minimum surfactant concentration might shift further downstream towards the surfactant rich regions where the disk was deposited. In all the cases with soap, no vortices were observed at the air water interface around the disk. This is important to note for comparison with the results from when IPA is used as the propellant.

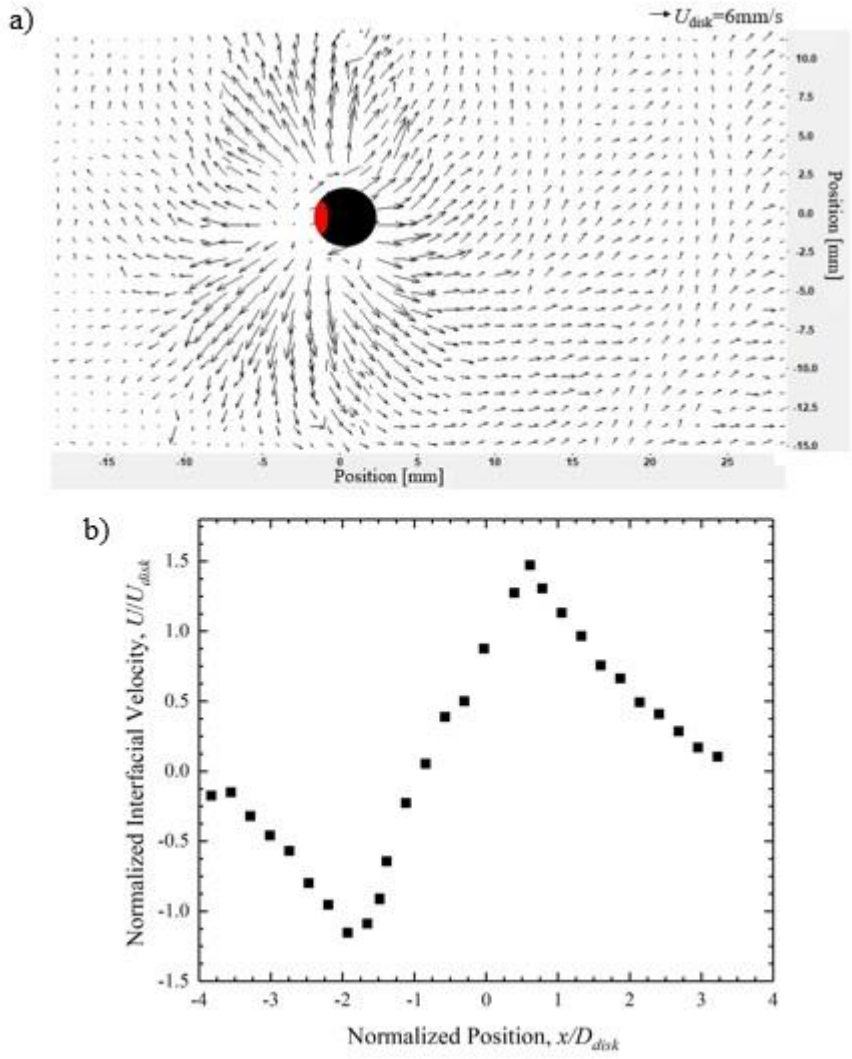

Figure 49. Plot of the particle image velocimetry measurements of the transient flow field around a floating disk propelled by the Marangoni flow induced by soap released on the left side of the disk in the area denoted in red region. The data was taken 0.2s after the disk was released b) Centerline velocity profile of the interfacial flow upstream and downstream of the floating disk. The disk velocity was measured to be U_{disk}=6mm/s. A scale bar is presented in a).

In order to better understand the details of the 3D flow profile around the disk, the laser light sheet was oriented vertically and passed into the Petri dish from below. The resulting PIV vector fields show the velocity profiles in a plane that bisects the disk along the direction of motion. A high speed camera capturing 100fps was used to image the flow

from the side. In Figure 50, PIV measurements are presented for a stationary disk, two disks shortly after release, and a disk at steady-state. In Figure 50a, the PIV measurements for the flow underneath the stationary disk is presented 0.2s after the disk was inserted onto the water interface. A wide, shallow vortex rotating clockwise can be observed in the wake of the disk. The center of the vortex was found to move away from the disk with time at a speed of 2mm/s. As time progressed, the strength of the vortex strength was found to decrease. The peak magnitude of the vorticity was found to be ω=8s^{-1} at t=0.2s and to ω =2s^{-1} at t=1s. A strong upward flow was observed below the disk with the vertical velocity appearing on the side of the disk where the surfactant was applied and where the stagnation point was observed along the interface. This vertical flow is required to satisfy continuity around the stagnation point. The velocity of the upward flow was found to increase as the flow approached the interface reaching a maximum velocity of U=12mm/s. The upward velocity is similar in magnitude to the maximum interfacial velocity which was found to be U=16mm/s.

In Figure 50b and 50c the flow beneath the disk is presented 0.1s and 0.5s after the disk was released on the water interface. These two PIV vector fields are shown so that the evolution of the vortex structure with time can be observed during start-up as the disk accelerates from U_{disk}=0mm/s to 4mm/s and finally to 8mm/s. As time progressed, the vortex formed in the wake of the disk was shed downstream of the disk. The strength of the radially outward flow was observed to increase and the flow underneath the disk transitioned from a purely vertical in the stationary case to moving with the disk velocity after the start-up. In Figure 50d, the flow underneath the disk is presented after the disk has attained a steady state velocity of U_{disk}=3mm/s. the flow field in Figure 50d is clearly

different from either the stationary or start-up cases in 50a-c. The main differences are the lack of attached vortex in the wake of the disk and the presence of an attached vortex rotating in the clock wise direction directly beneath the disk. This vortex was found to be stable with time and remain attached for all other steady-state measurements made. This vortex exists because in order to maintain conservation of mass in the Petri dish, if the interface is moving to the right then an equal mass fluid below the interface must be moving back to the left. This flow reversal with increasing depth in the water is clearly evident in Figure 50d.

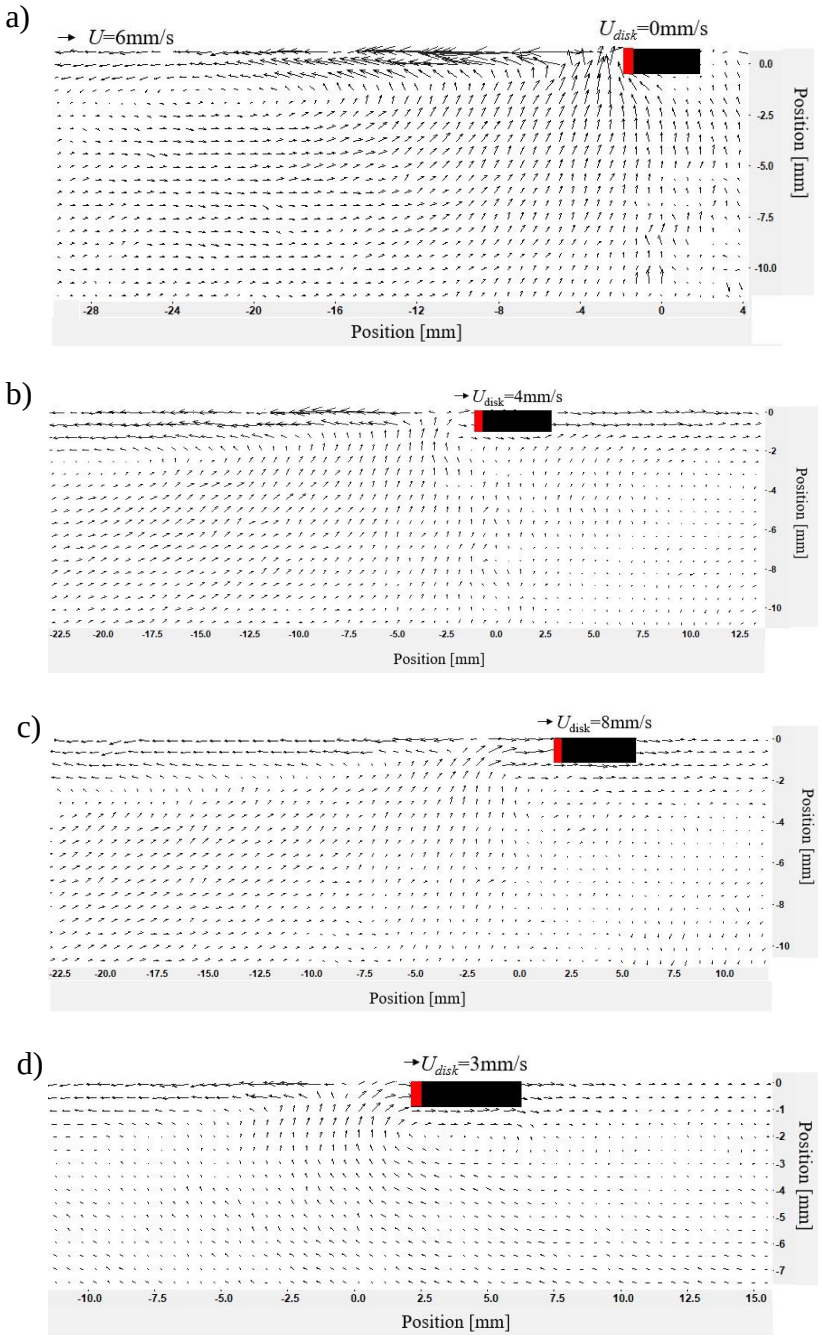

Figure 50. Plot of the particle image velocimetry measurements of the flow field underneath a floating disk propelled by the Marangoni flow induced by soap released on the right side of the disk in the area denoted in red for a) a stationary disk at *t*=0.2s after immersing it in water, b) the startup flow *t*=0.1 s after the disk was released, c) the startup flow 0.5s after the disk was released, and d) a steady state disk velocity of U_{disk}=3mm/s. Scale bars are presented in each sub figure.

5.3.3 Motion of Disk-Shaped Interfacial Swimmers Propelled by Isopropyl Alcohol

In this section the effect of changing the strength of the propulsion agent is investigated by switching to isopropyl alcohol (IPA). The interfacial tension of IPA and the air-water interface saturated with surfactant are similar. However, IPA is a smaller, more mobile molecule that does not need to adsorb to the air-water interface to change the local interfacial tension. It simply needs to dissolve in the water and mix. The result is a fast-acting intense propulsion that is depleted much more quickly than the soap. The velocity profiles for a series of disks propelled by Marangoni flow induced by IPA are presented in Figure 51. The propulsive strength of the IPA was varied by diluting it from 100% to 20% by weight IPA with water to investigate the effect of varying propulsion strength. For the case of 20wt% IPA in water, a straight-line motion was observed similar to the case of soap propulsion with a maximum velocity of U_{disk}=25mm/s. The disk velocity decayed to zero quite quickly after a time period of t=2s. Unlike the case for soap discussed previously, steady-state motion was observed for the case of 20wt% IPA or any of the other, higher concentrations. This is very different from the soap case and suggests that the IPA is dissolved and depleted very quickly. For more extended propulsion, a reservoir of IPA rather than the thin coating used previously is likely needed. As the strength of IPA was increased from 30wt% to 50wt% to 100wt%, an increase in the maximum velocity of the disk was observed. From U_{disk}=60mm/s, to U_{disk}=90mm/s and finally to U_{disk}=160mm/s respectively. With increasing propulsion strength came a new mode in the disk motion. As the concentration of IPA was increased to 30wt%, an initial straight-line translational motion was found to give way to a rotational motion of the disk. As discussed in the introduction, rotational motion of Marangoni surfers has been seen before [154, 155].

However, in each of these cases the rotation was induced by asymmetry in the boat/surfer design. Here rotation has been observed for the first time for a symmetric object propelled by a Marangoni flow. On further increasing the concentration of IPA to 50wt% and then to 100wt%, the number of the rotations and the angular velocity of the disk were found to increase as seen in the trajectories presented in Figure 51b-e. In all cases, rotation was found to occur after the peak velocity was achieved and during the deceleration of the disk. In Figure 51a, the signature of a rotation can be observed as local peaks and troughs in the velocity data. The increased number of rotations is due to the increase in the duration of disk propulsion and disk motion which increased with IPA concentration. An increase in the duration of motion of the disk by a factor of two was observed as the strength of the IPA was increased from 20wt% to 100wt%. It appears that there is a critical velocity that governs the transition between linear translation and rotation. The maximum velocities of the disk observed in the case of soap which did not rotate and 20wt% IPA solutions were found to be U_{disk}=15mm/s and U_{disk}=30mm/s respectively. While for the case of 30wt% IPA that did rotate the maximum velocity was found to be U_{disk}=60mm/s. The observed rotational motion of the disk can be more easily be understood if the velocity is recast as a Reynolds number, $Re = \rho U_{disk} D_{disk} / \mu$. In Table 6, the maximum velocity and maximum Reynolds number along with the velocity and Reynolds number at the moment the disk was observed to rotate are presented for the different concentrations of IPA and soap. The data in table 7, suggest that a critical Reynolds number governs the transition from a straight-line translational motion to a rotational motion. For the case of 20wt% IPA, which did not rotate, the maximum Reynolds number obtained was found to be *Re*=112. For the 30wt% case, the disk reached a maximum Reynolds number of *Re*=260 and began

to spin after decelerating to a Reynolds number of *Re*=120. For the 100wt% IPA cases, the maximum Reynolds number achieved was *Re*=640 and the spinning occurred at *Re*=450. The critical Reynolds number for transition is difficult to precisely determine due to the transient nature of the disk motion, but it is clear the maximum Reynolds number must be greater than that achieved for the 20wt% case. As a result, these experiments suggest that the critical Reynolds number disk rotation is between $112 < Re_{critical} < 180$ is required for the disk to spin. To further investigate the interfacial flows around the disk, PIV measurements of the interfacial flow and flow beneath the disk were performed.

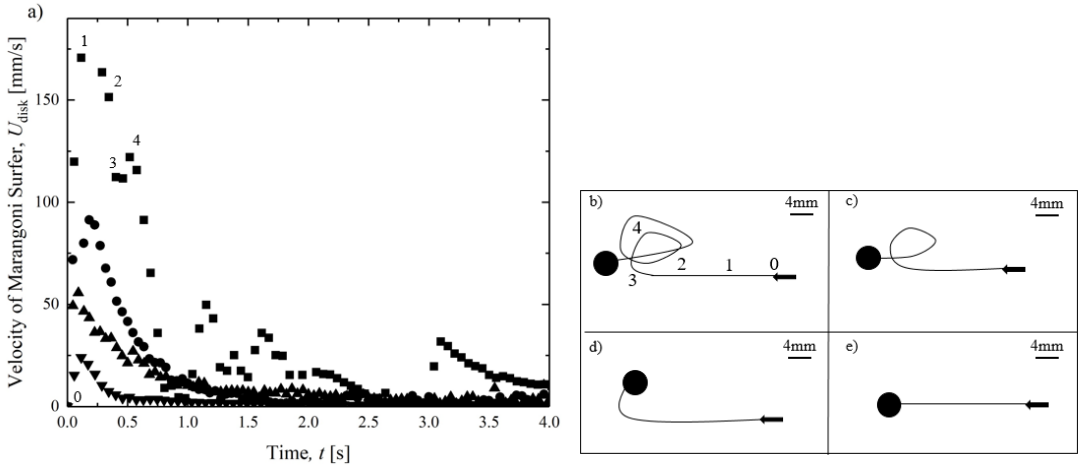

Figure 51. a) Plot of velocity of the cylindrical disk, U_{disk}, with time, t, for IPA strength of (▼) c=20wt%, (▲) 30wt%, (●) 50wt%, and (■) 100wt%. The path profile of the disk propelled by IPA showing the transition from a rotational motion to a straight-line translational motion for b) 100wt%, c) 50wt%, d) 30wt% and e) 20wt%.

Table 7. Variation of the velocity and Reynolds number for different concentration of IPA and soap used to propel the disk

IPA Concentration [wt%]	**Maximum Velocity** U_{max} [mm/s]	**Maximum Reynolds Number** Re_{max}	**Velocity Prior to Rotation** $U_{rotation}$ [mm/]	**Reynolds Number Prior to Rotation** $Re_{rotation}$
100%	160 ± 8	640 ± 30	120 ± 10	450 ± 35
50%	100 ± 10	400 ± 50	65 ± 10	280 ± 30
30%	65 ± 5	260 ± 20	40 ± 5	160 ± 20
25%	45 ± 5	180 ± 20	30 ± 5	120 ± 10
20%	28 ± 2	112 ± 8	NA	NA
Soap	15 ± 3	55 ± 10	NA	NA

5.3.4 PIV of a Disk Shaped Interfacial Swimmer Propelled by IPA

In this section, the PIV measurements of the flow field in the water around a disk-shaped Marangoni swimmer propelled by IPA are presented. Interfacial PIV measurements for the case of a stationary disk, U_{disk}=0mm/s, is presented below in Figure 52. Like the case of soap, a radially outward flow was observed downstream of the disk on the side where the alcohol was applied. Unlike in the case of soap, the presence of a pair of vortex can be observed upstream of the disk in Figure 52a. The vortices became more and more distinct as time progressed. Although the vortices of the stationary disk were observed to grow in intensity with time as seen in Figure 52b, they did not shed. The origin of these vortices arose from a feature in the IPA-induced Marangoni flow that was not intuitively expected. Upstream of the disk, the interfacial flow is not radially outward as it is in the case of soap. Instead, the flow upstream of the disk is directed towards the disk, where it then flows around and beneath the disk and into the wake downstream of the disk. This can

be seen more clearly in Figure 52c-d, which show the PIV vector fields from beneath the stationary disk. The observed flow reversal is likely due to the need for mass conservation to replace the interfacial fluid that is quickly dialating outward from the region of low surface tension in the wake of the disk. It is clear that the presence of the disk has a large impact on the resulting Marangoni flow field. For instance, if one deposits a drop of alcohol on the water surface without a disk present, a purely radial flow is observed on the interface. The main difference between the soap and the alcohol case is from the strength of the flow. Here, the outward velocity of the interface was found to reach more than 150mm/s while in the case of soap only 50mm/s was reached. The difference is enough to change the character of the flow and the dynamics of the disk motion once it is released. In Figure 52c-d, the Marangoni flow field underneath the stationary disk induced by 100wt% IPA is presented. A vortex is clearly visible downstream of the disk. With time, this vortex was observed to shed and move downstream away from the stationary disk. At t=1s the center of the vortex was found to be at x=-12mm and was found to move to x=-16mm at t=2s. The magnitude of the strength of vortex was found to decrease from $\omega=15s^{-1}$ at t=1s to $\omega=5s^{-1}$ at t=2s as the vortex was found to diffuse into the bulk as it moved away from the disk. Compared to the case of soap, for which the vortices were found to be shallow and to rotate in close proximity to the interface, the vortices observed in the case of IPA were found to be much deeper and extending further from the surface into the bulk. The strength of the vortices was also found to be larger for the case of IPA.

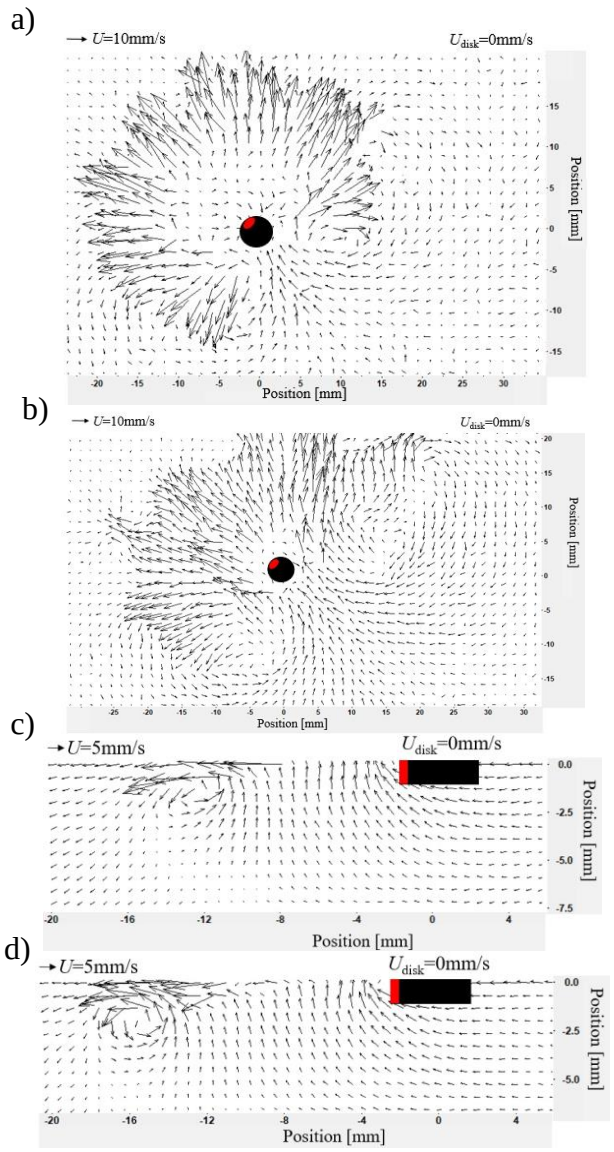

Figure 52. Plot of the particle image velocimetry measurements of the flow field upstream and downstream of a stationary disk (U_{disk}=0mm/s) within a Marangoni flow field induced by the release of 100% IPA from the back of the disk in the area denoted in red. The two figures denote time a) + c) *t*=1s and b) + d) *t*=2s after disk immersion.

In Figure 53, the Marangoni flow along the interface around a disk during its transient motion is shown at different times following deposition onto the interface. Here we are presenting the case of 30wt% IPA. The resulting flow field is quite different from

the case of a stationary disk. A radially outward flow originating from the wake of the disk was observed to propel the disk in the direction away from where IPA was introduced into the water and the surface tension was reduced. The attached interfacial vortices that were observed for the case of a stationary disk in Figure 52a+b were observed to shed as the disk was propelled forward. As the disk moved across the interface, two counter-rotating vortices attached were observed to form and remain attached to the side of the disk along its equator. These vortices were not initially obvious, t<0.3s, likely because of the resolution limitations of our PIV, but appeared quite visibly at longer times, t>0.3s, as the disk moved away from the start-up vortices that were formed upon deposition and shed in the wake of the disk. Interestingly, with the disk free to surf across the interface, the reversed flow observed for the stationary disk in Figure 52, was not seen, but instead replaced by a strong propulsive flow easily observed upstream of the disk where the interfacial tension is the largest. The formation and shedding of these interfacial vortices is not observed for the case of soap for which the maximum Reynolds number achieved was just Re=60. For the IPA cases, the Reynolds number was much greater, Re>200. The presence of interfacial the vortices is thus clearly an inertial effect. PIV measurements was also performed to investigate the flow underneath the disks propelled by IPA. In Figure 53c, the flow field induced by 30% IPA is presented for a disk t=0.5s after its release. The initial vortex produced at start-up as the disk was immersed and released onto the interface was observed to shed after 0.1s. That startup vortex can still be seen in Figure 53c, rotating counter-clockwise with positive vorticity at the time far left of the image centered around x=-15mm. After the initial startup vortex was shed a second vortex attached to the bottom of the disk was observed to grow and to rotate in the opposite direction, clockwise with

negative vorticity. Compared to the vortex observed in the case of soap, the attached vortex was not found to form beneath the center of the disk, but offset downstream towards the wake. This attached vortex was found to shed as the disc rotated. This is also quite different from the case of the soap for which the attached vortex was not observed to shed.

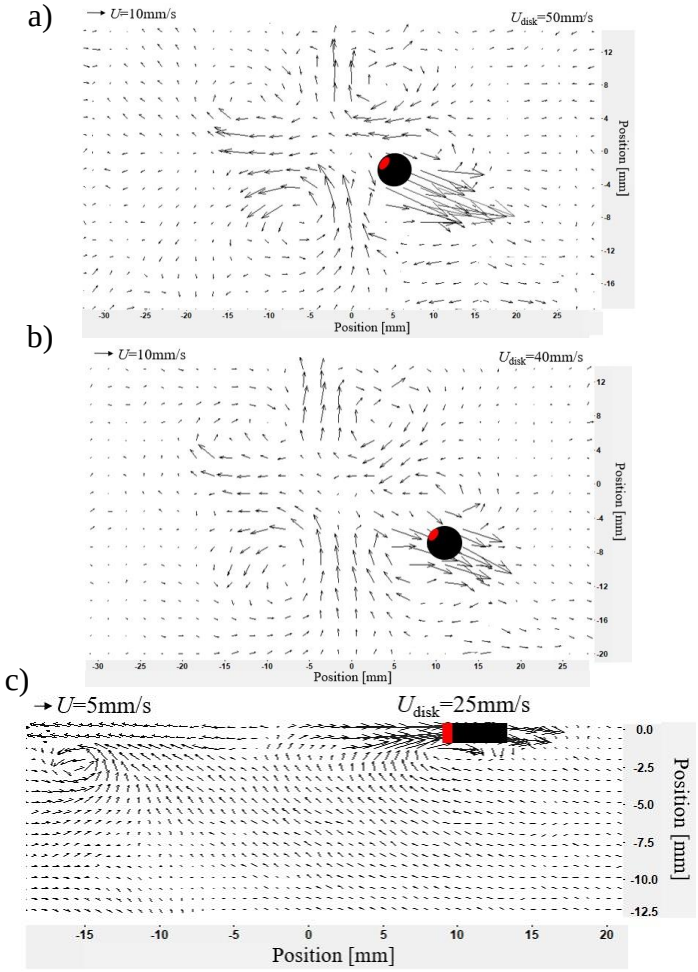

Figure 53. Plot of the particle image velocimetry measurements of the flow field upstream and downstream of a disk propelled by the Marangoni flow induced by IPA (30wt%) released on the back of the disk in the area denoted in red moving along its initial trajectory at a time of a) t=0.2 after release and a disk velocity of U_{disk}=50mm/s, b) t=0.3s and U_{disk}=40mm/s and c) flow field underneath the moving disk with disk velocity of U_{disk}=25mm/s at t=0.4s. The center of the disk was released at (0,0).

During the startup flow, three to four lobes of vortices were observed at the point of release for all the cases of different concentrations of IPA. For the case of 20wt% IPA, a straight-line motion similar to that of soap was observed. In this case, after the start-up vortices were shed, the subsequent vortices attached to the side and bottom of the disk show in Figure 54a did not shed. As the strength of IPA was increased to 30wt%, the pair of counter-rotating vortices remained attached to the side of the disk for roughly 20mm as the disc moved along its initial line of motion. However, with time, the vortex to the port side of the disk was observed to shed, resulting in a rotational motion of the disk. As the disk rotated away from its original trajectory, a jet of fluid was observed to move past its port side moving the disk to its starboard side. Multiple experiments were performed for each IPA concentration. From those experiments, it was found that the side from which the vortex shed was random and not biased to one side of the disk or the other. Similar vortex instability were observed for the case of 50wt% and 100wt%, although, with increasing IPA concentration, the shedding of vortex occurred at a higher disk velocity and Reynolds number. In each case, the shedding of vortex coincided with the transition from a straight-line motion to a rotational motion. As described previously, the strength of the rotational motion was found to increase with increasing IPA concentrations and is directly related to the vorticity of the shed vortex and the subsequent strength of the resulting jet of fluid.

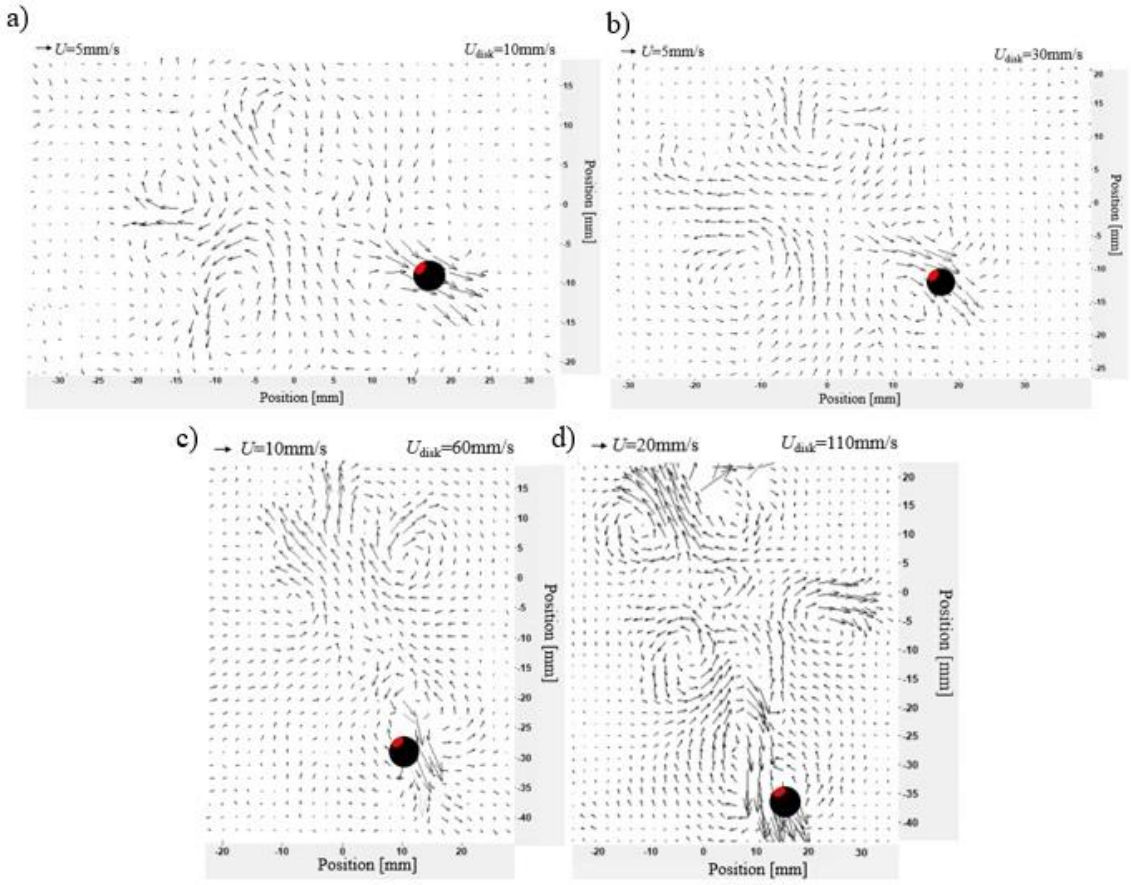

Figure 54. Plot of the particle image velocimetry measurements of the flow field upstream and downstream of a disk propelled by the Marangoni flow induced by IPA released on the back of the disk in the area denoted in red. The strength of the propulsion was varied by changing the IPA concentration from a) *c*=20wt%, to b) 30t%, to c) 50wt%, and finally to d) 100wt%. The initial point of release in each case was at (0,0).

5.3.5 Effect of Interface Curvature on the Motion of a Disk-Shaped Interfacial Swimmer

In the previous sections, the air-water interface was kept flat and the Petri dish was large enough to avoid interactions between the disk and the wall of the container. Here we will purposefully introduce end-effects and interfacial curvature to investigate their impact on the motion of a disk-shaped interfacial swimmer. Both soap and IPA will be used as the propulsion agent. The experiments were performed in a Petri dish of diameter, *D*=86mm,

and the cylindrical disk of diameter, D_{disk}=4mm, was released with the help of tweezers. As described in the experimental section, the interfacial curvature was set by pinning the air-water interface on the sharp edge of the Petri dish and then either adding or subtracting water to obtain the desired curvature.

In Figure 55, the velocity profile of the cylindrical disk propelled by soap is shown for the D=86mm Petri dishes with different interface curvature near the wall of the Petri dish. As seen in Figure 55a, for a flat interface, the disk roughly followed its initial trajectory towards the wall. After striking the boundary, the disk stopped for several seconds, rolled along the wall and eventually reversed its direction while in contact with the wall. After which, the disk was observed to move along the wall, maintaining a nearly constant distance from the boundary for a period of 30s before coming to rest. The peak velocity attained by the disk after the release was found to be U_{disk}=15mm/s for all three cases. This corresponded to a maximum observed Reynolds number of Re_{max}=60. For the case of a convex interface at the interface at the boundary of the Petri dish Figure 55b, the disk followed a straight-line motion directly into the boundary where it comes to rest and never resumed motion even though interfacial motion could still be observed around the arrested disk. Unlike in the case of the flat interface, an increase in the velocity of the disk was observed as it approached to within a diameter of the wall. This acceleration is likely due to the gravitational acceleration of the disk down the convex interface. For the case of a concave interface at the boundary of the Petri dish a straight-line motion was again observed towards the wall. However, as the disk approached the wall, it changed its direction, rotated by 180^o before striking the wall, and followed a path along the boundary. Unlike in the other two cases, the velocity never went to zero as the disk approached the

wall because it never hit the wall. Thus, a repulsive force was experienced by the cylindrical disk in the case of the concave interface likely due to the increase in gravitational potential energy needed to drive the disk up the slope of the concave air-water interface.

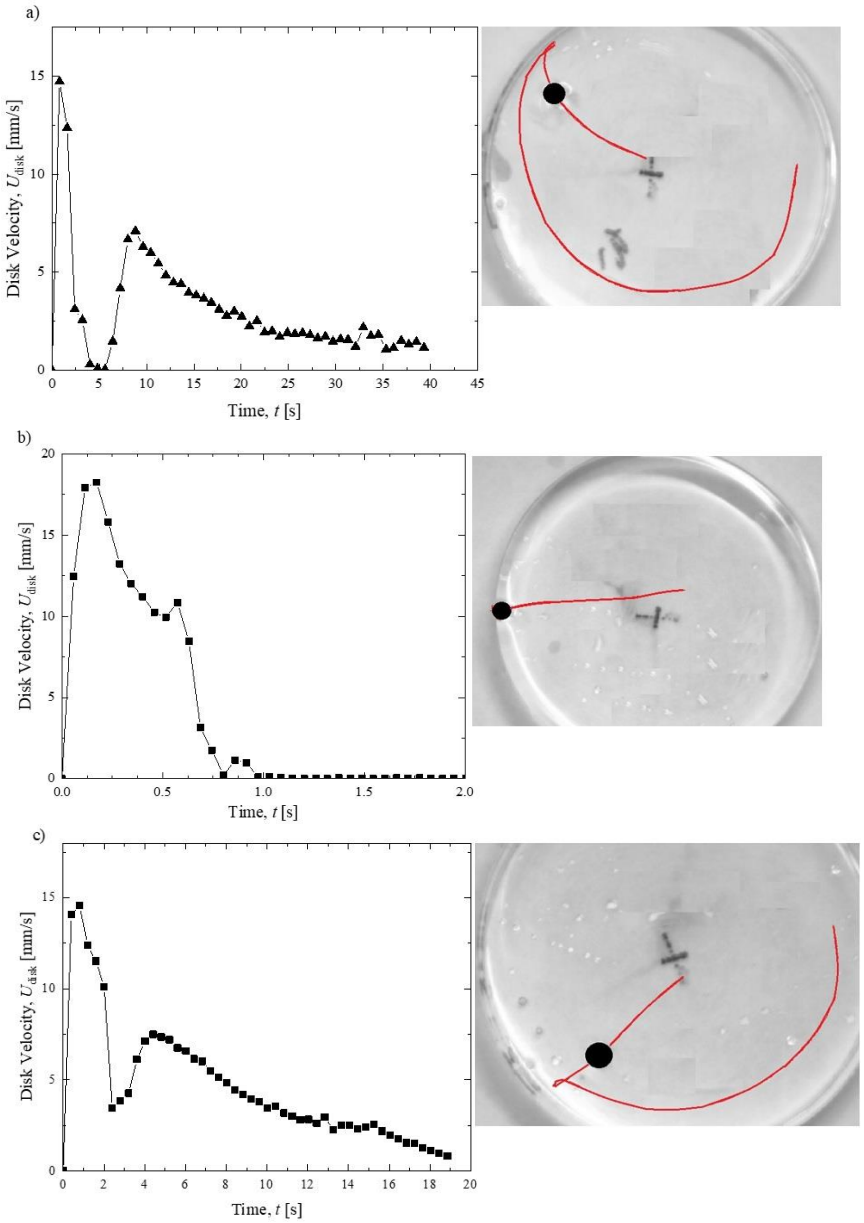

Figure 55. . Plot of the disk velocity magnitude, U_{disk}, as a function of time, t, for the disk propelled by soap for the case of a a) flat, b) convex, and c) concave interface at the boundary of the Petri-dish. The images on the right show a trace of the trajectory of the disk.

The effect of interfacial curvature at the boundary was also investigated using 100% IPA as the propulsion agent. As seen in Figure 56, an initial straight-line motion was observed in all cases. For the flat interface, the disk was observed to rotate and go through a series of loops before reaching the boundary wall. This is different from the case of soap which resulted in the disk impacting the wall. As the disk approached the wall, it must move through an adverse pressure gradient as the interfacial and bulk fluid velocity must come to rest at the wall. As a result, a pressure field is produced that decelerates the disk down. If the disk does not approach the wall along a perfectly radial path, this pressure field can provide a torque that can rotate the disk and can cause the attached vortices to shed. As before, both clockwise and counter-clockwise motions were observed based on the initial release conditions and how the particle approached the wall. A series of peaks and troughs can be seen in Figure 56a, which indicates times at which rotational motion of the disk was initiated. The average radius of curvature of the loops and the average period of rotation were found to be R=6.4mm and T=0.4s respectively for the case of flat interface. A maximum velocity of between U_{disk}=150m/s and U_{disk}=180m/s was observed in all the cases of IPA. The maximum velocity observed in the case of IPA was an order of magnitude higher than the case of the soap. For the case of a convex interface at the boundary of the Petri dish in Figure 56b, the disk followed a straight-line motion towards the wall and attached to the boundary just like the case of soap. In the case of a concave interface curvature at the boundary of the Petri dish in Figure 56c, the disk was found to follow a straight-line motion towards the wall, hit the wall, and remained pinned to the wall for 4s before propelling itself away from the wall. As the disk moved away from the boundary, a rotational motion similar to the flat interface case was observed. In some cases the disks

rotation observed for the concave interface was centered near the center of the Petri dish while in other cases the rotation was observed along the boundary of the Petri dish like in Figure 56a. Interestingly, for the case of the flat interface, the rotation was always observed as it approached the boundary wall. The average radius of curvature of the rotational motion and the average period of rotation for the concave case were found to be R=10mm and T=1.5s respectively resulting in an angular velocity of $\Omega = R/T = 6.7\text{mm/s}$. The angular velocity is significantly smaller than the value of $\Omega = R/T = 25.4\text{mm/s}$ observed for the flat interface. Finally, one interesting observation from the data. By reducing the percentage of the IPA used to propel the disk, the speed of the disk was also reduced. Whereas for the unconfined disk, a critical maximum Reynolds number of Re=120 was needed to observe disk rotation. For the case of a confined disk moving along a flat interface, a significantly lower critical Reynolds number of Re=40 was needed to observed disk rotation as it approached the confining wall.

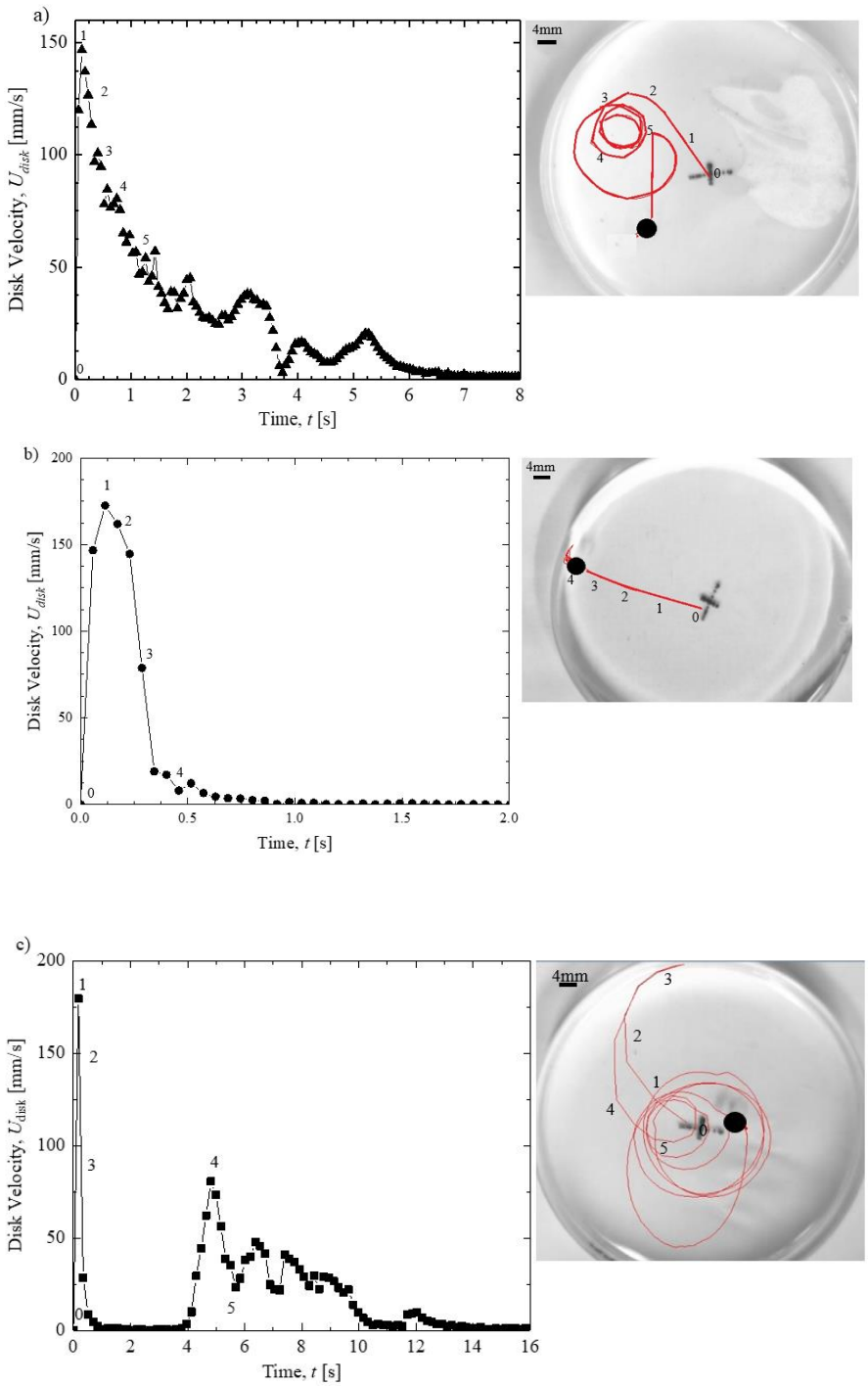

Figure 56. Plot of the disk velocity magnitude, U_{disk}, as a function of time, *t*, for a disk propelled along an air-water interface using IPA. Results are shown for a) a flat, b) a convex, and c) a concave interface at the boundary of the Petri dish. The images on the right show a trace of the trajectory of the disk.

5.4 Conclusion

In the experiments presented in this paper, we have investigated the dynamics of a disk-shaped Marangoni swimmer propelled by either soap or isopropyl alcohol (IPA) applied over one quarter of the surface of the disk. Both IPA and soap reduce the surface tension of water. The resulting surface tension gradient produces a Marangoni flow that can propel small objects, like the disks studied here, across the interface. The motion of the thin disk was tracked over time and the interfacial and bulk flows were characterized using Particle Image Velocimetry (PIV). Upon insertion of the disk onto the interface, the surface tension gradient caused the interface to dilate, spreading out radially from the side of the disk where the propulsion agent was applied and driving the motion of the floating disks. The interfacial fluid velocities and the resulting disk velocities were significantly larger when IPA was used as the propulsion agent. The maximum Reynolds number of $Re = 55$ was achieved by the disk in the case of soap, whereas, a Reynolds number greater than $Re > 600$ was achieved for IPA. At these intermediate Reynolds numbers, the role of inertia can no longer be ignored. Beyond a Reynolds number of $Re > 100$, the interfacial flow around the disk was found to separate and a pair of counter-rotating interfacial vortices were observed on the sides of the disk. At even larger Reynolds numbers, $Re > 120$, these vortices were became unstable and eventually shed. The unbalanced torques resulting from vortex shedding destabilized the straight-line translational motion of the disk-shaped Marangoni surfers and forced the disks to spin. This critical Reynolds number may limit the size of or speed at which self-propelled objects can use linear motion in the bottom-up fabrication of small functional systems [166].

Although a number of studies have used asymmetries in the design of Marangoni surfers to induce spontaneous interfacial spinning [154, 155], this study is the first to demonstrate that a symmetric Marangoni surfer can also rotate. The transition from translational to rotation motion is a strongly dependent on Reynolds number. As a result, similar rotational motion is not expected for small Marangoni surfers like bacteria because the Reynolds number of their motion is well below the critical Reynolds number observed here. However, the interfacial motion of water-walking insects fall quite nicely into this intermediate Reynolds number flow regime. Take for example, the whirligig beetle which are known to propel themselves by releasing a surface active substance into the water [167]. Velocities as high as 64cm/s have been observed for the case of whirligig beetles which translates into Reynolds number of over $Re > 1000$. Observations of whirligig beetle motion shows that they often spin giving rise to their name [167]. The high interfacial swimming velocities might give these beetles an advantage in predator avoidance, while the rotational motion induced by vortex shedding may help in evading predators by rapidly and perhaps unpredictably changing the trajectory of the beetle once it has propelled itself beyond the critical Reynolds number.

Changing the propulsion agent was found to result in a number of additional effects beyond just changing the maximum velocity achieved by the disk. The soap was found to slowly dissolve from the disk over the course of minutes, while the IPA dissolved in seconds. The result was a strong impulsive propulsion from the IPA resulting in a fast acceleration followed by a slow deceleration of the disk. For the IPA, steady state translational velocity was never achieved even in for the case where rotational motion was not observed. However, when soap was used as the propulsion agent, a slower acceleration

was observed and a steady stage velocity was achieved and maintained for quite some time. By achieving a steady-state velocity, disks propelled by soap appeared to a system that is more appropriate for fundamental studies where the effects of transient motion are undesirable. Although only the IPA cases displayed interfacial vortices attached to the side of the disk, both soap and IPA showed the presence of an attached vortex right beneath the disk and the presence of a stagnation point along the interface in its wake. This stagnation point represents the location of the lowest surface tension along the interface and the point from which the surface radially dilates. The location of the stagnation point was found to move further into the wake with increasing disk velocity.

By allowing the disk-shaped Marangoni surfers to interact with the edge of the Petri dish, the effects of the boundary and interface curvature were investigated. The presence of wall leads to an adverse pressure gradient which brought the interfacial flow to rest and decelerated the disks as they approached. For the flat interface, the presence of the boundary caused the disks to spin and rotate away from the wall. The critical Reynolds number for rotation near the wall was significantly less, $Re = 50$, then for unbound flows. The presence of concave or convex curvature at the edge of the Petri dish resulted in an additional repulsive or attractive force on the disk due to gravity which modified the flat interface behavior making it more likely to spin from or pin to the wall, respectively. The interactions between the disks and the wall are a useful first step in understanding the interaction between multiple Marangoni surfers on an interface. While the interface around the disk-shaped Marangoni surfer used here was essentially flat, interfacial curvature effects can be extremely strong at these length scales. Quite a bit of research has already been done to investigate the use of interfacial curvature and surface tension to induce self-

assembly of non-propelled objects into small scale structure [168]. Taking that work one step further, if one can understanding how particles propelled by interfacial tension gradients aggregate at an interface one might be able to better understand and control the dynamics of particle aggregation and assembly making it possible to build even more complex structures.

5.5 Acknowledgement

The authors would like to thank NSF for financial support of this research under grant CBET – 1705519.

5.6 Publication

The work described in this chapter has been submitted to the Physics Of Fluids Journal. The complete reference is S Sur, H Masoud and J P Rothstein “Translational and Rotational Motion Of Disk-Shaped Marangoni Surfer”, 2019).

CHAPTER 6

THE EFFECT OF SHAPE ON MOTION AND STABILITY OF MARANGONI SURFERS

6.1 Introduction

For small objects, insects or bacteria floating on a liquid interface, locomotion can be induced by localized manipulation of the chemical composition or temperature a liquid interface to produce surface tension gradients [144]. The Marangoni flow that results typically propels the interfacial surfers in the direction of higher surface tension. Perhaps the most prominent examples of Marangoni surfers in the literature are the camphor boats that are commonly used for demonstration in the classroom [151-153]. Symmetric boat designs propelled by a gradient in interfacial tension tend to move with a straight-line motion and speeds that can be in excess of 10cm/s. This is because at low enough Reynolds numbers, rotational perturbation to the flow field damp out resulting in symmetric surfers that follows a purely translational motion [169]. In order to achieve rotational motion at low Reynolds numbers, asymmetries in the boat or particle design are needed [153, 170]. The direction and strength of rotational motion has been shown to be primarily governed by the shape of the particle and the asymmetry of release of the surface active chemicals [154, 171]. With careful design, the rotation rate of the particles can be maximized [155, 172] making the design of interfacial rotors, for example, possible.

In biological systems, self-induced Marangoni propulsion has been observed in organisms ranging in size from bacteria to water-walking insects. Bacteria such as *Pseudomonas aeruginosa,* which tend to reside at the water interface, are known to use biomolecules exuded from their bodies to reduce the local surface tension in order to induce

a Marangoni flow and rapidly migrate towards nutrient-rich regions ripe for feeding and colonialization [145, 146]. Water-walking insects like Dianous (rove beetle) and Velia (small water strider) are known to secrete surface-active fluids to induce a Marangoni flow in order to boost their locomotion speed in emergency situations [147-150]. The path taken by these water walking insects is initially straight, however, a deviation of the insect from a straight line trajectory is often observed after a short distance [173]. This rotational motion could be induced by insect using its legs like oars to steer or, as recently shown by Sur et al. [170], the observed rotational motion could be the result of vortex shedding that can occur at the moderate Reynolds numbers resulting from the Marangoni flow generated by the insect.

Sur et al. [170] have experimentally investigated the interfacial and bulk flow dynamics of circular disk-shaped Marangoni surfers propelled by either soap or isopropyl alcohol (IPA) through particle tracking and particle image velocimetry (PIV) measurements. For the case of soap, the circular disk was found to follow a translational steady-state motion with a pair of attached counter rotating vortices along the side of the circular disk. For this steady, straight line motion a maximum Reynolds number of no more than $Re = \rho U D/\mu = 60$ was reached. Here, ρ is the density of the fluid, U is the velocity of the circular disk, D, is the diameter of the circular disk and μ is the dynamic viscosity. For the case of IPA, the driving force was larger and the corresponding circular disk and interfacial velocities were found to be much higher with Reynolds numbers greater than $Re > 600$. At these moderately-high Reynolds numbers, inertial effects become significant and a transition from a translational motion to a rotational orbital motion was observed at a maximum Reynolds number of $Re_{max} = 180$. From PIV investigation, it was found that

the rotation of the circular disk was caused by the shedding of an attached vortex. The vortex shedding provided a sufficiently large unbalanced torque to spin the circular disk and initiate its orbital motion. In this paper, our goal is to understand how the Marangoni surfer symmetry, shape and orientation affects its motion and stability.

The Marangoni flow of particles attached to an interface has also been investigated both theoretically and through numerical computations, but only in the regime of vanishingly small Reynolds numbers where straight line translational motion is expected [174-179]. Masoud and Stone [176] used the reciprocal theorem to derive closed-from expressions for the propulsion speed of chemically active oblate and prolate spheroids. To examine the collective motion of many particles attached to an interface, Masoud and Shelley [177] employed a Fourier spectral method. In a recent work, Vandadi et al. [178] used theory to examine the motion of particles in a Marangoni flow with a solid confining wall located below the liquid-gas interface. Their analytical calculations revealed that the propulsion speed and direction of the particles depend both on the particle geometry and the degree of confinement introduced by the presence of the bottom wall. Their calculations showed that when the thickness of the liquid layers between the floating particle and the bottom wall decreased below a critical threshold, the hemispherical particles changed direction and began moving towards the direction of lower surface tension. This reverse Marangoni flow was not observed for the flat disk-shaped particles. The calculations of Vandadi et al. [178] reveal, just how important the shape of particle above and below the water line can be. In this study, we experimentally investigate the effect that particle shape can have on the speed and stability of the Marangoni-induced motion of surfers at moderate Reynolds numbers by studying the dynamics of both

spherical particles and elliptical disk-shaped particles with cross sections of various aspect ratios. By comparing the results to each other and to the cylindrical disk-shaped particles studied previously [170], the effect of particle shape, orientation and symmetry will become clear.

In addition to shape variation of the particles, in this study we investigate the importance of particle buoyancy and interface deformation on the stability of Marangoni surfers. Unlike the elliptical disks used here and the circular disks used previously [170], the air-water interface around the spherical particles is not flat. Due to its density and shape, the spheres floats with more than 50% of the sphere submerged below the water line. To maintain the correct contact angle on the sphere, the air-water interface is forced to curve and become convex. The surface tension along this curved interface helps to support the weight of the spheres. On a flat interface, the interfacial curvature around a single particle will not result in spontaneous particle motion. However, the presence of a second particle or a bounding wall around which a similarly signed curvature exists will result in an attractive force [180] that scales like the inverse of the separation distance between the two objects [156]. Objects with like (concave or convex) interfacial curvature attract each other because both the gravitation potential energy and the capillary energy decreases as the objects approach each other [156]. This attractive force can result in the self-assembly of floating objects into particle rafts [157-161] or the accumulation of particles near regions of high interfacial curvature [162, 163]. The presence of curvatures at the boundary and its effect on the motion of the disks propelled by a Marangoni flow was investigated by Sur et al. [170]. In their experiments, the presence of a concave curvature at the boundary was found to lead to a transition from a straight-line motion to a rotational motion at a

significantly lower Reynolds number than on a flat unbounded interface. Flat and convex interface curvatures did not lead to additional destabilization of unbounded translational motion. In the experiments presented in this paper, we will investigate how the particle shape, the particle orientation and the local curvature that exists around particle affect its dynamics and stability as it approaches a series of bounding walls with different interface curvatures.

6.2 Experimental Setup

A series of experiments were performed in both the large, D_{dish}=150mm, and the small, D_{dish}=86mm, Petri dish shown in Figure 48. The depth of water was maintained at h=12mm and 50mm in the small and large Petri dish, respectively. In all cases, the depth of the water in the Petri dish was deep enough so that the motion of the Marangoni surfers was insensitive to the variation of the water depth. Experiments were performed in the large Petri dish to avoid interaction with the bounding walls, while experiments that were performed in the small Petri dish where specifically designed to study the effect that the interface curvature near the boundary wall had on the mode of motion of the spherical Marangoni surfer. Isopropyl alcohol (IPA) and a commercially available soap (Dawn) were used to induce the surface tension gradients needed to produce the desired Marangoni flow. Each D=6.35mm sphere was dip coated one millimeter deep into a number of different strength solutions of IPA and water or a solution of 50% soap and water as shown in Figure 57. This dip coating process resulted in the addition of roughly one milligram of the propulsion agent applied to the back of each sphere and elliptical disk. The surface tension of pure IPA was taken from literature to be σ = 22mN/m, while the surfactant in the Dawn soap is known to reduce the interfacial tension of water from σ = 72mN/m to 30mN/m

[164]. The spheres were made from polypropylene (PP) which has a density of ρ = 920kg/m^3 and a contact angle with water measured to be 70^o. A 2.4mm hole was drilled into the top of each sphere to a depth of 3mm in order to reduce the mass of the sphere by 10% so it would float more easily. The hole was also used to change the center of mass of the sphere so that it would float with a preferred orientation with the hole opening facing up. As it floated, 4.5mm of the sphere was below the air-water interface and the interface around the sphere was found to have a strong convex interfacial curvature. Elliptical disk of two different aspect ratios were also fabricated for shape comparative study. For an elliptical disk of aspect ratio, AR=1.5, the minor axis was D_{minor}=4mm and major axis was D_{major}=6mm whereas for an elliptical disk of AR=2, the minor axis was D_{minor}=3mm and major axis was D_{major}=6mm. The elliptical disks were t = 1.5mm thick. The elliptical disks were fabricated from polydimethylsiloxane (PDMS) which has a density of ρ=965Kg/m^3. A close optical inspection of the interface around the floating elliptical disk showed a flat interface.

The spheres and the elliptical disks were carefully placed on to the air-water interface with tweezers and released. To average out any errors resulting from fabrication, dip coating or surfer placement, all measurements were repeated at least five times using a minimum of three different spheres or elliptical disks to minimize bias errors due to fabrication. A digital camera was used to track the motion of the Marangoni surfers. The videos were captured at 17fps and the images fed into a particle tracking software (Tracker) which was used to analyze the motion of the surfers. For the particle image velocimetry (PIV) measurements, a 300mW argon ion laser was used to create a laser light sheet

roughly 0.5mm thick and illuminate 40μm diameter PIV particles dispersed in the water. The motion of the surfer was captured using a high-speed video camera (Phantom). PIV measurements were used to analyze the flow field induced by Marangoni flow along the air-water interface and underneath the sphere. The PIV videos were analyzed using a commercial PIV software (LaVision).

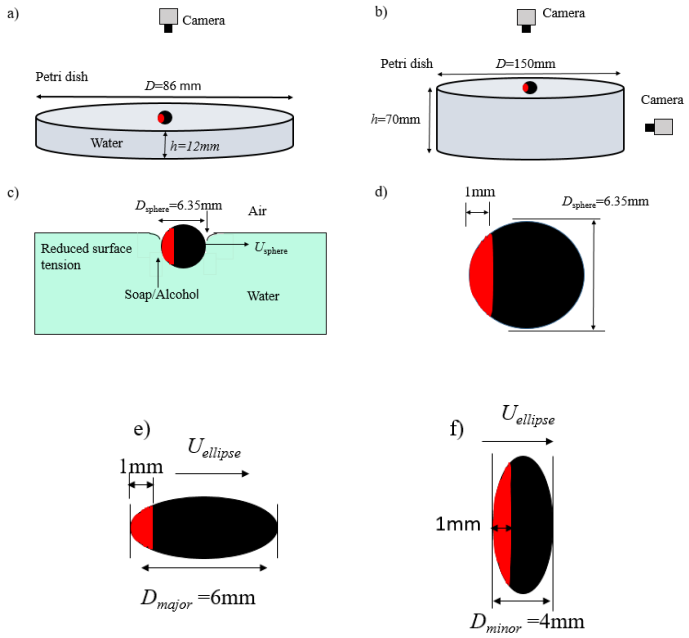

Figure 57. Schematic diagram of the experimental setup of a a) small and a b) large Petri dish. All necessary dimensions are given in the figure. Both a side and top mounted camera were used to record the motion of the particles as shown in b). Both the sphere shown in c) and d) and the *AR*=1.5 elliptical disk shown in e) and f) were propelled by a Marangoni flow induced by the release of soap or alcohol from a 1mm strip shown in red which was applied to the back of the particle through a dip coating process. The elliptical disks were *t* = 1.5mm thick.

In order to study the effect of confinement and the role that interface curvature can play on the motion of the surfers, a smaller Petri dish was used. At the edge of the small Petri dish, a concave, convex, or a flat interface was created by first filling the dish with water until the contact line was pinned to the top edge of the Petri dish producing a flat interface as shown in Figure 58. Once the contact line was pinned, a syringe pump was

then used to either add or withdraw 9ml of water to produce the desired curvature of the air-water interface. This resulted in a radius of curvature approximately 1mm at the edges of the Petri dish

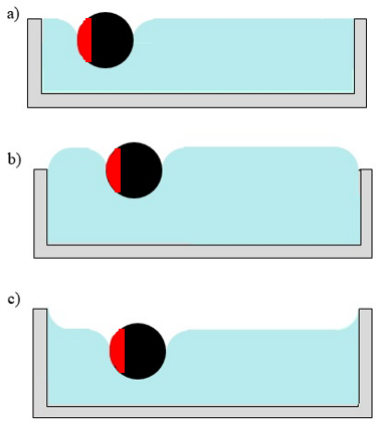

Figure 58. Schematic diagram of interface curvature at the boundary of a *D*=86mm Petri dish showing a) a flat b) a convex and c) a concave interface.

6.3 Results and Discussion

6.3.1 Motion of Spherical Interfacial Surfers Propelled by Soap

Here we will investigate the motion of a spherical Marangoni surfer using soap as the propulsion agent. One millimeter of the sphere was dip coated using a solution of 50% soap and water. As the sphere was deposited onto the air-water interface, the surfactants were found to populate the air-water interface, which reduced its interfacial tension to $\sigma = 30\mathrm{mN/m}$ as the air water interface was fully saturated with surfactant. It is expected that the minimum surface tension along the interface should arise close to the back of the sphere where it was coated with soap. The Marangoni flow produced as a result of the surface tension gradient drives the motion of the sphere. A linear, straight-line translation of the sphere was observed without rotation for the case of soap. As seen in Figure 59, upon its

release, the sphere, initially accelerated before reaching a maximum velocity of roughly U_{sphere}=18mm/s after a time of t=0.5s. This translates to a maximum Reynolds number of, $Re=\rho U_{sphere}D/\mu$=114 where, ρ is the density of the fluid U_{sphere} is the maximum velocity of the sphere, D, is the diameter of the sphere and μ is the dynamic viscosity. During the initial start-up of motion, the acceleration was found to remain roughly constant at a = 37mm/s^2. Beyond the peak velocity, the sphere was found to decelerate slowly before reaching a steady-state velocity of U_{sphere}=4mm/s (Re=25) approximately t=5s after the sphere was released. This steady state motion was observed for roughly 25s before the sphere collided with the wall of the Petri dish. These observations suggest that, at long times, a constant release rate of the soap was achieved to the interface. The duration of this steady-state motion is a function of the quantity of soap applied to the sphere, the rate at which the soap is dissolved into the water and the maximum distance the sphere can travel due to size constraints of the Petri dish. Similar observations of steady-state straight-line motion were observed for similarly sized circular disks propelled by soap in our previous experiments [170]. In those experiments, maximum and steady-state velocity of the circular disks were all within 10% of what was observed here for the spheres. However, the acceleration of the spheres was found to be more than 50% larger than the circular disks. It is also important to note that, in these experiments, convection process dominated the variations in the surfactant concentration field and not the diffusion of the surfactant molecules across streamlines. This can be easily observed by calculating the Peclét number, $Pe = D_{disk}U_{disk}/D$, where the appropriate length scale is the diameter of the disk, D_{disk}, U_{disk} is the velocity of the disk and D is the diffusion coefficient of the surfactant in water. The diffusion coefficients for the two surfactants in the soap, sodium laureth sulfate and sodium

lauryl sulfate, are approximately $D \sim 10^{-9}$ m^2/s, the resulting Peclét number becomes extremely large, $Pe \sim 10^5$.

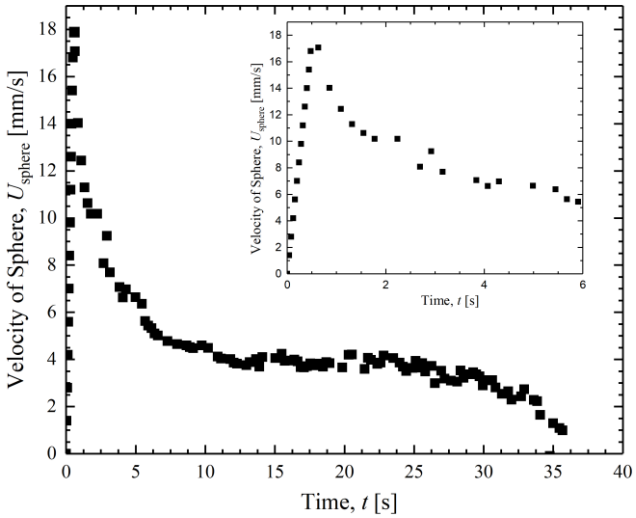

Figure 59. Plot of magnitude of velocity, $U_{sphere,}$ as a function of time, t, for a spherical Marangoni surfer using soap as the propulsion agent. Inset shows a close-up of the data at early times.

6.3.2 PIV of the Flow Field Around a Spherical Interfacial Surfer Propelled by Soap

In this section, Particle Image Velocimetry (PIV) measurements of the flow field in the water around a spherical Marangoni surfer propelled by soap are presented. In Figure 60, PIV measurements of the interfacial flows around the sphere is shown for the sphere undergoing a steady-state constant velocity translational motion corresponding to the time window between t = 15s and 20s in Figure 59. The motion of the sphere in all figures that are presented will be from left to right. As seen in Figure 60, the interface appears to dilate, spreading radially from a stagnation point roughly one diameter downstream of the soap-coated trailing edge of the sphere. The stagnation point in the PIV data represents the location of the minimum in the interfacial tension. The presence of a stagnation point in the wake of the sphere is not surprising; however, one would expect it to be located adjacent

to the coated region of the sphere where the bulk concentration of surfactant is maximized. As discussed in Sur et al.[168], it is important to note that a finite adsorption time, t_{ads}, is required for the surfactant to diffuse to and then populate the air-water interface. During the adsorption time, the sphere has moved a distance $L=U_{sphere}\ t_{ads}$, which, given the velocity of the sphere and typically adsorption times for surfactant, can mean the minimum interfacial tension can exist a millimeter or more downstream of the sphere.

A centerline velocity profile of the interfacial flow upstream and downstream of the sphere is shown in Figure 60b. Here, the interfacial velocity has been normalized by the sphere velocity, U/U_{sphere}, and the x-position has been normalized by the diameter of the sphere, x/D_{sphere}. Note that $x/D_{\text{sphere}}=0$ represents the center of the sphere. The presence of the stagnation point can be seen more clearly here at a position of $x/D_{sphere} = -0.9$. The stagnation point behind the circular disk was found to be at $x/D_{disk} = -1.5$[168]. Although this is further in non-dimensional form, the stagnation point observed in each case exists at a roughly the same physical distance of x = 6mm downstream of the center of the circular disk and the sphere. Given that the velocity of the sphere and circular disk are similar in these experiments, this observation is consistent with the hypothesis that a finite time is needed for the surfactant to find and adsorb to the air-water interface.

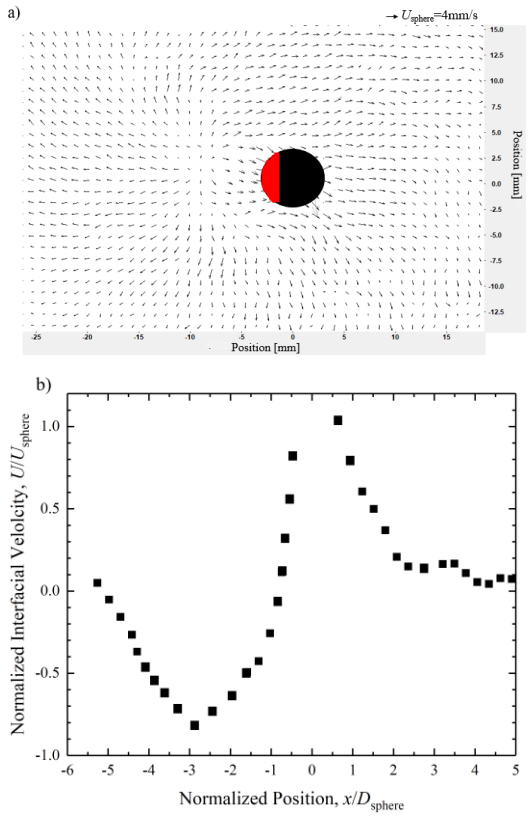

Figure 60. Plot of particle image velocimetry (PIV) measurements of the steady state flow field around a floating sphere propelled by the Marangoni flow induced by soap released from the sphere in the area denoted by red region at its rear. b) Plot of normalized interfacial centerline flow velocity, U/U_{sphere}, as a function of normalized position, x/D_{sphere}. The centre of the sphere is placed at x=0. A scale bar for the velocity vectors is presented in a).

Far from the sphere in its wake, the maximum velocity of the dilating interface was found to be slightly lower than the velocity of the sphere U/U_{sphere}=−0.9. Just upstream of the sphere, the maximum velocity was measured to be U/U_{sphere}=1.05. This 5% increase over the sphere velocity produces a small relative flow velocity, which in addition to the traction force produced by the interfacial tension gradients, provides the necessary fluidic forces to overcome the friction and form drag on the submerged portion of the sphere. In the case of the circular disk, the relative velocity upstream and downstream of the circular disk was found to be approximately 5-10% higher as compared to spheres. This

observation suggests that the floating sphere has a lower drag coefficient than the floating circular disk and highlight the impact that shape can have on the dynamics of relatively simply Marangoni surfers.

The three dimensionality of the flow field around the sphere was interrogated by orienting the laser light sheet vertically and passed into the Petri dish from below. The resulting PIV vector fields presented in Figure 61 shows the velocity profiles in a plane that bisects the sphere along the direction of motion. Note that due to the curvature of the air-water interface around the sphere, measurements of the velocity profile along the air-water interface were difficult to measure. As such, the data in Figure 60 should be used for accurate measurements of the interface velocity and the velocity data beneath the sphere and several millimeters below the interface is the focus of Figure 61. In Figure 61, PIV measurements are presented for a stationary sphere and a sphere shortly after its release. In Figure 61a, the PIV measurements for the flow underneath the stationary sphere is presented 0.5s after the sphere was inserted onto the water interface. A wide, shallow start-up vortex rotating clockwise can be observed in the wake of the sphere. The center of the vortex was found to move away from the sphere with time at a speed of 2mm/s. As time progressed, the strength of the vortex strength was found to decrease. The magnitude of the vorticity of the vortex was found to be $\omega = 10s^{-1}$ at $t = 0.2s$ and to $\omega = 4s^{-1}$ at $t = 1s$. The vortex observed beneath the sphere is weaker as compared to the vortex observed beneath a stationary circular disk [168].

A strong upward flow was observed below the sphere with the vertical velocity appearing on the side of the sphere where the surfactant was applied and where the stagnation point was observed along the interface. This vertical flow is required to satisfy

continuity around the stagnation point. The velocity of the upward flow was found to increase as the flow approached the interface, eventually reaching a maximum velocity of U=8mm/s. The upward velocity is similar in magnitude to the maximum lateral interfacial velocity in the wake of the sphere which was found to be U=10mm/s. The velocity of the upward flow was approximately 30% less than that measured for a circular disk [168]. The lower upwelling velocity might be due to the more streamlined path for flow to move into the wake of the sphere from below and from the sides making it easier to supply the outgoing fluid along the dilating interface to the stagnation point from locations other than just the region directly below the stagnation point as is the case with the circular disk.

In Figure 61b, the flow beneath the sphere is presented 0.5s after the sphere was released on the air-water interface. The release process takes roughly 0.15s from deposition to release from the tweezers so a Marangoni flow akin to the PIV vector field in Figure 52a has already begun to set up before the sphere is released. The PIV vector field shows the presence of a stagnation point in the wake of the sphere and also a region of weak recirculation, $\omega = 4s^{-1}$, right beneath the sphere as the sphere achieved a velocity of U_{sphere} =6mm/s. Under similar flow conditions, a recirculation area was also observed beneath the circular disk Marangoni surfers. However, in that case, the attached vortex was much more well defined with a significantly larger vorticity, $\omega = 16s^{-1}$[168]. In addition to the attached vortex beneath the sphere. A counter-rotating start-up vortex downstream of the sphere was also formed upon release. As time progressed, the start-up vortex was shed and convected downstream of the sphere by the dilating interface as was observed for the case of the stationary sphere.

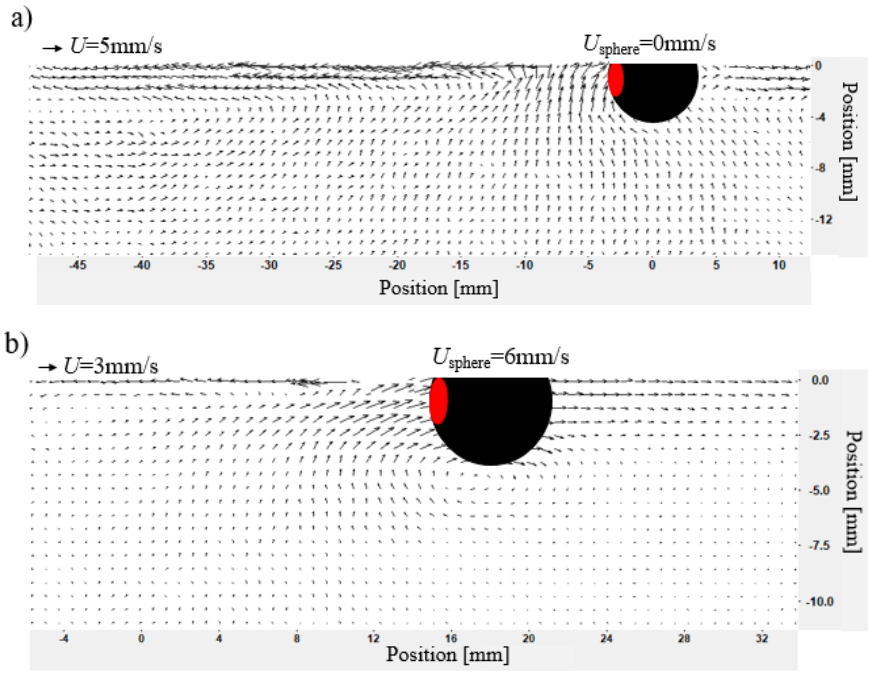

Figure 61. Plot of the particle image velocimetry measurements of the flow field underneath a floating sphere propelled by the Marangoni flow induced by soap released on the left side of the sphere in the area denoted in red for a) a stationary sphere at *t*=0.5s after immersing it in water and b) for the sphere moving with a velocity of U_{sphere}=6mm/s at *t*=0.5s after it was released. Scale bars are presented in each sub figure.

6.3.3 Motion of Spherical Interfacial Surfers Propelled by IPA

In this section, the effect of changing the strength of the propulsion agent is investigated by switching from soap to isopropyl alcohol (IPA). The interfacial tension of pure IPA and the air-water interface saturated with surfactant are similar. However, compared to the surfactant in the soap, IPA is a smaller, more-mobile molecule that can quickly change the local interfacial tension resulting in a fast-acting intense propulsion that is unfortunately also depleted much more quickly than soap. The velocity profiles for a series of spheres propelled by Marangoni flow induced by IPA are presented in Figure 6.

The propulsive strength of the IPA was systematically varied from 100wt% to 20wt% with water to investigate the effect of varying propulsion strength. For the case of 20wt% IPA in water, a straight-line motion was observed similar to the motion induced by soap with a maximum velocity of U_{sphere}=18mm/s and Reynolds number of Re = 110. The sphere velocity decayed to zero after a time period of just t=4s. No steady-state, constant velocity motion was observed for the 20wt% IPA case or any of the other higher IPA concentrations. This is a very different response from when soap was used as the propulsion agent, but consistent with the findings for disks although for the case of IPA, the maximum velocity attained by the sphere is more than 25% smaller than the velocity obtained by the disks [168].

As the strength of IPA was increased to 100wt%, the maximum velocity and Reynolds number of the sphere was observed to increase to U_{sphere}=120mm/s and Re = 760. The values of maximum velocity and Reynolds number are tabulated for each IPA concentration studied can be found in Table 8. As the concentration of IPA was increased from 25wt% to 30wt%, a transition from an initial straight-line translational motion to a rotational orbital motion of the sphere was observed. A similar transition was found to occur for all spheres that achieved a maximum velocity and Reynolds number of at least U_{sphere} = 45mm/s and Re = 285, respectively. With increasing maximum sphere velocity, the number of the rotations and the angular velocity of the sphere during its rotations were found to increase as seen in the trajectories presented in Figure 62b-e. In all cases, rotation was found to occur after the peak velocity was achieved and during the deceleration of the sphere. In Figure 62a, the signature of a rotation can be observed as local peaks and troughs in the velocity data. The increased number and speed of the rotations is likely due to the

larger velocity of the sphere at the onset of rotation. For the 30wt% case, the sphere reached a maximum velocity of U_{sphere}=45mm/s and a maximum Reynolds number of Re=285 before beginning to decelerate. After decelerating for roughly 0.5s to a velocity of U_{sphere}=15mm/s and a Reynolds number of Re=95, the sphere was observed to spin. Note that, even though the maximum Reynolds number for the stable 25wt% IPA case (Re_{max} = 180) was larger than the Reynolds number observed prior to rotation for the unstable 30wt% case, the sphere was not found to rotate. Thus, it appears that, rotation of the sphere requires a maximum Reynolds number greater than or equal to $Re_{\max} \geq 280$ to be achieved. However, because the motion is transient, we felt it important to list both the maximum Reynolds number that was achieved and the Reynolds number at which rotation was first observed as a function of IPA concentration in Table 8. For comparison, the 1mm thick circular disk-shaped Marangoni surfers studied in Sur et al. [168] were found to transition from translational to rotational motion if a maximum Reynolds number greater than or equal to $Re_{\max} \geq 180$ was achieved. For that specific case, rotation was first observed after the disk decelerated to a Reynolds number of Re = 120 [168]. Thus changing the shape of the Marangoni surfer from a circular disk to a sphere clearly affects the stability of the Marangoni surfer. Based on the maximum Reynolds number achieved prior to rotation, Re_{max}, the sphere was found to be more stable as compared to the circular disk.

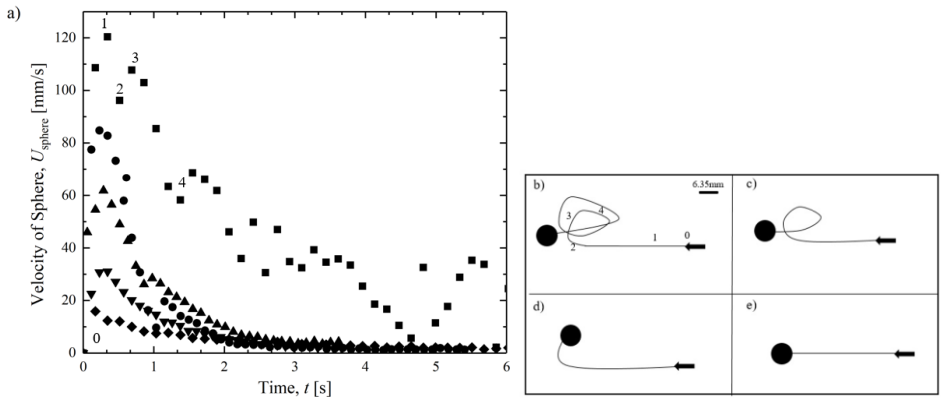

Figure 62. Plot of velocity of a sphere, U_{sphere}, with time, t, for IPA strength of (♦) 20wt%, (▼) 30wt%, (▲) 40wt%, (●) 50wt%, and (■) 100wt%. The path profile of the sphere propelled by IPA showing the transition from a rotational motion to a straight-line translational motion for b) 100wt%, c) 50wt%, d) 30wt% and e) 20wt%.

Table 8. Variation of the velocity and Reynolds number for different concentration of IPA and soap used to propel the sphere.

IPA Concentration [wt%]	**Maximum Velocity** U_{max} [mm/s]	**Maximum Reynolds Number** Re_{max}	**Velocity Prior to Rotation** $U_{rotation}$ [mm/s]	**Reynolds Number Prior to Rotation** $Re_{rotation}$
100%	120±5	760±30	95±5	600±30
50%	85±5	540±30	60±5	380±30
40%	70±5	430±30	42±3	265±15
30%	40±5	255±30	15±5	90±30
25%	30±5	190±30	NA	NA
20%	18±3	110±15	NA	NA
Soap	15±3	90±15	NA	NA

6.3.4 Motion of an Elliptical Disk Interfacial Surfers Propelled by IPA

In this section, the effect of changing the shape of the surfer from an axisymmetric sphere to a thin disk with an elliptical cross-section is studied. Here the dynamics and stability of an elliptical disk propelled by IPA was investigated for two different aspect

ratios, AR = 1.5 and AR = 2.0, and two different orientations with Marangoni propulsion aligned with the major and minor axis of the elliptical disk. As described in the experimental section, the elliptical disk with an aspect ratio AR=1.5 had a major axis of D_{major}=6mm and a minor axis of D_{minor}=4mm, while the elliptical disk with aspect ratio AR=2 had a major axis of D_{major}=6mm and a minor axis of D_{minor}=3mm. As shown in Figure 57, the elliptical disks were dip coated in a variable concentration solution of IPA in water to a depth of 1mm. Dip coating was performed in two orientation as shown in Figure 57 to induce flow along the major axis, Figure 63a, or minor axis, Figure 63b. For the two different aspect ratio elliptical disks, the velocity profile had the same general character. The elliptical disks were found to accelerate quickly, go through a maximum within the first 0.25s and decay to zero after 2 or 3 seconds. For case of 100wt% IPA shown in Figure 63, a series of local maxima can be seen during its deceleration phase. These peaks indicate times during which transition from straight-line to rotational motion was observed for the elliptical disks.

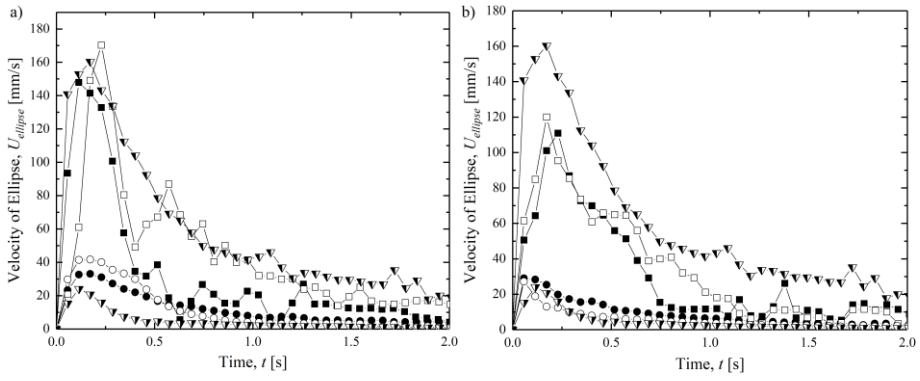

Figure 63. Plot of velocity of an elliptical disk, $U_{ellipse}$, with time, t, for IPA strength of (●) 20wt% and (■) 100wt% for motion along a) Major axis and b) Minor axis. Filled symbols correspond to aspect ratio AR=1.5 while hollow symbols correspond to AR=2. Along with velocity profile of elliptical disk the velocity of a cylindrical disk (AR=1) is also plotted for IPA strength of (▽) 100wt% and (▽) 20wt%. The data for AR = 1 was reproduced with permission from [168]

For the case of an elliptical disk with AR=1.5 at any a given concentration of IPA, the maximum velocity achieved while translating along the minor axis of the elliptical disk was consistently 40% lower than the maximum velocities achieved while moving along the major axis of the elliptical disk. For the case of 100wt% IPA, a maximum velocity of $U_{ellipse}$ = 170mm/s was achieved along the major axis whereas a maximum velocity of $U_{ellipse}$ = 120mm/s along the minor axis. This difference in velocity is due to the higher drag experienced by an elliptical disk during its motion along the minor axis as the object is more bluff and less streamlined. Although the physics are not the exactly the same as here, similar difference in the drag coefficient can be found based on the orientation of an elliptical cylinder in uniform cross flow.

Along with variation in the maximum velocity, the aspect ratio and orientation of the elliptical disk was found to have a substantial effect on the stability of the surfer. For all the different aspect ratio elliptical disks tested, translational motion along the minor axis of the elliptical disk was found to be more stable than motion along its major axis, The critical velocities and Reynolds number for rotation are presented in Table 2 for the AR=1.5 and AR=2 elliptical disk and the circular disk (AR=1) published previously [168]. As an example, take the AR=1.5 elliptical disk. For motion along the major axis, the elliptical disk became unstable at maximum Reynolds number of Re_{max}>110, whereas for motion along the minor axis this transition was observed at Re_{max} >250. Here Reynolds number is

defined as $Re=\rho UL/\mu$, where $L=D_{minor}$ for motion along the major axis and $L= D_{major}$ for motion along the minor axis. Increasing the aspect ratio of the elliptical disk from AR=1.5 to AR=2 was found to destabilize the motion along both the major and the minor axis. From Table 9, it can be observed that the transition from a linear translational motion to a rotational motion for the AR=2 elliptical disk was observed at just $Re_{\max}$ >60 for motion along the major axis and $Re_{\max}$ >140 for motion along the minor axis. The stability of the elliptical surfers appears to be extremely sensitive to changes in aspect ratio. With a 25% reduction in the aspect ratio from AR=2 to AR=1.5, a 100% increase in the critical Reynolds number was observed for flow along the two principle axes. Reducing the aspect ratio even further to a circular disk with AR=1 was previously shown to transition to rotation at a critical Reynolds number of Re_{max}=180 [168], while for the sphere presented in the previous section, the critical Reynolds number was Re=285. Accompanying the decrease in stability, an increase in the rotation rate of the elliptical disk was observed with increasing aspect ratio for motion along both orientations. Here for example we compare the rotation rate for 100wt% IPA case. For the case of an elliptical disk with AR=1.5, the rotation rate was found to be ω=6rot/s$\pm$1 and ω=3$\pm$1rot/s along the major and minor axis respectively. As the aspect ratio of the elliptical disk was increased to AR=2, the rotation rate was found to increase substantially to ω=9$\pm$2rot/s and ω=4$\pm$1rot/s along the major and minor axis respectively. A closer look at the surfer's motion shows a difference between the path profile followed by an elliptical disk and a symmetric surfer like a disk or a sphere. For the case of an elliptical disk, the surfer was found to rotate about its center of mass spinning in place like a top. For the case of the symmetric disks or spheres, the center of mass of the surfers were observed to trace out long slow circular paths. This difference

also show up in the rotation rate of the surfer as the symmetric disk and sphere were found to rotate much slower at ω=0.8$\pm$0.2rot/s and ω=0.2$\pm$0.1rot/s respectively. Thus from these observations, a high aspect ratio elliptical disk designed to translate along its major axis would be an excellent design for a high efficiency Marangoni propelled rotor or mixer.

Table 9. Variation of the velocity and Reynolds number for different concentration of IPA used to propel several aspect ratio elliptical disks along the major and minor axis. The data for AR = 1 was reproduced with permission from.

IPA Concentration [wt%]	**Maximum Velocity** U_{max} [mm/s]	**Maximum Reynolds Number** Re_{max}	**Velocity Prior to Rotation** $U_{rotation}$ [mm/s]	**Reynolds Number Prior to Rotation** $Re_{rotation}$
Motion along Major axis, AR=1.5				
100%	155 ± 5	620 ± 20	110 ± 15	400 ± 40
25%	45 ± 5	180 ± 20	25 ± 5	100 ± 20
20%	27 ± 3	107 ± 11	NA	NA
Motion along Minor axis, AR=1.5				
100%	110 ± 10	660 ± 60	80 ± 5	480 ± 30
30%	55 ± 5	330 ± 30	25 ± 5	150 ± 30
25%	40 ± 5	240 ± 30	NA	NA
Motion along Major axis, AR=2				
100%	170 ± 10	510 ± 30	140 ± 5	435 ± 15
20%	40 ± 5	120 ± 15	25 ± 5	75 ± 15
10%	20 ± 1	58 ± 3	NA	NA
Motion along Minor axis, AR=2				
100%	110 ± 10	660 ± 60	90 ± 5	540 ± 30
25%	40 ± 5	240 ± 30	20 ± 5	120 ± 30

20%	25 ± 3	160 ± 17	NA	NA
Motion of a cylindrical disk, AR=1				
100%	160 ± 8	640 ± 30	120 ± 10	450 ± 35
25%	45 ± 5	180 ± 20	30 ± 5	120 ± 20
20%	28 ± 2	112 ± 8	NA	NA

6.3.5 PIV of a Spherical Interfacial Surfer Propelled by IPA

In this section, PIV measurements of the flow field in the water around a spherical shaped Marangoni surfer propelled by IPA are presented. Interfacial PIV measurements for the case of a stationary sphere held fixed on the air-water interface, U_{sphere}=0mm/s, is presented below in Figure 64. Like the case of soap, a radially outward flow was observed downstream of the left side of the sphere where the IPA was applied. Unlike in the case of soap, the presence of a pair of counter-rotating vortex can be observed in Figure 64a on sides of the sphere upstream of its equator. These vortices were observed to grow more and more distinct as time progressed until the supply of IPA was depleted from the sphere. Although the vortices of the stationary sphere were observed to grow in intensity with time as seen in Figure 64a, they were not observed to shed. The appearance of these vorticies is counter-intuititve because upstream of the sphere, the interfacial flow is not radially outward as one would expect given the direction of surface tension gradient. However, it is the interfacial tension gradient that in fact drives this flow as large influx of fluid from beneath and around the sphere is needed to conserve mass as the interface quickly dilates from the wake of the sphere, where the surface tension is minimized, into the high surface tension areas downstream of the sphere. This can be seen more clearly in Figure 64b,

which shows the PIV vector fields from beneath the stationary sphere. It can be clearly seen that the presence of the sphere has a large impact on the resulting Marangoni flow field and clearly limits the dialation past the sphere. For example, from our experiments it was observed that if a drop of alcohol was deposited on the water surface without a sphere present, a purely radial flow is observed on the interface. The main difference between the soap, where these vortices are not observed, and the alcohol case, where they are, is the flow strength. For the case of IPA, the outward velocity of the interface was found to reach close to 50mm/s wheras in the case of soap only 15mm/s was reached. This difference in the flow was enough to change the dynamics of the sphere motion once it is released. In Figure 64b, the Marangoni flow field underneath the stationary sphere induced by 100wt% IPA is presented. A start-up vortex is clearly visible downstream of the sphere. With time, this vortex was observed to shed and move downstream away from the stationary sphere with its vorticity decreasing in magnitude as it moved away from the sphere.

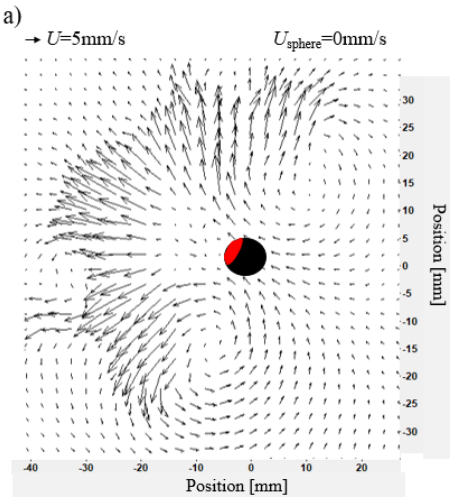

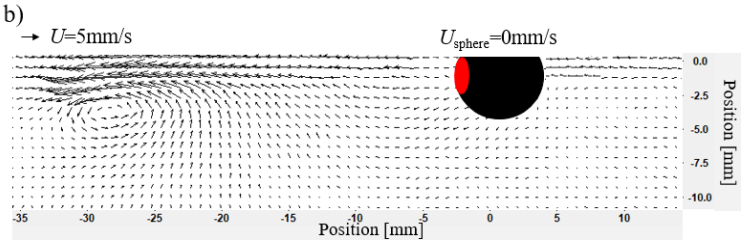

Figure 64. Plot of the Particle Image Velocimetry measurements of the flow field upstream and downstream of a stationary sphere (U_{sphere}=0mm/s) within a Marangoni flow field induced by the release of 100% IPA from the back of the sphere in the area denoted in red. The two figures denote time a) + c) t=0.5s.

In Figure 65, the Marangoni flow along the interface around a moving sphere propelled by 100wt% IPA is shown following deposition onto the interface. With the sphere free to surf across the interface, the reversed flow observed for the stationary sphere in Figure 64 was not seen, but instead a strong propulsive flow was observed upstream of the sphere where the interfacial tension is the largest. The flow field generated in the case of a moving sphere is quite different from the case of a stationary sphere. In the wake of the sphere, a radially outward flow originated which propelled the sphere in the direction away from the point where IPA was introduced. The attached interfacial vortices that were observed for the case of a stationary sphere in Figure 64a were observed to shed as the sphere was propelled forward. As the sphere moved across the interface, two counter-rotating vortices were observed to form and remain attached to the side of the sphere along its equator as shown in Figure 65a. With time, the vortex to the port side of the sphere was observed to shed, resulting in a rotational motion of the sphere and the initiation of an orbital trajectory that would continue until the sphere came to rest. A jet of fluid was observed to move past its port side moving the sphere to its starboard side as the sphere rotated away from its original trajectory. Similar vortex shedding was observed for disk-shaped Marangoni surfers as well [168]. From multiple experiments performed for each

IPA concentration, no particular bias in shedding of the vortex from the side of the sphere was found. For the case of soap for which the maximum Reynolds number achieved was just Re=60 no such formation and shedding of interfacial vortices were observed. For all the IPA cases that showed a transition from straight-line to rotational motion, the Reynolds number was greater than that achieved with soap. The presence of interfacial vortices is thus clearly an inertial effect that requires a minimum Reynolds number to observe. PIV measurements were also performed to investigate the flow underneath the spheres propelled by IPA. As the sphere was immersed and released onto the interface an intital startup vortex in the wake was produced which was observed to shed quite quickly. In Figure 65b the startup vortex can still be seen, rotating counter-clockwise with positive vorticity at the time far left of the image centered around $x = -10$mm. After the initial start-up vortex was shed, a second vortex attached to the bottom of the sphere was observed to grow and to rotate in the opposite direction, clockwise with negative vorticity. The attached vortex was found to be directly underneath sphere and very close to the bottom surface of the sphere. The location of this vortex is quite different from the case of the circular disk studied previously [168] and the elliptical disks that will be discussed in the next section. For both those disks, the attached vortex was found to be offset towards the rear edge of the disk where it appeared to be pinned to the sharp 90^o corner that forms the border between the bottom and side wall of the disk. The strength of the vortex underneath the sphere was found to be just $\omega = 4s^{-1}$, which was less than half of the vorticity measured for the vortex beneath the circular disk, $\omega = 10s^{-1}$, at a similar velocity of U=20mm/s velocity [168].

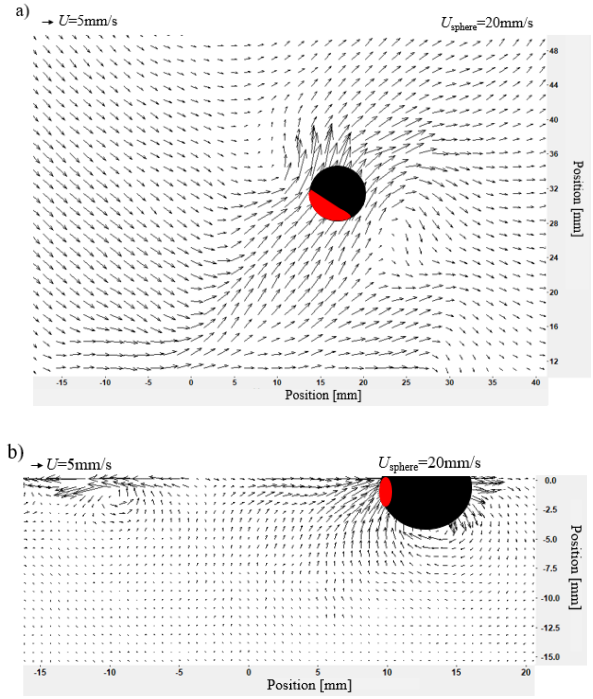

Figure 65. Plot of the Particle Image Velocimetry measurements of the flow field upstream and downstream of a sphere propelled by IPA (100wt%) released on the back of the sphere in the area denoted in red moving along its initial trajectory at a time of a) *t*=1 after release and a sphere velocity of U_{sphere}=20mm/s, b) flow field underneath the moving sphere with sphere velocity of U_{sphere}=20mm/s at *t*=1s. The center of the sphere was released at (0,0).

6.3.6 PIV of an Elliptical Marangoni Surfers Propelled by IPA

In Figure 66, the interfacial flow profiles around the two different aspect ratio and two different orientation elliptical shaped Marangoni surfers are directly compared to each other and to the interfacial flow profiles observed for the axisymmetric spheres and circular disks. All the PIV presented in Figure 66 are for the case of 30wt% IPA and were chosen to highlight differences in the flow field during the straight-line translational motion of each of the different Marangoni surfers. For all six cases, a pair of attached counter-rotating vortices can be observed to the sides of the surfers. It is evident from Figure 66 that the

position and strength of these vortices is affected by the shape and orientation of the surfer. For the case of the axisymmetric sphere described in the previous section and the circular disk shown in the work of Sur et al.[168], the attached vortices were closely aligned with the equator of the surfer at θ=83^o and θ=85^o, respectively. The angle reported here is the angle measured between the velocity vector of the Marangoni surfer and the line bisecting the center of the Marangoni surfer and the attached vortices. As such, an angle of θ=0^o corresponds to the direction of motion of the surfer. This is very different from the case of the non-axisymmetric elliptically shaped surfers. While moving along either the major or the minor axis, the attached counter-rotating vortices are clearly located more towards the wake. For the case of the AR=1.5 elliptical disk, while traversing along its major and minor axis, the vortices were found at θ=135$\pm$4^o and θ=125$^o\pm$3 , respectively. Similarly, the location of the vortices for the AR=2 elliptical disk were found at θ=123$^o\pm$2 and θ=115$^o\pm$3, respectively. The location of vortices may play a role on the change in the stability of the Marangoni surfers with shape. However, detailed numerical simulations are likely needed to fully understand the root causes of the change in stability with shape and orientation. One observation is clear, the increased torque arm resulting from the asymmetry of the elliptical surfers and the location of the vortices clearly amplifies the effect of vortex shedding by increasing the applied torque and dramatically increasing rotation rate of the surfer as the aspect ratio increases.

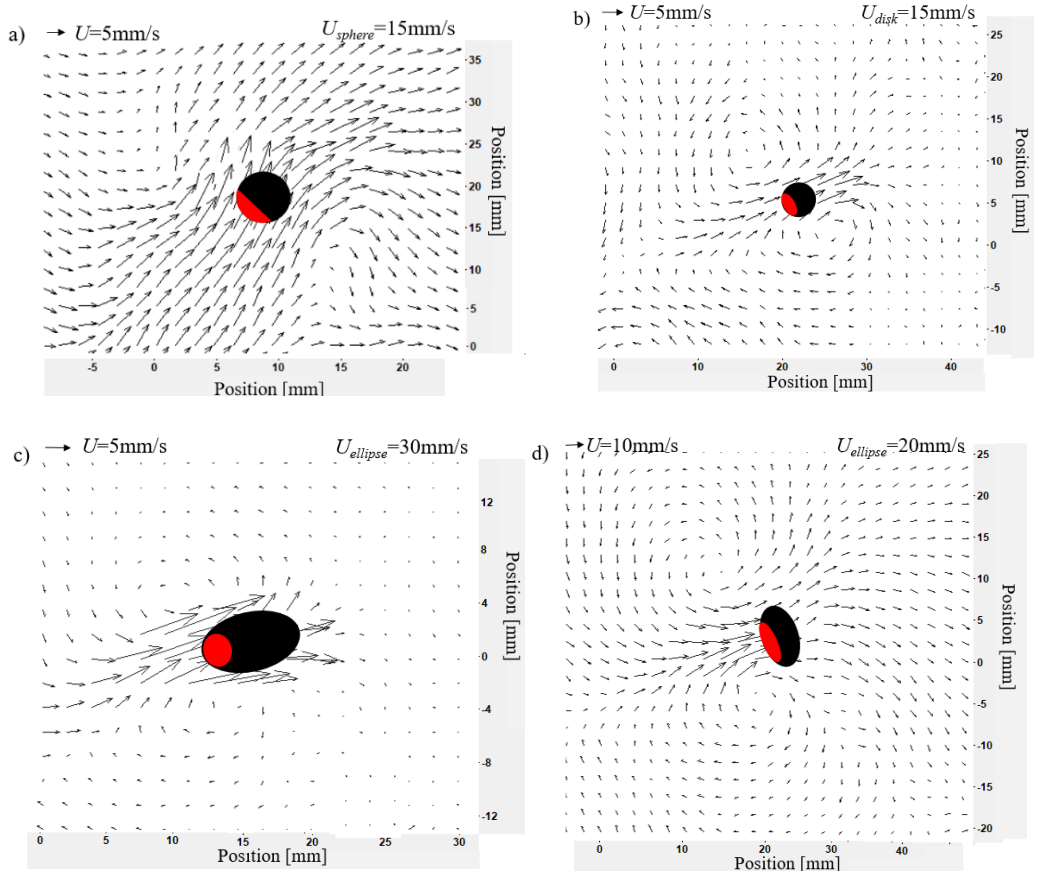
a)
U=5mm/s
U_sphere=15mm/s
Position [mm]
Position [mm]
b)
U=5mm/s
U_disk=15mm/s
Position [mm]
Position [mm]
c)
U=5mm/s
U_ellipse=30mm/s
Position [mm]
Position [mm]
d)
U=10mm/s
U_ellipse=20mm/s
Position [mm]
Position [mm]

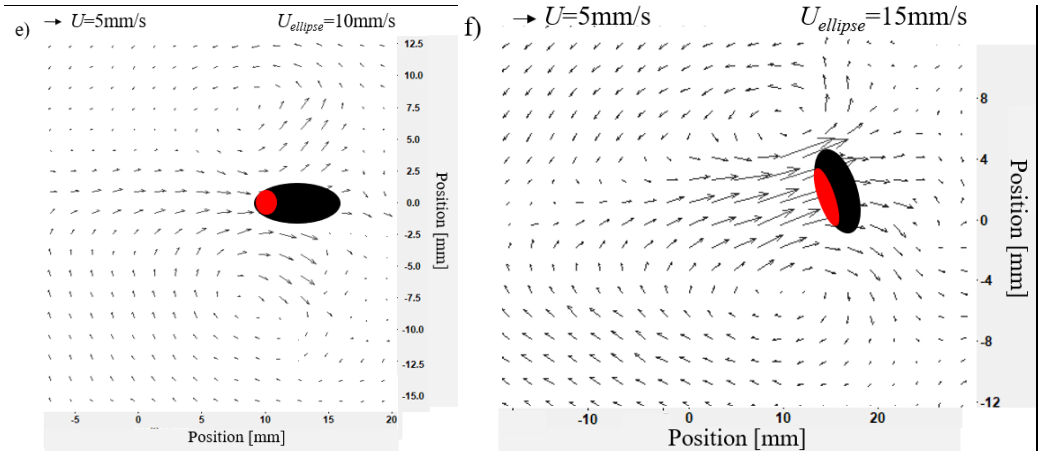

Figure 66. Plot of the Particle Image Velocimetry measurements of the flow field upstream and downstream of a sphere propelled by IPA (100wt%) released on the back of the Marangoni surfer in the area denoted in red moving along its initial trajectory. Data include vector fields around a) sphere, b) disk, c) elliptical disk (*AR*=1.5) moving along its major axis, d) elliptical disk (*AR*=1.5) moving along its minor axis, e) elliptical disk (*AR*=2) moving along its major axis, and f) elliptical disk (*AR*=2) moving along its minor axis.

6.3.7 Effect of Interface Curvature on the Motion of a Spherical and Elliptical Shaped Marangoni Surfer

The effect of interfacial curvature at the boundary on the motion of a spherical Marangoni surfer was investigated using 100% IPA as the propulsion agent. As seen in Figure 67, an initial straight-line motion was observed in all cases. For the flat interface, the sphere was observed to rotate and go through a series of orbital loops before reaching the boundary wall. Compared to the unbound case, the maximum Reynolds number needed to observe sphere rotation was reduced from Re_{max} = 285 to Re_{max} = 190 and the Reynolds number prior to rotation reduced from *Re*=90 to *Re*=60. The presence of the wall clearly provides some additional destabilizing perturbation to the straight-line motion of the sphere as the 25wt% IPA case rotates as it approaches the wall, but does not on an unbounded interface.

As the sphere was released and approached the wall, it must overcome an adverse pressure gradient as the interfacial and bulk fluid velocity come to rest at the wall. The resulting pressure field that is produced, led to the deceleration of the sphere. If the sphere does not approach the wall along a perfectly radial path, the pressure distribution around the sphere will provide a torque that, at a high enough Reynolds number, can cause the sphere to rotate and the attached vortices to shed. Additionally, because of the interfacial curvature around the sphere, an additional repulsive force exists in this case because of the mismatch in curvature between the concave interface around the sphere and the flat interface present at the wall of the Petri dish. As before, both clockwise and counter-clockwise motion were observed based on the initial release conditions and the orientation of the particle as it approached the wall. A series of peaks and troughs can be seen in Figure 67a, which indicate times at which rotational motion of the sphere was initiated. For the flat interface at the boundary, the sphere started a series of loops as it approached the wall. The average radius of curvature of the loops and the average period of rotation were found to be R =10$\pm$1mm and T=0.8$\pm$.1s, respectively for the case of flat interface. The average angular velocity observed for the flat case was found to be Ω = 10$\pm$2rad/s. It is important to note that the average angular velocity of the sphere as it approached the boundary was 50% larger than the angular velocity for the sphere rotating on an unbounded interface, Ω = 6$\pm$2rad/s. Interestingly, the angular velocity was larger on the bounded interface even though the maximum velocity attained was half as large as on the unbounded interface.

The case of a convex interface at the boundary of the Petri dish as shown in Figure 67b, the sphere followed a straight-line motion towards the wall and becomes attached to the boundary and ceases further motion. In this case, the curvature at the edge of the dish

and around the sphere are both convex resulting in a capillary attraction that effectively binds the sphere to the wall of the Petri dish. In addition to interfacial interactions, the convex curvature near the wall results in a decreased gravitational potential energy as the sphere moves to the wall resulting in an energy well that traps the sphere and inhibiting further motion. For the case of a concave interface curvature at the boundary of the Petri dish, as shown in Figure 67c, the sphere was found to begin a series of loop as it approached the wall. The mismatch in curvature between convex interface near the sphere and concave interface at the edge of the Petri dish provides an additional repulsive force and torque beyond the pressure gradient experienced near the boundary for the case of the flat interface. The average radius of curvature of the rotational motion and the average period of rotation for the concave case were found to be R=16$\pm$1mm and T=0.5$\pm$.1s, respectively, resulting in an average angular velocity of Ω=12$\pm$2rad/s. That is more than 30% larger than on the flat interface and twice as large as the angular velocity observed on an unconfined interface. This case, also highlights the main differences between the spheres, which have a convex interfacial curvature around them due to how they float and the circular disks studied previously [168] and the elliptical disks which will discussed shortly, which do not deform the interface. Without the additional repulsion of the mismatch in interfacial curvature, the circular disk-shaped Marangoni surfers where found to follow a straight line motion directly into the wall along an interface with concave curvature without rotating or changing direction before impacting the wall [168].

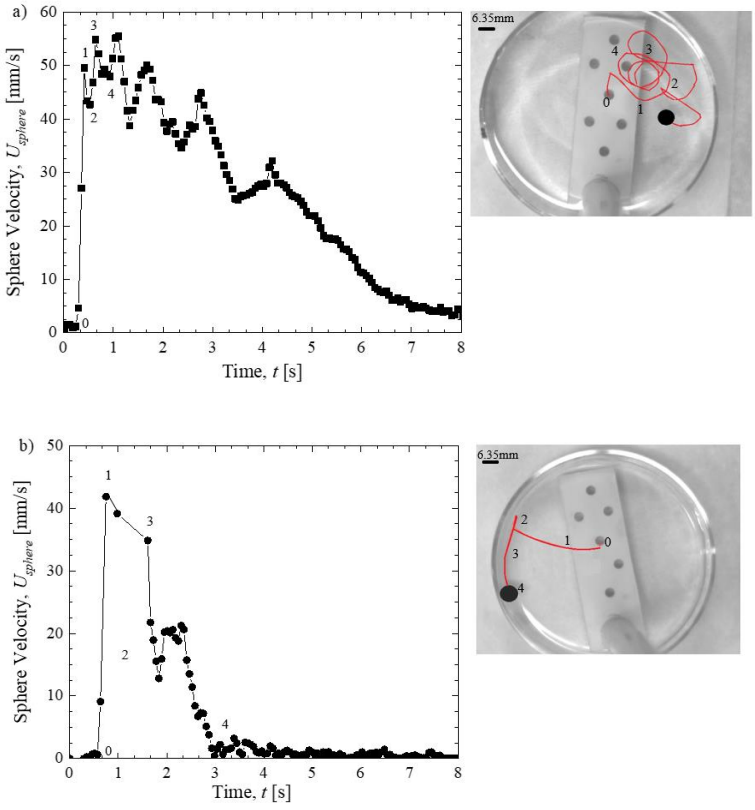
a)
Sphere Velocity, U_{sphere} [mm/s]
Time, t [s]
6.35mm
b)
Sphere Velocity, U_{sphere} [mm/s]
Time, t [s]
6.35mm

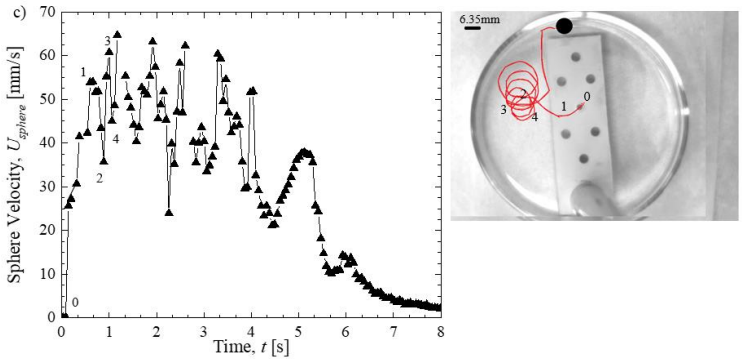

Figure 67. Plot of the sphere velocity magnitude, U_{sphere}, as a function of time, t, for a sphere propelled along an air-water interface using IPA. Results are shown for a) a flat, b) a convex, and c) a concave interface at the boundary of the Petri dish. The images on the right show a trace of the trajectory of the sphere.

In order to further probe the effect of particle symmetry, shape and orientation on the stability, the elliptical disks were also released in a small Petri dish of dimeter D_{dish}=86mm so that their interaction with a boundary could be studied and compared to the results for a spherical particle. Unlike the experiments performed with the spherical surfers, the elliptical surfers are essentially neutrally buoyant in the water and do not distort the interface. As a result, the strength of the interfacial curvature attraction and repulsion observed for the case of spheres are not expected to be as significant here. Thus, to simplify the discussion, the focus of the experiments for the elliptical surfers will be for the case of a flat interface along the wall of the Petri dish. In these experiments presented in Figure 68, the elliptical surfers were propelled by 100wt% IPA. For both the AR=1.5 and AR=2 elliptical disk, a similar result was observed. While moving along its major axes, the elliptical surfers were observed to deviate from their straight-line path and to start spinning as they approached the boundary wall. An example of the AR = 1.5 elliptical disk is shown in Figure 68a. Interestingly, under these very same conditions, the elliptical surfers traversing along their minor axes were not observed to spin. Instead, as seen in Figure 58b,

these surfers approached the wall of the Petri dish maintaining a straight-line path before ultimately hitting the boundary wall and coming to rest.

For the case of AR=1.5 elliptical disk traveling along its major axis, the maximum Reynolds number was found to be Re_{max}=440±20 and the Reynolds number prior to rotation was found to be Re=280±15. Whereas, for the case of AR=1.5 elliptical disk traveling along its minor axis, the maximum Reynolds number was found to be Re_{max}=450±10 without rotation. For the case of AR=2 traveling along its major axis, the maximum Reynolds was found to be Re_{max}=330±15 and the Reynolds number prior to rotation was found to be Re=240±10. Whereas, for the case of AR=2 traveling along its minor axis, the maximum Reynolds number was Re_{max}=480±20 without rotation. The presence of a boundary did not appear to affect the stability of either aspect ratio elliptical surfer as long as it was traveling long its major axis. For example, if one compares the AR=1.5 elliptical surfer for similar maximum Reynolds number of Re_{max}=440 in a bounded and an unbounded case, both were observed to rotate at the same Reynolds number prior to rotation of Re=280. The presence of a flat interface near a boundary, similarly had no effect on the stability of circular disk studied previously [168]. This is very different from the results for the axisymmetric sphere for which the presence of a mismatch in interfacial curvature near the bounding wall cause the surfer to be less stable and more likely to rotate even for a flat interface.

Perhaps, even more interesting is the case of an elliptical surfer traveling along its minor axis for which the presence of the bounding wall was found to stabilize the motion for both aspect ratios studied. For example, an elliptical Marangoni surfer traveling along its minor axis on an unbounded interface and reaching the same maximum Reynolds

number of Re_{max}=440, was found to rotate as it decelerated to Re=250 and Re=140 for an aspect ratio of AR=1.5 and AR=2, respectively. For the bounded case, even at 100wt% IPA and Reynolds numbers well above Re > 400, elliptical disk surfers traveling along their minor axis were never observed to rotate as they approached the boundary wall. The physical origin of the difference in stability based solely on the orientation of an elliptical Marangoni surfer is not entirely clear. However, these results might have some utility. The higher stability of an elliptical disk while traversing along the minor axis can be used to direct Marangoni flow driven assembly. This kind of assembly is quite different from the investigations performed on the assembly due to interface curvature, for which, the assembly between two particles is observed at the site of maximum deviatoric curvature. For a neutrally buoyant elliptical disk-shaped Marangoni surfer traveling along its minor axis, the assembly will most likely occur along the major axis of the elliptical disk whereas, if the surfer were not neutrally buoyant, the smallest interfacial curvature would exist. This side-to-side rather than tip-to-tip assembly provides new physical tool to guide self-assembly of objects along an interface and provides control over the spatial arrangements and final assembly of elliptical disk-shaped Marangoni surfers.

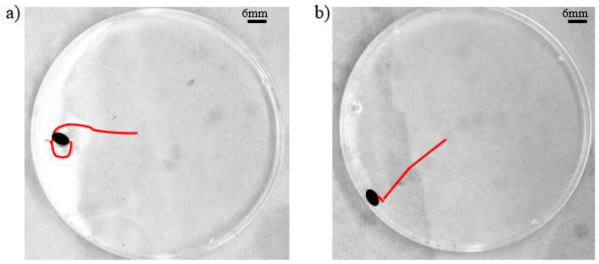

Figure 68. The trace of the trajectory of interaction of an *AR*=1.5 elliptical disk shaped surfer with a flat interface at the boundary for its motion along its a) major axis and b) minor axis.

6.4 Conclusion

In the experiments presented in this paper, the dynamics of both spherical and elliptical disk-shaped Marangoni surfers were studied at moderate Reynolds numbers to better understand the role that particle shape, symmetry and orientation play on motion and stability. The Marangoni surfers were propelled by applying either soap or isopropyl alcohol through a dip coating process to the backside of each sphere and elliptical disk. Both IPA and soap were used to reduce the surface tension of water. The elliptical disks were neutrally buoyant and did not distort the air-water interface. However, due to the density, shape and contact angle with the water, the air-water interface around the spheres was deformed resulting in a convex interfacial curvature that helped support the unsubmerged weight of the spheres. The flow dynamics around the surfers was investigated through particle image velocimetry. In addition to studying the motion of the sphere and elliptical disks on an unconfined interface, the effect of the interaction between the surfers and the boundary with varying interfacial curvature was also investigated.

For the case of soap as the propulsion agent, the velocity of the surfers went through a maximum before a steady-state straight-line translation velocity was achieved. For the case of the sphere, a steady state velocity and Reynolds number of U_{sphere}=4mm/s and a Re=25 was achieved. However, for the case of IPA as the propulsion agent, a steady-state translational velocity was never achieved. In all cases, a fast acceleration, more rapid than the case of soap, was observed until a maximum velocity was achieved. Beyond this maximum velocity, a continuous deceleration occurs until the motion had ceased. For the case of a sphere propelled by 100wt% IPA, a maximum velocity of U_{sphere} = 120mm/s and a maximum Reynolds number of Re = 750 was observed. For the case of an elliptical disk

propelled by 100wt% IPA, similar velocities were achieved when the elliptical disk was propelled along its minor axis. However, when the elliptical disk was propelled along its major axis, a 50% increase in velocity was observed due to its decreased drag coefficient. This variation in the maximum velocity clearly shows the effect of geometry and orientation can have on the steady motion of the surfers.

As the velocity of the surfers was increased with increasing concentration of IPA, a pair of counter-rotating attached vortices were observed to form to the side of the sphere and elliptical disks. These vortices appeared near the equator of the sphere. For the elliptical disks, the vortices appeared much further towards the wake in both orientations. These attached vortices were found to play a critical role in the stability of the straight-line motion of the surfers. A critical maximum Reynolds number was found beyond which a transition from a straight-line translational motion to a rotational motion was observed for each surfer and surfer orientation. This rotational motion was only ever observed after the surfer had gone through a maximum in its velocity and had begun to decelerate. Two critical Reynolds number conditions were observed for the transition from a translational to rotational motion; a maximum Reynolds number achieved during the transient motion of the surfer and a Reynolds number during the deceleration phase at which the surfer begins to rotate. Just prior to rotation, the flow field was observed to become asymmetric and one of the vortices attached to the side of the sphere was observed to shed. The unbalanced torques resulting from vortex shedding destabilized the straight-line translational motion of the spherical Marangoni surfers and forced the spheres to rotate and begin to follow an orbital path.

For the sphere, a critical maximum Reynolds number of $Re_{\max}$=285 was found. At that flow rate, rotation was observed after the sphere decelerated to Re = 90. The sphere was found to be more stable than similarly sized circular disk-shaped Marangoni surfers which was found to have a critical maximum Reynolds number of Re_{crit} = 180 [170]. This highlights the importance of surfer shape below the water line on stability. The stability of the elliptical disks were found to be strongly linked to their aspect ratio and their orientation. Independent of orientation, increasing the aspect ratio of the elliptical disk was found to make the disk more unstable. Additionally, at a given aspect ratio, elliptical disks traveling along their major axis where found to be more unstable than elliptical disks traveling along their minor axis or for that matter spheres or circular disks. Take for example an elliptical disk traveling along its major axis. For these surfers, a transition from straight-line motion to rotational motion was observed once a maximum Reynolds number of Re_{max}=180 and Re_{max}=120 was obtained for aspect ratios of AR=1.5 and AR=2, respectively. The same surfers traveling along their minor axis were significantly more stable up until Re_{max}=330 and Re_{max}=240. Thus, surfer geometry, symmetry and orientation plays a large role on its stability.

The surfer geometry was also found to have a significant impact on the rotation rate. Increasing the aspect ratio of the elliptical disk was found to increase the rotation rate. Additionally, the rotation rate of the non-axisymmetric elliptical disks was found to be more than an order of magnitude larger than the axisymmetric circular disks and spheres. It is clear from these observations, that breaking the surfer symmetry to produce a high aspect ratio elliptical disk designed to translate along its major axis would be an excellent

approach towards designing high efficiency Marangoni propelled rotors, propellers and mixers.

By allowing the spheres and the elliptical disks to interact with the edge of the Petri dish, the effects of the boundary and, in the case of the sphere, interface curvature were investigated. The presence of a rigid wall leads to an adverse pressure gradient necessary to bring the interfacial flow to rest. This adverse pressure gradient also decelerated the surfers as they approaches the wall and can apply a torque to the sphere if they do not approach the wall along a perfectly radial flow trajectory. As a result, even on a flat interface, the presence of the boundary wall can cause the surfer to rotate. The major difference between the elliptical disks and the spheres is that the elliptical disks are neutrally buoyant and do not deform the interface around them. On the other hand, the spheres float below the interface resulting in a convex interfacial curvature around them. When the interface at the boundary of the Petri dish was flat, the repulsive force due to the mismatch in interface curvature around the sphere and near the boundary destabilized the sphere causing it to rotate at a maximum Reynolds number significantly lower, Re_{crit}=190, than that observed for the unbounded case. Making the interface near the boundary concave increased this repulsive force further destabilizing the sphere, while making the interface convex resulted in an attractive force that fully stabilized the motion of the sphere at all Reynolds numbers tested.

For the case of an elliptical disk approaching the boundary of the Petri dish along a flat interface, the orientation of the surfer had a significant impact on its stability. For the elliptical disks traveling along its major axis, the presence of the boundary had little effect on its stability. The critical Reynolds number for rotation was statistically the same as the

unbound case. However, for the elliptical disk traveling along its minor axis, the presence of the bounding wall was found to completely stabilize the motion of the surfer. Even at 100wt% IPA and Reynolds numbers beyond $Re_{max} > 400$, no rotational motion was observed. This observation was quite different from the case of the axisymmetric spheres and circular disks [170] and suggests that surfer shape can be utilized to control the orientation and spatial arrangement of assemblies of Marangoni propelled surfers.

6.5 Acknowledgements

The authors would like to thank NSF for financial support of this research under grants CBET – 1705519 (J.P.R.) and CBET-1749634 (H.M.).

6.6 Publication

The work described in this chapter has been submitted to the Physical Review Fluids Journal (Under Review). The complete reference is S Sur, H Masoud and J P Rothstein "The Effect Of Shape On Motion and Stability Of Marangoni Surfers", 2019).

CHAPTER 7

REVERSE MARANGONI PROPULSION

7.1 Introduction

Surface tension gradients are known to induce motion of a floating solid fragment on a liquid interface. This mechanism has been employed to drive miniaturized objects on a water surface, which could potentially serve as rotators, mixers, locomotives, and so on. To properly apply these objects, it is important to understand their motions. In the past, Marangoni effect has been used for propulsion of small objects attached to a fluid-fluid interface. Recently Sur et al. [168] have experimentally looked at the Marangoni propulsion of objects of different shapes- disk, sphere and ellipses. In their work they

performed a parametric study on the effect of varying propulsion agent on the mode of motion of the objects and also on its stability. Through their work they have demonstrated that when inertia dominates, the Marangoni surfers undergo a transition from a linear path to a rotational motion beyond a critical Reynolds number. This critical Reynolds number varied based on shape of the Marangoni surfers and also on the axis of release. In biological systems, self-induced Marangoni propulsion has been observed in organisms ranging in size from bacteria to water-walking insects. For example, surface-associated bacteria such as *Pseudomonas aeruginosa* have been shown to use signaling molecules exuded from their bodies to reduce the local surface tension. They have been observed to use the resulting Marangoni flow to rapidly migrate across the air-water interface towards nutrient-rich regions ripe for colonization. In the case of water-walking insects like Dianous (rove beetle) and Velia (small water strider), these insects have been shown to secrete surface-active materials to boost their water walking speed in emergency situations. Surface tension driven motion of interface-bound particles has been investigated theoretically as well. For instance, Lauga and Davis [175] analytically calculated the propulsion speed of an active disk in the absence of inertia. The derivations involve simultaneously solving for the Stokes and Laplace equations for, respectively, the flow of the liquid and the transport of the released chemical species. The calculations showed that the translational propulsion speed is independent of the size of the disk. A similar study was also carried out by Würger [174] for a spherical particle. Masoud and Stone [176] used the reciprocal theorem to derive closed-from expressions for the propulsion speed of chemically active oblate and prolate spheroids. Employing a Fourier spectral method, Masoud and Shelley [177] examined the collective surfing of many interface-trapped active particles.

Experiments and theoretical studies have received much attention for Marangoni propulsion in an unbounded domain but very few studies are available for the case of Marangoni propulsion in a bounded or confined domain located below the air-water interface has not received much attention. In the work of Vandadi et al. [152] they have theoretically investigated the effect of confinement on the mode of motion of a chemically activated particle of two different shapes – an infinitely think cylindrical disk and a sphere. Generally, it has been observed that in Marangoni flow induced propulsion the surfers are propelled in the direction of higher surface tension. In the study by Vandadi et al [152] , they observed that the surfers propelled themselves in the lower surface tension direction depending on their geometry and the thickness of the liquid layer sandwiched between the interface and the wall contrary to the common instinct of being pulled towards the higher surface tension direction. These investigation were performed for low Reynolds number and Peclet number, $Re \sim 10^{-4}$ and $Pe \sim 10^{-3}$ (Inertia neglected). Reverse Marangoni motion was observed for the case of a finite thickness sphere whereas for the case of the infinitely thin cylindrical disk no reverse motion was observed. Although, reverse Marangoni phenomenon has been investigated theoretically there are no currently available experimental investigation in the literature. In this paper, we have experimentally investigated for the first time the effect of confinement below the air-water interface on the mode of motion of a finite thickness cylindrical disk and a hemi-sphere between low to high Reynolds number- Inertia dominated. Particle image velocimetry measurements were performed in order to better understand the flow fields underneath the Marangoni swimmer and how it varies with variation in the confinement. At higher water depths, the disk was pulled towards the higher surface tension direction and at a higher speed. As the depth of

water was reduced, the speed was found to reduce below a certain depth and finally reversed its direction and move towards the lower surface tension direction below a critical water depth. Along with critical depth, it was found that the Reynolds number also played a critical role in flow reversal. At higher Reynolds number, no reverse phenomenon was observed as inertia dominated the motion of the disk whereas at low Reynolds numbers and at the critical Depth, flow reversal was observed.

7.2 Experimental Setup

The experiments were performed in a rectangular flow cell with a maximum length of L=560mm, width of W=45mm and maximum water depth of H=20mm. The depth of the water in the rectangular flow cell was varied in order to investigate the effect of varying confinement depth on the propulsion of the cylindrical disk and hemisphere due to Marangoni flow. The depth of water in the channel was varied from H=1.8mm to H=10mm. The Marangoni flow was introduced by dip coating the disk and hemispheres into a solution of water and 50%soap (DAWN) in a water to a depth of 1mm as shown in Figure 69. The cylindrical disk of D_{disk}=4.5mm and thickness t=1.5mm and hemisphere of diameter $D_{hemisphere}$=4.75mm were fabricated from polydimethlysiloxane (PDMS) which has a density of ρ=965Kg/m^3. The surface tension of the soap was found to be σ = 30mN/m. The disk or the hemisphere was carefully placed on the air-water interface and released using tweezers. Particle image velocimetry (PIV) measurements were performed using a commercial code to analyze the flow field induced by Marangoni flow underneath the Marangoni swimmer and on the interface. Light reflecting tracer particles which were illuminated by an Argon-ion laser light sheet of thickness 1mm was used to perform the PIV measurements. The laser was oriented either parallel to the air-water interface just

below the surface in order to obtain the interfacial velocity profiles or normal to the surface passing up through the fluid from below the rectangular channel. Through this second configuration the vector fields underneath the air-water interface was measured. A high speed camera at a maximum frame rate of 110fps was used to capture the images.

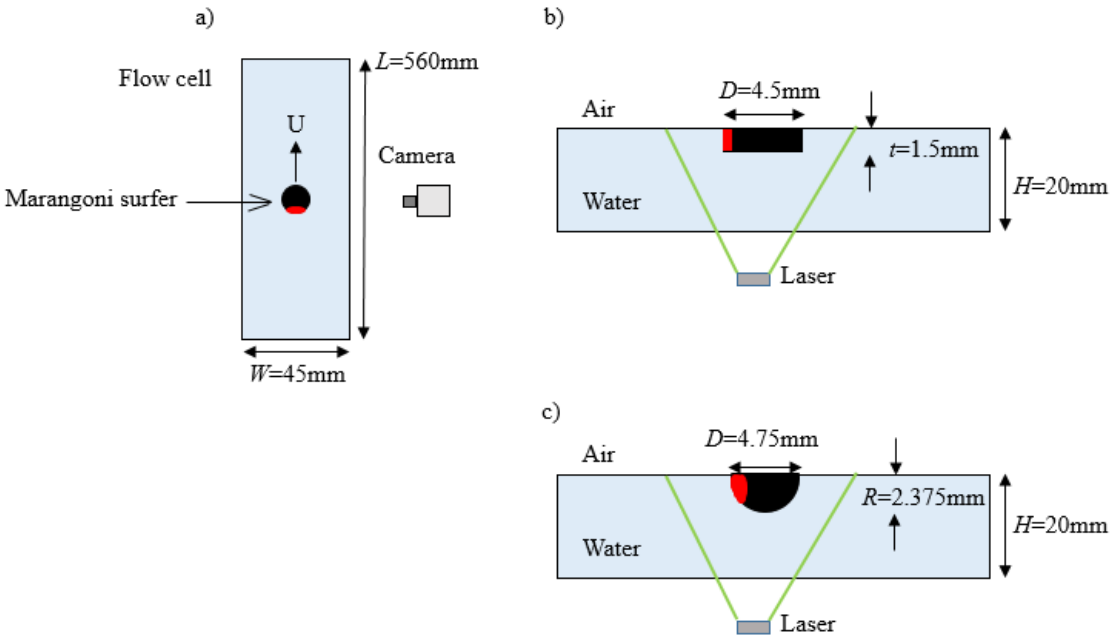

Figure 69. A schematic of the experimental setup of the flow cell a) the top view of the disk or hemisphere floating on the liquid interface is shown. The side view of the flow cell with the laser sheet underneath the liquid interface and the interface is shown around b) a cylindrical disk and c) a hemisphere. The disk and the hemisphere is propelled by Marangoni flow induced by soap/alcohol released on the back in the area denoted in the red region.

7.3 Results and Discussion

In this section, disk and hemisphere velocities as well as the Particle Image Velocimetry (PIV) measurements of the flow field underneath the air-water interface are presented as a function of the depth of the water and the degree of confinement. As seen in Figure 70, a plot of normalized velocity profile, U_{disk}/U_{∞}, of the disk and hemisphere are shown as a function of normalized water depth in the channel. The velocity of the disk and hemisphere have been normalized by the unconfined velocity, U_{∞}, of the disk and hemisphere, U_{∞}=15mm/s and U_{∞}=8mm/s. This corresponds to a Reynolds number of Re=$\rho UD/\mu$=68 for the disk and Re=36 for the hemisphere. As seen in Figure 70, for both the disk and hemisphere once the water depth is greater than $H\geq$10mm, the particle velocity reached an asymptote and did not feel the effect of confinement underneath the air-water interface. In the case of the disk, as the normalized water depth was varied from $3<H_{water}/t_{disk}<7$, there was no variation in the velocity of the disk. As the water depth was further reduced, a reduction in the velocity of the disk was observed. At a water depth of H/t_{disk}=1.33, the disk was observed to come to rest even as the fluid around it continued to flow. At this velocity, the interfacial tension pulling the disk to the right was exactly balanced by the drag forces to the left induced by the flow observed in figure 71 required to maintain continuity. A crossover from a positive normalized velocity to a negative normalized velocity was observed at H/t_{disk}=1.22. At that point, the interfacial forces are

now smaller than the shear forces that is experienced by the portion of disk below the water interface resulting in reverse Marangoni flow. The magnitude of the reverse flow of the disk was found to be only U/U_∞=0.03. The strength of the reverse flow was very weak. This result is consistent with the magnitude of reverse Marangoni flow observed by Vandadi et al. [152] for Marangoni surfers at zero Reynolds number. Interestingly, their calculations did not predict reverse flow for an infinitely thin disk but did for a hemisphere. Thus, those experiments demonstrate importance of disk thickness as reverse Marangoni flow clearly necessitates propulsion into the bulk flow. By contrast, Vandadi et al [152] did predict reverse flow for hemispheres. For the case of hemisphere too reverse flow was observed but at a lower *H/R* value. In contrast to disk, no variation in the velocity of the hemisphere was observed as the normalized water depth was varied from $4<H_{water}/t_{disk}<1.2$. The hemisphere was observed to come to rest at *H/R*=1.1 and the reverse flow was observed at *H/R*=1.05. The magnitude of the reverse flow of the hemisphere was found to be only U/U_∞=0.0025. The strength of the reverse flow for the case of hemisphere was much weaker as compared to the case of disk as much as by 10%. The transition from U/U_∞=1 to U/U_∞=0.0025 for the case of hemisphere was much sharper as compared to the transition for the case of disk.

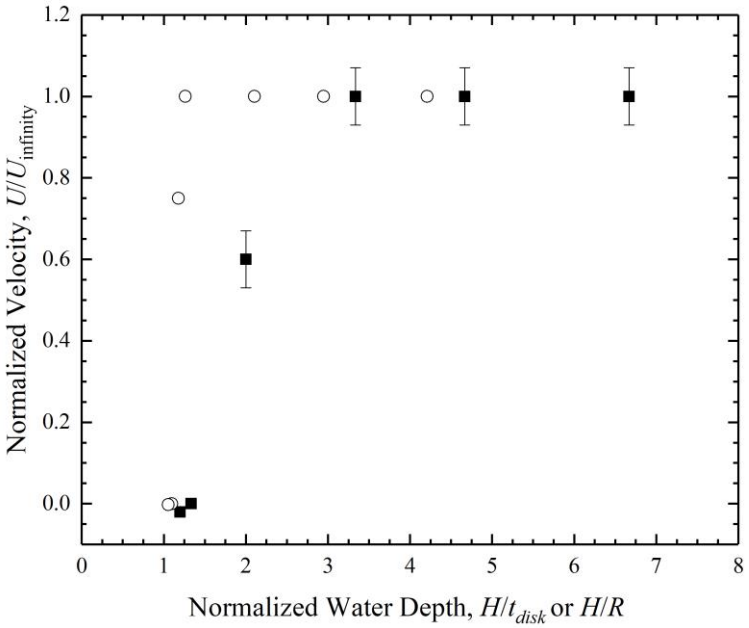

Figure 70. The normalized propulsion speed U/U_∞ as a function of the thickness of the water layer H/t_{disk} for (■) disk-shaped and H/R for (○) hemispherical shaped surfers propelled by a Marangoni flow generated by soap released from the back side of the surfer.

In Figure 71a-e, the flow field underneath the disk is shown as a function of varying water depth. As seen in Figure 71a-d, the interface appears to dilate, spreading radially from a stagnation point downstream of the trailing edge of the disk. The stagnation point in the PIV data represents the location of the minimum in the interfacial tension. As the confinement was increased the location of the stagnation point on the interface moved closer to the disk. For the case of H/t_{disk}=1.22, as shown in Figure 71e, the stagnation point moved to within 0.5mm from the trailing edge of the disk. Below the disk, an attached clockwise rotating vortex was observed. The vortex originated from the reversed flow in the bulk that is required in order to maintain the conservation of mass. Similar vector fields have been shown in the work of Sur et al. [168] for unconfined motion of disks. As the depth of water was reduced, the clockwise rotating vortex attached underneath the disk was compressed with its vorticity reduced and finally disappear as the water depth reached

H/t_{disk}=1.22 and reverse Marangoni flow was observed. In addition to a vortex attached to the bottom of the disk, a large vortex downstream of the disk, beyond the stagnation point was observed in each case. With increasing confinement, the vortex in the wake of the disk became more shallow, with its center moving towards the interface. Up until this point, all the data that has been presented for the disk has been for cases for which reverse Marangoni flow was observed if the confinement was increased sufficiently. However, our experiments have shown that the presence of reverse Marangoni flow of a disk is Reynolds number dependent. At higher Reynolds number, the reverse motion of the disk was not observed. Above an infinite depth Reynolds number of Re>20, reverse motion of the disk was not observed even at confinement of H/t_{disk}=1.2. If however, the infinite depth Reynolds number was decreased below the Re=18 shown in Figure 71, reverse Marangoni flow was observed with a cross-over value of H/t_{disk} that increased with decreasing Reynolds number. Thus inertia appears to dampen out the effects of the reverse flow predicted by Vandadi et al [152] at Re=0.

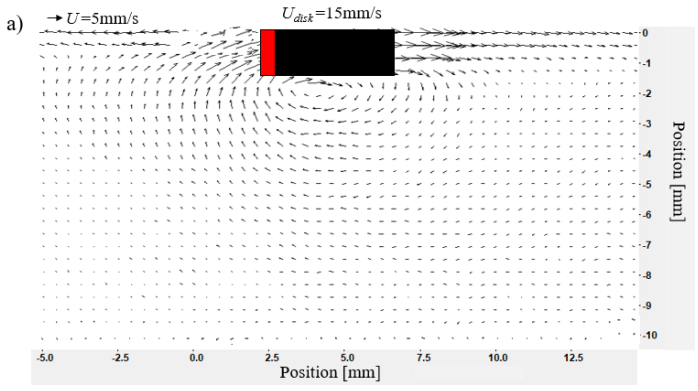

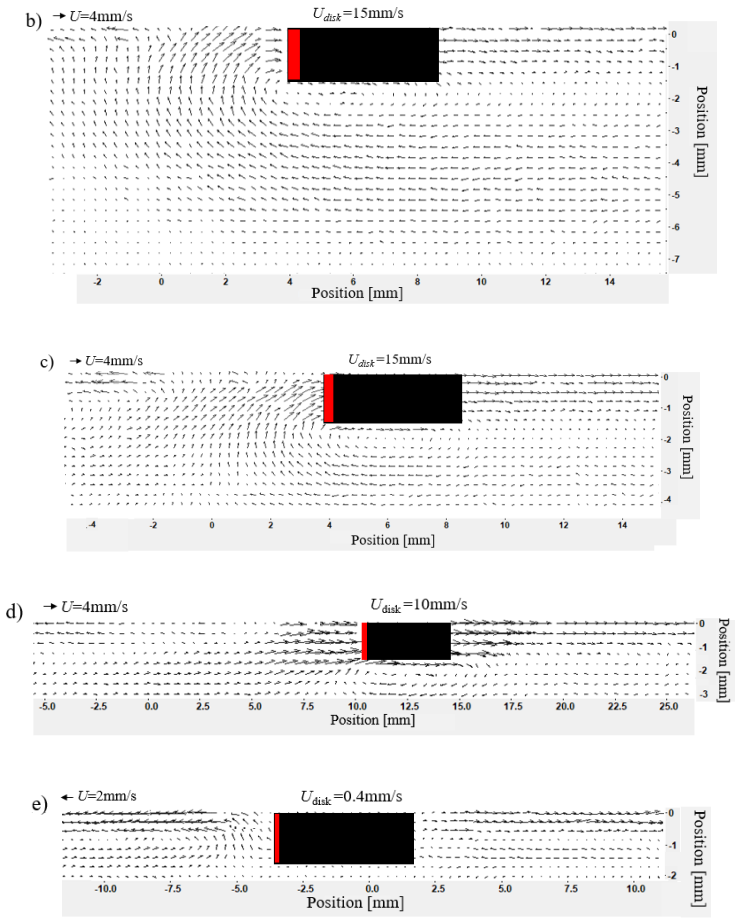

Figure 71. Plot of the particle image velocimetry measurements of the flow field underneath a floating disk propelled by the Marangoni flow induced by soap released on the left side of the disk in the area denoted in red for varying depths of water a) 10mm (H/t_{disk} =6.66), b) 7mm (H/t_{disk} =4.66), c) 5mm (H/t_{disk} =3.33), d) 3mm (H/t_{disk} =2) and e) 1.86mm (H/t_{disk} =1.22).

In Figure 72a-d, the flow field underneath the hemisphere is shown as a function of varying water depth. General characteristics of the flow field were similar to what was observed for the case of the disk. The dilation of the interface and presence of a stagnation point in the wake along with an attached clockwise rotating vortex attached underneath the sphere was observed. The strength of the attached vortex was lower as that compared to the disk at similar confinements. Similar to the observation made in the case of the disk,

the attached vortex became shallow as the confinement was increased and finally disappeared as the water depth reached H/R=1.17. Reverse Marangoni flow was observed at H/R=1.05. Even for the case of the hemisphere, the reverse Marangoni motion of the sphere was found to be Reynolds number dependent. Above an infinite depth Reynolds number of Re>10, reverse motion of the hemisphere was not observed even at confinement of H/R=1.05. If however, the infinite depth Reynolds number was decreased below the Re=8 the reverse Marangoni motion was observed. As compared to the case of the disk, the infinite depth Reynolds number was 55% lower for the case of the sphere to achieve the reverse Marangoni motion.

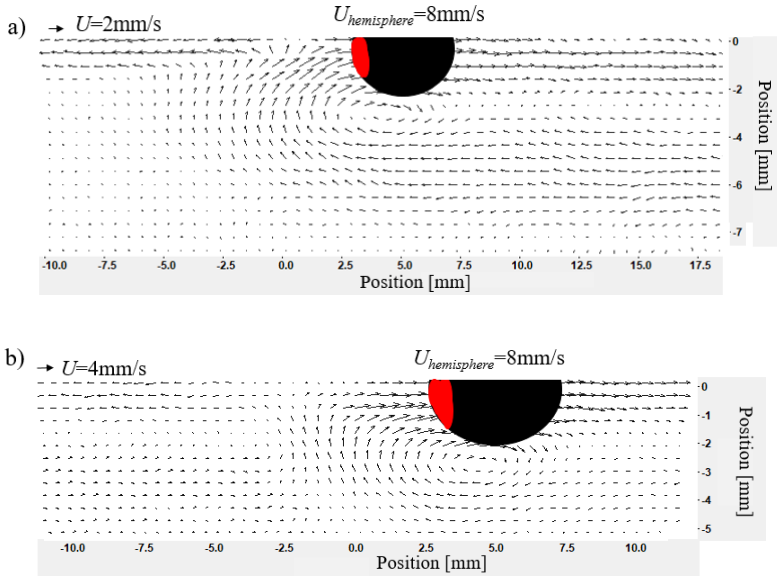

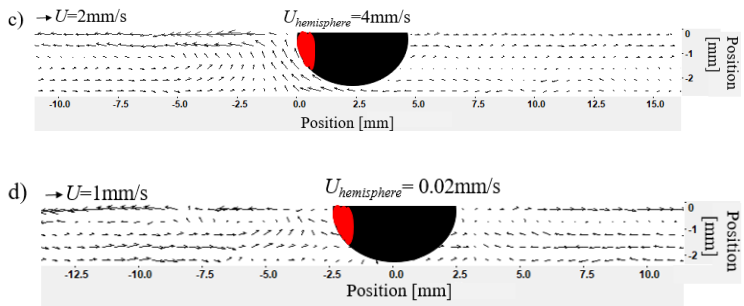

Figure 72. Plot of the particle image velocimetry measurements of the flow field underneath a floating hemisphere propelled by the Marangoni flow induced by soap released on the left side of the disk in the area denoted in red for varying depths of water a) 10mm (*H/ R* =4.2), b) 5mm (*H/ R*=2.1), c) 2.8mm (*H/R* =1.17) and d) 2.5mm (*H/R* =1.05).

7.4 Conclusion

We have experimentally investigated the effect of confinement on the Marangoni propulsion of a cylindrical disk and a hemisphere. Through our study we have demonstrated that at a certain critical confinement the Marangoni surfers propelled themselves in the direction of lower surface tension. Although reverse Marangoni propulsion was observed both for the case of disk and sphere, the magnitude of the reverse propulsion observed for the case of disk was approximately 20 times higher as compared to that of the hemisphere. Also, for the case of hemisphere the critical depth required to observe reverse Marangoni propulsion was achieved at a normalized water depth of H/t_{disk}=1.05 as compared to H/R=1.22 for the case of the disk. This also highlights the effect of shape of Marangoni surfers on the reverse Marangoni propulsion. During our investigation it was observed that higher Reynolds number reverse propulsion was not observed either for the case of disk or hemisphere. Thus, along with the critical depth or confinement the reverse Marangoni propulsion was found to be a function of Reynolds

number also. The critical infinite depth Reynolds number was found to be *Re*=18 and *Re*=8 for the case of disk and hemisphere respectively. At higher Reynolds number inertia appeared to dampen out the effect of reverse flow observed. In the works of Vandadi et al [178] they predicted reverse Marangoni propulsion for cases where Re<<1, but in our case we observed reverse Marangoni propulsion for Re>1 and Pe>1. This also shows that Reverse Marangoni propulsion can be achieved for cases where transport is convection dominated and also where inertia is dominant.

7.5 Acknowledgement's

The authors would like to thank NSF for financial support of this research under grants CBET – 1705519 (J.P.R.) and CBET-1749634 (H.M.).

7.6 Publications

The work described in this chapter is under preparation.

CHAPTER 8

FUTURE WORK

In the first two chapter we looked at the high temperature extensional rheology of Polycarbonates and Polycarbonates mixed with flame retardant salts. We were able to predict the dripping behaviors and its UL94 ratings based on the temperature at which the extensional viscosity was found to diverge. We looked at the effect of different molecular architecture and addition of various flame retardant salts on its dripping behavior. In the future work it would be interesting to look at different polymer systems. For example,

Polyetherimide whose glass transition temperature is T_g=217^{o}C. Since these systems are stable at temperatures close to T=360^{o}C, it's almost impossible to perform shear rheology measurements to detect any temperature effects. Thus using our high temperature extensional rheology instrument it would be interesting to see how this polymer systems behaves predict its UL94 ratings. One could also look at the effect of addition of heat stabilizers, fillers (different types of fillers), and other flame retardant salts on its dripping behavior. In depth thermal analysis should also be performed along with the extensional rheology measurements in order to better understand the mechanism of degradation. Extensional rheology measurements combined with thermogravimetric and differential scanning calorimetry measurements can be a powerful tool in prediction and optimization of better anti-dripping polymers.

Fused deposition modelling (FDM), which is the most widely used 3D printing technique uses a thermoplastic filament which is then extruded layer by layer to create 3D structures. These extrusion of thermoplastic happens at temperatures between T=220^o to T=250^o. To form filaments, the polymer should have enough extensional viscosity, else if the polymer is not stable or drools at those temperature then the printing process is affected. Most common polymers that are used are ABS (Acrylonitrile butadiene styrene), PLA (Polylactic acid), Nylon (PA), PEI (Polyethylenimine). A study can be performed using the high temperature extensional rheometry measurements to have an idea about the formation of filaments. The formation is critical in the printing process. Also, at such temperatures, no crosslinking should happen which can also be detected through our measurement technique. One can further probe the factor's affecting the filament formation. For example, ambient temperature. As the hot thermoplastic comes out of the nozzle, there is

a sudden decrease in the temperature. How does this temperature affect the filament formation? By heating upto the desired temperature, and colling it down instantly with the help of air or nitrogen pumped into the surrounding environment and then performing the stretch could help us investigate these effects.

In chapter 3 and 4 we discussed about the use of a newly developed technique known as “Dripping onto substrate Capillary breakup extensional rheomtery”. This is a very powerful technique which have pushed the measurement limitations of extensional rheology measurements. This technique was used to probe the effect of addition of different polymer to inks and predict its breakup behavior in drop on demand techniques (inkjet printing technique). In our study we looked at the effect of addition of different binders (varying molecular weight and molecular architecture) on the droplet breakup dynamics. An ink consists of various other components such as – pigments, solvent, surfactant and other necessary additives. They are all mostly polymer systems and affect the breakup dynamics. Thus using the DOS-CaBER technique the effect of all these single components can be measured and can be used to better predict the jettability of the inks. One can also look at the effects of varying chain lengths, finite extensibility of polymer chains, rigidity of polymer chains, surface tension, density and viscosity effects on the droplet breakup dynamics. This technique can be used in optimization of different components in the ink and improve the performance of the inks. Nowadays, conductive inks are gaining a lot of attention. In these conductive systems mostly silver nanoparticles are used. Thus a parametric study can be performed to look at the effects of addition of nanoparticles on the jettablity and droplet breakup dynamics. One can also look at the effects of varying

morphology, particle size and size distribution of these nanoparticles on the performance of the inks- Jettablity and its breakup.

In the last three chapters- 5, 6 and 7 we have investigated the Marangoni propulsion of surfers of various shapes. We also investigated the effect of varying propulsion agent, effect of confinement on the mode of motion of Marangoni surfers of varying shape. We have also looked at the interaction of Marangoni surfers with boundaries having different curvatures. One interesting step could be to look at the interaction and assembly of multiple Marangoni surfers. In chapter 6, we observed that an elliptical disk shaped surfer is much more stable while traversing along its minor axis than compared to its minor axis. Thus, one can further investigate assembly of elliptical disk shaped surfers in two different orientations. Firstly by starting with two elliptical disk and investigate their interactions when they are propelled towards each other with different velocities and angles. Different velocities can be achieved by using different propulsion agent- Soap or IPA. One can create a map of interaction based on the velocity and angle of propulsion and then proceed to interaction of multiple swimmers. It would be also interesting to look at the effect of increasing aspect ratio on mode of motion and the stability of Marangoni surfers. In chapter, we have look at the effect of confinement on the mode of motion of the Marangoni swimmer. We observed that below a certain critical confinement, reverse Marangoni propulsion was achieved. This phenomenon can be used as sorting techniques. One can investigate the possibility of the sorting by using an inclined rectangular channel which will have a varying water depth across its length and can sort swimmers of different thickness as the thicker swimmers would come to a stop or have reverse flow as soon as it

approaches the rectangular channel with shallow waters whereas for the case of thinner swimmers it will keep follow its line of trajectory.

BIBLIOGRAPHY

1. Laoutid, F., et al., *New prospects in flame retardant polymer materials: from fundamentals to nanocomposites.* Materials Science and Engineering: R: Reports, 2009. **63**(3): p. 100-125.

2. Beyler, C.L. and M.M. Hirschler, *Thermal decomposition of polymers.* SFPE handbook of fire protection engineering, 2002. **2**: p. 32.

3. Pielichowski, K. and J. Njuguna, *Thermal degradation of polymeric materials*. 2005: iSmithers Rapra Publishing.

4. Lu, S.-Y. and I. Hamerton, *Recent developments in the chemistry of halogen-free flame retardant polymers.* Progress in Polymer Science, 2002. **27**(8): p. 1661-1712.

5. Wang, Y. and J. Zhang, *Thermal stabilities of drops of burning thermoplastics under the UL 94 vertical test conditions.* Journal of hazardous materials, 2013. **246**: p. 103-109.

6. Rayleigh, L., *On the instability of jets.* Proc. Lond. Math. Soc., 1879. **10**: p. 4-13.
7. Stone, H.A., *Dynamics of Drop Deformation and Breakup in Viscous Fluids.* Annu. Rev. Fluid Mech., 1994. **26**: p. 65.

8. McKinley, G.H., *Visco-elasto-capillary thinning and break-up of complex fluids*, in *Annual Rheology Reviews*, D.M. Binding and K. Walters, Editors. 2005, The British Society of Rheology: Aberystwyth, Wales, UK. p. 1-49.

9. Clasen, C., et al., *Dispensing of Rheologically Complex Fluids: The Map of Misery.* AIChE J., 2012. **58**: p. 3242-3255.

10. McKinley, G.H., *Visco-elasto-capillary thinning and break-up of complex fluids*, in *Annual Rheology Reviews*, D.M. Binding and K. Walters, Editors. 2005. p. 1-49.
11. McKinley, G.H. and T. Sridhar, *Filament Stretching Rheometry.* Annu. Rev. Fluid Mech., 2002. **34**: p. 375-415.

12. Rothstein, J.P., *Transient extensional rheology of wormlike micelle solutions.* Journal of Rheology, 2003. **47**(5): p. 1227-1247.

13. Renardy, M., *A numerical study of the asymptotic evolution and breakup of Newtonian and viscoelastic jets.* J. Non-Newtonian Fluid Mech., 1995. **59**: p. 267-282.

14. Mun, R.P., J.A. Byars, and D.V. Boger, *The effect of polymer concentration and molecular weight on the break-up of laminar capillary jets.* J. Non-Newtonian Fluid Mech., 1998. **74**: p. 285-297.

15. Papageorgiou, D.T., *On the breakup of viscous liquid threads.* Phys. Fluids, 1995. **7**: p. 1529-1544.

16. Liang, J., et al., *Melt elongation flow behaviour of LDPE/LLDPE blends.* Polymer Testing, 2015. **41**: p. 133-139.

17. Huang, Q., et al., *A new look at extensional rheology of low-density polyethylene.* Rheologica Acta, 2016. **55**(5): p. 343-350.

18. Hachmann, P. and J. Meissner, *Rheometer for equibiaxial and planar elongations of polymer melts.* Journal of Rheology, 2003. **47**(4): p. 989-1010.

19. Wagner, M.H. and V.H. Rolón-Garrido, *Constant force elongational flow of polymer melts: Experiment and modelling.* Journal of Rheology, 2012. **56**(5): p. 1279.

20. Baldi, F., A. Franceschini, and T. Riccò, *Determination of the elongational viscosity of polymer melts by melt spinning experiments. A comparison with different experimental techniques.* Rheologica acta, 2007. **46**(7): p. 965-978.

21. Schulze, J.S., et al., *A comparison of extensional viscosity measurements from various RME rheometers.* Rheologica Acta, 2001. **40**(5): p. 457-466.

22. Bach, A., H.K. Rasmussen, and O. Hassager, *Extensional viscosity for polymer melts measured in the filament stretching rheometer.* Journal of Rheology (1978-present), 2003. **47**(2): p. 429-441.

23. Sentmanat, M., B.N. Wang, and G.H. McKinley, *Measuring the transient extensional rheology of polyethylene melts using the SER universal testing platform.* Journal of rheology, 2005. **49**(3): p. 585-606.

24. Park, J.H., et al., *Extensional and complex viscosities of linear and branched polycarbonate blends.* Macromolecular research, 2002. **10**(3): p. 135-139.

25. Kim, H., H. Lee, and J.W. Lee, *Rheological properties of branched polycarbonate prepared by an ultrasound-assisted intensive mixer.* Korea-Australia Rheology Journal, 2007. **19**(1): p. 1-5.

26. Mercier, J., et al., *Viscoelastic behavior of the polycarbonate of bisphenol A.* Journal of Applied Polymer Science, 1965. **9**(2): p. 447-459.

27. Rodd, L.E., et al., *Capillary break-up rheometry of low-viscosity elastic fluids.* Appl. Rheol., 2005. **15**(1): p. 12-27.

28. Anna, S.L. and G.H. McKinley, *Elasto-capillary thinning and breakup of model elastic liquids.* J. Rheol., 2001. **45**(1): p. 115-138.

29. McKinley, G.H. and A. Tripathi, *How to extract the Newtonian viscosity from capilary breakup measurements in a filament rheometer.* J. Rheol., 2000. **44**(3): p. 653-670.

30. Stelter, M., et al., *Validation and application of a novel elongational device for polymer solutions.* J. Rheol., 2000. **44**(3): p. 595-616.

31. Entov, V.M. and E.J. Hinch, *Effect of a spectrum of relaxation times on the capillary thinning of a filament of elastic liquid.* J. Non-Newtonian Fluid Mech., 1997. **72**: p. 31-53.

32. Bazilevsky, A.V., V.M. Entov, and A.N. Rozhkov. *Liquid filament microrheometer and some of its applications*. in *Proc. Third European Rheology Conference*. 1990. Edinburgh.

33. Plog, J.P., W.M. Kulicke, and C. Clasen, *Influence of the molar mass distribution on the elongational behaviour of polymer solutions in capillary breakup.* Applied Rheology, 2005. **15**(1): p. 28-37.

34. Clasen, C., et al., *How dilute are dilute solutions in extensional flows?* Journal of Rheology, 2006. **50**(6): p. 849-881.

35. Yesilata, B., C. Clasen, and G.H. McKinley, *Nonlinear shear and extensional flow dynamics of wormlike surfactant solutions.* Journal of Non-Newtonian Fluid Mechanics, 2006. **133**(2-3): p. 73-90.

36. Kojic, N., et al., *Ex vivo rheology of spider silk.* Journal of Experimental Biology, 2006. **209**(21): p. 4355-4362.

37. He, C., S. Costeux, and P. Wood-Adams, *A technique to infer structural information for low level long chain branched polyethylenes.* Polymer, 2004. **45**(11): p. 3747-3754.

38. Kulicke, W.-M. and R. Kniewske, *The shear viscosity dependence on concentration, molecular weight, and shear rate of polystyrene solutions.* Rheologica acta, 1984. **23**(1): p. 75-83.

39. Najafi, N., et al., *Rheological and foaming behavior of linear and branched polylactides.* Rheologica Acta, 2014. **53**(10-11): p. 779-790.

40. Kruse, M. and M.H. Wagner, *Time-resolved rheometry of poly (ethylene terephthalate) during thermal and thermo-oxidative degradation.* Rheologica Acta, 2016. **55**(10): p. 789-800.

41. Filippone, G., et al., *Time-resolved rheology as a tool to monitor the progress of polymer degradation in the melt state–Part II: Thermal and thermo-oxidative degradation of polyamide 11/organo-clay nanocomposites.* Polymer, 2015. **73**: p. 102-110.

42. Winter, H.H. and F. Chambon, *Analysis of linear viscoelasticity of a crosslinking polymer at the gel point.* Journal of rheology, 1986. **30**(2): p. 367-382.

43. Salehiyan, R., T. Malwela, and S.S. Ray, *Thermo-oxidative degradation study of melt-processed polyethylene and its blend with polyamide using time-resolved rheometry.* Polymer Degradation and Stability, 2017. **139**: p. 130-137.

44. Shangguan, Y., et al., *Study on degradation and crosslinking of impact polypropylene copolymer by dynamic rheological measurement.* Polymer, 2010. **51**(2): p. 500-506.

45. Li, X.G. and M.R. Huang, *Thermal degradation of bisphenol A polycarbonate by high-resolution thermogravimetry.* Polymer international, 1999. **48**(5): p. 387-391.

46. McNeill, I. and A. Rincon, *Degradation studies of some polyesters and polycarbonates—8. Bisphenol A polycarbonate.* Polymer degradation and stability, 1991. **31**(2): p. 163-180.

47. Oba, K., et al., *Characterization of branching and/or cross-linking structures in polycarbonate by reactive pyrolysis− gas chromatography in the presence of organic alkali.* Macromolecules, 2000. **33**(22): p. 8173-8183.

48. Jang, B.N. and C.A. Wilkie, *A TGA/FTIR and mass spectral study on the thermal degradation of bisphenol A polycarbonate.* Polymer Degradation and Stability, 2004. **86**(3): p. 419-430.

49. Carroccio, S., C. Puglisi, and G. Montaudo, *Mechanisms of thermal oxidation of poly (bisphenol A carbonate).* Macromolecules, 2002. **35**(11): p. 4297-4305.

50. Montaudo, G. and C. Puglisi, *Thermal decomposition processes in bisphenol a polycarbonate.* Polymer degradation and stability, 1992. **37**(1): p. 91-96.

51. Pretsch, E., et al., *Structure determination of organic compounds*. 2000: Springer.

52. Sur, S., M. Chellamuthu, and J. Rothstein, *High-temperature extensional rheology of linear, branched, and hyper-branched polycarbonates.* Rheologica Acta, 2019: p. 1-16.

53. Laoutid, F., et al., *New prospects in flame retardant polymer materials: from fundamentals to nanocomposites.* Materials Science and Engineering: R: Reports, 2009. **63**(3): p. 100-125.

54. Ban, D.-M., et al., *A novel non-dripping oligomeric flame retardant for polyethylene terephthalate.* European Polymer Journal, 2004. **40**(8): p. 1909-1913.

55. Horrocks, A., et al., *Developments in flame retardant textiles–a review.* Polymer Degradation and stability, 2005. **88**(1): p. 3-12.

56. Wu, N., C. Ding, and R. Yang, *Effects of zinc and nickel salts in intumescent flame-retardant polypropylene.* Polymer Degradation and Stability, 2010. **95**(12): p. 2589-2595.

57. Jenewein, E., B. Nass, and W. Wanzke, *Synergistic flame retardant combination of salts of 1-hydroxy-dihydrophosphole oxides and/or 1-hydroxyphospholane oxides and nitrogen compounds for use in polymers*. 2003, Google Patents.

58. Zhang, Y., et al., *Phosphorus-containing copolyesters: the effect of ionic group and its analogous phosphorus heterocycles on their flame-retardant and anti-dripping performances.* Polymer, 2015. **60**: p. 50-61.

59. Hu, Z., et al., *Flame retardation of glass-fibre-reinforced polyamide 6 by a novel metal salt of alkylphosphinic acid.* Polymer degradation and stability, 2011. **96**(9): p. 1538-1545.

60. Matzen, M., et al., *Influence of flame retardants on the melt dripping behaviour of thermoplastic polymers.* Materials, 2015. **8**(9): p. 5621-5646.

61. Kandola, B., et al., *Development of a novel experimental technique for quantitative study of melt dripping of themoplastic polymers.* Polymer degradation and stability, 2013. **98**(1): p. 52-63.

62. Beyler, C.L. and M.M. Hirschler, *Thermal decomposition of polymers.* SFPE handbook of fire protection engineering, 2002. **2**: p. 111-131.

63. Lu, S.-Y. and I. Hamerton, *Recent developments in the chemistry of halogen-free flame retardant polymers.* Progress in polymer science, 2002. **27**(8): p. 1661-1712.

64. Zhang, J., et al., *Flame retarding polyamide 6 with melamine cyanurate and layered silicates.* Polymers for Advanced Technologies, 2008. **19**(7): p. 928-936.

65. Kandola, B., M. Ndiaye, and D. Price, *Quantification of polymer degradation during melt dripping of thermoplastic polymers.* Polymer Degradation and Stability, 2014. **106**: p. 16-25.

66. Kandola, B., et al., *Development of a novel experimental technique for quantitative study of melt dripping of themoplastic polymers.* Polymer degradation and stability, 2013. **98**(1): p. 52-63.

67. McKinley, G.H. and T. Sridhar, *Filament stretching rheometry.* Annu. Rev. Fluid Mech., 2002. **34**: p. 375-415.

68. Sur, S. and J. Rothstein, *Drop breakup dynamics of dilute polymer solutions: Effect of molecular weight, concentration, and viscosity.* Journal of Rheology, 2018. **62**(5): p. 1245-1259.

69. Rosello, M., et al., *Dripping-onto-Substrate Capillary Breakup Extensional Rheometry of Low-Viscosity Printing Inks.* Journal of Non-Newtonian Fluid Mechanics, 2019.

70. Jang, B.N. and C.A. Wilkie, *The thermal degradation of bisphenol A polycarbonate in air.* Thermochimica acta, 2005. **426**(1): p. 73-84.

71. Zhou, W., H. Yang, and C. Fang, *Thermal degradation of polycarbonate.* Chemical Industry and Engineering Progress, 2007. **26**(1): p. 23.

72. Lee, L.H., *Mechanisms of thermal degradation of phenolic condensation polymers. I. Studies on the thermal stability of polycarbonate.* Journal of Polymer Science Part A: Polymer Chemistry, 1964. **2**(6): p. 2859-2873.

73. Huang, X., et al., *Mechanistic study on flame retardance of polycarbonate with a small amount of potassium perfluorobutane sulfonate by TGA–FTIR/XPS.* Polymer degradation and stability, 2006. **91**(3): p. 606-613.

74. Levchik, S.V. and E.D. Weil, *Overview of recent developments in the flame retardancy of polycarbonates.* Polymer International, 2005. **54**(7): p. 981-998.

75. Liu, S., et al., *Study on flame-retardant mechanism of polycarbonate containing sulfonate-silsesquioxane-fluoro retardants by TGA and FTIR.* Polymer degradation and stability, 2006. **91**(8): p. 1808-1814.

76. Odochian, L., C. Moldoveanu, and G. Carja, *Contributions to the thermal degradation mechanism under air atmosphere of PTFE by TG–FTIR analysis: Influence of the additive nature.* Thermochimica acta, 2013. **558**: p. 22-28.

77. Odochian, L., et al., *Contributions to the thermal degradation mechanism under nitrogen atmosphere of PTFE by TG-FTIR analysis. Influence of the additive nature.* Thermochimica acta, 2011. **526**(1): p. 205-212.

78. Pawlowski, K.H. and B. Schartel, *Flame retardancy mechanisms of triphenyl phosphate, resorcinol bis (diphenyl phosphate) and bisphenol A bis (diphenyl phosphate) in polycarbonate/acrylonitrile–butadiene–styrene blends.* Polymer International, 2007. **56**(11): p. 1404-1414.

79. McKinley, G.H. and T. Sridhar, *Filament-stretching rheometry of complex fluids.* Annual Review of Fluid Mechanics, 2002. **34**(1): p. 375-415.

80. Clasen, C., et al., *How dilute are dilute solutions in extensional flows.* Journal of Rheology, 2006. **50**(6): p. 849-881.

81. Entov, V. and A. Yarin, *Influence of elastic stresses on the capillary breakup of jets of dilute polymer solutions.* Journal of Fluid Dynamics, 1984. **19**(1): p. 21-29.

82. Kolte, M.I. and P. Szabo, *Capillary thinning of polymeric filaments.* Journal of Rheology, 1999. **43**(3): p. 609-625.

83. McKinley, G.H., *Visco-elasto-capillary thinning and break-up of complex fluids.* 2005.

84. Rodd, L.E., et al., *Capillary break-up rheometry of low-viscosity elastic fluids.* Journal Of Applied Rheology, 2004.

85. Tirtaatmadja, V., G.H. McKinley, and J.J. Cooper-White, *Drop formation and breakup of low viscosity elastic fluids: Effects of molecular weight and concentration.* Physics of Fluids, 2006. **18**(4): p. 043101.

86. Morrison, N.F. and O.G. Harlen, *Viscoelasticity in inkjet printing.* Rheologica Acta, 2010. **49**(6): p. 619-632.

87. Lampe, J., et al., *Impact dynamics of drops on thin films of viscoelastic wormlike micelle solutions.* Journal of Non-Newtonian Fluid Mechanics, 2005. **125**(1): p. 11-23.

88. Dinic, J., et al., *Extensional relaxation times of dilute, aqueous polymer solutions.* ACS Macro Letters, 2015. **4**(7): p. 804-808.

89. Dinic, J., L.N. Jimenez, and V. Sharma, *Pinch-off dynamics and dripping-onto-substrate (DoS) rheometry of complex fluids.* Lab on a Chip, 2017. **17**(3): p. 460-473.

90. Kolte, M.I., H.K. Rasmussen, and O. Hassager, *Transient filament stretching rheometer.* Rheologica Acta, 1997. **36**(3): p. 285-302.

91. Szabo, P., *Transient filament stretching rheometer.* Rheologica Acta, 1997. **36**(3): p. 277-284.

92. Anna, S.L., et al., *An interlaboratory comparison of measurements from filament-stretching rheometers using common test fluids.* Journal of Rheology, 2001. **45**(1): p. 83-114.

93. Tirtaatmadja, V. and T. Sridhar, *A filament stretching device for measurement of extensional viscosity.* Journal of Rheology, 1993. **37**(6): p. 1081-1102.

94. Spiegelberg, S.H., D.C. Ables, and G.H. McKinley, *The role of end-effects on measurements of extensional viscosity in filament stretching rheometers.* Journal of Non-Newtonian Fluid Mechanics, 1996. **64**(2-3): p. 229-267.

95. Bach, A., H.K. Rasmussen, and O. Hassager, *Extensional viscosity for polymer melts measured in the filament stretching rheometer.* Journal of Rheology, 2003. **47**(2): p. 429-441.

96. Anna, S.L. and G.H. McKinley, *Elasto-capillary thinning and breakup of model elastic liquids.* Journal of Rheology, 2001. **45**(1): p. 115-138.

97. Vadillo, D.C., W. Mathues, and C. Clasen, *Microsecond relaxation processes in shear and extensional flows of weakly elastic polymer solutions.* Rheologica Acta, 2012. **51**(8): p. 755-769.

98. Campo-Deano, L. and C. Clasen, *The slow retraction method (SRM) for the determination of ultra-short relaxation times in capillary breakup extensional rheometry experiments.* Journal of Non-Newtonian Fluid Mechanics, 2010. **165**(23): p. 1688-1699.

99. Vadillo, D.C., et al., *Evaluation of the inkjet fluid's performance using the "Cambridge Trimaster" filament stretch and break-up device.* J. Rheol., 2010. **54**: p. 261-282.

100. Greiciunas, E., et al., *Design and operation of a Rayleigh Ohnesorge jetting extensional rheometer (ROJER) to study extensional properties of low viscosity polymer solutions.* Journal of Rheology, 2017. **61**(3): p. 467-476.

101. Keshavarz, B., et al., *Studying the Effects of Elongational Properties on Atomization of Weakly Viscoelastic Solutions Using Rayleigh Ohnesorge Jetting Extensional Rheometry (ROJER).* J. Non-Newtonian Fluid Mech., 2015. **222.** : p. 234-247.

102. Muthukumar, M., *Concentration dependent relaxation times of linear polymers in dilute solutions.* Macromolecules, 1984. **17**(4): p. 971-973.

103. Dinic, J., L.N. Jimenez, and V. Sharma, *Pinch-off dynamics and dripping-onto-substrate (DoS) rheometry of complex fluids.* Lab on a Chip, 2017.

104. Mun, R.P., J.A. Byars, and D.V. Boger, *The effects of polymer concentration and molecular weight on the breakup of laminar capillary jets.* Journal of Non-Newtonian Fluid Mechanics, 1998. **74**(1): p. 285-297.

105. Clasen, C., P.M. Phillips, and L. Palangetic, *Dispensing of rheologically complex fluids: the map of misery.* AIChE Journal, 2012. **58**(10): p. 3242-3255.

106. Papageorgiou, D.T., *On the breakup of viscous liquid threads.* Physics of Fluids, 1995. **7**(7): p. 1529-1544.

107. Graessley, W.W., *The entanglement concept in polymer rheology*, in *The Entanglement Concept in Polymer Rheology*. 1974, Springer. p. 1-179.

108. Takamura, K., H. Fischer, and N.R. Morrow, *Physical properties of aqueous glycerol solutions.* Journal of Petroleum Science and Engineering, 2012. **98**: p. 50-60.

109. Wagner, C., L. Bourouiba, and G.H. McKinley, *An analytic solution for capillary thinning and breakup of FENE-P fluids.* Journal of Non-Newtonian Fluid Mechanics, 2015. **218**: p. 53-61.

110. Rodd, L.E., et al., *Capillary break-up rheometry of low-viscosity elastic fluids.* Journal Of Applied Rheology, 2004.

111. Rubinstein, M. and R.H. Colby, *Polymer Physics*. Vol. 23. 2003: Oxford university press New York.

112. Bazilevskii, A., V. Entov, and A. Rozhkov, *Breakup of an Oldroyd liquid bridge as a method for testing the rheological properties of polymer solutions.* Polymer Science Series Of Vysokomolekuliarnye Soedineniia, 2001. **43**(7): p. 716-726.

113. He, C., S. Costeux, and P. Wood-Adams, *A technique to infer structural information for low level long chain branched polyethylenes.* Polymer, 2004. **45**(11): p. 3747-3754.

114. de Gans, B.-J., P.C. Duineveld, and U.S. Schubert, *Inkjet Printing of Polymers: State of the Art and Future Developments.* Adv. Mater, 2004. **16**: p. 203-213.

115. Basaran, O.A., H. Gao, and P.P. Bhat, *Nonstandard Inkjets.* Annu. Rev. Fluid Mech., 2013. **45**: p. 85-113.

116. Martin, G.D., S.D. Hoath, and I.M. Hutchings, *Inkjet printing - the physics of manipulating liquid jets and drops.* J. Phys., 2008. **105**: p. 012001.

117. Morrison, N.F. and O.G. Harlen, *Viscoelasticity in inkjet printing.* Rheol. Acta, 2010. **49**: p. 619-632.

118. Hoath, S.D., et al., *Inkjet printing of weakly elastic polymer solutions.* J. Non-Newt. Fluid Mech, 2014. **205**: p. 1-10.

119. Christanti, Y. and L.M. Walker, *Surface tension driven jet break up of strain-hardening polymer solutions.* J. Non-Newtonian Fluid Mech., 2001. **100**: p. 9-26.

120. Christanti, Y. and L.M. Walker, *Effect of fluid relaxation time of dilute polymer solutions on jet breakup due to a forced disturbance.* J. Rheol., 2002. **46**: p. 733-748.

121. Gordon, M., J. Yerushalmi, and R. Shinnar, *Instability of Jets of Non-Newtonian Fluids.* J. Rheol., 1973. **17**: p. 303-324.

122. Dinic, J., et al., *Extensional Relaxation Times of Dilute, Aqueous Polymer Solutions.* ACS Macro Lett., 2015. **4**: p. 804-808.

123. Dinic, J., L.N. Jimenez, and V. Sharma, *Pinch-off dynamics and dripping-onto-substrate (DoS) rheometry of complex fluids.* Lab on a Chip, 2017. **17**: p. 460-473.

124. Spiegelberg, S.H. and G.H. McKinley, *Stress relaxation and elastic decohesion of viscoelastic polymer solutions in extensional flow.* J. Non-Newtonian Fluid Mech., 1996. **67**: p. 49-76.

125. Greiciunas, E., et al., *Design and operation of a Rayleigh Ohnesorge jetting extensional rheometer (ROJER) to study extensional properties of low viscosity polymer solutions.* J. Rheol., 2017. **61**: p. 467-476.

126. Sur, S. and J.P. Rothstein, *Drop breakup dynamics of dilute polymer solutions: Effect of molecular weight, concentration and viscosity* J. Rheol., 2018. **62**(5): p. 1245-1259.

127. Clasen, C., *Capillary breakup extensional rheometry of semi-dilute polymer solutions.* Korea-Australia Rheol. J., 2010. **22**: p. 331-338.

128. Clasen, C., et al., *The beads-on-string structure of viscoelastic threads.* J. Fluid Mech., 2006. **556**: p. 283-308.

129. Clasen, C., et al., *How dilute are dilute solutions in extensional flows?* J. Rheol., 2006. **50**: p. 849-881.

130. Brandrup, J. and E.H. Immergut, *Polymer Handbook.* 1989, New York: John Wiley & Sons.

131. Crooks, R., J.J. Cooper-White, and D.V. Boger, *The role of dynamic surface tension and elasticity on the dynamics of drop impact.* Chem. Eng. Sci., 2001. **56**: p. 5575-5592.

132. Rothstein, J.P., *Transient extensional rheology of wormlike micelle solutions.* J. Rheol., 2003. **47**(5): p. 1227-1247.

133. Doi, M. and S.F. Edwards, *The Theory of Polymer Dynamics*. 1986, Oxford: Oxford University Press.

134. Bhattacharjee, P.K., et al., *Extensional rheometry of entangled solutions.* Macromol., 2002. **35**: p. 10131-10148.

135. Rothstein, J.P. and G.H. McKinley, *A comparison of the stress and birefringence growth of dilute, semi-dilute and concentrated polymer solutions in uniaxial extensional flows.* J. Non-Newtonian Fluid Mech., 2002. **108**: p. 275-290.

136. Palangetic, L., et al., *Dispersity and spinnability: Why highly polydisperse polymer solutions are desirable for electrospinning.* Polymer, 2014. **55**: p. 4920-4931.

137. Campo-Deano, L. and C. Clasen, *The slow retraction method (SRM) for the determination of ultra-short relaxation times in capillary breakup extensional rheometry experiments.* J. Non-Newt. Fluid Mech., 2010. **2010**(165).

138. Rosello, M., et al., *Influence of the Nozzle Shape on the Breakup Behavior of Continuous Ink Jets.* J. Fluid Eng., 2018. **140**: p. 031202.

139. Eggers, J., *Nonlinear dynamics and breakup of free-surface flows.* Reviews of Modern Physics, 1997. **69**(3): p. 865-929.

140. Wagner, C., L. Bourouiba, and G.H. McKinley, *An analytic solution for capillary thinning and breakup of FENE-P fluids.* J. Non-Newt. Fluid Mech, 2015. **218**: p. 53-61.

141. Ng, S.L., et al., *Extensional viscosity measurements of dilute solutions of various polymers.* J. Non-Newt. Fluid Mech, 1996. **65**: p. 291-298.

142. Dinic, J., M. Biagioli, and V. Sharma, *Pinch-off dynamics and extensional relaxation times of intrinsically semi-dilute polymer solutions characterized by dripping-onto-substrate rheometry.* Journal of Polymer Science Part B: Polymer Physics, 2017. **55**(22): p. 1692-1704.

143. Arnolds, O., et al., *Capillary breakup extensional rheometry (CaBER) on semi-dilute and concentrated polyethyleneoxide (PEO) solutions.* Rheologica acta, 2010. **49**(11-12): p. 1207-1217.

144. Scriven, L.E. and C.V. Sternling, *The Marangoni effects.* Nature, 1960. **187**: p. 186-188.

145. Angelini, T.E., et al., *Bacillus subtilis spreads by surfing on waves of surfactant.* PNAS, 2009. **106**: p. 18109-18113.

146. Fauvart, M., et al., *Surface tension gradient control of bacterial swarming in colonies of Pseudomonas aeruginosa.* Soft Matter, 2012. **8**: p. 70-76.

147. Schildknecht, H., *Chemical ecology-a chapter of modern natural products chemistry.* Angewandte Chemie International, 1976. **15**: p. 214-222.

148. Andersen, N.M., *A comparative study of locomotion on the water surface in semiaquatic bugs (Insects, Hemiptera, Gerromorpha).* Vidensk. Meddr. Dan. Naturhist. Foren. , 1976. **139**: p. 337-96.

149. Betz, O., *Performance and adaptive value of tarsal morphology in rove beetles of the genus Stenus (Coleoptera, Staphylinidae).* J. Exp. Biol., 2002. **205**: p. 1097-113.

150. Bush, J.W. and D.L. Hu, *Walking on water: biolocomotion at the interface.* Annu. Rev. Fluid Mech., 2006. **38**: p. 339-369.

151. Rayleigh, L., *Measurements of the amount of oil necessary in order to check the motions of camphor upon water.* Proc. R. Soc. Lond., 1889. **47**: p. 364-367.

152. Suematsu, N.J., et al., *Mode-switching of the self-motion of a camphor boat depending on the diffusion distance of camphor molecules.* The Journal of Physical Chemistry C, 2010. **114**(21): p. 9876-9882.

153. Renney, C., A. Brewer, and T.J. Mooibroek, *Easy demonstration of the Marangoni Effect by prolonged and directional motion:"Soap Boat 2.0".* Journal of Chemical Education, 2013. **90**(10): p. 1353-1357.

154. Nakata, S., et al., *Self-rotation of a camphor scraping on water: new insight into the old problem.* Langmuir, 1997. **13**(16): p. 4454-4458.

155. Koyano, Y., et al., *Relationship between the size of a camphor-driven rotor and its angular velocity.* Physical Review E, 2017. **96**(1): p. 012609.

156. Kralchevsky, P.A. and K. Nagayama, *Capillary interactions between particles bound to interfaces, liquid films and biomembranes.* Adv. Coll. Int. Sci., 2000. **85**: p. 145-192.

157. Vella, D. and L. Mahadevan, *The "Cheerios Effect".* American Journal of Physics, 2005. **73**: p. 817-825.

158. Zeng, C., H. Bissig, and A.D. Dinsmore, *Particles on droplets: from fundamental physics to novel materials.* Solid State Com., 2006. **139**: p. 547-556.

159. Daniello, R., et al., *The effect of contact angle and density on the orientation, stability and assembly of floating cubes.* Phys. Rev. E, 2014. **89**: p. 023014.

160. Kassuga, T.D. and J.P. Rothstein, *Buckling of particle laden interfaces.* J. Colloid Int. Sci., 2015. **448**: p. 287-296.

161. Kassuga, T.D. and J.P. Rothstein, *The Effect of Shear and Confinement on the Buckling of Particle-Laden Interfaces* J. Phys.: Condens. Matter, 2016. **28**(2): p. 025101.

162. Cavallaro, M., et al., *Curvature-driven capillary migration and assembly of rod-like particles.* Proc. Natl. Acad. Sci., 2011. **108**: p. 20923-20928.

163. Loudet, J.C. and B. Pouligny, *How do mosquito eggs self-assemble on the water surface?* Eur. Phys. J. E, 2011. **34**: p. 76.

164. Sane, A., S. Mandre, and I. Kim, *Surface tension of flowing soap films.* Journal of Fluid Mechanics, 2018. **841**.

165. Akella, V., et al., *Dynamics of a camphoric acid boat at the air–water interface.* Physics Letters A, 2018. **382**(17): p. 1176-1180.

166. Ismagilov, R.F., et al., *Autonomous Movement and Self-Assembly.* Angew. Chem. Int. Ed., 2002. **41**: p. 652-654.

167. Vulinec, K., *Swimming in whirligig beetles (Coleoptera: Gyrinidae): a possible role of the pygidial gland secretion.* The Coleopterists' Bulletin, 1987: p. 151-153.

168. Whitesides, G.M. and B. Grzybowski, *Self-assembly at all scales.* Science, 2002. **295**(5564): p. 2418-2421.

169. Gidituri, H., M.V. Panchagnula, and A. Pototsky, *Dynamics of a fully wetted Marangoni surfer at the fluid–fluid interface.* Soft matter, 2019. **15**(10): p. 2284-2291.

170. Sur, S., H. Masoud, and J.P. Rothstein, *Translational and Rotational Motion of Disk-Shaped Marangoni Surfers.* submitted Physics of Fluids, 2019.

171. Takabatake, F., et al., *Spontaneous mode-selection in the self-propelled motion of a solid/liquid composite driven by interfacial instability.* The Journal of chemical physics, 2011. **134**(11): p. 114704.

172. Nagai, K.H., et al., *Rotational motion of a droplet induced by interfacial tension.* Physical Review E, 2013. **87**(1): p. 013009.

173. Bush, J.W.M. and D.L. Hu, *Walking on Water: Biolocomotion at the Interface.* Annu. Rev. Fluid Mech., 2006. **38**: p. 339-69.

174. Würger, A., *Thermally driven Marangoni surfers.* Journal of Fluid Mechanics, 2014. **752**: p. 589-601.

175. Lauga, E. and A.M. Davis, *Viscous marangoni propulsion.* Journal of Fluid Mechanics, 2012. **705**: p. 120-133.

176. Masoud, H. and H.A. Stone, *A reciprocal theorem for Marangoni propulsion.* Journal of Fluid Mechanics, 2014. **741**.

177. Masoud, H. and M.J. Shelley, *Collective surfing of chemically active particles.* Physical review letters, 2014. **112**(12): p. 128304.

178. Vandadi, V., S.J. Kang, and H. Masoud, *Reverse Marangoni surfing.* Journal of Fluid Mechanics, 2017. **811**: p. 612-621.

179. Fei, W., Y. Gu, and K.J. Bishop, *Active colloidal particles at fluid-fluid interfaces.* Current opinion in colloid & interface science, 2017. **32**: p. 57-68.

180. Vella, D. and L. Mahadevan, *The "cheerios effect".* American journal of physics, 2005. **73**(9): p. 817-825.